

Syracuse University

SURFACE at Syracuse University

Dissertations - ALL

SURFACE at Syracuse University

Summer 7-16-2021

Performance Analysis and Learning Algorithms in Advanced Wireless Networks

Xueyuan Wang
Syracuse University

Follow this and additional works at: <https://surface.syr.edu/etd>



Part of the [Electrical and Computer Engineering Commons](#)

Recommended Citation

Wang, Xueyuan, "Performance Analysis and Learning Algorithms in Advanced Wireless Networks" (2021).
Dissertations - ALL. 1421.
<https://surface.syr.edu/etd/1421>

This Dissertation is brought to you for free and open access by the SURFACE at Syracuse University at SURFACE at Syracuse University. It has been accepted for inclusion in Dissertations - ALL by an authorized administrator of SURFACE at Syracuse University. For more information, please contact surface@syr.edu.

ABSTRACT

Over the past decade, wireless data traffic has experienced an exponential growth, especially with multimedia traffic becoming the dominant traffic, and such growth is expected to continue in the near future. This unprecedented growth has led to an increasing demand for high-rate wireless communications. Key solutions for addressing such demand include extreme network densification with more small-cells, the utilization of high frequency bands, such as the millimeter wave (mmWave) bands and terahertz (THz) bands, where more bandwidth is available, and unmanned aerial vehicle (UAV)-enabled cellular networks. With this motivation, different types of advanced wireless networks are considered in this thesis. In particular, mmWave cellular networks, networks with hybrid THz, mmWave and microwave transmissions, and UAV-enabled networks are studied, and performance metrics such as the signal-to-interference-plus-noise ratio (SINR) coverage, energy coverage, and area spectral efficiency are analyzed. In addition, UAV path planning in cellular networks are investigated, and deep reinforcement learning (DRL) based algorithms are proposed to find collision-free UAV trajectory to accomplish different missions.

In the first part of this thesis, mmWave cellular networks are considered. First, K -tier heterogeneous mmWave cellular networks with user-centric small-cell deployments are studied. Particularly, a heterogeneous network model with user equipments (UEs) being distributed according to Poisson cluster processes (PCPs) is considered. Distinguishing features of mmWave communications including directional beamforming and a detailed path loss model are taken into account. General expressions for the association probabilities of different tier base stations (BSs) are determined. Using tools from stochastic geometry, the Laplace transform of the interference is characterized and general expressions for the SINR coverage probability and area spectral efficiency are derived. Second, a distributed multi-agent learning-based algorithm for beamforming in mmWave multiple input multiple output (MIMO) networks is proposed to maximize the sum-rate of all UEs.

Following the analysis of mmWave cellular networks, a three-tier heterogeneous network is

considered, where access points (APs), small-cell BSs (SBSs) and macrocell BSs (MBSs) transmit in THz, mmWave, microwave frequency bands, respectively. By using tools from stochastic geometry, the complementary cumulative distribution function (CCDF) of the received signal power, the Laplace transform of the aggregate interference, and the SINR coverage probability are determined.

Next, system-level performance of UAV-enabled cellular networks is studied. More specifically, in the first part, UAV-assisted mmWave cellular networks are addressed, in which the UE locations are modeled using PCPs. In the downlink phase, simultaneous wireless information and power transfer (SWIPT) technique is considered. The association probability, energy coverages and a successful transmission probability to jointly determine the energy and SINR coverages are derived. In the uplink phase, a scenario that each UAV receives information from its own cluster member UEs is taken into account. The Laplace transform of the interference components and the uplink SINR coverage are characterized. In the second part, cellular-connected UAV networks is investigated, in which the UAVs are aerial UEs served by the ground base stations (GBSs). 3D antenna radiation combining the vertical and horizontal patterns is taken into account.

In the final part of this thesis, deep reinforcement learning based algorithms are proposed for UAV path planning in cellular networks. Particularly, in the first part, multi-UAV non-cooperative scenarios is considered, where multiple UAVs need to fly from initial locations to destinations, while satisfying collision avoidance, wireless connectivity and kinematic constraints. The goal is to find trajectories for the cellular-connected UAVs to minimize their mission completion time. The multi-UAV trajectory optimization problem is formulated as a sequential decision making problem, and a decentralized DRL approach is proposed to solve the problem. Moreover, multiple UAV trajectory design in cellular networks with a dynamic jammer is studied, and a learning-based algorithm is proposed. Subsequently, a UAV trajectory optimization problem is considered to maximize the collected data from multiple Internet of things (IoT) nodes under realistic constraints. The problem is translated into a Markov decision process (MDP) and dueling double deep Q-network (D3QN) is proposed to learn the decision making policy.

PERFORMANCE ANALYSIS AND LEARNING ALGORITHMS IN ADVANCED WIRELESS NETWORKS

By

Xueyuan Wang

B.E., Beijing University of Posts and Telecommunications, 2013

M.S., Syracuse University, 2016

DISSERTATION

Submitted in partial fulfillment of the requirements for the degree of
Doctor of Philosophy in Electrical and Computer Engineering

Syracuse University
July 2021

Copyright © Xueyuan Wang, 2021

All Rights Reserved

ACKNOWLEDGMENTS

Throughout the writing of this dissertation and my doctoral study, I have received a great deal of support and assistance.

First, I would like to take this opportunity to thank my advisor, Prof. Mustafa Cenk Gursoy, for his invaluable advice and consistent support throughout my doctoral study. His immense knowledge and supportive understanding have inspired me to find interesting research ideas and encouraged me to solve the difficulties in research. Without his guidance, this dissertation would not have been possible.

I would like to extend sincere thanks to my defense committee members Prof. Lixin Shen, Prof. Pramod Varshney, Prof. Biao Chen, Prof. Makan Fardad, and Prof. Qinru Qiu for their great support and valuable suggestions.

I would also like to thank the past and current “Wireless Communication and Networking Lab” members for all the helpful discussions and technical assistance in the process of writing this dissertation.

Last but not the least, I would like to thank my family and my boyfriend for their understanding and sustained backing. Thanks to their unconditional love, care and support, I could complete my study with great peace of mind. In my life and study, I also received care and help from my friends. They gave me many wonderful memories. Thank you all for always being there for me.

TABLE OF CONTENTS

Acknowledgments	v
List of Tables	xv
List of Figures	xvii
1 Introduction	1
1.1 Background	1
1.1.1 MmWave and Terahertz Communication Networks	1
1.1.2 User-Centric Deployment of Small Cells in Heterogeneous Networks	2
1.1.3 UAV-Enabled Networks	3
1.1.4 Deep Reinforcement Learning	5
1.2 Related Prior Work	6
1.2.1 MmWave Cellular Networks	6
1.2.2 Terahertz Communication Networks	7
1.2.3 User-Centric Small Cell Deployment	8
1.2.4 Beamforming in MIMO Networks	10
1.2.5 System-Level Analysis of UAV-Enabled Networks	11
1.2.6 Trajectory Design for Cellular-Connected UAVs	13
1.2.7 UAV Path Planning for Data Collection	15
1.2.8 Path Design for UAVs in the Presence of Jamming Attacks	17
1.3 Outline and Main Contributions	18

1.4	Bibliographic Note	23
2	Preliminaries	26
2.1	Point Processes	26
2.1.1	Poisson Point Process	26
2.1.2	Neyman-Scott Cluster Process	28
2.2	Channel Modeling	29
2.2.1	Path Loss	29
2.2.2	Shadowing	33
2.2.3	Small-Scale Fading	34
2.2.4	Antenna Gain	34
2.3	Reinforcement Learning	39
3	Coverage in Downlink Heterogeneous mmWave Cellular Networks with User-Centric Small Cell Deployment	43
3.1	System Model	43
3.1.1	Base Station Distribution Modeling	43
3.1.2	User Distribution Modeling	44
3.1.3	Channel Modeling	44
3.2	Path Loss Statistics	46
3.2.1	Path Loss in the 0^{th} Tier	46
3.2.2	Path Loss in the j^{th} Tier ($j \in \mathcal{K}$)	47
3.3	User Association	48
3.3.1	Association Criterion	49
3.3.2	Association Probability	49
3.3.3	Analysis of Special Cases for Association Probability	51
3.4	SINR Coverage Probability Analysis	53
3.4.1	Signal to Interference Plus Noise Ratio	53

3.4.2	SINR Coverage Probability	54
3.4.3	Analysis of Special Cases for Coverage Probability	56
3.4.4	Analysis of Noise-Limited Networks	57
3.4.5	Area Spectral Efficiency Analysis	58
3.4.6	Analysis of Practical Antenna Radiation Patterns	58
3.4.7	Analysis with Shadowing	59
3.5	Numerical Results and Discussions	60
3.5.1	Association and Coverage Probabilities	61
3.5.2	Impact of the Small-Scale Fading and Shadow Fading	63
3.5.3	Impact of the Interference	65
3.5.4	Impact of Antenna Modeling	65
3.5.5	Biasing Factor Design of the Picocell BSs	67
3.5.6	Dense Networks	69
3.5.7	Comparison between PCP Model and PPP Model	70
4	Uplink Coverage in Heterogeneous mmWave Cellular Networks with Clustered Users	72
4.1	System Model	72
4.1.1	Base Station Distribution Modeling	72
4.1.2	User Equipment Distribution Modeling	73
4.1.3	Directional Beamforming	73
4.1.4	Channel Model	74
4.2	Distance Characterization	74
4.2.1	Distance from the Typical UE to its Cluster Center BS r_{i0} ($i \in \mathcal{K}_u$)	75
4.2.2	Distance from the Typical UE (the origin) to the Nearest j^{th} Tier LOS/NLOS BS r_j ($j \in \mathcal{K}$)	75
4.2.3	Distance from the k^{th} Tier UE to the j^{th} tier BSs r_{jk} ($j \in \mathcal{K}, k \in \mathcal{K}_u$)	75
4.3	Association Probability	76
4.3.1	Association Criterion	76

4.3.2	Association Probability	77
4.3.3	Conditional PDF of the Distance from the Typical UE to the Associated BS $r_{ij,s}$ Given $S_{ij,s}$	78
4.4	Coverage Analysis	79
4.4.1	Signal-to-Interference-Plus-Noise Ratio	79
4.4.2	SINR Coverage Probability	80
4.4.3	Laplace Transforms of the Interference Terms	80
4.5	Extensions and Special Cases	81
4.5.1	Extension to Nakagami Fading	82
4.5.2	Extension to UE Fractional Power Control	82
4.5.3	Average Ergodic Spectral Efficiency	84
4.5.4	Special Cases	85
4.6	Numerical Results	87
4.6.1	Impact of the Cluster Size	88
4.6.2	Impact of Interference and the Small-Scale Fading	91
4.6.3	Impact of the LOS Probability Exponent ϵ	92
4.6.4	Impact of the Biasing Factor and Transmit Power	94
4.6.5	Impact of the Density of BSs	96
5	Multi-Agent Double Deep Q-Learning for Beamforming in mmWave MIMO Net- works	98
5.1	System Model	98
5.1.1	System Model	98
5.1.2	Channel Model	99
5.1.3	Achievable Rate	101
5.2	Distributed multi-agent DDQN for mmWave MIMO networks	101
5.2.1	State	102
5.2.2	Action	104

5.2.3	Reward	104
5.3	Performance Evaluation	105
5.3.1	Environment Setting	105
5.3.2	Hyperparameters	105
5.3.3	Experiment results	106
6	Coverage in Networks with Hybrid Terahertz, Millimeter Wave, and Microwave Trans-	
	missions	109
6.1	System Model	109
6.1.1	Deployment Model	109
6.1.2	Channel Modeling	110
6.2	Path Loss Based Association	112
6.2.1	Characterization of the Nearest 2D Distance	112
6.2.2	Association Criterion	112
6.2.3	Association Probabilities	113
6.2.4	Conditional PDF of the Distance of the Main Link	114
6.3	Coverage Analysis	114
6.3.1	Distribution of the Received Signal Power	114
6.3.2	Laplace Transform of the Aggregate Interference	115
6.3.3	SINR Coverage Probability	116
6.4	Numerical Results	117
6.4.1	Impact of the Density of THz APs	118
6.4.2	Impact of the Beamwidth of the Main Lobe at the THz APs	120
7	Coverage Analysis for Energy-Harvesting UAV-assisted mmWave Cellular Networks	123
7.1	System Model	123
7.1.1	BS and UE Deployment	123
7.1.2	Downlink and Uplink Transmission	124

7.1.3	Path Loss Modeling	125
7.1.4	Antenna Gain	126
7.1.5	Small-Scale Fading	126
7.2	Distance Distributions	126
7.2.1	The Distance R_0 from the Typical UE to the 0^{th} Tier UAV	126
7.2.2	The Distance R_U^s from the Typical UE to the Nearest LOS/NLOS UAV from the 1^{st} Tier	128
7.2.3	The Distance R_G^s from the Typical UE to the Nearest LOS/NLOS GBS from the 2^{nd} Tier	128
7.2.4	The Distance R_{UU} from a UE to the Other Cluster Center UAV	128
7.3	User Association	129
7.3.1	Downlink Association	129
7.3.2	Uplink Association	131
7.4	Downlink Coverage Analysis	131
7.4.1	Interference	131
7.4.2	Harvested Energy and Signal to Interference Plus Noise Ratio	132
7.4.3	Energy Coverage Probability	132
7.4.4	SINR Coverage Probability	134
7.4.5	Successful Transmission Probability	134
7.5	Uplink Coverage Analysis	135
7.5.1	Uplink SINR Coverage	136
7.5.2	Average Throughput	137
7.6	Generalizations and Special Cases	138
7.6.1	Multi-Tier Multi-Height Model	138
7.6.2	Noise-Limited Model	139
7.7	Extensions to UAV-assisted IoT Networks with 3D Antenna Patterns	140
7.7.1	3D Antenna Pattern	140

7.7.2	Association analysis	141
7.7.3	Successful Transmission Probability	142
7.8	Numerical Results	142
7.8.1	Impact of the Cluster Size	142
7.8.2	Impact of the Interference	146
7.8.3	Impact of the UAV Height	147
7.8.4	Impact of the Power Splitting Component	149
7.8.5	Impact of the τ	150
7.8.6	Numerical Results when Considering 3D Antenna Patterns	151
8	Coverage Analysis for Cellular-Connected UAVs with 3D Antenna Patterns	154
8.1	System Model	154
8.1.1	Ground-to-Air Channel Model	154
8.1.2	3D Antenna Patterns for GBSs/UAVs	155
8.2	SINR Coverage Analysis	155
8.2.1	SINR Coverage Probability	156
8.3	Numerical Results	157
9	Learning-Based Trajectory Optimization for Cellular-Connected UAVs	160
9.1	Learning-Base UAV Trajectory Optimization with Collision Avoidance and Connectivity Constraints	160
9.1.1	System Model	160
9.1.2	Multi-UAV Trajectory Optimization	163
9.1.3	Reinforcement Learning Based Approach	167
9.1.4	Decentralized Deep Reinforcement Learning Algorithm	171
9.1.5	Numerical Results	175
9.2	Jamming-Resilient Path Planning for Multiple UAVs via Deep Reinforcement Learning	184

9.2.1	System Model	184
9.2.2	Proposed Algorithm	185
9.2.3	Numerical Results	188
10	Collision-Aware UAV Trajectories for Data Collection via Reinforcement Learning	193
10.1	System Model and Problem Formulation	193
10.1.1	System Model	193
10.1.2	Channel Model	195
10.1.3	Signal-to-Noise Ratio (SNR) and Rate	195
10.1.4	Scheduling	196
10.1.5	Problem Formulation	197
10.2	Algorithm	199
10.2.1	Reinforcement Learning Formulation	199
10.2.2	D3QN Path Planning Algorithm for Data Collection	202
10.3	Numerical Results	205
10.3.1	Environment Setting and Hyperparameters	205
10.3.2	Training	206
10.3.3	Testing of Navigation in Different Scenarios	207
10.3.4	Impact of the SNR Threshold	212
10.3.5	Comparison with Other Algorithms	212
11	Conclusion and Future Directions	214
11.1	Summary	214
11.2	Future Research Directions	220
11.2.1	UAV-to-UAV Communications	220
11.2.2	Power Constrained UAV Trajectory Design	220
11.2.3	Three-Dimensional (3D) UAV Path Planning	220
11.2.4	Jamming Attacks in UAV-Enabled Networks	220

A	Proof of Theorems and Lemmas	222
1	Proof of Lemma 3.1	222
2	Proof of Lemma 3.2	223
3	Proof of Lemma 3.3	224
4	Proof of Theorem 3.1	225
5	Proof of Lemma 3.4	226
6	Proof of Lemma 3.5	228
7	Proof of Lemma 3.6	228
8	Proof for Lemma 4.1	229
9	Proof for Lemma 4.2	229
10	Proof of Theorem 4.1	231
11	Proof of Theorem 4.2	232
12	Proof of Lemma 4.3	233
13	Proof of Lemma 4.4	234
14	Proof of Theorem 6.1	235
15	Proof of Theorem 6.2	236
16	Proof of Theorem 6.3	236
17	Proof of Theorem 6.4	237
18	Proof of Lemma 7.1	238
19	Proof of Lemma 7.2	238
20	Proof of Theorem 7.1	240
21	Proof of Theorem 7.2	241
22	Proof of Theorem 7.3	242
	References	244

LIST OF TABLES

3.1	Parameter Values Table	60
4.1	Parameters Table	88
6.1	Table of Parameters	118
7.1	Tiers in the Network	124
7.2	Table of Parameter Values	142
8.1	Table of Parameter Values	157
9.1	Performance of different algorithms in different environments in terms of success rate (SR), collision rate (CR), and disconnection rate (DR) (all rates are in %).	180
9.2	Performance for Multi-Agent Navigation	183
9.3	Performance comparison in terms of success rate, disconnection rate, and collision rate.	191
10.1	SR, DR, DSR and CR performance when different number of nodes (N) need to upload data, and $D_0^L \in [1, 3]$, $J \in [2, 10]$	208
10.2	SR, DR, and DSR performance when different amount of data D_0^L needs to be collected from each node, and $N \in [5, 10]$, $J \in [2, 10]$	209
10.3	CR, SR, and DR performance when different number of other UAVs J exist, and $N \in [5, 10]$, $D_0^L \in [1, 3]$	211

10.4	SR, and DR, DSR and CR performance of different algorithms, when $N \in [5, 10]$, $D_0^L \in [1, 3]$ data unit and $J \in [2, 10]$	213
------	--	-----

LIST OF FIGURES

2.1	Illustrations for PPP and PCPs.	29
2.2	LOS ball model	31
2.3	Illustrations of the antenna pattern of GBSs on the vertical plane.	37
2.4	An illustration of the vertical antenna configuration at the UAVs, where H is the height difference.	37
2.5	An illustration of reinforcement learning Scheme.	40
2.6	The structure of the dueling deep Q-network.	42
3.1	Association probabilities as a function of the cluster size.	61
3.2	SINR coverage probability of each tier as a function of the SINR threshold when the cluster size is 30 (i.e., $\sigma_u = 30$ and $R_{clu} = 30$).	61
3.3	SINR coverage probability as a function of the cluster size when $T = 30$ dB.	62
3.4	SINR coverage probability as a function of the SINR threshold for Nakagami and Rayleigh fading.	63
3.5	SNR coverage probability as a function of the threshold when shadowing is considered for Thomas cluster process.	64
3.6	Comparison of SINR coverage probability and SNR coverage probability as a function of the threshold for different values of the cluster size.	65
3.7	SINR coverage probability as a function of the threshold in dB for different values of antenna main lobe gain M and the beamwidth of the main lobe θ	66
3.8	SINR coverage probability as a function of the threshold in dB for Thomas cluster process ($\sigma_u = 10$) considering sectored and cosine antenna radiation patterns.	67

3.9	Association probability and coverage probability as a function of B_1/B_2 when $T = 30\text{dB}$ for the Thomas cluster process. (b) plots the total coverage of the network with different cluster sizes.	67
3.10	Association probability, SNR coverage probability of each tier, and SINR coverage probability of each tier as a function of λ_1/λ_2 for the Matérn cluster process when the cluster size is 30 and $T = 30\text{dB}$	68
3.11	Area spectrum efficiency as a function of λ_1/λ_2 for the Matérn cluster process, when the cluster size is 30 and $T = 30\text{dB}$	69
3.12	SINR coverage probability as a function of (a) the SINR threshold, (b) B_1/B_2 and (c) λ_1/λ_2 for three different types of UE distribution, namely, Poisson point process (PPP), Thomas cluster process (TCP) with $\sigma_u = 30$ and Matérn cluster process (MCP) with $R_{clu} = 30$ except (c).	70
4.1	Two-tier heterogeneous network model, where macrocells (blue triangles) and small-cells (black squares) are distributed as independent PPPs, and UEs are distributed around small-cells according to a Gaussian distribution. The average number of UEs per cluster is 5.	73
4.2	An illustration of different distances from the BSs to UEs.	74
4.3	APs and SINR CPs as a function of the standard derivation of UE distribution when $T = 10\text{dB}$	88
4.4	APs and SINR CPs as a function of σ when $T = 10\text{dB}$ in a three-tier heterogeneous network.	90
4.5	SINR CPs as a function of threshold T	90
4.6	SNR and SINR CPs as a function of threshold for different cluster size σ	91
4.7	SNR and SINR CPs as a function of threshold for different cluster size σ	92
4.8	APs and SINR CPs for different tier as a function of the LOS probability function exponent ϵ when $\sigma = 25$ and $T = 10\text{dB}$	92

4.9	APs as a function of the biasing factor ratio B_1/B_2 and the BS transmit power ratio P_1/P_2 when $\sigma = 25$ and $T = 10\text{dB}$	94
4.10	SINR CP as a function of B_1/B_2 when $\sigma = 25$ and $T = 10\text{dB}$	95
4.11	APs as a function of the density of small-cell BSs λ_1 , when $\sigma = 25$ and $T = 10\text{dB}$	96
4.12	SINR CPs of each tier and the entire network as a function of the density of small-cell BSs λ_1 , when $\sigma = 25$ and $T = 10\text{dB}$	97
5.1	An illustration of the procedure in one time step.	102
5.2	An illustration of the simulation environment.	106
5.3	Sum-rate as a function of number of UEs for different number of BSs.	107
5.4	A performance comparison of testing results, when the DDQN is trained for the exact number of UEs and the DDQN is trained for 6 UEs. The number of BS is one.	108
6.1	An illustration of a three-tier HetNet.	110
6.2	Association probability as a function of the density of the APs.	118
6.3	CCDF of the receive signal power as a function of the density of APs, when $T = -30\text{ dB}$ and $\theta_1 = 15^\circ$	119
6.4	SINR coverage probability as a function of the density of APs, when $T = -5\text{ dB}$ and $\theta_1 = 15^\circ$	120
6.5	CCDF of the receive signal power as a function of beamwidth of the main lobe at the APs, when $T = -30\text{ dB}$ and $\lambda_1 = 10^{-2}/\text{m}^2$	121
6.6	SINR coverage probability as a function of beamwidth of the main lobe at the APs, when $T = -5\text{ dB}$ and $\lambda_1 = 10^{-2}/\text{m}^2$	122
7.1	An illustration of the system model of a UAV-assisted mmWave cellular network.	125
7.2	An illustration of difference distance in the network.	127
7.3	Association probability as functions of the cluster size with parameter values listed in Table 7.2.	143

7.4	STP of the network and each tier BSs as a function of the cluster size when $\tau = T$, $\gamma_E = -40$ dB, $\gamma_{sinr} = 0$ dB and $\rho = 0.5$	143
7.5	STP, EC and SINRC probabilities as functions of the cluster size when $\tau = T$, $\gamma_E = -40$ dB, $\gamma_{sinr} = 0$ dB. And $\rho = 0.5$ for the SWIPT scenario.	144
7.6	Uplink SINR coverage probability as a function of the cluster size when $\tau = 0.5T$, $\rho = 0$, $\gamma^{UL} = -20$ dB, and $\sigma = 10$	145
7.7	Association probability and STP as a function of σ for Thomas cluster process, when $\gamma_E = -40$ dB, $\gamma_{sinr} = 0$ dB, $\rho = 0.5$ and heights for 0^{th} - 3^{rd} tier UAVs are 50m, 50m, 60m, and 70m, respectively. The GBS is regarded as the 4^{th} tier.	146
7.8	STP, EC and SINRC as a function of the threshold when $\sigma = 10$, $\tau = T$ and $\rho = 0.5$ for the SWIPT scenario.	147
7.9	Association probability as a function of the UAV height with parameter values listed in Table 7.2.	148
7.10	STP, EC and SINRC as functions of the UAV height H when $\sigma = 10$, $\tau = T$, $\gamma_E = -40$ dB, $\gamma_{sinr} = 0$ dB. And $\rho = 0.5$ for the SWIPT scenario.	148
7.11	Uplink SINR coverage probability as a function of the UAV height, when $\tau = 0.5T$, $\rho = 0$, $\gamma^{UL} = -20$ dB, and $\sigma = 10$	149
7.12	STP, EC and SINRC as functions of the power splitting parameter ρ when $\sigma = 10$, $\tau = T$, $\gamma_E = -40$ dB, $\gamma_{sinr} = -15$ dB. To show the impact of ρ , we use $\sigma_c = -10$ dB in this figure.	150
7.13	Averaged uplink throughput as a function of τ and ρ for Thomas cluster process, when $\gamma_E = -40$ dB, $\gamma_{sinr} = 0$ dB, $\gamma^{UL} = -20$ dB, and $\sigma = 10$	150
7.14	AP, EC as a function of cluster size σ , when $H = 50$ m, $\gamma_E = -80$ dB and $\gamma_{sinr} = -40$ dB.	151
7.15	AP, EC and SINRC as a function of UAV height H , when $\sigma = 30$, $\gamma_E = -80$ dB and $\gamma_{sinr} = -40$ dB.	152

8.1	SINR coverage probability as a function of the UAV altitude in a suburban and urban environments.	158
8.2	SINR coverage probability as a function of the GBS tilting angle in degrees.	159
9.1	An illustration of multi-UAV multi-GBS cellular networks.	161
9.2	Value of the value network and accuracy of the SINR-prediction network as functions of the number of episodes.	177
9.3	Trajectory examples at different episodes during training.	178
9.4	Illustrations of different environments used in navigation testing, and trajectory examples when using proposed RLTCW-SP algorithm. In (a) and (d), the two BSs in black are not operational for the UAVs.	179
9.5	Trajectory examples in environments with different settings, i.e., in (a) and (d), $H_V = 50$ m, $\theta^{tilt} = 10^\circ$ and $\theta^{3dB} = 15^\circ$; in (b) and (e), $H_V = 100$ m, $\theta^{tilt} = 10^\circ$ and $\theta^{3dB} = 15^\circ$; and in (c) and (f), $H_V = 50$ m, $\theta^{tilt} = 15^\circ$ and $\theta^{3dB} = 35^\circ$	181
9.6	Trajectory examples in environments with obstacles/no-fly zones.	182
9.7	Trajectory examples for multi-agent navigation.	182
9.8	Collision rate comparison between two methods: 1) the proposed approach, in which the collision avoidance is taken into account in training; 2) the approach in which collision with other UAVs is not considered in training.	183
9.9	An illustration of the cellular networks with multiple UAVs, multiple GBSs, and a jammer.	184
9.10	Accumulated reward per episode for two distinct training cases and the straight path scenario, as functions of episode.	189
9.11	Accuracy of the SINR mapping DNN as a function of training time.	189
9.12	Illustrations of trajectories in environments, where jammer does not exit or the jammer is located at different positions.	190
10.1	An illustration of data collection in a multi-UAV scenario.	195
10.2	Accumulated reward per episode in training with different DNN structures.	206

10.3	Accumulated reward per episode, average success rate per 100 episodes and data collection rate per episode for different training cases.	206
10.4	Illustrations of navigation in different scenarios that $N \in \{8, 9, 10\}$ nodes are randomly located, and $D_0^L = 1$ data unit, $J \in [2, 10]$	208
10.5	Illustrations of navigation in different scenarios that $D_0^L \in \{1, 2, 3\}$ data units need to be collect at each node, and $N = 7, J = 2$	209
10.6	Illustrations of navigation in different scenarios involving $J \in \{2, 10, 20\}$ other UAVs, and $N = 6, D_0^L = 1$ data unit.	210
10.7	Collision rate comparison in testing between two methods: 1) the proposed approach with setting 1 and setting 2, in which the collision avoidance in the presence of arbitrary number of other UAVs is taken into account in training; and 2) the approach in which collision with other UAVs is not considered in training.	211
10.8	Illustrations of navigation when SNR threshold \mathcal{T}_s is different, and $N = 5, D_0^L = 1$ data unit, $J = 2$	212

CHAPTER 1

INTRODUCTION

1.1 Background

1.1.1 MmWave and Terahertz Communication Networks

In the presence of the severe spectrum shortage in conventional cellular bands, millimeter wave (mmWave) frequencies between 30 and 300 GHz have been attracting growing attention for deployment in next-generation wireless heterogeneous networks [1]. Larger bandwidths available in mmWave frequency bands make them attractive to meet the exponentially growing demand in data traffic [2]. On the other hand, communication in mmWave frequency bands has several limitations such as increase in free-space path loss with increasing frequency and poor penetration through solid materials. However, with the use of large antenna arrays by utilizing the shorter wavelengths of mmWave frequency bands, and enabling beamforming at the transmitter and receiver, frequency dependent path loss can be compensated [3]. Additionally, with the employment of directional antennas, out-of-cell interference can be substantially reduced.

Furthermore, to realize the vision of next-generation 6G wireless networks supporting, there is interest in moving to even higher frequencies in the terahertz (THz) band of 0.1 - 10 THz. However, THz transmissions also encounter a challenging propagation environment. For instance,

compared to the ultra-high frequency and mmWave frequency bands, electromagnetic waves in THz bands experience high molecular absorption loss in addition to spreading loss and scattering attenuation [4–7]. The ultimate effect is a more complex path loss model that additionally includes an exponential decay in power [8]. Human-body blockage effects also have a strong impact on the communication quality of THz channels [6]. Moreover, THz waves cannot reach objects that are behind obstacles whose dimensions are greater than the wavelength. Effectively, any object whose size is greater than few millimeters including users themselves, acts as a blocker. Transceivers operating in THz bands are expected to be characterized by high antenna directivities in both transmit and receive directions [8] to compensate such severe path loss. And this would in turn have significant influence on the interference levels and the coverage performance [6].

1.1.2 User-Centric Deployment of Small Cells in Heterogeneous Networks

Heterogeneous cellular wireless networks are being developed to support higher data rates to satisfy the increasing user equipment (UE) demand for broadband wireless services, by supporting the coexistence of denser but lower power small-cell base stations (BSs) with the conventional high-power and low density macrocell BSs [9–12].

While macrocell BSs were deployed fairly uniformly to provide a ubiquitous coverage blanket, the small-cell BSs are deployed to complement capacity of the cellular networks or to patch the coverage dead zones [13]. A common approach is to model the locations of BSs and UEs randomly and independently using the Poisson point process (PPP) distribution. However, assuming BS and UE locations independent from each other may not be quite accurate all the time. In practice, while macrocell BSs are deployed fairly uniformly to provide a ubiquitous coverage blanket, several types of small-cells, such as picocells, are deployed to enhance coverage and capacity [14]. Therefore, the small-cell BSs are expected to be deployed in crowded areas or hotspots to patch coverage dead-zones. In addition, in such areas (high-density areas and hotspots), UEs are very likely to be clustered, e.g., in coffee shops, bookstores, subway/bus stations, sports/concert cen-

ters. Moreover, PPP-based models will not correctly reflect the locations of the non-uniformly distributed UEs. In such cases, it is important to accurately capture not only the non-uniformity but also the coupling across the locations of the UEs and small-cell BSs [15]. In such architectures, one can envision the small-cells being deployed to serve clusters of UEs. Such models have been used by the standardization bodies, such as third generation partnership project (3GPP). 3GPP has considered the clustered configurations in which locations of the user and small-cell BSs are coupled, in addition to the uniformly distributed UEs [16]. Among different point processes, Poisson cluster processes (PCPs) have been shown to lead to realistic and accurate models for characterizing the statistical nature of user-centric BS deployments and clustered UE distributions in urban areas [17]. The authors in [13] have proved that the model in which UEs are distributed according to PCP around PPP distributed small-cell BSs closely resemblances the 3GPP configuration of single small-cell BS per UE hotspot in a heterogeneous network. Therefore, user-centric deployment of small cells is becoming an important part of future wireless architectures [18] in heterogeneous networks.

1.1.3 UAV-Enabled Networks

Unmanned aerial vehicles (UAVs), also commonly known as drones, are aircrafts piloted by remote control or embedded computer programs without human onboard [19]. UAVs have been one of the main targets of industrial and academic research in recent years. Initially, UAVs were primarily used in military applications. With the advances in the technology, UAVs have become lighter, cheaper and easier to deploy, and have gradually entered civilian life. In particular, due to their mobility, autonomy and flexibility, UAVs can be used in a variety of real-world scenarios, such as delivery of medical supplies, disaster relief, environment monitoring, aerial surveillance and inspection, traffic control, and emergency search and rescue [20, 21]. If properly deployed and operated, UAVs can also provide reliable and cost-effective wireless communications, such as in large-scale temporary events and disaster scenarios, and support capacity enhancement in the occasional demand of super dense base stations [22, 23]. Therefore, UAVs are expected to be

integrated into next-generation wireless networks.

Due to the advantages of UAVs, UAV-enabled communication is expected to be a critical part of future wireless communication networks. More specifically, in order to take advantage of flexible deployment opportunities and high possibility of LoS connections with ground UEs, UAVs can be deployed as BSs/relays to support wireless connectivity and improve the performance of cellular networks [23]. The flexibility of aerial BSs/relays allows them to adapt their locations to the demand of UEs, leading to a UAV-assisted cellular network architecture. On the other hand, UAVs in certain applications will be regarded as aerial UEs that need to be supported by the ground communication infrastructure, which brings both opportunities and challenges to cellular communications. These aerial UEs can be referred to as cellular-connected UAVs that access the cellular network from the sky for data communications [24].

As aerial BSs, UAVs can be used as (quasi-)stationary aerial communication platforms which remain static for a very long period of time once deployed [19]. Under such a setup, extensive research effort has been devoted to UAV placement optimization and performance analysis by taking into account the unique characteristics of air-to-ground channels. One important issue is to validate/evaluate its performance after/before the deployment [19]. This can be achieved by conducting experimental field test [25], and computer-based simulations [26, 27] or theoretical analysis [28–30], respectively. Specifically, theoretical performance analysis can not only predict the expected performance of the system to be deployed without extensive simulations time, but also provide useful guidelines and insights to design the UAV-assisted system. On the other hand, UAVs can be used as dynamic BSs to serve stationary/mobile UEs in static/changing environments. UAVs have shown particular promising in collecting data from distributed Internet of Thing (IoT) sensor nodes, as IoT operators can deploy UAV data harvester in the absence of other expensive cellular infrastructure nearby [31]. UAV trajectory design scheme allows the UAVs to adapt their movement based on the rate requirements of both the UAV-UEs and the ground UEs, thus improving the overall network performance [32].

Cellular-connected UAV is a cost-effective solution since it reuses the millions of ground base

stations (GBSs) without the need of building new infrastructure [19]. As aerial UEs, the UAVs need efficient trajectories and also should keep connected with GBSs during their flights. Therefore, the trajectory of cellular-connected UAVs need to be carefully designed to meet their mission specifications, while at the same time ensuring that the communication requirements are satisfactorily met.

In scenarios involving multiple UAVs or more generally multiple autonomous systems, a fundamental challenge is to safely control the interactions with other dynamic agents in the environment. Specifically, it is important for the autonomous devices (e.g., robots and drones) to navigate in an environment with or without obstacles, and stay free of collisions with each other and the obstacles, based on local observations of the environment. Finding solutions to this problem is challenging, since one robot's action is based on others' motions (intentions) and policies which are in general unknown, and, furthermore, explicit communication of such hidden quantities is often impractical due to physical limitations. In addition, the UAV-enabled wireless communication systems can be easily vulnerable to jamming and eavesdropping attacks due to the broadcast nature of wireless transmissions [33]. In particular, jamming is a malicious attack whose objective is to disrupt the communication in the victim network by intentionally causing interference at the receiver side [34]. Once attacked, the quality of communication will decline, leading even to link loss and mission interruptions. Therefore, finding jamming-resilient UAV trajectory is challenging and important.

1.1.4 Deep Reinforcement Learning

Reinforcement learning (RL) is the study of how an agent can interact with its environment to learn a policy which maximizes expected cumulative rewards for a task [35]. RL has experienced dramatic growth recently due to promising results in areas like: controlling continuous systems in robotics [36], playing Go [37], Atari [38], and competitive video games [39, 40], communications and networking [41]. However, regular RL algorithms can require substantial time to reach the best policies as they have to explore and gain knowledge of an entire system [41], making

them unsuitable and inapplicable to solve problems with large-scale state/action spaces. In deep learning, deep neural networks can automatically find compact low-dimensional representations (features) of high-dimensional data (e.g., images, text and audio) [42]. As a result, deep reinforcement learning (DRL), a combination of RL with deep learning, has been developed to overcome the shortcomings of RL. In the areas of communications and networking, DRL has been recently used as an emerging tool to effectively address various problems and challenges. In particular, DRL has been applied to solve problems in networks, such as IoT networks [43–45], heterogeneous networks [46–48], and UAV networks [49–54], in which the network entities such as IoT devices, mobile UEs, and UAVs need to make local and autonomous decisions, e.g., spectrum access, data rate selection, transmit power control, BS association, and path planning, to achieve the goals.

1.2 Related Prior Work

1.2.1 MmWave Cellular Networks

Heterogeneous mmWave cellular networks have been addressed in several recent studies. An energy-efficient mmWave backhauling scheme for small cells in 5G is considered in [55], where the small cells are densely deployed and a macrocell is coupled with small cells to some extent. Mobile users are associated with BSs of the small cells, and have the communication modes of both fourth-generation access and mmWave backhauling operation. The macrocell BS and small-cell BSs are also equipped with directional antennas both for 4G communications and transmissions in the mmWave band. A general multi-tier mmWave cellular network is studied in [56] and [57]. The BSs in each tier are distributed according to a homogeneous PPP with certain densities. Moreover, in [56] a two-ball approximation is considered, modeling the state of links in line-of-sight (LOS), non-LOS (NLOS), and outage. In [57], a K -tier heterogeneous mmWave cellular network is considered, and signal-to-interference-plus-noise-ratio (SINR) coverage probability is derived by incorporating the distinguishing features of mmWave communications, and a D -ball approximation

for blockage modeling is employed. In [58], authors investigate an ultra dense heterogeneous network, and study the energy efficient BS deployment considering LOS and NLOS transmission. [59] discusses how to combine a realistic mmWave channel model with a tractable network analysis, and derives the signal-to-interference ratio (SIR) coverage probability. The coverage probability in urban areas is derived for a heterogeneous mmWave network in [60].

Recent studies have addressed the uplink analysis in mmWave networks. In [61], a framework to evaluate the SINR coverage in the uplink of mmWave cellular networks with fractional power control (FPC) is presented. Conventional path loss based FPC and distance based FPC are considered. The locations of LOS UEs and NLOS UEs are modeled as two independent non-homogeneous PPPs which are independent of the locations of BSs. A hybrid network with traditional sub-6 GHz macrocells coexisting with mmWave small-cells is addressed in [62] and [63]. The authors in [62] have analyzed the decoupled downlink and uplink association strategies. In [63], different decoupled uplink and downlink cell association strategies are investigated based on two different criteria, namely maximum biased received power and maximum achievable rates. Similarly as in mmWave studies, a path loss model incorporating both LOS and NLOS transmissions in uplink of dense small-cell networks is considered in [64]. Additionally, the UE density is assumed to be higher than the BS density, while they are still spatially distributed according to independent PPPs. Moreover, the energy efficiency maximization problem were investigated for uplink mmWave systems with non-orthogonal multiple access (NOMA) in [65, 66].

1.2.2 Terahertz Communication Networks

Recently, there has been increasing interest in THz communications. In [67], the authors have derived a expression for the coverage probability of downlink transmission in THz communication systems within a three-dimensional (3D) environment. A 3D propagation model that took into account the molecular absorption loss, 3D directional antennas at both access points (APs) and UEs, interference from nearby access points and dynamic blockages caused by moving humans, was established. Coverage probability was evaluated based on the dominant interference analysis.

In [68], on the basis of THz channel modeling, the interference from surrounding omnidirectional nanosensors and beamforming base stations were derived in closed-form by using stochastic geometry methods. SINR coverage probability was obtained. The authors in [7] studied the systems operating in the mmWave and THz bands by explicitly capturing three phenomena inherent at these frequencies: 1) high directivity of the transmit and receive antennas; 2) molecular absorption; and 3) blocking of high-frequency radiation. A cone model and a cone-plus-sphere model were considered for antenna radiation patterns. Mean interference and SINR were investigated. In [4], mean interference power and probability of outage in THz networks were studied. The authors showed that the log-logistic distribution provided a good fit for the SIR distribution in the case of two dimensional (2D) path loss, but failed to estimate the interference distribution for 3D path loss. [8] provided analytical approximations for the probability density function (PDF) of interference from a randomly chosen node, and derived the Laplace transform of the aggregated interference and the SIR of the network. The authors showed that failure to capture the atmospheric absorption, blocking or antenna directivity leads to significant modeling errors. In the aforementioned prior studies, small-scale fading was not considered, and the distance from the typical UE to the serving AP was assumed fixed and known. A more general model is addressed in [6], where the typical UE was assumed to be served by the nearest AP, and the exact distribution of the received signal power and the approximated distribution of the interference with its moments were derived. However, the coexistence of the transmission in microwave and mmWave frequency bands are not taken into account either.

1.2.3 User-Centric Small Cell Deployment

Several recent studies have attempted to model the UEs as clustered around the small-cell BSs. A unified HetNet model in which a fraction of UEs and some BS tiers are modeled as PCPs is developed in [13] to reduce the gap between the real-word deployments and the popular PPP-based analytical model. In [69], the authors consider Neyman-Scott cluster process, in which the centers of the clusters and cluster members are assumed to be distributed according to some stationary

PPP independent from each other. Although the cluster process is considered, the correlation between the locations of the cluster centers and members is not taken into account. In [70], PPP-PCP model is employed in which macrocell BS locations are modeled according to a PPP, while picocell BS locations are distributed according to a PCP. Authors investigate the effect of the distance between the BS and UEs on coverage probability. In [71], a multi-cell uplink non-orthogonal multiple access system is provided. BSs are distributed according to a homogeneous PPP, and UEs are uniformly clustered around the BSs within a circular region. Three scenarios are considered in [71], including perfect successive interference cancellation (SIC), imperfect SIC and imperfect worst case SIC at the receiver side. Moreover, the Laplace transform of the interference is analyzed. In [72], authors consider a K -tier heterogeneous network model with user-centric small cell deployments in which the locations of UEs are modeled by a PCP with one small-cell BS located at the center of each cluster process, and discover the coverage probability of the network. In addition to modeling locations of UEs as a PCP, small-cell BS clustering is considered in [15] to capture the correlation between the large-cell and small-cell BS locations. However, these prior studies that considered clustered users have not addressed transmission in mmWave frequency bands. A clustered mmWave network in which NOMA techniques are employed, is introduced in [73], where the NOMA UEs are modeled as PCP distributed and each cluster contains a BS located at the center. Three distance-dependent UE selection strategies are proposed in this chapter to evaluate the impact of the path loss on the network performance.

PCPs are also used in device-to-device (D2D) networks, e.g. [74–78], where the locations of the D2D devices were modeled as PCPs. For instance, D2D enabled mmWave cellular networks with clustered UEs are analyzed in [77] and [78], transceivers are modeled according to a PCP in [77], and both PPP-distributed cellular UEs and PCP-distributed D2D UEs are considered in [78]. Coverage probability and area spectral efficiency of the networks are analyzed in both papers.

Moreover, uplink analysis in PCP distributed networks has recently been conducted in several studies. The authors in [79] have provided a framework to analyze single-tier multi-cell uplink NOMA systems where the UE locations are modeled following a Matérn cluster process. Rate cov-

erage probability of NOMA users and the mean rate coverage probability of all users in a cell are characterized. [80] considered a decoupled downlink and uplink access scenario in a heterogeneous network, where the distribution of UEs are modeled as a Matern cluster process. Closed-form expressions for system coverage probability, spectral efficiency and energy efficiency are obtained. We note that these prior studies have not considered uplink analysis in mmWave networks.

1.2.4 Beamforming in MIMO Networks

Leveraging recent advances in machine learning, optimal beamforming schemes can be determined in real time with low computational complexity using learning techniques. For instance, the authors in [81] have considered a network where a number of distributed BSs simultaneously serve one mobile UE. The UE ideally transmits one uplink training pilot sequence to all BSs equipped with omni or quasi-omni directional beam patterns, and the deep-learning model leverages the signals to train its neural network. After training, the deep-learning predicts the BS radio frequency (RF) beamforming vectors in downlink data transmission. [82] has proposed an algorithm that combines three neural networks for performance optimization in massive multiple input multiple output (MIMO) beamforming. In the proposed system, one neural network is trained to generate realistic user mobility patterns, which are then used by a second neural network to produce relevant antenna diagrams. Meanwhile, a third neural network estimates the efficiency of the generated antenna diagrams and returns the corresponding reward to both networks. The authors in [83] have proposed a deep learning framework for the optimization of downlink beamforming. In particular, the solution is obtained based on convolutional neural networks and exploitation of expert knowledge, such as the uplink-downlink duality and the structure of known optimal solutions. In [84], a neural network architecture is used to jointly sense the millimeter wave channel and design hybrid precoding matrices. The neural network is first trained in a supervised manner, where a dataset of the mmWave channels and the corresponding RF beamforming/combining matrices are constructed and fed as the input and the target of the neural network, respectively. Then the trained neural network is applied online. Reinforcement learning is also shown to be a useful tool for

beamforming schemes. For instance, the authors in [85] used deep Q learning algorithm to jointly optimize the beamforming vectors and the transmit power of the BSs, and eventually to maximize the SINR of UEs. [86] presented a deep reinforcement learning framework to optimize MIMO broadcast beams autonomously and dynamically based on users' mobility patterns or changes in user distribution, which can vary periodically. Using ray-tracing data, deep reinforcement learning engine is first trained offline, and then deployed online for real-time operation.

1.2.5 System-Level Analysis of UAV-Enabled Networks

The system-level analysis of UAV-assisted networks has also attracted much attention in recent literature. For instance, references [87], [23] and [88] considered a 2D PPP UAV-assisted cellular network, where UAVs were distributed according to a PPP at the same height in the air. In [87], the downlink coverage probability was explored, as well as the influence of UAV height and density. In [23], different path loss models for high-altitude, low-altitude and ultra-low-altitude models were discussed. In addition to the coverage probability, the area spectral efficiency was investigated. The model in [88] also took into account the system parameters such as building density and UAV antenna beamwidth. Besides the 2D PPP distributed UAV-assisted cellular networks, the authors in [22] considered a network in which a serving UAV was assumed to be located at fixed altitude, while a given number of interfering UAVs were assumed to have 3D mobility based on the mixed random waypoint mobility. Moreover, [89] considered a finite UAV network which was modeled as a uniform binomial point process (BPP). Several limiting cases were discussed, including the no fading case and the dominant interferer based case.

PCP models have also been considered in the system-level analysis of UAV-assisted networks. In [90], the UAVs were assumed to form a PCP with the destroyed macro BSs as the parent nodes. The downlink network performance, i.e. the SINR coverage probability, area spectral efficiency and energy efficiency, were investigated. In [91], UAVs were considered as BSs serving the users. The UE locations were considered as PCPs. SINR coverage probability was investigated as the network performance metric. [92] considered the UAV networks in mmWave communications.

The UAVs were the parent nodes and were 3D deployed at same height, while the UEs were the daughter nodes and their locations formed a Thomas cluster process. [93] proposed a unified 3D spatial framework to evaluate the average performance of UAV-aided networks with mmWave communications. The UAVs and BSs were assumed to be PPP distributed and the UEs were distributed according to a PCP. During communication, a UAV received a message from a UE in the uplink transmission and forwarded the message to a ground BS in the downlink transmission. The heights of the UAVs were all assumed to be the same.

Integration of UAVs as aerial UEs would require a system-level understanding to both modify and extend the existing terrestrial network infrastructure [94]. The network performance of the cellular-connected UAV has been investigated recently. For instance, the authors in [95] considered a heterogeneous network comprising aerial and terrestrial base stations, where the GBSs were assumed to be distributed according to an infinite 2D PPP, while the locations of the aerial-BSs were modeled as a finite 3D binomial point process deployed at a particular height. The downlink coverage probability and average achievable rate of an aerial UE were analyzed. Similarly, [24] considered homogeneous PPP distributed GBSs serving an aerial UAV-UE, and investigated the SINR coverage probability, achievable throughput and the area spectral efficiency of the network. Additionally, a tilted directional antenna was considered for the UAVs.

In UAV-enabled cellular networks, one of the key questions that have not been adequately explored in the existing state of the art is the impact of UAV antenna configuration on their connectivity to GBSs [96, 97]. The antenna of the UAVs should be carefully designed, since the variation in antenna design will significantly affect the network performance [98]. In particular, the use of different antenna patterns can have significant impact on the interference levels and hence can help alleviate the severe air-to-ground interference issue due to strong LOS links [99]. However, capturing the antennas' movement and orientation is challenging in air-to-ground channel modeling [21]. 3D beamforming can significantly improve the performance compared to the conventional 2D beamforming methods [100]. A 3D antenna pattern was considered in [101], and the authors assumed the UAV was equipped with a directional antenna whose boresight direction

was pointing downward to the ground. The authors in [102] considered the 3D antenna pattern for the GBSs in a multiple-input single-output downlink single UE system, where the antenna gain was controlled by adjusting the boresight of the antennas in directional transmissions. In [103], the authors adopted a 3D antenna pattern for GBSs in a cellular massive multiple-input multiple-output network. Different heights for UEs were considered in the 3D environment. A 3D system model for the UAV-GBS uplink/downlink communications was studied in [99]. 3D antenna patterns of the GBSs and UAV, and 3D air-to-ground channel were taken into account. Three different types of antennas were compared in [96]. These were an omni-directional antenna with antenna gain set at 1; a directional antenna tilted down to give a cone-shaped radiation lobe directly beneath the UAV; and a directional antenna which the UAV could intelligently steer and align with its serving GBS.

1.2.6 Trajectory Design for Cellular-Connected UAVs

Trajectory design for cellular-connected UAVs has been extensively investigated in the literature. For instance, the authors in [104] studied the trajectory design for a single cellular connected UAV under delay-limited communication. The authors in [105] applied convex optimization and linear programming to find the optimal set of waypoints and speed for a UAV to ensure the minimum connection time constraint with the ground terminals. A circular trajectory with optimized flight radius and speed for a UAV was considered in [106] to maximize the energy efficiency. [107] aimed to find UAV path planning strategy to optimize the wireless coverage for the UAV. In [108], the UAV trajectory optimization was studied to minimize the total propulsion related power consumption while satisfying a cellular-connectivity constraint. A connectivity-aware UAV path planning problem was formulated in [109] to find the shortest path subject to connectivity constraints. Three-dimensional path planning for a cellular-connected UAV was studied in [110] to minimize its flying distance from initial to final locations, while satisfying an expected SINR requirement, and also an SINR map was constructed. In [111], the authors formulated a problem to minimize the UAV mission completion time by jointly optimizing the UAV trajectory and UAV-GBS associ-

ation order. In addition, the authors in [112, 113] considered how to determine the optimal path for the UAV to minimize its mission completion time, subject to wireless connectivity constraint. Optimization techniques, graph theory and dynamic programming were used to solve the single-UAV path planning problems formulated in these prior studies.

Reinforcement learning has also been utilized to obtain solutions to trajectory optimization for cellular-connected UAVs in the literature. The authors in [114] proposed a double Q-learning method to solve the UAV trajectory optimization problem under a maximum continuous disconnection time constraint or a total disconnection time constraint. In [115], a dueling double deep Q network with multi-step learning algorithm was formulated as a solution to the UAV trajectory optimization problem to minimize the weighted sum of its mission completion time and expected communication outage duration. Additionally, an interference-aware path planning scheme for a network of cellular-connected UAVs was proposed in [32] to achieve a trade-off between maximizing energy efficiency and minimizing both wireless latency and the interference. A deep reinforcement learning algorithm, based on echo state network cells, was developed to solve the problem. However, these prior works considered single-UAV scenarios as well.

Different approaches for the collision avoidance of multiple UAVs have also been developed in the literature. For instance, a rolling horizon approach using dynamic programming was used to solve the problem in a multi-agent cooperative system in [116]. A neuro-dynamic programming algorithm is proposed in [117] for multi-UAV cooperative path planning. A mixed integer linear programming method is used in [118]. Partially observable Markov decision process based methods are applied in [119–121] for UAV collision avoidance. In addition, authors in [122] used reachable sets to represent the collection of possible trajectories of the obstacle aircraft. Once a collision is detected, a sampling-based method is used to generate a collision avoidance path for the UAV. In [123], predictive state space was utilized to present the waypoints of the UAVs, with which initial collision-free trajectories are generated and then improved by a rolling optimization algorithm to minimize the trajectory length. Artificial potential field method with an additional control force was proposed for multi-UAV path planning in [124]. The authors in [125] presented

path planning algorithms using rapidly-exploring random trees to generate paths for multiple UAVs in obstacles rich environment. Moreover, the authors in [31] used DDQN algorithm to solve the UAV path planning problem for data collection from distributed IoT nodes. However, considering collision avoidance in multiple cellular-connected UAV navigation with wireless communication requirements, addressing these challenges via deep reinforcement learning methods, and obtaining decentralized solutions have not been adequately explored yet.

1.2.7 UAV Path Planning for Data Collection

Effective UAV trajectory planning allows the UAVs to adapt their movement based on the communication requirements of both the UAVs and the ground UEs, thus improving the overall network performance [32], and therefore UAV path plans and control policies need to be carefully designed such that the application requirements are satisfied [112, 113]. UAV trajectory design for data collection in IoT networks has been extensively studied in the literature. For example, to minimize the weighted sum of the propulsion energy consumption and operation costs of all UAVs, and the energy consumption of all sensor nodes, the nodes' wake-up time allocation and the transmit power and the UAV trajectories were jointly optimized in [126], and collision avoidance constraint was also considered in this paper. In [127], the authors aimed to minimize the energy consumption of IoT devices by jointly optimizing the UAV trajectory and device transmission scheduling over time. In [128], the UAV trajectory, altitude, velocity and data links with the ground UEs were optimized to minimize the total mission time for UAV-aided data collection. The authors in [129] aimed to optimize the UAV trajectory and the radio resource allocation to maximize the number of served IoT devices, where each device has a data upload deadline. The minimum throughput over all ground UEs in downlink communication was maximized in [130], by optimizing the multiuser communication scheduling and association jointly with the UAV's trajectory and power control. Moreover, UAV path planning for data collection has also been investigated in [131–134]. Traditional optimization techniques were adopted to solve the problems in these studies.

Specifically, RL-based algorithms have recently been proposed as solutions to UAV path plan-

ning for data collection tasks. For example, [135–140] addressed the trajectory optimization in single-UAV data collection scenarios. In [135], the authors used double deep Q-network (DDQN) algorithms to find the optimal flight trajectory and transmission scheduling to minimize the weighted sum of the age of the information. In [136], the authors used Deep Q-network (DQN) algorithms to decide the UAV trajectory to collect the required data, and determine the charging car trajectory to arrive its destination to charge the UAV. DQN was also used in [137] to decide the transmission schedule to minimize the data loss, given the waypoint of the UAV’s trajectory. The authors in [138] first used deep deterministic policy gradient (DDPG) algorithm to find the trajectory with no collision with obstacles, and then used Q-learning (QL) to find the scheduling strategy to minimize the data collection time. Authors in [139] provided a Q-learning framework as an energy-efficient solution for the UAV trajectory optimization. Moreover, Q-learning was also used in [140] to find the UAV trajectory to maximize the sum rate of transmissions.

Multi-UAV control with reinforcement learning techniques has also been investigated in the literature. For example, the authors in [141] studied the joint problem of dynamic multi-UAV altitude control and multi-cell wireless channel access management of IoT devices. Online model-free constrained deep reinforcement learning (CDRL) algorithm based on Lagrangian primal-dual policy optimization was proposed to solve the problem. In [142], the authors developed a deep DRL-based self regulation approach to maximize the accumulated user satisfaction score in multi-UAV networks with UAV and UE dynamics. Moreover, authors in [143] proposed learning-based algorithms to solve the problem of joint trajectory design and power control for multiple UAVs with the goal to maximize the instantaneous sum transmission rate of mobile UEs. However, collision avoidance constraint was not taken into account in these papers.

Different RL-based path planning approaches for data collection in multi-UAV networks have been developed in the literature as well, such as in [31, 143, 144]. Particularly, the authors in [31] used the DDQN algorithm to solve the UAV path planning problem to maximize the collected data from IoT nodes, subject to flying time and collision avoidance constraints. However, the learning was centralized, and the UAVs were cooperative, i.e., the UAVs needed to share their information

and a part of their reward with each other. The authors in [144] considered a scenario where the UAVs took charge of delivering objects in the forward path, and collected data from IoT devices in the backward path. Q-learning was used to solve the forward collision avoidance problem, and auxiliary no-return traveling salesman algorithm was used to find the shortest backward path. However, the collision avoidance and communication constraints were not taken into account together. Moreover, authors in [143] considered the problem of joint trajectory design and power control for multi-UAVs for maximizing the instantaneous sum transmit rate of mobile UEs. To solve the problem, a framework that involves a multi-agent QL-based placement algorithm for initial deployment of UAVs, an echo state network based algorithm for predicting the mobility of UEs, and a multi-agent QL-based trajectory-acquisition and power control algorithm for UAVs, is proposed. However, collision avoidance constraint was not taken into account in this paper. In these works, all agents were assumed to use the same policy and operate cooperatively. The key challenge for these models is that they cannot generalize well to crowded scenarios or scenarios with non-cooperating agents.

1.2.8 Path Design for UAVs in the Presence of Jamming Attacks

A series of strategies to resist jamming attacks have been proposed in wireless networks, which are generally divided into two categories: 1) adapting to the jamming signal; 2) retreating away from or avoiding the jammer [145].

In the first category, physical-layer security has emerged as a promising approach to secure UAV communications against jamming attacks. For instance, authors in [146] proposed deep Q-learning based UAV power allocation strategies to improve the static UAV-enabled communications against smart jamming attacks. In [147], a reinforcement learning based power control algorithm was proposed to improve the performance of the multi-UAV relay communication systems in the presence of a random jammer. The authors in [148] introduced a UAV as a friendly jammer in the UAV-enabled network to work against multiple eavesdroppers, aiming to maximize the minimum average secrecy rate over all information receivers.

Owing to the mobility and flexibility of UAVs, it is also feasible to use the avoidance strategy against jamming attacks. Furthermore, spatial evasion based methods do not impose high requirements on communications devices [145]. By taking advantage of the mobility of UAVs, jamming-resistant trajectory designs in UAV-enabled communication systems have been studied in the literature. For instance, authors in [149] investigated the maximization of the uplink data throughput of UAV-enabled communication in presence of a potential jammer. An alternating algorithm that leverages the block coordinate descent method, successive convex approximation, and S-procedure, was proposed to optimize the UAV trajectory. A similar problem was studied in [150], where the goal is to improve the minimum uplink data throughput for multi-UAV enabled communication in the presence of jammers with imperfect location information. In [151], the authors aimed to maximize the minimum (average) expected data collection rate from ground sensors in the presence of a malicious ground jammer, by jointly optimizing the ground sensor transmission schedule and UAV horizontal and vertical trajectories over a finite flight duration. In [152], the authors had the objective to maximize the sum throughput received by the UAV in the presence of jammer signals, by designing the UAV deployment and trajectory planning in 3D space. [153] proposed a deep Q-learning based UAV trajectory and power control scheme against smart jamming attacks on transmissions with ground nodes, given the predefined UAV sensing waypoints. The prior work in this area has mostly concentrated on either single-UAV scenarios or multiple UAVs operating as aerial BSs, and hence has not addressed cellular-connected UAVs, connectivity constraints and collisions avoidance requirements especially with a jammer present, using a learning framework.

1.3 Outline and Main Contributions

In Chapter 2, we provide a detailed overview on point processes, channel modeling, and reinforcement learning. More specifically, Poisson point processes and Neyman-Scott cluster processes are introduced, as well as their properties. General channel modeling approaches involving e.g., path

loss, shadowing, small-scale fading, and antenna gains are summarized. Finally, we provide basics of reinforcement learning and introduce some widely used RL algorithms.

In Chapter 3, we analyze a K -tier heterogeneous downlink mmWave cellular network with UE-centric small cell deployments. We develop a new and more practical heterogeneous mmWave cellular network model by considering the correlation between the locations of UEs and BSs. Cell association probabilities are determined by employing a cell association criterion based on the long-term average biased received power. General expressions for association probabilities with each tier BS including the cluster center BS are provided. In addition, we provide simpler expressions for association probabilities by considering several special cases to provide more insight on the impact of different system parameters. For example, we show that our model specializes to the PPP-based model when the cluster size grows without bound. We characterize the Laplace transform of the interferences. General expressions for SINR coverage probabilities for each tier BS including the cluster center BS are also derived. The coverage probability expressions are also applicable to any PCP. Upper and lower bounds on the Laplace transform of the interference from the cluster center BS are obtained, leading to bounds on the total coverage probability of the entire network. It is also demonstrated that as the cluster size increases, performance within the PCP model approaches that of the PPP-based model. Area spectral efficiency (ASE) of the entire network is determined based on the derived coverage probabilities. Moreover, several extensions on the coverage analysis are provided to the baseline model by considering the more practical antenna gain patterns and also shadowing.

In Chapter 4, we present a mathematical framework for evaluating the performance of multi-tier heterogeneous uplink mmWave cellular networks. We employ PCPs to accurately model the locations of the clustered UEs. In particular, Thomas cluster process is adopted, with which the UEs are clustered around the small-cell BSs according to a Gaussian distribution. Coupled association strategy is considered, and the UEs are assumed to be served by BSs which provide the strongest long-term averaged biased received power in downlink. Then, with this association strategy, we characterize: 1) the association probability of BSs in each tier; and 2) the distance from

the typical UE to each serving BS. Subsequently, we derive the Laplace transforms of the inter-cell interference and the interference from the cluster member UE. In addition, we derive general expressions for the SINR coverage probability. We extend the analysis to incorporate Nakagami fading and also consider several special cases, e.g., the noise-limited case, interference-limited case, and one-tier model. Furthermore, we provide extensions to include fractional power control in the analysis and reformulate the Laplace transforms of the interference in this case. Average ergodic spectral efficiency of the network is also analyzed.

In Chapter 5, we consider a general setting and propose a distributed multi-agent DDQN solution for beamforming in mmWave MIMO networks, where multiple BSs serve multiple mobile UEs. In this system, UEs move to different locations at each time, and may be served by different BSs according to the adopted largest received power association criterion. Each BS is a reinforcement learning agent and has its own DDQN. BSs, at each time, can only get information from the associated UEs, based on which the BSs predict the UEs mobility pattern and choose their beamforming vectors.

In Chapter 6, we consider a three-tier heterogeneous network, in which access points (APs), small-cell base stations (SBSs) and macrocell BSs (MBSs) transmit in THz, mmWave, microwave frequency bands, respectively. We incorporate the distinguishing features of transmission in each type of frequency band, and consider a path loss based association criterion for UEs. As main contributions, we analyze and derive general expressions for three key system performance metrics: 1) complementary cumulative distribution function (CCDF) of the received signal power; 2) the Laplace transform of the aggregate interference; and 3) the SINR coverage probability of the whole network.

In Chapter 7, a practical UAV-assisted mmWave cellular network with PCP distributed UEs is addressed and studied in detail. In addition to GBSs, UAVs are also deployed according to a PPP distribution, and the UEs are considered to be clustered around the projections of UAVs according to PCPs. We jointly consider the downlink SWIPT scenario and uplink information transmission, where in downlink phase UEs both harvest energy and decode the information from

the same received signal provided by the associated BS (either a UAV or a GBS), and in the uplink phase the UAVs collect data from their cluster member UEs. In the downlink phase, the largest received power association criterion is adopted and the power splitting technique is considered for the SWIPT scenario. Association probability and energy coverage of the proposed network are analyzed and general expressions are provided. Laplace transform of the interference is determined. We also define a realistic successful transmission probability to jointly address the energy coverage and SINR coverage performances of the considered network. In the uplink phase, each UAV is assumed to communicate with its cluster member UEs. According to the harvested energy of each UE in the downlink phase, UEs in the uplink phase are considered to be in either active mode or inactive mode. The Laplace transform of the inter-cell interference is again determined and the SINR coverage probability is derived. In addition, the average uplink throughput subject to a constraint on the downlink throughput is investigated to jointly address the downlink and uplink network performance. We provide an extension to multi-tier multi-height networks. Additionally, we address the special case of noise-limited networks and derive closed-form expressions for the uplink SINR coverage probability and the optimal power splitting factor ρ , maximizing the downlink successful transmission probability. Extension to UAV-assisted cellular networks with 3D antenna patterns in downlink transmission is provided.

In Chapter 8, we consider cellular-connected UAV networks and compare the performances of different antenna patterns for UAVs in different environments. In addition, practical 3D air-to-ground channel model is also taken into account for the links between the UAV and GBSs. More specifically, antenna patterns combining the vertical and horizontal gains are taken into account for the GBSs. Also, four types of 3D antenna patterns are considered for the UAVs. In particular, we compare the performances of a omni-directional pattern, a doughnut-shaped sine pattern, a doughnut-shaped cosine pattern, and a directional pattern with tilting angle toward the serving GBS.

In Chapter 9, we study multi-UAV trajectory optimization to minimize the UAVs' mission completion time under realistic constraints, e.g., collision avoidance, wireless connectivity, and

kinematic constraints, while also taking into account antenna patterns and interference levels. Particularly, in Section 9.1, we formulate the problem as a sequential decision making problem, and develop a decentralized deep reinforcement learning algorithm to solve it. We formulate the problem as a Markov decision process (MDP) with properly designed state space, action space, and reward function. We optimize the value function of the MDP to find the optimal policy, and design a value neural network to approximate the value function. Due to the fact that the UAVs do not communicate with each other in the considered network, uncertainty exists in the UAVs' unobservable intents. Thus, we employ a velocity filter to estimate the UAVs' intentions to address this uncertainty. In addition, we further design an SINR-prediction neural network to estimate the SINRs experienced at the UAVs. Particularly, using accumulated SINR measurements obtained when interacting with the cellular network, the SINR-prediction network is learned to map the nearby GBSs' locations into the SINR levels in order to predict the UAV's SINR. We delineate the initialization, refining, and training steps of the algorithm and describe the real-time navigation process. In Section 9.2, we aim to find collision-free paths for multiple cellular-connected UAVs, while satisfying requirements of connectivity with GBSs in the presence of a dynamic jammer. We propose an offline temporal difference (TD) learning algorithm with online SINR mapping to solve the problem.

In Chapter 10, we study the UAV trajectory optimization to maximize the collected data from distributed IoT nodes in multi-UAV non-cooperative scenarios under realistic constraints, e.g., collision avoidance, mission completion deadline, and kinematic constraints. The considered multi-UAV non-cooperative scenarios involve random number of other UAVs in addition to the typical UAV, and UAVs do not communicate and share information among each other. Due to the uncertainty in the environment, other UAVs' existence and unobservable intents, the considered problem is translated to an MDP with parameterized states, permissible actions and detailed reward functions. Dueling double deep Q network (D3QN) framework is proposed for learning the policy without any prior knowledge of the environment and other UAVs.

1.4 Bibliographic Note

- The results in Chapter 3 appeared in the journal paper:
 - X. Wang E. Turgut and M. C. Gursoy, “Coverage in Downlink Heterogeneous mmWave Cellular Networks With User-Centric Small Cell Deployment,” in *IEEE Transactions on Vehicular Technology*, vol. 68, no. 4, pp. 3513-3533, April 2019.

and in the conference paper:

- X. Wang, E. Turgut and M. C. Gursoy, “Coverage in Downlink Heterogeneous mmWave Cellular Networks With User-Centric Small Cell Deployment,” in *Proc. of the IEEE 28th Annual International Symposium on Personal, Indoor, and Mobile Radio Communications (PIMRC)*, Montreal, QC, 2017, pp. 1-7.
- The results in Chapter 4 appeared in the journal paper:
 - X. Wang and M. C. Gursoy, “Uplink Coverage in Heterogeneous mmWave Cellular Networks With Clustered Users,” in *IEEE Access*, vol. 9, no. 4, pp. 69439-69455, April 2021.

and in the conference paper:

- X. Wang and M. C. Gursoy, “Uplink Coverage in Heterogeneous mmWave Cellular Networks With Clustered Users,” in *Proc. of the IEEE 88th Vehicular Technology Conference (VTC-Fall)*, Chicago, IL, 2018, pp. 1-5.
- The results in Chapter 5 appeared in the conference paper:
 - X. Wang and M. C. Gursoy, “Multi-Agent Double Deep Q-Learning for Beamforming in mmWave MIMO Networks,” in *Proc. of the IEEE 31st Annual International Symposium on Personal, Indoor and Mobile Radio Communications (PIMRC)*, London, UK, 2020.

- The results in Chapter 6 appeared in the conference paper:
 - X. Wang and M. C. Gursoy, “Coverage in Networks with Hybrid Terahertz, Millimeter Wave, and Microwave Transmissions,” in *Proc. of the IEEE 18th Annual Consumer Communications & Networking Conference (CCNC)*, Las Vegas, NV, 2021, pp. 1-4.
- The results in Chapter 7 appeared in the journal paper:
 - X. Wang and M. C. Gursoy, “Coverage Analysis for Energy-Harvesting UAV-Assisted mmWave Cellular Networks,” in *IEEE Journal on Selected Areas in Communications*, vol. 37, no. 12, pp. 2832-2850, Dec. 2019.

and in the conference papers:

- X. Wang and M. C. Gursoy, “Simultaneous Information and Energy Transfer in mmWave UAV-assisted Cellular Networks,” in *Proc. of the IEEE 20th International Workshop on Signal Processing Advances in Wireless Communications (SPAWC)*, Cannes, France, 2019, pp. 1-5.
 - X. Wang, M. C. Gursoy and I. Guvenc, “Simultaneous Wireless Information and Power Transfer in UAV-assisted Cellular IoT Networks,” in *Proc. of the IEEE 17th Annual Consumer Communications & Networking Conference (CCNC)*, Las Vegas, NV, 2020.
- The results in Chapter 8 appeared in the conference paper:
 - X. Wang and M. C. Gursoy, “Coverage Analysis for Cellular-Connected UAVs with 3D Antenna Patterns,” in *Proc. of the IEEE Global Conference on Signal and Information Processing (GlobalSIP)*, Ottawa, ON, 2019.
- The results in Section 9.1 are reported in the submitted paper:
 - X. Wang and M. C. Gursoy, “Learning-Based UAV Trajectory Optimization with Collision Avoidance and Connectivity Constraints,” in *IEEE Transactions on Wireless Communications*

and will appear in the accepted conference paper:

- X. Wang and M. C. Gursoy, “Learning-Based UAV Trajectory Optimization with Collision Avoidance and Connectivity Constraints,” in *Proc. of the IEEE International Conference on Communications (ICC)*, Montreal, QC, 2021.
- The results in Section 9.2 will appear in the accepted conference paper:
 - X. Wang, M. C. Gursoy, T. Erpek and Y. E. Sagduyu, “Jamming-Resilient Path Planning for Multiple UAVs via Deep Reinforcement Learning,” in *Proc. of the IEEE International Conference on Communications Workshops (ICC Workshops)*, Montreal, QC, 2021.
- The results in Chapter 10 are reported in the submitted paper:
 - X. Wang, M. C. Gursoy, T. Erpek and Y. E. Sagduyu, “Collision-Aware UAV Trajectories for Data Collection via Reinforcement Learning,” in *Proc. of the IEEE Global Communications Conference (GLOBECOM)*, Madrid, Spain 2021.

CHAPTER 2

PRELIMINARIES

2.1 Point Processes

A point process can be depicted as a random collection of points in space.

2.1.1 Poisson Point Process

Poisson point processes (PPPs) provide a computational framework for different network quantities of interest [154]. The homogeneous PPP may be considered as the simplest point process. The homogeneous PPP has the following properties [4] :

- It has evenly and homogeneously distributed nodes.
- It is stationary, which means that the PPP is independent of translations.
- It is simple in the sense that there cannot be multiple points at the same location.
- It is isotropic, which means that the PPP is independent on rotations.
- The superposition of two or more independent PPPs is again a ppp.
- The independent thinning of a PPP is again a PPP.

Intensity of the Thinned PPP

The point process obtained by displacing point X_i independently of everything else according to some Markov kernel $K(X_i, \cdot)$ that defines the distribution of the displaced position of the point X_i yields another PPP. The intensity of the resulting PPP can be obtained in closed form from that of the initial PPP and the involved transformations (e.g., the thinning probability or the kernel K). If $\rho(x, \cdot)$ is the probability density pertaining to the Markov kernel applied to a PPP of intensity $\lambda(x)$ on \mathbb{R}^d , the displaced points form a PPP of intensity

$$\lambda'(y) = \int_{\mathbb{R}^d} \lambda(x) \rho(x, y) dx. \quad (2.1)$$

Laplace Transform

The Laplace functional is defined for a general point process Φ as

$$\mathcal{L}_\Phi(f) \triangleq \mathbb{E} \left[e^{-\int_{\mathbb{R}^d} f(x) \Phi(dx)} \right] = \mathbb{E} \left[e^{\sum_{X \in \Phi} f(X)} \right], \quad (2.2)$$

where f is a non-negative function on \mathbb{R}^d . In the Poisson case,

$$\mathcal{L}_\Phi(f) = \exp \left(- \int_{\mathbb{R}^d} (1 - e^{-f(x)}) \lambda(dx) \right). \quad (2.3)$$

Characterization of Distance

Let x denote the distance from origin to the nearest node in Φ , which is a homogeneous PPP. Then the complementary cumulative distribution function (CCDF) and probability density function (PDF) of x are given as

$$\text{CCDF:} \quad \bar{F}(x) = \exp(-\pi \lambda x^2), \quad (x \geq 0), \quad (2.4)$$

$$\text{PDF:} \quad f(x) = 2\pi \lambda x \exp(-\pi \lambda x^2), \quad (x \geq 0), \quad (2.5)$$

where λ is the density of PPP Φ .

2.1.2 Neyman-Scott Cluster Process

Neyman-scott cluster processes are Poisson cluster processes (PCPs) that result from homogeneous independent clustering applied to a stationary PPP [155, 156], i.e., the parent points form a stationary PPP $\Phi_p = \{p_1, p_2, \dots\}$ of intensity λ_p . The clusters are of the form $N^p = N + p$ for each $p \in \Phi_p$. N^p is a family of i.i.d. finite point sets with distribution independent of the parent process. The complete process Φ_d is given by

$$\Phi_d = \bigcup_{p \in \Phi_p} N^p. \quad (2.6)$$

The parent points themselves are not included. It is assumed that the scattering density of the daughter process is isotropic. This makes the process Φ_d isotropic. The intensity of the cluster process $\lambda_d = \lambda_p(\bar{p})$, where \bar{p} is the average number of the points in the representative cluster.

We further focus on more specific models for the representative cluster, namely Thomas cluster processes and Matérn cluster processes. Let us use x to denote the distance from a daughter node to the parent node in the representative cluster. For Thomas cluster processes, each point is scattered according to a symmetric normal distribution with variance σ^2 around the origin. Then, the CCDF and PDF of x are given as

$$\text{CCDF:} \quad \bar{F}(x) = \exp\left(\frac{-x^2}{2\sigma^2}\right), \quad (x \geq 0), \quad (2.7)$$

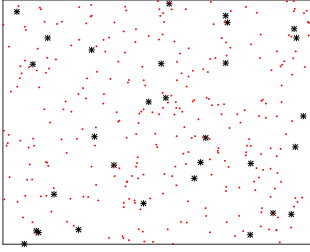
$$\text{PDF:} \quad f(x) = \frac{x}{\sigma^2} \exp\left(\frac{-x^2}{2\sigma^2}\right), \quad (x \geq 0), \quad (2.8)$$

In Matérn cluster processes, each point is uniformly distributed in a ball of radius R_c around the origin. So, the CCDF and the PDF of x are given as

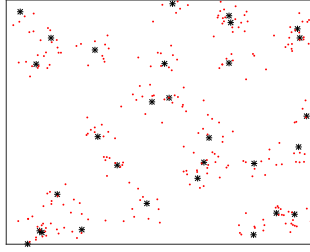
$$\text{CCDF:} \quad \bar{F}(x) = 1 - \frac{x^2}{R_c^2}, \quad (0 \leq x \leq R_c), \quad (2.9)$$

$$\text{PDF : } f(x) = \frac{2x}{R_c^2}, \quad (0 \leq x \leq R_c). \quad (2.10)$$

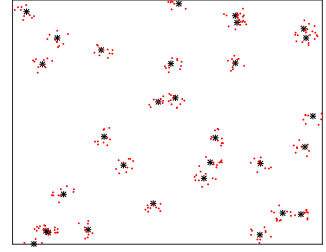
The illustrations for PPP and PCPs are shown in Fig. 2.1, where the black stars are distributed according to a homogeneous PPP. In Fig. 2.1(a) the red dots are distributed according to an independent homogeneous PPP. In Figs. 2.1(b) and (c), the red dots are distributed according to a Thomas cluster process and a Matérn cluster process, respectively, where the black stars are the parent nodes. The average number of user equipments (UEs) per cluster is 10 in Figs. 2.1(b) and (c).



(a) Poisson point process.



(b) Thomas cluster process.



(c) Matérn cluster process.

Fig. 2.1: Illustrations for PPP and PCPs.

2.2 Channel Modeling

2.2.1 Path Loss

Path loss characteristics generally depend on whether the link is line-of-sight (LOS) or non-line-of-sight (NLOS). A LOS link occurs when there is no blockage between the transmitter and the receiver, while a NLOS link occurs if blockage exists. Typically, LOS probabilities are assumed to be independent between different links, i.e., the potential correlations of blockage effects between links are not taken into account. Note that the LOS probabilities for different links are not independent in reality. For instance, neighboring base stations might be blocked by a large building simultaneously. Numerical results in [157], however, indicated that ignoring such correlations

causes a minor loss in accuracy in the network performance evaluation.

Millimeter Wave (mmWave) Transmissions

Differences between LOS and NLOS paths are significant in mmWave communications [1]. Measurements in [158, 159], showed that mmWave signals propagate as in free space with a path loss exponent of 2. The situation was however different for NLOS paths where a log distance model was fitted with a higher path loss exponent and additional shadowing [158, 159]. The NLOS path loss laws tend to be more dependent on the scattering environment. The attenuation and atmospheric and molecular absorption characteristics of mmWave propagation limit the range of mmWave communications [160]. However, with smaller cell sizes applied to improve spectral efficiency today, the attenuation and atmospheric absorption do not create significant additional path loss for cell sizes on the order of 200 m [161].

The LOS probability function in a network can be derived from field measurements or stochastic blockage models, where the blockage parameters are characterized by some random distributions. The LOS probability in mmWave transmissions can be formulated as [160]

$$p^L(x) = e^{-\epsilon x} \quad (2.11)$$

where ϵ is a parameter determined by the density and the average size of the blockages. A multi-ball approximation with piece-wise LOS probability functions is adopted in [56, 57, 162]. As shown in Fig. 2.2, a link is in LOS state with probability $p(x) = \beta_1$ inside the first ball with radius R_1 , while NLOS state occurs with probability $1 - \beta_1$. Similarly, LOS probability is equal to $p(x) = \beta_d$ for x between R_{d-1} and R_d for $d = 2, \dots, D$, and all links with distances greater than R_D are assumed to be in outage state. Additionally, LOS and NLOS links have different path loss exponents in different ball layers. Therefore, the D -ball approximation model can be formulated

as

$$p^L(x) = \begin{cases} \beta_1, & \text{if } x \leq R_1 \\ \beta_2, & \text{if } R_1 \leq x \leq R_2 \\ \vdots & \\ \beta_D \text{ if } R_{D-1} \leq x \leq R_D \\ 0, & \text{if } x \geq R_D. \end{cases} \quad (2.12)$$

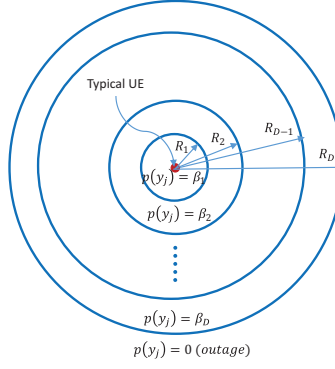


Fig. 2.2: LOS ball model

In mmWave transmissions, the path loss can be formulated as

$$L(x) = \begin{cases} \kappa^L x^{\alpha^L} & \text{w.p. } p^L(x) \\ \kappa^N x^{\alpha^N} & \text{w.p. } 1 - p^L(x) \end{cases} \quad (2.13)$$

where x is the distance of the link, α^L and α^N are the LOS and NLOS path loss exponents, respectively, κ^L and κ^N are the path loss of LOS and NLOS links at a distance of 1 meter, respectively, and $p^L(x)$ is the probability of LOS at distance x .

Terahertz (THz) Transmissions

THz transmissions encounter a more challenging propagation environment. Compared to the ultra high frequency and mmWave frequency bands, electromagnetic waves in THz bands experience high molecular absorption loss in addition to spreading loss and scattering attenuation [4–7]. The ultimate effect is a more complex path loss model that additionally includes an exponential decay in power [8]. Human-body blockage effects also have a strong impact on the communication quality of THz channels [6]. Moreover, THz waves cannot reach objects that are behind obstacles whose dimensions are greater than the wavelength. Effectively, any object whose size is greater than few millimeters including users themselves, acts as a blocker. Transceivers operating in THz bands are expected to be characterized by high antenna directivities in both transmit and receive directions [8] to compensate such severe path loss. And this would in turn have significant influence on the interference levels and the coverage performance [6].

In the terabit wireless local area networks, the links between base stations (BSs) and UEs (both the main link and the interfering links) can be easily blocked by other UEs (due to human body blockage) and the BSs [6, 7]. When the LOS path from a BS to a UE is cut off by any part of the blockers, the LOS channel is converted to the NLOS channel. The blockers can be modeled as circular objects with a radius of R_B . According to [7, 8, 67], the probability of non-blocking can be formulated as

$$p^L(x) = e^{-\lambda_B(x-R_B)R_B} \quad (2.14)$$

where x is the link distance, $\lambda_B = \lambda_{UE} + \sum \lambda_{BS}$, and λ_{UE} and λ_{BS} are the densities of the UEs and BSs, respectively.

An exponential power loss propagation model is introduced to describe the path loss in the THz

band [5, 6]. In particular, the path loss is formulated as

$$L(x) = \begin{cases} \kappa^L e^{\kappa x} x^{\alpha^L} & \text{for LOS with prob. (w.p.) } p^L(x), \\ \kappa^N e^{\kappa x} x^{\alpha^N} & \text{for NLOS w.p. } p^N(x), \end{cases} \quad (2.15)$$

where κ indicates the molecular absorption coefficient.

Microwave Transmissions

Due to their more favorable propagation characteristics, microwave transmissions experience comparable path loss in LOS and NLOS links. With this, the links in microwave transmissions are assumed to be LOS, i.e. $p^L = 1$. The path loss can be expressed as

$$L(x) = x^\alpha. \quad (2.16)$$

Air-to-Ground Links

Links between the UAV and the ground UEs/BSs all experience LOS or NLOS. Similarly as in [163], we formulate the probability of the LOS link between the UAVs and the ground UEs/BSs as

$$p^L(x) = \frac{1}{1 + C \exp(-B(\theta - C))} \quad (2.17)$$

where $\theta = \frac{180}{\pi} \arcsin(\frac{H}{x})$ is the elevation angle, H denotes the height of the UAVs, x is the link distance, and B and C are specific constants that depend on the environment (rural, urban, dense urban, etc.). The path gain of the links are be formulated the same as 2.13.

2.2.2 Shadowing

The shadowing can be incorporated by scaling the path loss with a given v and then taking the expectation of coverage probability with respect to v . Shadowing can be modeled as a log-normal random variable $10 \log v \sim N(\mu, \sigma^2)$.

2.2.3 Small-Scale Fading

Nakagami- m fading¹ is a general fading model suitable under various conditions [87]. Denoted by h_s , the small-scale fading gains (i.e., magnitude-squares of fading coefficients) follow Gamma distributions $h_l \sim \Gamma(N_l, 1/N_l)$ for LOS, while $h_n \sim \Gamma(N_n, \frac{1}{N_n})$ for NLOS, where N_l, N_n are the Nakagami fading parameters for LOS and NLOS links, respectively, and are assumed to be positive integers.

2.2.4 Antenna Gain

To compensate frequency-dependent path and penetration losses, antenna arrays can be enabled at the transmitter and receiver. [3, 164]. As the wavelength decreases, antenna sizes also decrease, reducing the antenna aperture [160], therefore it is possible to pack multiple antenna elements into the limited space at transceivers. With large antenna arrays, mmWave/THz cellular systems can implement beamforming at the transmitter and receiver to provide array gain that compensates for the frequency dependent path loss, overcomes additional noise power, and as a bonus also reduces out-of-cell interference [165]. MmWave/THz links are inherently directional. By controlling the phase of the signal transmitted by each antenna element, the antenna array steers its beam towards any direction electronically and to achieve a high gain at this direction, while offering a very low gain in all other directions [55].

Two-Dimensional (2D) Antenna Patterns

The followings are the 2D array gain functions recently discussed in the literature.

- Actual antenna pattern [166]

$$G(x) = \frac{\sin^2(\pi N_t^2 x)}{N_t \sin^2(\pi x)} \quad (2.18)$$

¹Note that Nakagami fading specializes to Rayleigh fading when $m = 1$.

- Sinc antenna pattern [166]

$$G(x) = \frac{\sin^2(\pi N_t x)}{(\pi N_t x)^2} \quad (2.19)$$

- Cosine antenna pattern [166]

$$G(x) = \begin{cases} \cos^2\left(\frac{\pi N_t x}{2}\right) & |x| \leq \frac{1}{N_t} \\ 0 & \text{otherwise} \end{cases} \quad (2.20)$$

- Multi-cosine antenna pattern [167]

$$G(x) = \begin{cases} \cos^2\left(\frac{\pi N_t x}{2}\right) & |x| \leq \frac{1}{N_t} \\ G_{act}(\phi) \cos^2(\pi N_t(|x| - \phi)) & \frac{k}{N_t} < |x| < \frac{k+1}{N_t} \\ 0 & \text{otherwise} \end{cases} \quad (2.21)$$

where N_t is total number of the antenna elements, $\phi = \frac{2k+1}{2N_t}$, and $k \in [0, \lfloor \frac{N_t}{2} \rfloor - 1]$.

- Sectored antenna pattern approximation

The sectored antenna model² is a well-used approximation in the literature. M_* and m_* are the the main lobe gain and side lobe gain, respectively, and $*$ $\in \{b, u\}$ denotes the BS side or the UE side. It is assumed that the antenna gain between the UE and the serving BS can achieve the maximum antenna gain $G_0 = M_b M_u$, due to the directionality. The beam direction of the interfering links can be modeled as uniformly distribution over $[0, 2\pi)$.

²Note that the sectored antenna model is also called the corn-shaped model.

Therefore, we can formulate the antenna gain of an interfering link as [160]

$$G = \begin{cases} M_b M_u & w.p. & p_{M_b M_u} = (\frac{\theta_b}{2\pi})(\frac{\theta_u}{2\pi}) \\ M_b m_u & w.p. & p_{M_b m_u} = (\frac{\theta_b}{2\pi})(1 - \frac{\theta_u}{2\pi}) \\ m_b M_u & w.p. & p_{m_b M_u} = (1 - \frac{\theta_b}{2\pi})(\frac{\theta_u}{2\pi}) \\ m_b m_u & w.p. & p_{m_b m_u} = (1 - \frac{\theta_b}{2\pi})(1 - \frac{\theta_u}{2\pi}), \end{cases} \quad (2.22)$$

where θ_* for $* \in \{b, u\}$ denotes the main lobe beamwidth.

Three-Dimensional (3D) Antenna Pattern at the GBSs

According to [168], the 3D antenna pattern at the GBSs can be divided into horizontal and vertical components. In the horizontal plane, the antenna attenuation can be expressed in dB as

$$G_H(\phi) = \min \left[12 \left(\frac{\phi}{\phi_{3dB}} \right)^2, G_m \right] \quad (2.23)$$

where ϕ indicates the horizontal angle between the BS antenna boresight and the UE, ϕ_{3dB} is the horizontal 3 dB beamwidth, and G_m is the maximum attenuation of the BS. On the other hand, the vertical antenna attenuation can be written as

$$G_V(\theta) = \min \left[12 \left(\frac{\theta - \theta_{etilt}}{\theta_{3dB}} \right)^2, G_m \right] \quad (2.24)$$

where $\theta = \arcsin(\frac{H}{x})$ is the vertical angel, θ_{etilt} stands for the electrical antenna downtilting angle, and θ_{3dB} represents the vertical 3 dB beamwidth of the GBS antennas. Then, combining the antenna attenuation in two planes and the maximum antenna gain G^0 at the antenna boresight, we can formulate the 3D antenna gain from the BS to the UE in dB as

$$G(\phi, \theta) = G^0 - \min(G_H(\phi) + G_V(\theta), G_m). \quad (2.25)$$



Fig. 2.3: Illustrations of the antenna pattern of GBSs on the vertical plane.

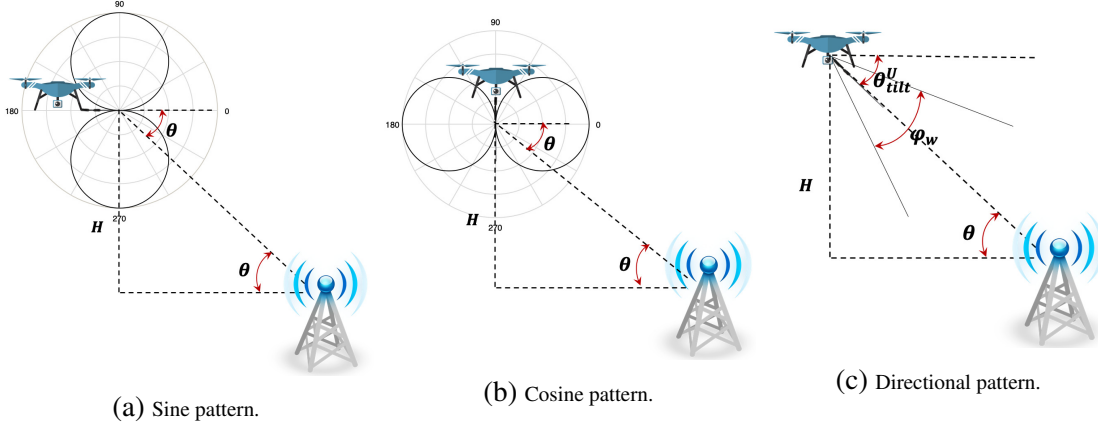


Fig. 2.4: An illustration of the vertical antenna configuration at the UAVs, where H is the height difference.

The vertical antenna pattern at GBSs is illustrated in Fig. 2.3.

3D Antenna Pattern at the UAVs

Four types of antenna patterns that the UAV may use to communicate with the GBSs/GUEs. The 3D antenna pattern of the UAV can be determined by considering the gains in the vertical and horizontal planes. It is assumed that on the horizontal plane, the antenna gain is omni-directional with 0 dB. In the vertical plane, the expressions of the antenna patterns are provided in detail in the subsections below. For a given GBS/GUE, the different UAV vertical antenna patterns are illustrated in Fig. 2.4.

- Omni-directional pattern:

If the UAV is equipped with an omni-directional antenna, the antenna gain can be formulated

as

$$G(x) = 1 \quad (2.26)$$

- Sine pattern:

If the UAV is equipped with an ultra-wideband receiver with a horizontally oriented antenna, a simple analytical approximation as a function of the elevation angle θ can be expressed as [169]

$$G(x) = G^0 \sin(\theta) = G^0 \frac{H}{\sqrt{x^2 + H^2}} \quad (2.27)$$

where G^0 is the maximum antenna gain of the UAV when $\sin(\theta)$ is 1, i.e., when the UAV is right above the GBS.

- Cosine pattern:

If the UAV is equipped with an ultra-wideband receiver with a vertically oriented antenna, the antenna gain can be written as [169]

$$G(x) = G^0 \cos(\theta) = G^0 \frac{x}{\sqrt{x^2 + H^2}}. \quad (2.28)$$

It is worth noting that this cosine approximation is a more general formulation for a directional antenna pattern with a fixed beamwidth, i.e. the directional antenna is tilting down to give a cone-shaped radiation lobe directly beneath the UAV and the main lobe and side lobe provide constant antenna gains.

- Directional pattern with tilting angle:

If the UAV is equipped with a directional antenna which can be intelligently steered and aligned with the serving GBS [96], the serving GBS is in the main lobe and has antenna gain

$G = \frac{16\pi}{\psi_w^2}$. In addition, the antenna gain of the interfering GBS can be given as

$$\begin{aligned} G(x) &= \frac{16\pi}{\psi_w^2} \mathbb{1} \left(\min \left(\frac{\pi}{2}, \frac{\psi_w}{2} + \theta_{tilt}^U \right) \geq \theta \geq \left| \theta_{tilt}^U - \frac{\psi_w}{2} \right| \right) \\ &= \frac{16\pi}{\phi_w^2} \mathbb{1} \left(H \tan \left(\min \left(\frac{\pi}{2}, \frac{\psi_w}{2} + \theta_{tilt}^U \right) \right) \geq x \geq H \tan \left(\left| \theta_{tilt}^U - \frac{\psi_w}{2} \right| \right) \right) \end{aligned} \quad (2.29)$$

where $\theta_{tilt}^U = \theta = \arctan(H/D_0)$ is the tilting angle of the UAV antenna, $\psi_w \in (0, \pi]$ is the beamwidth of the main lobe, and D_0 is the horizontal distance from the typical UAV to the serving GBS/GUE. The antenna gain of the side lobe (i.e. outside the beamwidth) is 0.

2.3 Reinforcement Learning

Reinforcement learning (RL) is a class of machine learning methods that can be utilized for solving sequential decision making problems with unknown state-transition dynamics [170] [171]. Typically, a sequential decision making problem can be formulated as a Markov decision process (MDP) [172], which is described by the tuple $\langle \mathcal{S}, \mathcal{A}, \mathcal{P}, \mathcal{R}, \gamma \rangle$, where \mathcal{S} is the state space, \mathcal{A} is the action space, \mathcal{P} is the state-transition model, \mathcal{R} is the reward function, and $\gamma \in [0, 1]$ is a discount factor that trades-off the importance of the immediate and future rewards. More specifically, at each time step, an agent, in state $s_t \in \mathcal{S}$, chooses an action $a_t \in \mathcal{A}$, transitions to next state s_{t+1} , and receives reward \mathcal{R}_t from the environment \mathcal{E} . A policy, π , is a mapping from states, s , and actions a , to the probability $\pi(s, a)$ of taking action a when in state s . An illustration of reinforcement learning scheme is displayed in Fig. 2.5.

Almost all reinforcement learning algorithms are based on estimating value functions, i.e., functions of states or state-action pairs, that estimate how good it is for the agent to be in a given state or how good it is to perform a given action in a given state [172]. For MDPs, the state-value function, denoted as $V^\pi(s_t)$, is defined as the value of a state s_t under a policy π . The cumulative

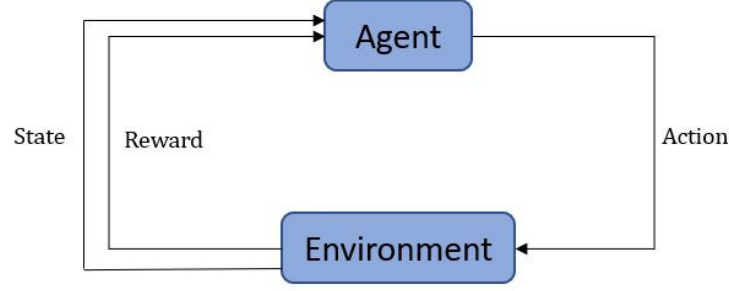


Fig. 2.5: An illustration of reinforcement learning Scheme.

discounted reward \mathcal{R}_t^C is

$$\mathcal{R}_t^C \triangleq \sum_{\tau=0}^{\infty} \gamma^{\tau} \mathcal{R}_{t+\tau}. \quad (2.30)$$

The state-value is the expected return when starting s_t and following π , and can be expressed as

$$V^{\pi}(s_t) \triangleq E_{\pi}[\mathcal{R}_t^C | s_t] = E_{\pi} \left[\sum_{\tau=0}^{\infty} \gamma^{\tau} \mathcal{R}_{t+\tau} | s_t \right]. \quad (2.31)$$

Similarly, the state-action-value, denoted as $Q^{\pi}(s_t, a_t)$, is the value of taking action a in state s under a policy π , and can be expressed as

$$Q^{\pi}(s_t, a_t) \triangleq E_{\pi}[\mathcal{R}_t^C | s_t, a_t] = E_{\pi} \left[\sum_{\tau=0}^{\infty} \gamma^{\tau} \mathcal{R}_{t+\tau} | s_t, a_t \right]. \quad (2.32)$$

The value functions satisfies the Bellman optimality equation [172]

$$V^{\pi}(s_t) = E_{\pi}[r_t + \gamma V^{\pi}(s_{t+1}) | s_t] \quad (2.33)$$

$$Q^{\pi}(s_t, a_t) = E_{\pi}[r_t + \gamma \max_{a'} Q^{\pi}(s_{t+1}, a') | s_t, a_t]. \quad (2.34)$$

The essential task of many RL algorithms is to seek the optimal policy, π^* , that maximizes the expected cumulative discounted reward, i.e., to find the optimal value functions

$$V^*(s) = \max_{\pi} V^{\pi}(s) \quad (2.35)$$

or

$$Q^*(s, a) = \max_{\pi} Q^{\pi}(s, a). \quad (2.36)$$

Q-learning is one of the most widely used algorithms for RL. In traditional Q-learning, a table (referred to Q-table) is constructed, in which the component in row s and column a is the Q-value $Q(s, a)$. The Q-learning update rule can be written as [173]

$$Q(s, a) \leftarrow Q(s, a) + \alpha[\mathcal{R} + \gamma \max_{a'} Q(s', a') - Q(s, a)], \quad (2.37)$$

where α is a scalar step size, s' is the state in the next time step.

In problems with large state and action spaces, it becomes infeasible to use the Q-table. A typical approach is to convert the update problem of Q-table into a function fitting problem, i.e., we can learn a parameterized value function $Q(s, a; \xi) \approx Q(s, a)$ with parameters ξ . When combined with deep learning, this leads to DQN. The operation of DQN consists of an online deep Q-learning phase and an offline deep neural network (DNN) construction phase, which is used to learn the value function $Q(s, a; \xi)$. Generally, the parameter set ξ is optimized by minimizing the following loss function [174]

$$\mathcal{L}_t(\xi_t) = E[(y_t - Q(s_t, a_t; \xi_t))^2], \quad (2.38)$$

where $y_t = \mathcal{R}_t + \gamma \max_{a'} Q(s_{t+1}, a'; \xi_t^-)$ is the target, and ξ_t^- is copied at certain steps from ξ_t .

The maximization operator in standard Q-learning and DQN uses the same values both to select and to evaluate an action, which increases the probability to select overestimated values and results in overoptimistic value estimates. DDQN can be used to mitigate the above problem by using the following target [175]

$$y_t = \mathcal{R}_t + \gamma Q(s_{t+1}, \arg\max_{a'} Q(s_{t+1}, a'; \xi_t); \xi_t^-), \quad (2.39)$$

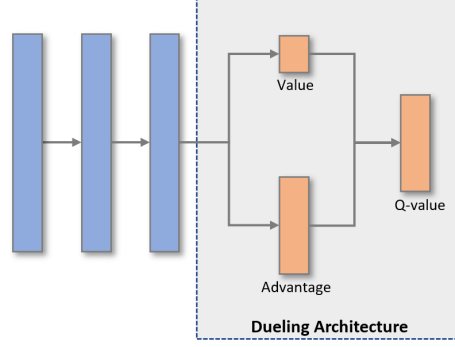


Fig. 2.6: The structure of the dueling deep Q-network.

where ξ_t is used for action selection, and ξ_t^- is used to evaluate the value of the policy, and ξ_t^- can be updated symmetrically by switching the roles of ξ_t and ξ_t^- .

Furthermore, considering that Q-value measures how beneficial a particular action a is when taken in state s , the dueling architecture is introduced to obtain a value $V(s)$ and an advantage $A(s, a) = Q(s, a) - V(s)$ [176]. The value $V(s)$ is to measure how good it is in a particular state s . The advantage $A(s, a)$ describes the advantage of the action a compared with other possible actions while in state s [177]. Therefore, the difference in dueling DQN, compared with DQN, is that the last layer of the DQN is split into two separate layers, ξ^V and ξ^A . ξ^V is used to obtain the value $V(s; \xi, \xi^V)$, and the output of ξ^A is the advantage for each action $A(s, a; \xi, \xi^A)$. The Q-value in dueling DQN can be expressed as [176]

$$\begin{aligned}
 & Q(s, a; \xi, \xi^V, \xi^A) \\
 &= V(s; \xi, \xi^V) + A(s, a; \xi, \xi^A) - \frac{1}{|\mathcal{A}|} \sum_{a'} A(s, a'; \xi, \xi^A).
 \end{aligned} \tag{2.40}$$

The general structure of dueling DQN is displayed in Fig. 2.6. Dueling DDQN (D3QN) is a combination of dueling DQN and DDQN.

CHAPTER 3

COVERAGE IN DOWNLINK

HETEROGENEOUS MMWAVE CELLULAR

NETWORKS WITH USER-CENTRIC SMALL

CELL DEPLOYMENT

3.1 System Model

3.1.1 Base Station Distribution Modeling

In this chapter, a K -tier heterogeneous downlink mmWave cellular network is considered. BSs in all tiers are distributed according to a homogeneous PPP (more specifically, the BSs in the j^{th} tier are distributed according to PPP Φ_j of density λ_j on the Euclidean plane for $j \in \mathcal{K} = \{1, 2, \dots, K\}$), and are assumed to be transmitting in a mmWave frequency band. BSs in the j^{th} tier are distinguished by their transmit power P_j , biasing factor B_j , and blockage model parameters.

3.1.2 User Distribution Modeling

We consider a realistic network scenario where the UEs are clustered around the smaller cell BSs. In this network scenario, smaller cell BSs are parent nodes and are located at the center of the clustered UEs where the locations of the UEs are modeled as a PCP. UEs in each cluster are called cluster members. Cluster members are assumed to be symmetrically independently and identically distributed (i.i.d.) around the cluster center. Assume that the cluster center is a BS in the j^{th} tier, then the union of the cluster members' locations forms a PCP, denoted by Φ_u^j . In this chapter, Φ_u^j is modeled as either (i) a Thomas cluster process, where the UEs are scattered according to a Gaussian distribution with variance σ_j^2 , or (ii) a Matérn cluster process, where the UEs are scattered according to a uniform distribution, i.e., UEs are symmetrically uniformly spatially distributed around the cluster center within a circular disc of radius R_j .

Let Y_0 and Y_j denote the distance from typical UE to the cluster center BS and the nearest BS in the j^{th} tier, respectively. Therefore, the CCDF and PDF of Y_0 are given as (2.7) (2.9) and (2.8) (2.10), respectively. And the CCDF and PDF of Y_j are given in (2.4) and (2.5), respectively. Similar to [72], to distinguish the difference between the distributions of Y_0 and Y_j , we form an additional tier, named as 0^{th} tier, which includes the cluster center BS of the typical UE. Thus, our model is denoted as a $\mathcal{K}_1 = \{0\} \cup \mathcal{K} = \{0, 1, 2, \dots, K\}$ tier model.

3.1.3 Channel Modeling

In this setting, we have the following assumptions regarding the antenna and channel models of the K -tier heterogeneous downlink mmWave cellular network:

Directional Beamforming

Antenna arrays at all BSs and UEs are assumed to perform directional beamforming. For analytical tractability, sectorized antenna model is employed where M , m , θ denote the main lobe directivity gain, side lobe gain and beamwidth of the main lobe, respectively [57, 160, 178]. The effective

antenna gain G between the typical UE and an interfering BS are provided in (2.22), where $M_b = M_u = M$ and $m_b = m_u = m$.

Path Loss and Blockage Modeling

The D -ball approximation model for LOS probability in (2.12) is adopted in this chapter. Consider an arbitrary link of length y_j ($j \in \mathcal{K}$), and define the LOS probability function $p(y_j)$ as the probability that the link is LOS. Therefore, the path loss on each link in the j^{th} tier ($j \in \mathcal{K}$) can be expressed as follows:

$$L_j(y_j) = \begin{cases} \begin{cases} \kappa_1^L y_j^{\alpha_1^{jL}} \text{ with prob. } \beta_{j1} \\ \kappa_1^N y_j^{\alpha_1^{jN}} \text{ with prob. } (1 - \beta_{j1}) \end{cases} & \text{if } y_j \leq R_{j1} \\ \begin{cases} \kappa_2^L y_j^{\alpha_2^{jL}} \text{ with prob. } \beta_{j2} \\ \kappa_2^N y_j^{\alpha_2^{jN}} \text{ with prob. } (1 - \beta_{j2}) \end{cases} & \text{if } R_{j1} \leq y_j \leq R_{j2} \\ \vdots & \\ \begin{cases} \kappa_D^L y_j^{\alpha_D^{jL}} \text{ with prob. } \beta_{jD} \\ \kappa_D^N y_j^{\alpha_D^{jN}} \text{ with prob. } (1 - \beta_{jD}) \end{cases} & \text{if } R_{j(D-1)} \leq y_j \leq R_{jD} \\ \text{outage} & \text{if } y_j \geq R_{jD}, \end{cases} \quad (3.1)$$

where $\alpha_d^{jL}, \alpha_d^{jN}$ are the LOS and NLOS path loss exponents, respectively, for the d^{th} ball of the j^{th} tier, κ_d^L, κ_d^N are the path loss of LOS and NLOS links at a distance of 1 meter in the d^{th} ball, respectively, and R_{jd} is the radius for d^{th} ball in the j^{th} tier ($j \in \mathcal{K}$), for $d = 1, 2, \dots, D$.

For the 0^{th} tier, there is only one BS, called the 0^{th} tier BS, at the cluster center and cluster members are clustered around it. Since the link distance between the cluster center BS and cluster members is generally relatively small, we assume that the link between the cluster center BS and the cluster members can be either LOS or NLOS with path loss exponents α_1^{0L} or α_1^{0N} , respectively, without an outage state. Therefore, the path loss of the link in the 0^{th} tier can be expressed as

follows:

$$L_0(y_0) = \begin{cases} \kappa_1^L y_0^{\alpha_1^{0L}} & \text{with prob. } \beta_{01}, \\ \kappa_1^N y_0^{\alpha_1^{0N}} & \text{with prob. } (1 - \beta_{01}), \end{cases} \quad (3.2)$$

where similar notations are used for path loss parameters.

We note that shadowing is not taken into account in our baseline model for computational tractability in the main analysis similarly as in [57], [160], and [178]. However, our model can be extended by incorporating log-normal shadowing, and the analysis for this extended channel model is addressed in section 3.4.7.

3.2 Path Loss Statistics

In this section, the CCDF and the PDF of the path loss for all tiers are characterized.

3.2.1 Path Loss in the 0^{th} Tier

Lemma 3.1. *The CCDF and PDF of the path loss from a typical UE to the LOS/NLOS BS in the 0^{th} tier can be expressed as follows:*

(i) *If Φ_u^j is a Thomas cluster process,*

$$CCDF : \bar{F}_{L_{0,s}}(x) = \exp \left(-\frac{1}{2\sigma_j^2} \left(\frac{x}{\kappa_1^s} \right)^{\frac{2}{\alpha_1^{0s}}} \right), \quad (3.3)$$

$$PDF : f_{L_{0,s}}(x) = \frac{x^{\frac{2}{\alpha_1^{0s}} - 1}}{\alpha_1^{0s} \kappa_1^s \alpha_1^{\frac{2}{\alpha_1^{0s}}} \sigma_j^2} \exp \left(-\frac{1}{2\sigma_j^2} \left(\frac{x}{\kappa_1^s} \right)^{\frac{2}{\alpha_1^{0s}}} \right), \quad (3.4)$$

where $x > 0$, $s \in \{LOS, NLOS\}$, and σ_j^2 is the variance of the Gaussian UE distribution.

(ii) If Φ_u^j is a Matérn cluster process,

$$\text{CCDF :} \quad \bar{F}_{L_{0,s}}(x) = 1 - \frac{x^{\frac{2}{\alpha_1^{ks}}}}{\kappa_1^s \alpha_1^{\frac{2}{ks}} R_j^2}, \quad (0 \leq x \leq \kappa_1^s R_j^{\alpha_1^{ks}}), \quad (3.5)$$

$$\text{PDF :} \quad f_{L_{0,s}}(x) = \frac{2x^{\frac{2}{\alpha_1^{ks}}-1}}{\alpha_1^{ks} \kappa_1^s \alpha_1^{\frac{2}{ks}} R_j^2}, \quad (0 \leq x \leq \kappa_1^s R_j^{\alpha_1^{ks}}), \quad (3.6)$$

where $s \in \{\text{LOS}, \text{NLOS}\}$, and R_j is the radius of the cluster.

Proof: See Appendix 1.

Therefore, the CCDF and PDF of the path loss from a typical UE to the BS in the 0^{th} tier can be expressed as

$$\bar{F}_{L_0}(x) = \sum_{s \in \{\text{LOS}, \text{NLOS}\}} p_{L_{0,s}} \bar{F}_{L_{0,s}}(x), \quad (3.7)$$

where $p_{L_{0,\text{LOS}}} = \beta_{01}$ and $p_{L_{0,\text{NLOS}}} = 1 - \beta_{01}$ are the LOS and NLOS probabilities in the 0^{th} tier, respectively.

3.2.2 Path Loss in the j^{th} Tier ($j \in \mathcal{K}$)

The CCDF of the path loss from the typical UE to the LOS/NLOS BS in the j^{th} tier can be formulated as [57, Lemma 2]

$$\bar{F}_{L_{j,s}}(x) = \exp \left(-\Lambda_{j,s}([0, x]) \right), \quad \text{for } j \in \mathcal{K}, \quad (3.8)$$

where $s \in \{\text{LOS}, \text{NLOS}\}$ and $\Lambda_{j,s}([0, x])$ is expressed in (3.9) and (3.10) for LOS and NLOS links, respectively.

$$\Lambda_{j,\text{LOS}}([0, x]) = \pi \lambda_j \sum_{d=1}^D \beta_{jd} \left[(R_{jd}^2 - R_{j(d-1)}^2) \mathbb{1} \left(x > \kappa_d^L R_{jd}^{\alpha_d^{jL}} \right) \right]$$

$$+ \left(\left(\frac{x}{\kappa_d^L} \right)^{\frac{2}{\alpha_d^{jL}}} - R_{j(d-1)}^2 \right) \mathbb{1} \left(\kappa_d^L R_{j(d-1)}^{\alpha_d^{jL}} < x < \kappa_d^L R_{jd}^{\alpha_d^{jL}} \right) \Big], \quad (3.9)$$

$$\begin{aligned} \Lambda_{j,\text{NLOS}}([0, x)) &= \pi \lambda_j \sum_{d=1}^D (1 - \beta_{jd}) \left[(R_{jd}^2 - R_{j(d-1)}^2) \mathbb{1} \left(x > \kappa_d^N R_{jd}^{\alpha_d^{jN}} \right) \right. \\ &\quad \left. + \left(\left(\frac{x}{\kappa_d^N} \right)^{\frac{2}{\alpha_d^{jN}}} - R_{j(d-1)}^2 \right) \mathbb{1} \left(\kappa_d^N R_{j(d-1)}^{\alpha_d^{jN}} < x < \kappa_d^N R_{jd}^{\alpha_d^{jN}} \right) \right]. \end{aligned} \quad (3.10)$$

Therefore, the CCDF and PDF of the path loss from a typical UE to the BS in the j^{th} tier can be expressed as

$$\overline{F}_{L_j}(x) = \exp \left(- \Lambda_j([0, x)) \right), \quad \text{for } j \in \mathcal{K}, \quad (3.11)$$

where

$$\Lambda_j([0, x)) = \Lambda_{j,\text{LOS}}([0, x)) + \Lambda_{j,\text{NLOS}}([0, x)). \quad (3.12)$$

Also, the PDF of $L_{j,s}(y)$, denoted by $f_{L_{j,s}}$ is given by

$$f_{L_{j,s}}(x) = - \frac{d\overline{F}_{L_{j,s}}(x)}{dx} = \Lambda'_{j,s}([0, x)) \exp \left(- \Lambda_{j,s}([0, x)) \right), \quad \text{for } j \in \mathcal{K}, \quad (3.13)$$

where

$$\Lambda'_{j,\text{LOS}}([0, x)) = 2\pi \lambda_j \sum_{d=1}^D \frac{\beta_{jd} x^{\frac{2}{\alpha_d^{jL}} - 1}}{\alpha_d^{jL} \kappa_d^L \alpha_d^{\frac{2}{\alpha_d^{jL}}}} \mathbb{1} \left(\kappa_d^L R_{j(d-1)}^{\alpha_d^{jL}} < x < \kappa_d^L R_{jd}^{\alpha_d^{jL}} \right), \quad (3.14)$$

and

$$\Lambda'_{j,\text{NLOS}}([0, x)) = 2\pi \lambda_j \sum_{d=1}^D \frac{(1 - \beta_{jd}) x^{\frac{2}{\alpha_d^{jN}} - 1}}{\alpha_d^{jN} \kappa_d^N \alpha_d^{\frac{2}{\alpha_d^{jN}}}} \mathbb{1} \left(\kappa_d^N R_{j(d-1)}^{\alpha_d^{jN}} < x < \kappa_d^N R_{jd}^{\alpha_d^{jN}} \right). \quad (3.15)$$

3.3 User Association

3.3.1 Association Criterion

UEs are assumed to be associated with the BS offering the strongest long-term average biased received power similarly as in [179]. This can be mathematically expressed as

$$P = \max_{j \in \mathcal{K}_1, i \in \Phi_j} P_{j,i} B_{j,i} G_0 L_{j,i}^{-1} \quad (3.16)$$

where P is the average biased received power of the typical UE, $P_{j,i}$, $B_{j,i}$, $L_{j,i}^{-1}$ are the transmission power, biasing factor, and path loss of the i^{th} BS in the j^{th} tier, respectively, and G_0 is the effective antenna gain. Since $P_{j,i}$ and $B_{j,i}$ are the same for all BSs in the j^{th} tier, the strongest average biased received power within each tier comes from the BS providing the minimum path loss. Therefore, we can write

$$P = \max_{j \in \mathcal{K}_1} P_j B_j G_0 L_{j,min}^{-1} \quad (3.17)$$

where $L_{j,min}$ is the minimum path loss of the typical UE from a BS in the j^{th} tier.

3.3.2 Association Probability

Association probability is defined as the probability that a typical UE is associated with a LOS/NLOS BS in the j^{th} tier for $j \in \mathcal{K}_1$. The association probabilities with a BS in the j^{th} tier are provided in the following lemma.

Lemma 3.2. *The probability that the typical UE is associated with a LOS/NLOS BS in the j^{th} tier for $j \in \mathcal{K}_1$, is*

$$A_{j,s} = \begin{cases} \mathbb{E}_{L_{0,s}} \left[p_{L_{0,s}} \left(\prod_{k=1}^K \bar{F}_{L_k}(C_{k,0} l_{0,s}) \right) \right], & \text{for } j = 0, \\ \mathbb{E}_{L_{j,s}} \left[\bar{F}_{L_{j,s'}}(l_{j,s}) \left(\bar{F}_{L_0}(C_{0,j} l_{j,s}) \prod_{\substack{k=1 \\ k \neq j}}^K \bar{F}_{L_k}(C_{k,j} l_{j,s}) \right) \right], & \text{for } j \in \mathcal{K}, \end{cases} \quad (3.18)$$

where $s, s' \in \{LOS, NLOS\}$, $s \neq s'$, $C_{k,j} = \frac{P_k B_k}{P_j B_j}$, $l_{j,s}$ is the path loss from a LOS/NLOS BS in the

j^{th} tier, $\overline{F}_{L_0}(\cdot)$ is given by (3.7), (3.3) or (3.5) (depending on the cluster process), and $\overline{F}_{L_k}(\cdot)$, and $\overline{F}_{L_{j,s'}}(\cdot)$ are given by (3.11) and (3.8), respectively.

Proof. See Appendix 2.

Corollary 3.1. When Φ_u^j is a Thomas cluster process, the association probability with a LOS/NLOS BS in the j^{th} tier for $j \in \mathcal{K}_1$, is given in (3.19), where $s \in \{\text{LOS}, \text{NLOS}\}$, $\Lambda_k([0, \cdot))$ is given in (3.12), $\Lambda'_{j,\text{LOS}}([0, \cdot))$ and $\Lambda'_{j,\text{NLOS}}([0, \cdot))$ are given in (3.14) and (3.15), respectively.

$$A_{j,s} = \begin{cases} \frac{p_{L_{0,s}}}{\alpha_1^{0s} \kappa_1^s \alpha_1^{0s} \sigma_j^2} \int_0^\infty e^{\left(-\frac{1}{2\sigma_j^2} \left(\frac{l_{0,s}}{\kappa_1^s}\right)^{\frac{2}{\alpha_1^{0s}}} - \sum_{k=1}^K \Lambda_k\left([0, \frac{P_k B_k}{P_0 B_0} l_{0,s})\right)\right)} dl_{0,s}, & \text{for } j = 0, \\ \int_0^\infty \left(\sum_{m \in \{\text{LOS}, \text{NLOS}\}} p_{L_{0,m}} e^{-\frac{1}{2\sigma_j^2} \left(\frac{P_0 B_0 l_{j,s}}{P_j B_j \kappa_1^m}\right)^{\frac{2}{\alpha_1^{0,m}}}} \right) \Lambda'_{j,s'}([0, l_{j,s})) \\ e^{\left(-\sum_{k=1}^K \Lambda_k\left([0, \frac{P_k B_k}{P_j B_j} l_{j,s})\right)\right)} dl_{l,s}, & \text{for } j \in \mathcal{K}. \end{cases} \quad (3.19)$$

Proof. The proof follows by substituting (3.3), (3.7), (3.8), and (3.11) into (3.18).

Corollary 3.2. When Φ_u^j is a Matérn cluster process, the association probability with a LOS/NLOS BS in the j^{th} tier for $j \in \mathcal{K}_1$, is given as.

$$A_{j,s} = \begin{cases} \frac{2p_{L_{0,s}}}{\alpha_1^{ks} \kappa_1^s \alpha_1^{ks} R_j^2} \int_0^{\kappa_1^s R_j^{\alpha_1^{ks}}} l_{0,s}^{\frac{2}{\alpha_1^{ks}} - 1} e^{-\sum_{k=1}^K \Lambda_k\left([0, \frac{P_k B_k}{P_0 B_0} l_{0,s})\right)} dl_{0,s}, & \text{for } j = 0, \\ \int_0^\infty \left(\sum_{m \in \{\text{LOS}, \text{NLOS}\}} p_{L_{0,m}} \left(1 - \frac{1}{R_j^2} \left(\frac{P_0 B_0 l_{j,s}}{P_j B_j \kappa_1^m}\right)^{\frac{2}{\alpha_1^{k,m}}}\right) \right) \Lambda'_{j,s'}([0, l_{j,s})) \\ e^{\left(-\sum_{k=1}^K \Lambda_k\left([0, \frac{P_k B_k}{P_j B_j} l_{j,s})\right)\right)} dl_{l,s}, & \text{for } j \in \mathcal{K}. \end{cases} \quad (3.20)$$

Proof. The proof follows by substituting (3.5), (3.7), (3.8), and (3.11) into (3.18).

Furthermore, given that the serving BS is from the j^{th} tier and in a LOS/NLOS transmission, the PDF of the path loss from the typical UE to its serving BS is provided in the following Lemma.

Lemma 3.3. Given that the typical UE is associated with a LOS/NLOS BS from the j^{th} tier, the

PDF of the path loss is

$$\hat{f}_{L_{j,s}}(x) = \begin{cases} \frac{p_{L_{0,s}}}{A_{0,s}} f_{L_{0,s}}(x) \left(\prod_{k=1}^K \bar{F}_{L_k}(C_{k,0}x) \right), & \text{for } j = 0, \\ \frac{1}{A_{j,s}} f_{L_{j,s}}(x) \bar{F}_{L_{j,s'}}(x) \left(\bar{F}_{L_0}(C_{0,j}x) \prod_{\substack{k=1 \\ k \neq j}}^K \bar{F}_{L_k}(C_{k,j}x) \right), & \text{for } j \in \mathcal{K}. \end{cases} \quad (3.21)$$

where $C_{k,j} = \frac{P_k B_k}{P_j B_j}$.

Proof. See Appendix 3.

3.3.3 Analysis of Special Cases for Association Probability

In this section, we provide simplified association probability expressions for several special cases to give more insights on the impact of different system parameters. Specifically, we consider a 2-tier model, where the UEs are clustered around the 1st tier BSs. We further consider a 1-ball model with radii R_1 and R_2 for tiers 1 and 2, respectively, and assume that the probability of LOS is equal to one inside the ball while outage occurs outside the ball. In addition, the path loss exponent α_L is set as 2. Performing several algebraic operations and assuming that the standard deviation of the Gaussian UE distribution is σ , we simplify the association probability expressions in (3.19) (obtained for the Thomas cluster process) as follows:

$$A_0 = \frac{1}{2\sigma^2 \kappa^L} \int_0^\infty e^{-\frac{l}{2\kappa^L \sigma^2} - \Lambda_1([0,l]) - \Lambda_2\left([0, \frac{P_2 B_2}{P_1 B_1} l]\right)} dl \quad (3.22)$$

$$A_1 = \int_0^\infty \Lambda'_1([0,l]) e^{-\frac{l}{2\kappa^L \sigma^2} - \Lambda_1([0,l]) - \Lambda_2\left([0, \frac{P_2 B_2}{P_1 B_1} l]\right)} dl \quad (3.23)$$

$$A_2 = \int_0^\infty \Lambda'_2([0,l]) e^{-\frac{l P_1 B_1}{2\kappa^L \sigma^2 P_2 B_2} - \Lambda_1\left([0, \frac{P_1 B_1}{P_2 B_2} l]\right) - \Lambda_2([0,l])} dl \quad (3.24)$$

where

$$\Lambda_j([0,x]) = \pi \lambda_j \left(R_j^2 \mathbb{1}(x > \kappa^L R_j^2) + \frac{x}{\kappa^L} \mathbb{1}(x < \kappa^L R_j^2) \right) \quad (3.25)$$

$$\Lambda'_j([0,x]) = \frac{\pi \lambda_j}{\kappa^L} \mathbb{1}(x < \kappa^L R_j^2). \quad (3.26)$$

Moreover, if we let R_1 and R_2 grow without bound, i.e., we have $R_1 \rightarrow \infty, R_2 \rightarrow \infty$, we can simplify the expressions further and obtain the following closed-form expressions:

$$A_0 = \frac{P_1 B_1}{P_1 B_1 + 2\pi\sigma^2(\lambda_1 P_1 B_1 + \lambda_2 P_2 B_2)} \quad (3.27)$$

$$A_1 = \frac{2\pi\sigma^2\lambda_1 P_1 B_1}{P_1 B_1 + 2\pi\sigma^2(\lambda_1 P_1 B_1 + \lambda_2 P_2 B_2)} \quad (3.28)$$

$$A_2 = \frac{2\pi\sigma^2\lambda_2 P_2 B_2}{P_1 B_1 + 2\pi\sigma^2(\lambda_1 P_1 B_1 + \lambda_2 P_2 B_2)}. \quad (3.29)$$

The association probability expressions above are simple functions of the key system parameters such as transmission power P_i , biasing factor B_i , BS density λ_i for tiers $i = 1, 2$ as well as the variance σ^2 of the Gaussian cluster distribution, and the impact of these parameters can be determined immediately. For instance, we readily note that as the UEs are spread more widely around the cluster center, i.e., as the variance σ^2 grows, association probability A_0 to the cluster center diminishes, as expected. Indeed, in the limit as σ^2 approaches infinity, UEs are no longer clustered around BSs, and correspondingly our model specializes to the 2-tier PPP model for which association probabilities become (in addition to having $A_0 \approx 0$)

$$A_1 \approx \frac{\lambda_1 P_1 B_1}{\lambda_1 P_1 B_1 + \lambda_2 P_2 B_2} \quad (3.30)$$

$$A_2 \approx \frac{\lambda_2 P_2 B_2}{\lambda_1 P_1 B_1 + \lambda_2 P_2 B_2}, \quad (3.31)$$

recovering the results in [12] and [57] obtained for the PPP model with no clustered users.

On the other hand, if we consider a 2-tier Matérn cluster process model with cluster radius R , association probabilities in (3.20) can be simplified as

$$A_0 = \frac{1}{\kappa^L R^2} \int_0^{\kappa^L R^2} e^{-\Lambda_1[0,l] - \Lambda_2\left[0, \frac{P_2 B_2}{P_1 B_1} l\right]} dl \quad (3.32)$$

$$A_1 = \int_0^\infty \left(1 - \frac{l}{R^2}\right) \Lambda'_1[0,l] e^{-\Lambda_1[0,l] - \Lambda_2\left[0, \frac{P_2 B_2}{P_1 B_1} l\right]} dl \quad (3.33)$$

$$A_2 = \int_0^\infty \left(1 - \frac{l P_1 B_1}{R^2 P_2 B_2}\right) \Lambda'_2[0,l] e^{-\Lambda_1\left[0, \frac{P_1 B_1}{P_2 B_2} l\right] - \Lambda_2[0,l]} dl. \quad (3.34)$$

If the radii R_1 , R_2 and the cluster radius R all grow without bound, we obtain the same expressions as in (3.30) and (3.31) for the association probabilities.

3.4 SINR Coverage Probability Analysis

In this section, an analytical framework is developed to analyze the downlink SINR coverage probability for a typical UE of Φ_u^j using stochastic geometry and employing the results obtained in Section III.

3.4.1 Signal to Interference Plus Noise Ratio

According to the association policy, a typical UE is served by the BS providing the strongest average biased received power. Therefore, if the typical UE is served by a BS in the j^{th} tier located at a distance y_j , there exists no BSs in the k^{th} tier ($\forall k \in \mathcal{K}_1$), within a disc Q_k whose center is the location of the typical UE and whose radius is proportional to $\frac{P_k B_k}{P_j B_j} l_{j,s}$. We refer to this disc as the exclusion disc throughout this chapter .

If the typical UE is associated with a BS in the j^{th} tier, the interference is due to the BSs lying beyond the exclusion disc. Therefore, the interference from the BSs in the k^{th} tier can be expressed as

$$I_{j,k} = \sum_{i \in \Phi_k \setminus Q_k} P_k G_{k,i} h_{k,i} L_{k,i}^{-1} \quad (3.35)$$

where P_k is the transmit power of the BSs in the k^{th} tier, and $G_{k,i}$, $h_{k,i}$, $L_{k,i}$ are the effective antenna gain, the small-scale fading gain and the path loss from the i^{th} BS in the k^{th} tier, respectively. We assume that all links are subject to independent Nakagami fading, and hence the small-scale fading gain h is the magnitude-square of the Nakagami fading coefficient.

The SINR experienced at a typical UE associated with a LOS/NLOS BS in the j^{th} tier can

expressed as

$$\text{SINR}_{j,s} = \frac{P_j G_0 h_j L_{j,s}^{-1}}{\sigma_{n,j}^2 + \sum_{k=0}^K \sum_{i \in \Phi_k \setminus Q_k} P_k G_{k,i} h_{k,i} L_{k,i}^{-1}} \quad (3.36)$$

where $s \in \{\text{LOS}, \text{NLOS}\}$, P_j is the transmit power in the j^{th} tier, G_0 is the effective antenna gain of the link between the serving BS and the typical UE which is assumed to be MM , h_j is the fading gain from the serving BS to the typical UE and $\sigma_{n,j}^2$ is the variance of the additive white Gaussian noise component.

3.4.2 SINR Coverage Probability

A typical UE is said to be in coverage if the received SINR is larger than a certain threshold $T_j > 0$ required for successful reception.

Definition 3.1. *Given that the typical UE is associated with a LOS/NLOS BS in the j^{th} tier, the conditional SINR coverage probability of the j^{th} tier is defined as*

$$P_{C_{j,s}}^c = \mathbb{P}(\text{SINR}_{j,s} > T_j | t = j) \quad (3.37)$$

where t indicates the associated tier and $s \in \{\text{LOS}, \text{NLOS}\}$. Therefore, the total SINR coverage probability of the K -tier heterogeneous mmWave cellular network with user-centric small cell deployment can be defined as follows:

$$P_C = \sum_{j=0}^K P_{C_j} = \sum_{s \in \{\text{LOS}, \text{NLOS}\}} A_{0,s} P_{C_{0,s}}^c + \sum_{j=1}^K \sum_{s \in \{\text{LOS}, \text{NLOS}\}} A_{j,s} P_{C_{j,s}}^c \quad (3.38)$$

where $A_{j,s}$ is the association probability of a LOS/NLOS BS in the j^{th} tier, which is given in 3.18.

P_{C_j} is the coverage probability of each tier and $P_{C_j} = \sum_{s \in \{\text{LOS}, \text{NLOS}\}} A_{j,s} P_{C_{j,s}}^c$.

The exact expressions for the coverage probabilities of each tier are given in the following theorem.

Theorem 3.1. *Given that the UE is associated with a LOS/NLOS BS from the j^{th} tier ($j \in \mathcal{K}_1$), the conditional SINR coverage probabilities are given in (3.39) at the top of the page, where $s, a \in \{LOS, NLOS\}$, N_s is the Nakagami fading factor, $\mu_{j,s} = \frac{n\eta_s T_j l_{j,s}}{P_j G_0}$, $\eta_s = N_s(N_s!)^{-\frac{1}{N_s}}$, $I_{j,k}^s$ is the interference from the LOS/NLOS BSs in the k^{th} tier to the j^{th} tier, $I_{j,0}$ is the interference from the 0^{th} tier to the j^{th} tier, and $\mathcal{L}_{I_{j,k}^s}(\mu_{j,s})$ is the Laplace transform of $I_{j,k}^s$ evaluated at $\mu_{j,s}$.*

$$P_{C_{j,s}}^c = \begin{cases} \mathbb{E}_{L_{0,s}} \left[\sum_{n=1}^{N_s} (-1)^{n+1} \binom{N_s}{n} e^{-\mu_{0,s} \sigma_{n,0}^2} \prod_{k=1}^K \left(\mathcal{L}_{I_{0,k}^{LOS}}(\mu_{0,s}) \mathcal{L}_{I_{0,k}^{NLOS}}(\mu_{0,s}) \right) \right], & \text{for } j = 0, \\ \mathbb{E}_{L_{j,s}} \left[\sum_{n=1}^{N_s} (-1)^{n+1} \binom{N_s}{n} e^{-\mu_{j,s} \sigma_{n,j}^2} \left(\sum_a p_{L_{0,a}} \mathcal{L}_{I_{j,0}^a}(\mu_{j,s}) \right) \prod_{k=1}^K \left(\mathcal{L}_{I_{j,k}^{LOS}}(\mu_{j,s}) \mathcal{L}_{I_{j,k}^{NLOS}}(\mu_{j,s}) \right) \right], & \text{for } j \in \mathcal{K}. \end{cases} \quad (3.39)$$

Proof. See Appendix 4.

Lemma 3.4. *Suppose the typical UE is associated with a LOS/NLOS BS in the j^{th} ($j \in \mathcal{K}_1$) tier, the Laplace transform of the interference from a LOS/NLOS BS in the k^{th} ($k \in \mathcal{K}_1$) tier can be expressed as in (3.40) provided at the top of the page, where $s \in \{LOS, NLOS\}$ and $a \in \{LOS, NLOS\}$ indicating whether the associated BS and interfering BS, respectively, are LOS or NLOS.*

$$\mathcal{L}_{I_{j,k}^a} = \begin{cases} \sum_G p_G \int_{\frac{P_0 B_0}{P_j B_j} l_{j,s}}^{\infty} \frac{1}{(1 + \mu_{j,s} P_0 G l_{0,a}^{-1} N_a^{-1})^{N_a}} \frac{f_{L_{0,a}}(l_{0,a})}{F_{L_{0,a}}\left(\frac{P_0 B_0}{P_j B_j} l_{j,s}\right)} dl_{0,a} & \text{for } j = 0, \\ e^{-\sum_G \int_{\frac{P_k B_k}{P_j B_j} l_{j,s}}^{\infty} \left(1 - \frac{1}{(1 + \mu_{j,s} P_k G l_{k,a}^{-1} N_a^{-1})^{N_a}} \right) p_G \Lambda'_{k,a}([0, dl_{k,a}])} & \text{for } j \in \mathcal{K}. \end{cases} \quad (3.40)$$

Proof. See Appendix 5.

The general coverage probability expressions in Theorem 3.1 specialized to Thomas and Matérn cluster processes can be readily obtained by substituting (3.4) - (3.6) into (3.39) and (3.40).

Next, we provide upper and lower bounds on the Laplace transform of the interference.

Lemma 3.5. *The Laplace transform of the interference from the cluster center LOS/NLOS BS, $\mathcal{L}_{I_{j,0}^{s,G}}$, is bounded as*

$$\left(1 + \frac{n\eta_s G B_j T_j}{G_0 B_0 N_s}\right)^{-N_s} \leq \mathcal{L}_{I_{j,0}^{s,G}} \leq 1. \quad (3.41)$$

Proof. See Appendix 6.

We note that the result in Lemma 5 can be used to obtain upper and lower bounds on the coverage probability P_C of the network.

3.4.3 Analysis of Special Cases for Coverage Probability

In this section, we again analyze (similarly as in Section 3.3.3) the special case in which the cluster size grows without bound. As defined before, y_0 is the distance from the typical UE to its own cluster center, and $l_{0,s} = \kappa_s y_0^{\alpha_s}$ is the path loss of the link given the link is in a LOS/NLOS transmission. When the cluster size increases, the typical UE moves farther away from its cluster center with high probability. One way to model this notion is to scale the distance to the cluster center as $\varsigma' y_0'$ (see e.g., [13, Section IV-B]), and also scale $l_{0,s} = \varsigma l_{0,s}'$ where $\varsigma = \varsigma'^{\alpha_s}$. As the cluster size tends to infinity, we let $\varsigma \rightarrow \infty$.

Lemma 3.6. *As the cluster size goes to infinity, the Laplace transform of the interference from the cluster center BS satisfies $\mathcal{L}_{I_{j,0}^a} \rightarrow 1$.*

Proof. See Appendix 7.

From Section III-C, we know that when the cluster size approaches infinity, association probability with the 0^{th} tier BS satisfies $A_0 \rightarrow 0$. Then, since $P_{C_0}^c \leq 1$, the coverage probability of the cluster center approaches zero as well, i.e., $P_{C_0} \rightarrow 0$. Moreover, we can obtain the coverage

probability of the j^{th} tier BSs ($j \in K$) as

$$P_{C_{j,s}} = A_{j,s} \mathbb{E}_{L_{j,s}} \left[\sum_{n=1}^{N_s} (-1)^{n+1} \binom{N_s}{n} e^{-\mu_{j,s} \sigma_{n,j}^2} \prod_{k=1}^K \left(\mathcal{L}_{I_{j,k}^{\text{LOS}}}(\mu_{j,s}) \mathcal{L}_{I_{j,k}^{\text{NLOS}}}(\mu_{j,s}) \right) \right] \quad (3.42)$$

which is the same as the coverage result in [57] obtained for the PPP-based model with no clustered users. Therefore, we can conclude that when the cluster size tends to infinity, our PCP model performs similar to a PPP-based model.

3.4.4 Analysis of Noise-Limited Networks

In previous sections, we have addressed the general case in which both noise and interference are taken into account. In this section, we provide coverage expressions for noise-limited networks. When interference is ignored, SNR coverage probabilities of j^{th} tier BSs given that the typical UE is associated with this tier can be expressed as

$$P_{C_{j,s}}^c = \mathbb{E}_{L_{j,s}} \left[\sum_{n=1}^{N_s} (-1)^{n+1} \binom{N_s}{n} e^{-\mu_{j,s} \sigma_{n,j}^2} \right]. \quad (3.43)$$

Similarly as in Section 3.3.3, we consider a 2-tier model and assume only LOS links for all BSs with $\alpha_L = 2$. Then, for Thomas cluster processes, coverage probabilities simplify to

$$P_{C_0}^c = \frac{P_1 G_0}{2T\kappa^L \sigma_{n,0}^2 \sigma^2 + P_1 G_0}, \quad (3.44)$$

$$P_{C_1}^c = \frac{\pi \lambda_1 P_1 G_0}{T\kappa^L \sigma_{n,1}^2 + \pi \lambda_1 P_1 G_0}, \quad (3.45)$$

$$P_{C_2}^c = \frac{\pi \lambda_2 P_2 G_0}{T\kappa^L \sigma_{n,2}^2 + \pi \lambda_2 P_2 G_0}. \quad (3.46)$$

For Matérn cluster processes, we have

$$P_{C_0}^c = \frac{P_1 G_0}{T\kappa^L \sigma_{n,0}^2 R^2} \left(1 - e^{-\frac{T\kappa^L \sigma_{n,0}^2 R^2}{P_1 G_0}} \right), \quad (3.47)$$

and $P_{C_1}^c$ and $P_{C_2}^c$ are the same as (3.45) and (3.46), respectively. When the cluster size tends to infinity, we have $P_{C_0}^c \approx 0$ while $P_{C_1}^c$ and $P_{C_2}^c$ do not change. And the SNR coverage probability of the entire network can be expressed as $P_C = A_1 P_{C_1}^c + A_2 P_{C_2}^c$, where A_1 and A_2 are provided in (3.30) and (3.31), respectively.

3.4.5 Area Spectral Efficiency Analysis

In the preceding analysis, we have obtained the downlink SINR coverage probability expressions for clustered UEs. In this section, we consider another performance metric, namely area spectral efficiency (ASE), to measure the network capacity. ASE is defined as the average achievable data rate per unit bandwidth per unit area [180], and it is a useful metric to measure the quality of the network performance especially for dense networks. Therefore, in order to evaluate the network performance, we formulate the ASE based on the SINR coverage probability results.

Note that we have an additional 0^{th} tier in our network model. We suppose that the typical UE clustered around the 0^{th} tier BS is from the j^{th} tier, and therefore ASE is defined as follows:

$$R(\lambda_j, T) = \left(\lambda_j (P_{C_j}(T) + P_{C_0}(T)) + \sum_{i=1, i \neq j}^K \lambda_i P_{C_i}(T) \right) \log_2(1 + T) \quad (3.48)$$

which implicitly assumes a fixed rate transmission from all BSs in the network, and has the units of bps/Hz/km². $P_{C_j}(T)$ and λ_j are the coverage probability and density of the j^{th} ($j \in \mathcal{K}_1$) tier, respectively.

3.4.6 Analysis of Practical Antenna Radiation Patterns

In this section, we extend our analysis by considering several more practical antenna pattern formulations provided in (2.18)-(2.21).

Because of the perfect beam alignment assumption between the typical UE and its serving BS, the antenna gain of the serving link is still constant even when we consider these antenna gain functions. Therefore, these more practical antenna patterns affect only the interference power as

follows:

$$I_{j,k} = \sum_{i \in \Phi_k \setminus Q_k} P_k G_0 G \left(\frac{d}{\lambda} \theta_{k,i} \right) h_{k,i} L_{k,i}^{-1} \quad (3.49)$$

where d is the antenna spacing, λ is the wavelength and θ is a uniformly distributed random variable over $[-1, 1]$.

The general expression for the coverage probability given in Theorem 3.1 remains same, while the Laplace transform of the interference in Lemma 3.4 is modified as follows:

$$\mathcal{L}_{I_{j,k}^a} = \begin{cases} \int_{\theta} \int_{C_0}^{\infty} \frac{f_{\theta}(\theta)}{(1 + \mu_{j,s} P_0 G_0 G \left(\frac{d}{\lambda} \theta_{k,i} \right) l_{0,a}^{-1} N_a^{-1})^{N_a}} \frac{f_{L_{0,a}}(l_{0,a})}{F_{L_{0,a}}(C_0)} dl_{0,a} d\theta & \text{for } j = 0, \\ e^{-\int_{\theta} f_{\theta}(\theta) \int_{C_k}^{\infty} \left(1 - \frac{1}{(1 + \mu_{j,s} P_k G_0 G \left(\frac{d}{\lambda} \theta_{k,i} \right) l_{k,a}^{-1} N_a^{-1})^{N_a}} \right) \Lambda'_{k,a}([0, dl_{k,a}]) d\theta} & \text{for } j \in \mathcal{K}. \end{cases} \quad (3.50)$$

where $C_0 = \frac{P_0 B_0}{P_j B_j} l_{j,s}$, $C_k = \frac{P_k B_k}{P_j B_j} l_{j,s}$ and the PDF of θ $f_{\theta}(x) = \frac{1}{2}$ for $x \in [-1, 1]$.

3.4.7 Analysis with Shadowing

In the preceding analysis, shadowing is not considered in the channel modeling. However, association and coverage probability analyses can be extended to incorporate shadowing. In this section, we describe how we can obtain the association and coverage probability results with shadowing which is modeled as a log-normal random variable, i.e. $10 \log v \sim N(\mu_v, \sigma_v^2)$ with μ_v and σ_v^2 being the mean and variance of the channel power under shadowing, respectively. When shadowing is taken into account, the received power P' at the typical UE can be written as

$$P' = P_j B_j G h_j v_j L_j^{-1} = P_j B_j G h_j L_j'^{-1} \quad (3.51)$$

where the scaled path loss (that now includes shadowing) is expressed as $L_j' = v_j^{-1} L_j$.

PDF and CCDF of the scaled path loss L_j' can be obtained by conditioning on the shadowing

gain v_j as $f_{L'_j|v_j}(x) = v_j f_{L_j}(v_j x)$ and $\bar{F}_{L'_j|v_j}(x) = \bar{F}_{L_j}(v_j x)$, where $x > 0$. Then, we can obtain the conditional association probability $A_{j,s|v_j}$ and coverage probability $P_{C_{j,s}|v_j}^c$ using the same analysis in the previous sections with the modified $f_{L'_j|v_j}(x)$ and $\bar{F}_{L'_j|v_j}(x)$. Finally, coverage probability can be obtained by deconditioning on shadowing gain v_j , i.e. by averaging over the distribution of v_j , as $P_{C_{j,s}} = E_{v_j}[P_{C_{j,s}|v_j}]$.

3.5 Numerical Results and Discussions

In this section, we present several numerical results based on our analyses in sections 3.3 and 3.4. Simulation results are also provided to validate the accuracy of our analysis.

In the numerical evaluations and simulations, a 2-tier heterogeneous network model with an additional 0^{th} tier, which is the cluster center of the typical UE, is considered. For this 2-tier scenario, $j = 1$ and $j = 2$ correspond to the picocell BSs and microcell BSs, respectively. In other words, a relatively high-power microcell network coexists with denser but lower-power picocell. UEs are clustered around the picocell BSs. Therefore, transmit power of BSs in the 0^{th} tier is the same as in the 1^{st} tier. For both 1^{st} and 2^{nd} tiers, D -ball approximation is used with $D = 2$, and the ball parameters are learned from [56]. In the numerical evaluations and simulations, unless stated otherwise, the parameter values listed in Table 3.1 are used.

Table 3.1: Parameter Values Table

Parameters	Values
P_0, P_1, P_2	33dBm, 33dBm, 53dBm
B_0, B_1, B_2	1, 1, 1
λ_1, λ_2	$10^2, 10^1$ (1/km ²)
$(R_{11}, R_{12}), (\beta_{11}, \beta_{12})$	(40, 60), (1, 0)
$(R_{21}, R_{22}), (\beta_{21}, \beta_{22})$	(50, 200), (0.8, 0.2)
$\alpha_d^{j,L}, \alpha_d^{j,N} \forall j, \forall d$	2, 4 [162]
N_L, N_N	3, 2 [160]
M, m, θ	10dB, -10dB, $\pi/6$ [1] [160]
Carrier frequency (F_c)	28 GHz
$\kappa_d^L = \kappa_d^N \forall d$	$(F_c/4\pi)^2$
$\sigma_{n,j}^2 \forall j$	-174dbm/Hz + 10log10(W) + 10dB

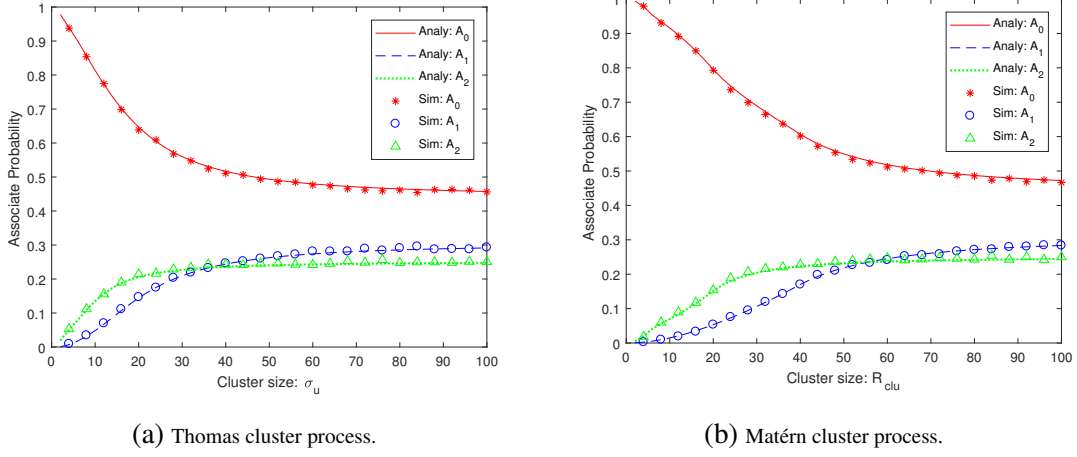


Fig. 3.1: Association probabilities as a function of the cluster size.

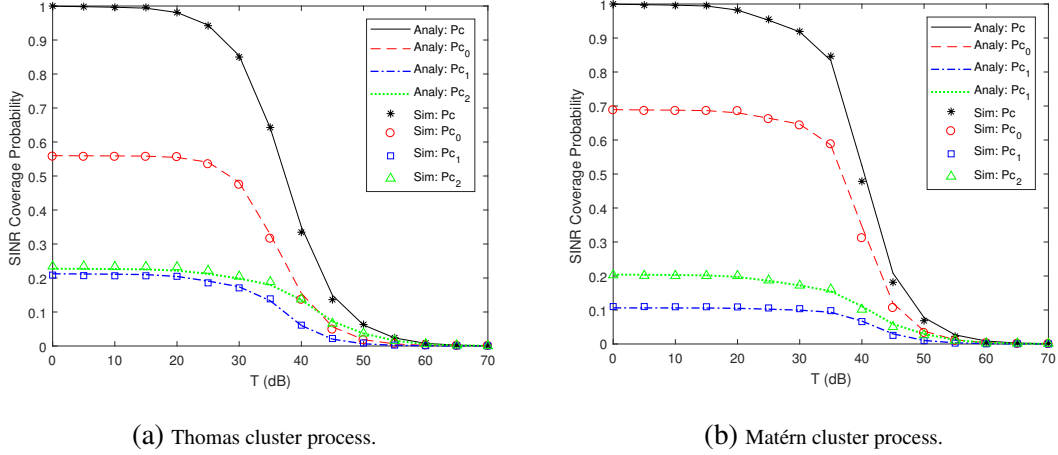


Fig. 3.2: SINR coverage probability of each tier as a function of the SINR threshold when the cluster size is 30 (i.e., $\sigma_u = 30$ and $R_{clu} = 30$).

3.5.1 Association and Coverage Probabilities

First, we analyze the effect of UE distribution on the association probability (AP). In Fig. 3.1, we plot the APs as a function of the cluster size, which is quantified by the standard deviation σ_u of Gaussian UE distribution for the Thomas cluster process, and is given by the cluster size R_{clu} of the Matérn cluster process. Since cluster size increases with the increase in σ_u and R_{clu} , UEs are located relatively farther away from their own cluster center for larger σ_u and R_{clu} . Therefore, UEs become more likely to connect with the BSs in other picocells and microcells. In other words, AP with the 0th tier, A_0 , decreases, while APs with the 1st and 2nd tiers, A_1 and A_2 , increase with the

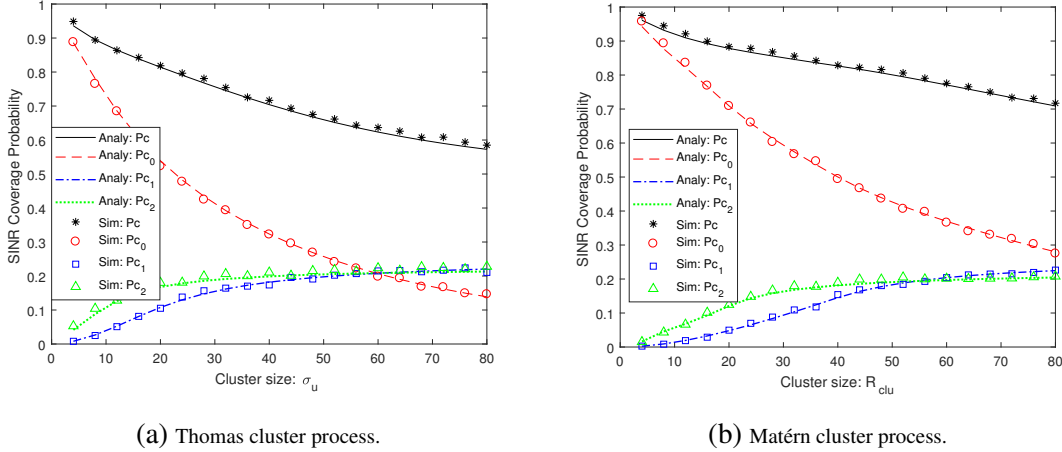


Fig. 3.3: SINR coverage probability as a function of the cluster size when $T = 30\text{dB}$.

increasing cluster size. However, note that UEs are still more likely to associate with the 0^{th} tier rather than 1^{st} and 2^{nd} tiers. We further note that we generally have excellent agreement between simulation and analytical results.

Moreover, we notice in Fig. 3.1(a) that for the Thomas cluster process, when σ_u is less than a certain value (which is approximately $\sigma_u = 38$ for this setting), AP with the 1^{st} tier is less than that with the 2^{nd} tier, while the opposite happens as σ_u exceeds 38. Note again that with the increase in σ_u , UEs are more likely to be located farther away from their own cluster center. Since picocell BSs are more densely deployed than microcell BSs, UEs are more likely to be close to other picocell BSs. Thus, A_1 becomes greater than A_2 for $\sigma_u > 38$. However, for the Matérn cluster process, since UEs are uniformly distributed around the cluster center inside a circular disc, UEs cannot be located outside the clusters as shown in Fig. 1(c), and are more compactly distributed. Therefore, A_2 is larger than A_1 for $R_{clu} < 56$, owing primarily to the larger power in the microcell tier (i.e., the second tier). Note that $P_2 = 53\text{ dBm} > P_1 = 33\text{ dBm}$ as assumed in Table II. The cluster size difference between two cluster processes is because of the fact that for Thomas cluster process with $\sigma_u = 38$, UEs can still go beyond this size. But for Matérn cluster process, UEs cannot go further than R_{clu} .

In Fig. 3.2, we plot the SINR coverage probability (CP) as a function of the threshold for both Thomas cluster process (upper sub-figure) and Matérn cluster process (lower sub-figure). Because

of the definition of CP, P_C diminishes with the increasing threshold. Moreover, when comparing the CP of each tier, we find that the cluster center BSs provide the largest CP (i.e., P_{C_0} is the largest), indicating that the UEs are more likely to be covered by their cluster center BSs. In Fig. 3.3, we plot the SINR CP as a function of the cluster size σ_u for Thomas cluster process and R_{clu} for Matérn cluster process. As cluster size increases, we note in both Fig. 3.3(a) and Fig. 3.3(b) that the total SINR CP decreases. When UEs are close to their cluster center, they are mostly covered by the cluster center BS (i.e., the 0^{th} tier BS). As UEs are distributed further away, probability of being covered by the cluster center BS goes down rapidly while SINR CP of the 1^{st} tier P_{C_1} and 2^{nd} tier P_{C_2} increase. However, the increase in P_{C_1} and P_{C_2} cannot compensate the rapid decrease in P_{C_0} , and hence the total SINR CP decreases.

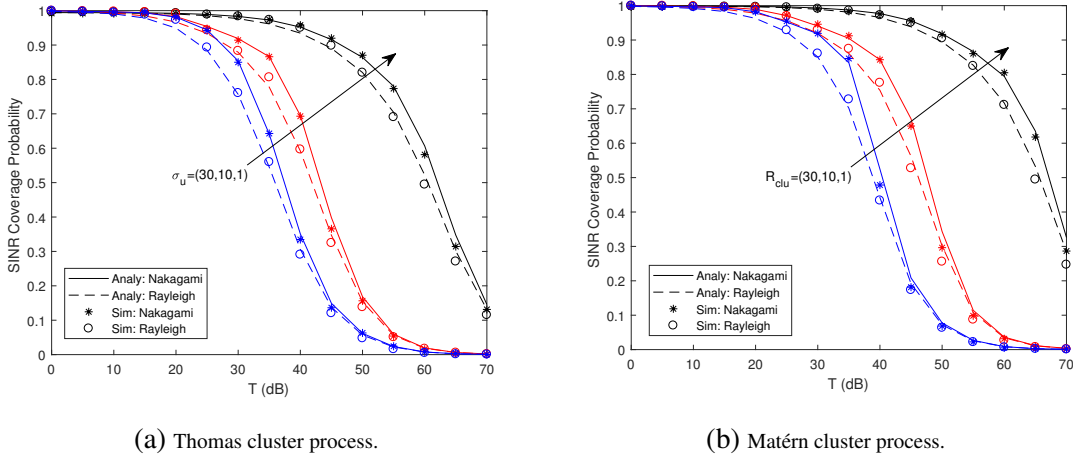


Fig. 3.4: SINR coverage probability as a function of the SINR threshold for Nakagami and Rayleigh fading.

3.5.2 Impact of the Small-Scale Fading and Shadow Fading

In Fig. 3.4, we investigate the effect of small-scale fading type on the coverage performance and plot the SINR CPs when small-scale fading for all paths are considered as either Nakagami or Rayleigh fading. Rayleigh fading is a special case of Nakagami fading with parameters $N_L = N_N = 1$. As clearly seen in the figures, better CP is achieved with Nakagami fading than Rayleigh fading because Nakagami fading leads to more favorable channel conditions. However, the dif-

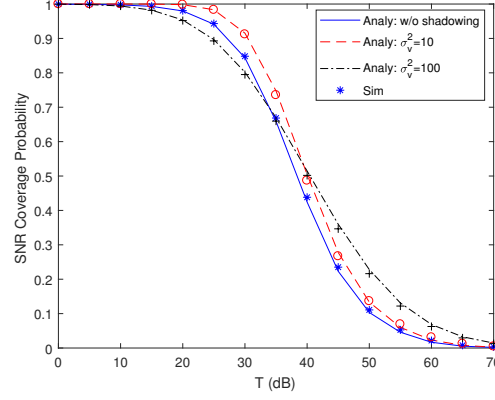


Fig. 3.5: SNR coverage probability as a function of the threshold when shadowing is considered for Thomas cluster process.

ference in the CPs for these two different fading distributions is interestingly not very significant. Moreover, it is shown in [181] that a more general fading such as Nakagami fading does not provide additional design insight, and [158] also shows that small-scale fading has a relatively little effect on mmWave communications. Therefore, together with our observation in Fig. 3.4, we consider Rayleigh fading in the following subsections for lower computational complexity. In Fig. 3.5, we investigate the effect of the log-normal shadowing for different values of the σ_v^2 . In particular, we plot the SNR coverage probability with and without shadowing taken into account. We again observe excellent agreements with the simulation results. We also notice that for $\sigma_v^2 = 10$, shadowing can help improve the SNR coverage performance slightly, indicating that fluctuations due to log-normal shadowing can lead to small increases in the coverage probability. On the other hand, when the variance is increased to $\sigma_v^2 = 100$, we have lower coverage probability with respect to the case without shadowing at small values of the threshold T while we have increased coverage probability for larger values of T . We note that the coverage probability at large values of T is already very small without shadowing taken into account. Therefore, fluctuations that tend to increase the received power in some cases result in higher coverage probabilities comparatively.

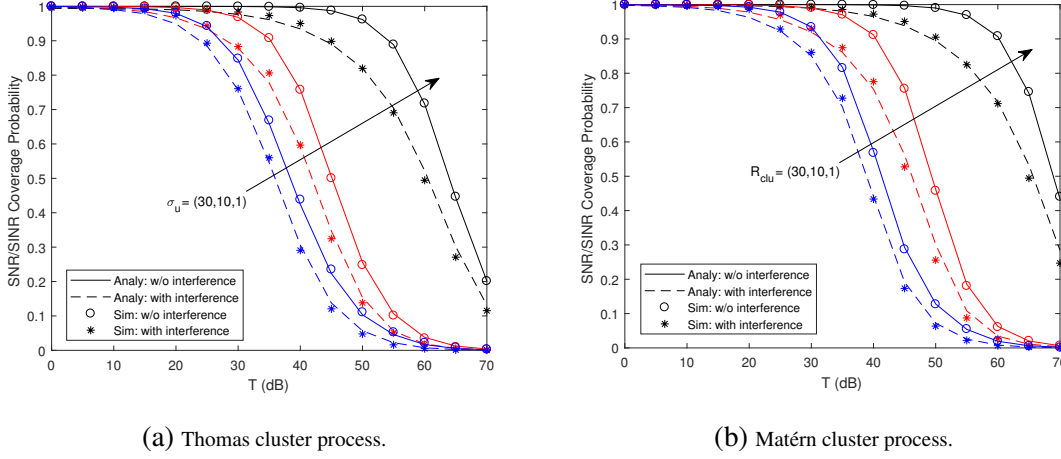


Fig. 3.6: Comparison of SINR coverage probability and SNR coverage probability as a function of the threshold for different values of the cluster size.

3.5.3 Impact of the Interference

In Fig. 3.6, we plot the total SINR CP and SNR CP as a function of the threshold in dB for different values of standard deviation of UE distribution for Thomas cluster process or the cluster size for Matérn cluster process. In our model, when UE is connected to a picocell or microcell BS outside of its cluster, interference from the 0^{th} tier BS at the cluster center is not necessarily negligible due to the relative proximity in the clustered distributions. As expected, relatively large gaps between SINR CP and SNR CP are seen in Fig. 3.6, indicating that interference has noticeable influence on the CP performance in this clustered system model. We note that this is a departure from mmWave studies with PPP-distributed users, where performance is regarded as noise-limited as in [56], [57], [182] rather than being interference-limited. Moreover, the impact of interference is slightly larger for small sized clusters as shown in Fig. 3.6(a) and Fig. 3.6(b).

3.5.4 Impact of Antenna Modeling

We also investigate the effect of the main lobe gain M and the main lobe beamwidth θ on the SINR CP performance in the sectorized antenna model. In Fig. 3.7 (a), the M and θ are the same for all BSs and UEs. As shown in the figure, improved SINR coverage is achieved when the main lobe gain M is increased for the same value of θ . The long term averaged received power of the typical

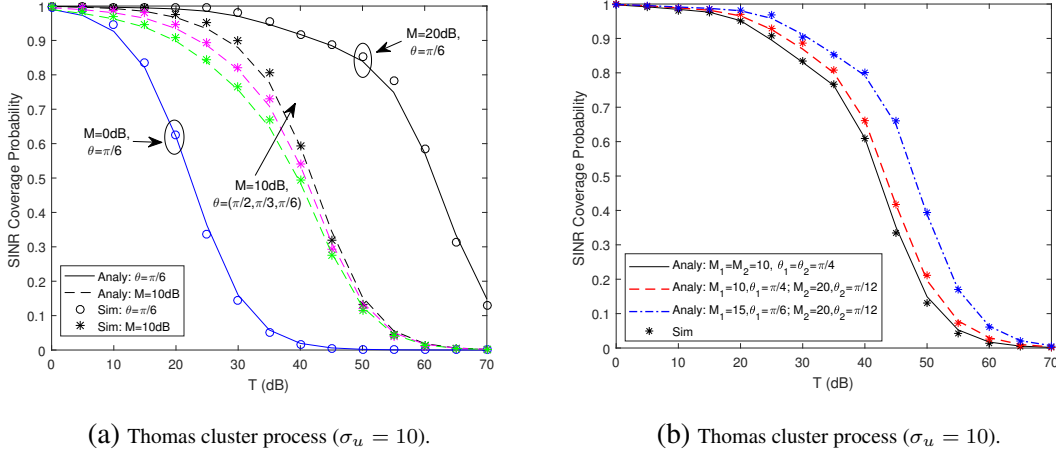


Fig. 3.7: SINR coverage probability as a function of the threshold in dB for different values of antenna main lobe gain M and the beamwidth of the main lobe θ .

UE greatly increases with the increase in M while the interference does not change much, and thus SINR becomes larger with increasing M resulting in a better coverage performance. On the other hand, when the main lobe beamwidth θ increases for the same value of M , SINR CP decreases as a result of the growing impact of the interference.

Fig. 3.7 (b) presents a relatively more general case where M , m and θ are different for the UEs and different tier BSs. In particular, we have $M_u = 10$ dB, $m_u = -10$ dB, $\theta_u = \frac{\pi}{2}$ for the UEs [160], and for the BSs, we set $m_j = -10$ dB, while different values of M_j, θ_j are considered as shown in the figure legend. From this figure, we essentially draw the same conclusions as in Fig. 3.7 (a). In addition, this result demonstrates that our analysis can be readily applied to a model in which antenna parameters are different for UEs and BSs.

We also investigate the impact of the practical cosine antenna pattern, using the same parameters as in [166], where the antenna spacing is $d = \frac{\lambda}{4}$ and the total number of antenna elements is $N_t = 64$. As shown in Fig. 3.8, compared to the sectored antenna model, the cosine antenna gain pattern results in a relatively larger coverage probability while exhibiting similar performance trends. The improved coverage with the cosine radiation pattern can be attributed to the fact that the side lobe gains decay faster and become smaller compared to the sectored antenna sidelobe gain (which is fixed), leading to smaller interference at the receivers.

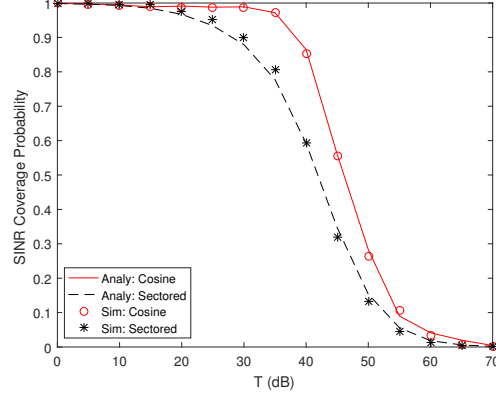


Fig. 3.8: SINR coverage probability as a function of the threshold in dB for Thomas cluster process ($\sigma_u = 10$) considering sectored and cosine antenna radiation patterns.

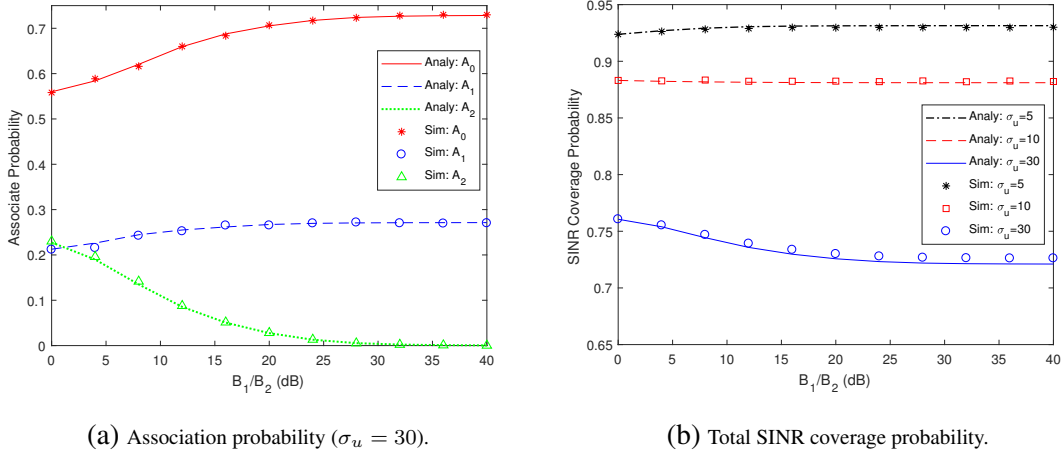


Fig. 3.9: Association probability and coverage probability as a function of B_1/B_2 when $T = 30$ dB for the Thomas cluster process. (b) plots the total coverage of the network with different cluster sizes.

3.5.5 Biasing Factor Design of the Picocell BSs

In Fig. 3.9, we investigate the impact of biasing factor of picocell BSs B_1 on the coverage performance for a fixed $B_2 = 0$ dB, considering the Thomas cluster process. First, in Fig. 3.9 (a), we plot the APs as a function of B_1/B_2 . With the increasing biasing factor ratio B_1/B_2 , UEs are more likely to be associated with picocell BSs. Therefore, in the figure, A_0 and A_1 are increasing. Another observation is that both A_0 and A_2 all converge to constants while A_2 diminishes to zero, indicating that further increase in the biasing factor of all picocell BSs will not influence the AP with each tier.

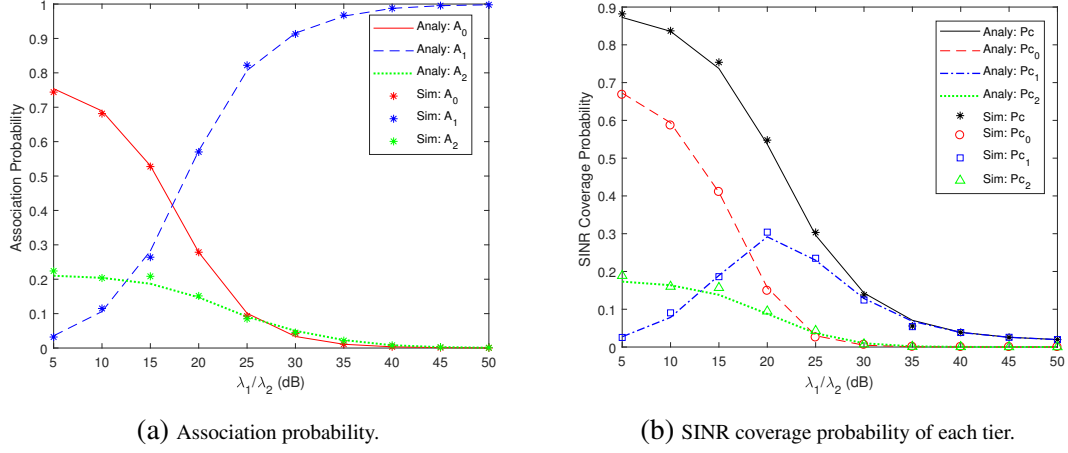


Fig. 3.10: Association probability, SINR coverage probability of each tier, and SINR coverage probability of each tier as a function of λ_1/λ_2 for the Matérn cluster process when the cluster size is 30 and $T = 30$ dB.

Fig. 3.9 (b) displays the total SINR CPs with different cluster sizes. Interestingly, total SINR CPs exhibit different behaviors for the different values of the cluster size. In particular, the total SINR CPs increase with increasing B_1/B_2 for small values of the cluster size. On the other hand, larger values of the cluster size result in a decrease in the total SINR CP. When cluster size is small, the distance between the typical UE and the cluster center picocell BS is relatively small and the typical UE is already more likely to be associated with its cluster center BS. Therefore, increasing the biasing ratio B_1/B_2 encourages the typical UE to connect with its cluster center BS which is not far away, and leads to a small increase in the coverage performance. However, the opposite happens for larger values of the cluster size. The typical UE is forced to be associated with its cluster center BS which is located relatively far away due to larger value of the cluster size. As a result, the total SINR CP decreases. We finally note that a recent work [183] has employed a random-restart hill-climbing algorithm to find the optimal biasing factor to achieve near-optimal SINR coverage probability. The authors conclude that with certain blockage conditions, such as the LOS radii, the optimal basing factor exists. However, in our case, as shown in Fig. 3.9, the total coverage probability is maximized at the extremes of very small or large values of B_1/B_2 .

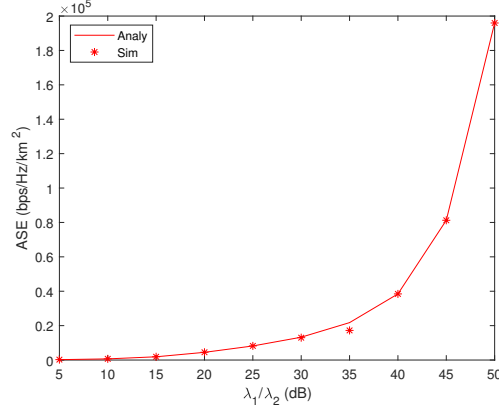


Fig. 3.11: Area spectrum efficiency as a function of λ_1/λ_2 for the Matérn cluster process, when the cluster size is 30 and $T = 30$ dB.

3.5.6 Dense Networks

In Fig. 3.10, we consider the Matérn cluster process and investigate the network performance of an ultra dense network by fixing the density of microcell BSs to $\lambda_2 = 10$ (1/km²) and increasing the density λ_1 of picocell BSs. In Fig. 3.10(a), we plot the AP as a function of λ_1/λ_2 . As can be seen, AP with the 1st tier, A_1 , increases, while APs with the 0th and 2nd tiers, A_0 and A_2 , decrease with the increasing λ_1/λ_2 . Since the cluster size is relatively large meaning that UEs are not located closer to cluster center BSs, the typical UE is more likely to be associated with the 1st tier BSs due to their increasing density, λ_1 . When the network become ultradense, i.e., λ_1 is very large, almost all UEs are associated with the 1st tier BSs, and the APs with the 0th and 2nd tier BSs approach zero.

Total SINR CPs converge to zero with the increase in λ_1 as shown in Fig. 3.10(b) due to the growing impact of interference. It is obvious that interference has a significant impact on the total coverage performance. Therefore, coverage performance of the proposed model is sensitive to the density of picocell BSs. This result is consistent with [184], where the authors indicate that if the picocell BS density is larger than 10 BSs/km², then the mmWave network is interference-dominated, and it becomes interference-limited when the density goes larger than a certain threshold. It is also shown in [162] and [185] that when λ_1 goes to infinity, CP diminishes to zero.

Finally, considering both Thomas and Matérn cluster processes, we present the ASE as a func-

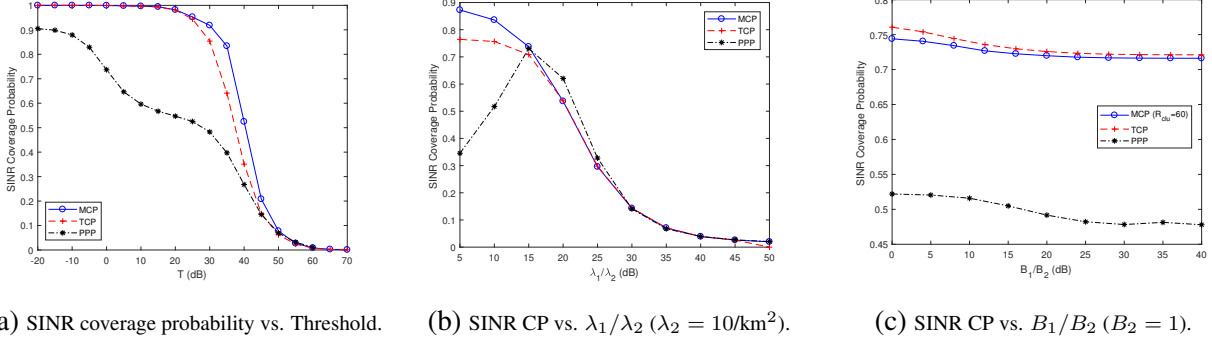


Fig. 3.12: SINR coverage probability as a function of (a) the SINR threshold, (b) B_1/B_2 and (c) λ_1/λ_2 for three different types of UE distribution, namely, Poisson point process (PPP), Thomas cluster process (TCP) with $\sigma_u = 30$ and Matérn cluster process (MCP) with $R_{clu} = 30$ except (c).

tion of λ_1/λ_2 , when we fix $\lambda_2 = 10$ ($1/\text{km}^2$) and the cluster size is 10. Fig. 3.11 shows that the ASE performance increases with increasing λ_1 , indicating that adding more picocell BSs greatly benefits the ASE of the network. This is because as shown, for instance in Fig. 3.10 (c), even in ultra dense networks, the coverage probability is not exactly zero and the decrease in coverage probability is slower than the increase in the picocell BS density.

3.5.7 Comparison between PCP Model and PPP Model

In Fig. 3.12, we investigate the effect of UE clustering on the coverage performance. In other words, we compare the SINR CPs for PPP and PCP distributed UEs. The black dot-dashed curve represents the scenario in which UEs are uniformly distributed according to a homogeneous PPP and their locations are independent of BS locations. Red dashed and blue solid curves are for PCP models with UEs being distributed according to a Thomas cluster process and Matérn cluster process, respectively. Although the cluster sizes are relatively large meaning that UEs are widely spread, the SINR CPs of the PCP models are still much higher than the SINR CP of the PPP model. In addition, the performance trends for Thomas and Matérn cluster processes are similar, while the performance trends for the PPP-based model are quite different, as shown in the figures. For instance, as seen in Fig. 3.12 (b), while the coverage probability with PCP distributed UEs decreases with increasing density (primarily due to increased interference), coverage probability with PPP

distributed UEs initially increases and then starts diminishing. These show that considering the correlation between the UEs and the BSs influences the system performance significantly.

CHAPTER 4

UPLINK COVERAGE IN HETEROGENEOUS MMWAVE CELLULAR NETWORKS WITH CLUSTERED USERS

4.1 System Model

In this section, we introduce the system model of the considered network. BS and UE spatial distributions, and the channel models are described in detail.

4.1.1 Base Station Distribution Modeling

Same as in previous chapter, we consider a K -tier heterogeneous uplink mmWave cellular network. $\mathcal{K} = \{1, 2, \dots, K\}$ is used to denote the set of tier indices. BSs in the i^{th} tier are distributed according to the independent homogeneous PPP Φ_i . BSs in different tiers differ in spatial density λ_i , transmit power P_i and biasing factor B_i (which is used to describe the association priority), and they are assumed to transmit in mmWave frequency bands. Out of K tiers, it is assumed that there are K_u tiers of small-cell BSs, around which UEs are clustered, and we denote the set as \mathcal{K}_u .

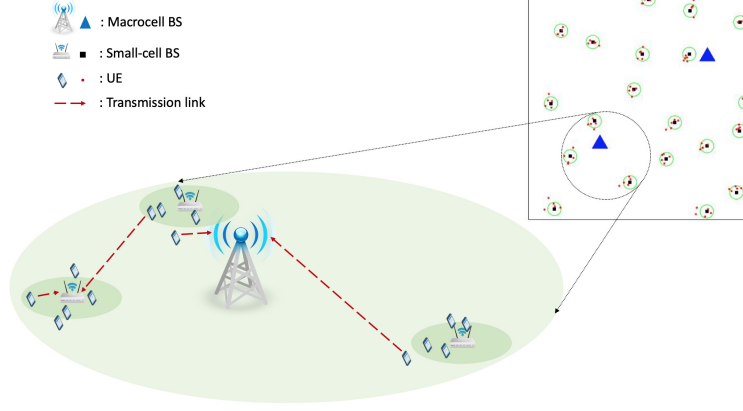


Fig. 4.1: Two-tier heterogeneous network model, where macrocells (blue triangles) and small-cells (black squares) are distributed as independent PPPs, and UEs are distributed around small-cells according to a Gaussian distribution. The average number of UEs per cluster is 5.

4.1.2 User Equipment Distribution Modeling

UEs are assumed to be clustered around the small-cell BSs. In each cluster, small-cell BS and the UEs are regarded as the cluster center and cluster members, respectively. Assume that the cluster center is a BS from the i^{th} tier, then the cluster members are regarded as the i^{th} tier UEs, and then we can use \mathcal{K}_u denote the set of tier indices for UEs. The union of the cluster members form a PCP, denoted as Φ_u^i . In this chapter Φ_u^i is modeled as a Thomas cluster process with standard deviation σ_i . Initially, in the main analysis of this chapter, we do not consider power control for the UEs, and the UEs are assumed to transmit at the same power level of P_u . Subsequently, we extend the analysis to incorporate fractional power control in section 4.5.2. We use 0^{th} tier to stand for the cluster center to the UEs, or the cluster members to the BSs. Two different two-tier heterogeneous network models are depicted in Fig. 4.1.

4.1.3 Directional Beamforming

In mmWave networks, BSs and UEs are equipped with directional antenna arrays to compensate the high path loss. We assume that the antenna arrays at the BSs and UEs perform directional beamforming, and the sectorized antenna pattern given in this chapter. Therefore, the antenna gain of the main link can achieve the largest antenna gain $G_0 = M_b M_u$, and the antenna gain between

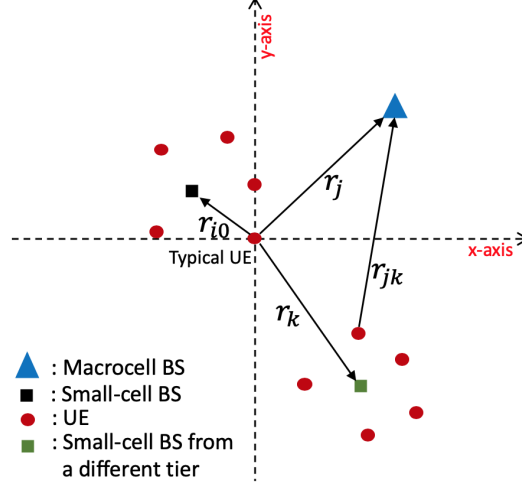


Fig. 4.2: An illustration of different distances from the BSs to UEs.

the typical BS and the interfering UEs can be expressed as in (2.22). Let p_G denote the probability of having antenna gain $G \in \{M_b M_u, M_b m_u, m_b M_u, m_b m_u\}$.

4.1.4 Channel Model

Blockage models and path loss models given in (2.11) and (2.13) are considered in this chapter. All transmission links are assumed to experience independent Rayleigh fading with unit mean, i.e., channel fading power is exponentially distributed, $h \sim \exp(1)$. However, our analysis can be extended by incorporating Nakagami fading for the main transmission link, and this extension is addressed in section 4.5.1.

4.2 Distance Characterization

In this section, we statistically describe the distances between the BSs and UEs. A representative scenario displaying different distances is shown in Fig. 4.2. Assume that the typical UE is from the i^{th} tier and is located at the origin. The PDF and CCDF of these distances are discussed below, and will be used in the analysis of association probability and the system performance matrices.

4.2.1 Distance from the Typical UE to its Cluster Center BS r_{i0} ($i \in \mathcal{K}_u$)

Lemma 4.1. *Given the link is in $s \in \{\text{LOS}, \text{NLOS}\}$ channel, the PDF and CCDF of r_{i0} can be expressed as*

$$f_{r_{i0}^s}(x) = p_{\alpha i}^s(x) f_{r_{i0}}(x) / D_{i0}^s \quad (4.1)$$

$$\overline{F}_{r_{i0}^s}(x) = \int_x^\infty p_{\alpha i}^s(x) f_{r_{i0}}(t) dt / D_{i0}^s \quad (4.2)$$

where $D_{i0}^s = \mathbb{E}_{r_{i0}}[p_{\alpha i}^s(r_{i0})]$ is the probability that the link between the UEs and their cluster center small-cell BSs is in s channel.

Proof : See Appendix 8.

4.2.2 Distance from the Typical UE (the origin) to the Nearest j^{th} Tier LOS/NLOS BS r_j ($j \in \mathcal{K}$)

Given that the typical UE can observe at least one LOS/NLOS BS in the j^{th} tier, the PDF and CCDF of the distance can be expressed as [160]

$$\overline{F}_{r_j^s}(x) = e^{-2\pi\lambda_j \int_0^x t p_{\alpha j}^s(t) dt} / D_j^s \quad (4.3)$$

$$f_{r_j^s}(x) = 2\pi\lambda_j x p_{\alpha j}^s(x) e^{-2\pi\lambda_j \int_0^x t p_{\alpha j}^s(t) dt} / D_j^s \quad (4.4)$$

where $D_j^s = 1 - e^{-2\pi\lambda_j \int_0^\infty x p_{\alpha j}^s(x) dx}$ is the probability that the typical UE has at least one $s \in \{\text{LOS}, \text{NLOS}\}$ j^{th} BS around.

4.2.3 Distance from the k^{th} Tier UE to the j^{th} tier BSs r_{jk} ($j \in \mathcal{K}, k \in \mathcal{K}_u$)

For a UE from the k^{th} tier, the distance from the cluster center BS to the j^{th} tier BSs is notated by v_{jk} . Since the cluster members are distributed according to a Gaussian distribution with variance

σ_k^2 , the conditional distribution of r_{jk} given v_{jk} is a Rice distribution, and the PDF is given by [74]

$$f_{r_{jk}}(r|v_{jk}) = \text{Ricepdf}(r, v_{jk}; \sigma_k^2) \quad (r \geq 0) \quad (4.5)$$

where $\text{Ricepdf}(a, b; \sigma^2) = \frac{a}{\sigma^2} \exp(-\frac{a^2+b^2}{2\sigma^2}) I_0(\frac{ab}{\sigma^2})$ and $I_0(\cdot)$ is the modified Bessel function of the first kind with order zero. This distance formulation is used in the analysis of interference.

4.3 Association Probability

In this section, we first describe the downlink-uplink coupled association strategy, then derive expressions for the association probability, and finally provide discussions on the conditional PDF of the distance from the typical UE to the reference BSs. Since the typical UE can be served by its cluster center BS, other small-cell BSs, and the macrocell BSs, we have three types of reference BSs in the network. Association probability describes the probability that the typical UE is served by a reference BS. In Section V, we investigate the coverage probabilities at each reference BS, and together with the association probability we eventually investigate the coverage performance of the entire network.

4.3.1 Association Criterion

Coupled association strategy is adopted in this chapter, which constrains the serving BS to be the same in both uplink and downlink. More specifically, all BSs send pilot signals to the UEs in downlink transmission, and the UEs choose the BS providing the largest long-term averaged biased received power [62] to connect in both downlink and uplink transmissions. Here, long-term averaging indicates that we average over the small-scale fading. Biasing factor describes the association priority of each UEs to different tiers of BSs, and is denoted by B_j for the j^{th} tier BSs. Larger B_j indicates that UEs have higher preference to be associated with j^{th} tier BSs. This largest

long-term averaged biased received power at a UE can be formulated as

$$P = \max_{j \in (\mathcal{K} \cup 0), n \in \Phi_j} P_{j,n} B_{j,n} G_0 L_{j,n}^{-1} \quad (4.6)$$

where $P_{j,n}$, $B_{j,n}$, $L_{j,n}$ are the transmit power, biasing factor, and the path loss of the n^{th} BS in the j^{th} tier, respectively. G_0 is the effective antenna gain. Since in the j^{th} tier, the transmit power and the biasing factor are the same, the BS in this tier with the minimum path loss to the UE provides the maximum received power P . Now, we can rewrite

$$P = \max_{j \in (\mathcal{K} \cup 0)} P_j B_j G_0 L_{j,min}^{-1} \quad (4.7)$$

where $L_{j,min} = \kappa r_{min}^\alpha$ is the minimum path loss in the j^{th} tier.

4.3.2 Association Probability

Based on the coupled association strategy, we can define the association probability (denoted by $A_{ij,s}$) as the probability that an i^{th} tier UE is served by a j^{th} tier BS in s channel, indicating that this BS provides the largest long-term averaged biased received power to the typical UE in downlink transmission. We define the event $S_{ij,s} = \{\text{the typical UE from the } i^{th} \text{ tier is served by a BS from the } j^{th} \text{ tier with a } s \in \{\text{LOS, NLOS}\} \text{ link}\}$. Again, we note that the typical UE can be served by its cluster center BS and in this case we set $j = 0$.

Lemma 4.2. *The probability that the typical UE from the i^{th} tier is associated with a BS from the j^{th} tier in a LOS/NLOS transmission is given by the following expressions in two different cases:*

$$A_{ij,s} =$$

$$\begin{cases} D_{i0}^s \mathbb{E}_{r_{i0}^s} \left[\prod_{k=1}^K \prod_b D_k^b \bar{F}_{r_k^b} [(C_{k0}^{bs} r_{i0}^{s\alpha_s})^{\frac{1}{\alpha_b}}] \right], & j = 0, \\ \mathbb{E}_{r_j^s} \left[D_j^s D_j^{s'} \bar{F}_{r_j^{s'}} \left(\frac{\kappa_{s'}}{\kappa_s} r_j^{s\frac{\alpha_s}{\alpha_{s'}}} \right) \left[\sum_a D_{i0}^a \bar{F}_{r_{i0}^s} ((C_{0j}^{as} r_j^{s\alpha_s})^{\frac{1}{\alpha_a}}) \right] \left[\prod_{\substack{k=1 \\ k \neq i}}^K \prod_b D_k^b \bar{F}_{r_k^b} ((C_{kj}^{bs} r_j^{s\alpha_s})^{\frac{1}{\alpha_b}}) \right] \right], & j \in \mathcal{K}, \end{cases} \quad (4.8)$$

where $s, s', a, b \in \{LOS, NLOS\}$, $C_{kj}^{sb} = \frac{P_k B_k \kappa_s}{P_j B_j \kappa_b}$, $D_k^b = 1 - e^{-2\pi\lambda_k \int_0^\infty x p_{\alpha_k}^b(x) dx}$ is the probability that a UE has at least one $b \in \{LOS, NLOS\}$ k^{th} tier BS around, $D_{i0}^s = \mathbb{E}_{r_{i0}}[p_{\alpha_i}^s(r_{i0})]$ is the probability that the link from the typical UE to its cluster center BS is in $s \in \{LOS, NLOS\}$ condition, and $\bar{F}_r(x)$ is the CCDF of r given in (4.2) and (4.3) in Section III.

Proof: See Appendix 9.

4.3.3 Conditional PDF of the Distance from the Typical UE to the Associated BS $r_{ij,s}$ Given $S_{ij,s}$

The conditional CDF of $r_{ij,s}$ given $S_{ij,s}$ can be expressed as

$$\hat{F}_{r_{ij,s}}(x) = \mathbb{P}(r_{ij,s} < x | S_{ij,s}) = \frac{\mathbb{P}(r_{ij,s} < x, S_{ij,s})}{\mathbb{P}(S_{ij,s})} = \frac{\mathbb{P}(r_{ij,s} < x, S_{ij,s})}{A_{ij,s}} \quad (4.9)$$

Following a similar approach as in the analysis of the association probability, we obtain the conditional PDF as

$$\begin{cases} \hat{f}_{r_{ij,s}}(x) = \frac{\hat{F}_{r_{ij,s}}(x)}{dx} = \frac{f_{r_{i0}^s}(x)}{A_{i0,s}} D_{i0}^s \prod_{k=1}^K \prod_b D_k^b \bar{F}_{r_k^b} [(C_{k0}^{bs} x^{\alpha_s})^{\frac{1}{\alpha_b}}], & j = 0, \\ \frac{f_{r_j^s}(x)}{A_{ij,s}} D_j^s D_j^{s'} \bar{F}_{r_j^{s'}} \left(\frac{\kappa_{s'}}{\kappa_s} x^{\frac{\alpha_s}{\alpha_{s'}}} \right) \left[\sum_a D_{i0}^a \bar{F}_{r_{i0}^s} ((C_{0j}^{as} x^{\alpha_s})^{\frac{1}{\alpha_a}}) \right] \left[\prod_{\substack{k=1 \\ k \neq i}}^K \prod_b D_k^b \bar{F}_{r_k^b} ((C_{kj}^{bs} x^{\alpha_s})^{\frac{1}{\alpha_b}}) \right], & j \in \mathcal{K}. \end{cases} \quad (4.10)$$

4.4 Coverage Analysis

In this section, coverage probabilities are analyzed. First by utilizing tools from stochastic geometry, we provide general expressions for coverage probabilities. Subsequently, the Laplace transforms of the inter-cell interference terms are characterized for Thomas cluster processes.

4.4.1 Signal-to-Interference-Plus-Noise Ratio

Due to orthogonal resource allocation among users in a cell, there is only one UE from each outside cell causing interference to a reference BS. We note that if the reference BS is the cluster center BS to the typical UE, this BS only experiences inter-cell interference; otherwise the reference BS experiences both inter-cell and the interference from a cluster member UE. We model the interfering UEs as Φ'_{uk} .

Therefore, the interference can be expressed as follows:

$$\text{Inter-cell interference: } I_{jk} = \sum_{n \in \Phi'_{uk}} P_u G_{k,n} h_{k,n} \kappa^{-1} r_{k,n}^{-\alpha} \quad (4.11)$$

$$\text{Interference from a cluster member UE: } I_{j0} = P_u G h \kappa^{-1} r_{j0}^{-\alpha} \quad (4.12)$$

where P_u is the transmit power of the UEs, and $G_{k,n}$ and $h_{k,n}$ are the effective antenna gain and the small-scale fading gain of the n^{th} interfering UE in Φ'_{uk} , respectively. We note that if the reference BS is the cluster center BS, $I_{j0} = 0$.

The SINR experienced at the reference BS can be expressed as

$$\text{SINR}_{ij,s} = \frac{P_u G_0 h_j \kappa_s r^{-\alpha_s}}{\sigma_n^2 + I_{j0} + \sum_{k \in \mathcal{K}_u} I_{jk}} \quad (4.13)$$

where $s \in \{\text{LOS}, \text{NLOS}\}$, $G_0 = M_b M_u$ and σ_n^2 is the variance of the additive white Gaussian noise component.

4.4.2 SINR Coverage Probability

The association probability is the probability that the typical UE is served by a reference BS. In this subsection, we analyze the SINR coverage probability $P_{C_{ij,s}}^c$ which is defined as the probability that the experienced SINR at the reference BS is above a certain threshold $T > 0$ given $S_{ij,s}$, i.e., $P_{C_{ij,s}}^c = \mathbb{P}(\text{SINR}_{ij,s} > T | S_{ij,s})$. The coverage probability of the entire network can be formulated as

$$P_C = \sum_{j=0}^K P_{C_{ij}} = \sum_{j=0}^K \sum_{s \in \{L, N\}} \mathbb{P}(\text{SINR}_{ij,s} > T | S_{ij,s}) \mathbb{P}(S_{ij,s}) = \sum_{j=0}^K \sum_{s \in \{L, N\}} P_{C_{ij,s}}^c A_{ij,s} \quad (4.14)$$

where $A_{ij,s}$ is the association probability given in (4.8). The following result characterizes the coverage probabilities.

Theorem 4.1. *Given the event $S_{ij,s} = \{\text{the typical UE from the } i^{\text{th}} \text{ tier is served by a BS from the } j^{\text{th}} \text{ tier with an } s \in \{\text{LOS}, \text{NLOS}\} \text{ link}\}$, the SINR coverage probability is formulated as*

$$P_{C_{ij,s}}^c = \mathbb{P}(\text{SINR}_{ij,s} > T_j | S_{ij,s}) = \mathbb{E}_{r_{ij,s}} \left[e^{-\mu_{ij}^s \sigma_n^2} \mathcal{L}_{I_{j0}}(\mu_{ij}^s) \prod_{k=1}^{K_u} \mathcal{L}_{I_{jk}}(\mu_{ij}^s) \right], \quad (4.15)$$

where $s \in \{\text{LOS}, \text{NLOS}\}$, $\mu_{ij}^s = \frac{T_j \kappa_s r_{ij,s}^{\alpha_{ij,s}}}{P_u G_0}$, I_{jk} is the interference from the UEs in the k^{th} tier to the reference BS in the j^{th} tier, I_{i0} is the interference to the reference BS from its cluster members. $\mathcal{L}_I(\mu) = \mathbb{E}\{\exp(-\mu I)\}$ is the Laplace transform of I evaluated at μ , and $\mathcal{L}_{I_{i0}}(\mu) = 1$ when $I_{i0} = 0$.

Proof: See Appendix 10.

4.4.3 Laplace Transforms of the Interference Terms

In this subsection, we provide characterizations for the Laplace transforms of the interference terms.

Theorem 4.2. *If the UEs are distributed around small cell BSs according to Gaussian distribu-*

tions, the Laplace transform of the inter-cell interference is given by the following:

1) If the interference arises from the cluster member, we have

$$\mathcal{L}_{I_{j0}}(\mu_{ij}^s) = \sum_G \sum_{a \in \{L, N\}} p_G D_{j0}^a \mathcal{L}_{I_{j0}^{Ga}}(\mu_{ij}^s) \quad (4.16)$$

where

$$\mathcal{L}_{I_{j0}^{Ga}}(\mu_{ij}^s) = \int_0^\infty \frac{1}{1 + \mu_{ij}^s P_u G \kappa_a^{-1} r_{j0}^{-\alpha_a}} f_{R_{j0}^s}(r_{j0}) dr_{j0}. \quad (4.17)$$

2) If the interference arises from the UEs in the k^{th} ($k \in \mathcal{K}_u$) tier, we have

$$\mathcal{L}_{I_{jk}}(\mu_{ij}^s) = \prod_G \prod_{a \in \{L, N\}} \mathcal{L}_{I_{jk}^{Ga}}(\mu_{ij}^s) \quad (4.18)$$

where

$$\mathcal{L}_{I_{jk}^{Ga}}(\mu_{ij}^s) = e^{-2\pi \int_0^\infty \lambda_k p_G P_{\alpha k}^a(r_{jk,n}) \left(\frac{1}{1 + (\mu_{ij}^s P_u G \kappa_a^{-1} r_{jk,n}^{-\alpha_a}) - 1} \right) r_{jk,n} dr_{jk,n}}. \quad (4.19)$$

Above, $s, a \in \{LOS, NLOS\}$, $G \in \{M_b M_u, M_b m_u, m_b M_u, m_b m_u\}$ is the antenna gain, p_G is probability of having different antenna gains.

Proof: See Appendix 11.

4.5 Extensions and Special Cases

In this section, we extend our analysis to incorporate Nakagami fading and also fractional power control. We also address average ergodic spectral efficiency. Finally, we consider special cases for which we obtain simplified expressions for the association and coverage probabilities.

4.5.1 Extension to Nakagami Fading

It is well known that Rayleigh fading is a special case of Nakagami fading and is obtained by setting the Nakagami parameter $N_s = 1$. Hence, Nakagami is a more general fading distribution that provides a better fit to several practical scenarios and experimental results. In this subsection, we extend the coverage analysis to Nakagami fading.

Corollary 4.1. *When small-scale Nakagami fading with Nakagami parameter N_s (where $s \in \{LOS, NLOS\}$) is considered for the main link, the SINR coverage probability of each tier is given by the following:*

$$P_{C_{ij,s}}^c = \mathbb{E}_{r_{ij,s}} \left[\sum_{n=1}^{N_s} (-1)^{n+1} \binom{N_s}{n} e^{-\mu_{ij}^s \sigma_n^2} \mathcal{L}_{I_{j0}}(\mu_{ij}^s) \prod_{k=1}^{K_u} \mathcal{L}_{I_{jk}}(\mu_{ij}^s) \right]. \quad (4.20)$$

where when $j = 0$, $I_{j0} = 0$ and $\mathcal{L}_{I_{j0}}(\mu_{ij}^s) = 1$. In the above coverage probability expressions, the Laplace transforms of the interference terms follow (4.16)-(4.19) with the same expressions.

Proof: The proof follows along the same lines as in the proof of Theorem 4.1. The only change is that the moment generating function (MGF) of the now gamma-distributed fading gain h is applied in the computation of the expectation $\mathbb{E}_h[\cdot]$.

4.5.2 Extension to UE Fractional Power Control

Two types of fractional power control can be considered for UEs: 1) path loss based fractional power control is performed by compensating the path loss of the UE irrespective of whether its path to the serving BS is LOS or NLOS; 2) distance based fractional power control is performed by inverting with the LOS path loss exponent [61]. The transmit power of UEs can be expressed as follows:

$$P'_u = \begin{cases} P_u t^{\tau \alpha_L}, & \text{if distance based,} \\ P_u L^\tau, & \text{if path loss based,} \end{cases} \quad (4.21)$$

where $\tau \in [0, 1]$ is the power control factor, t is the distance from the UE to its serving BS, α_L is the LOS path loss exponent, and L is the path loss of the link. When $\tau = 0$, no power control is performed. We consider the path loss based fractional power control as in LTE [186].

With fractional power control, the general expression for SINR coverage probability essentially remains the same as in (4.14) and (4.15), with only P_u replaced by P'_u . However, the Laplace transform of the interference should be modeled differently. To determine the Laplace transforms of interference terms, we need to make an assumption as in [187] [188]. Since there is only one UE in one cell inflicting interference, we assume that the active users also form a PPP, i.e., Φ'_{uk} is a PPP, and the density of interfering UEs is set to be equal to the small cell BS density λ_k in the k^{th} tier. Because of the blockage model, the interfering links can be LOS/NLOS. Therefore, the density of LOS/NLOS inter-cell interfering UEs in the k^{th} tier be modeled as [186]

$$\lambda_{us}^{jk}(r) = \lambda_k p_{\alpha k}^s(r) \quad (4.22)$$

where λ_k is the density of the reference BSs in the k^{th} tier, r is the distance from the reference BS to the interfering UE.

Let us use I_{jk}^{Ga} to denote the interference from the k^{th} tier UEs to a j^{th} tier reference BS. Since the transmit power of UEs depend on the path loss from its serving BS (the cluster center BS, small-cell BSs, or macro BSs), we need to distinguish different cases considering the transmit power of interfering UEs. Therefore, we have

$$I_{jk}^{Ga} = \sum_{\substack{m=0 \\ m \neq j}}^K (I_{jkmL}^{Ga} + I_{jkmN}^{Ga}) \quad (4.23)$$

where interference I_{jkmL}^{Ga} occurs when the k^{th} tier interfering UEs are served by an m^{th} tier BS over a LOS link. Next we characterize the Laplace transforms of the interference terms.

Lemma 4.3. 1) If the interference arises from the cluster member, we have

$$\mathcal{L}_{I_{j0}}(\mu_{ij}^s) = \sum_G \sum_{a \in \{L, N\}} \sum_{m=1}^K \sum_{b \in \{L, N\}} p_G D_{j0}^a A_{km,b} \mathcal{L}_{I_{j0mb}^{Ga}}(\mu_{ij}^s) \quad (4.24)$$

where

$$\mathcal{L}_{I_{j0}^{Ga}}(\mu_{ij}^s) = \int_0^\infty \int_0^\infty \frac{1}{1 + \mu_{ij}^s P_u(\kappa_b t^{\alpha_b})^\tau G \kappa_a^{-1} r_{j0}^{-\alpha_a}} \hat{f}_{r_{km,b}}(t) f_{R_{j0}^s}(r_{j0}) dt dr_{j0}. \quad (4.25)$$

2) If the interference arises from the UEs in the k^{th} ($k \in \mathcal{K}_u$) tier, we have

$$\mathcal{L}_{I_{jk}}(\mu_{ij}^s) = \prod_G \prod_{a \in \{L, N\}} \prod_{\substack{m=0 \\ m \neq j}}^K \prod_{b \in \{L, N\}} \mathcal{L}_{I_{jkm b}^{Ga}}(\mu_{ij}^s) \quad (4.26)$$

where

$$\mathcal{L}_{I_{jkm b}^{Ga}}(\mu_{ij}^s) = e^{-2\pi A_{km,b} \int_0^\infty \lambda_k p_G P_{\alpha k}^a(r_{jk,n}) \left(1 - \left(\int_0^\infty \frac{\hat{f}_{r_{km,b}}(t)}{1 + \mu_{ij}^s P_u(\kappa_b t^{\alpha_b})^\tau G \kappa_a^{-1} r_{jk,n}^{-\alpha_a}} dt \right) \right) r_{jk,n} dr_{jk,n}}, \quad (4.27)$$

where $\mu_{ij}^s = \frac{T_j(\kappa_s r_{ij,s}^{\alpha_s})^{1-\tau}}{P_u G_0}$, t is the distance from the interfering UE to its serving BS, and $r_{jk,n}$ is the distance from the interfering UE to the reference BS.

Proof: See Appendix 12.

4.5.3 Average Ergodic Spectral Efficiency

According to [61] [157], given the SINR coverage probability $P_C(T_j)$, the average ergodic spectral efficiency of the uplink of a mmWave cellular network can be expressed as

$$\begin{aligned} \mathcal{R} &= \frac{1}{\ln 2} \int_0^\infty \frac{P_C(T)}{1+T} dT = \frac{1}{\ln 2} \int_0^\infty \frac{\sum_{j=0}^K \sum_{s \in \{L, N\}} A_{ij,s} P_{C_{ij,s}}^c(T)}{1+T} dT \\ &= \sum_{j=0}^K \sum_{s \in \{L, N\}} \frac{A_{ij,s}}{\ln 2} \int_0^\infty \frac{P_{C_{ij,s}}^c(T)}{1+T} dT = \sum_{j=0}^K \sum_{s \in \{L, N\}} A_{ij,s} \mathcal{R}_{ij,s}^c. \end{aligned} \quad (4.28)$$

The average achievable rate can be computed as $W\mathcal{R}$, where W is the bandwidth assigned to a UE.

4.5.4 Special Cases

To simplify the general expressions provided in the previous sections, we now address several special cases.

Noise-Limited Scenario

When the mmWave network is not densely deployed and the impact of interference is negligible (due to blockages experienced in mmWave bands), the network can be assumed to be noise-limited. In this case, the coverage probability of each tier can be simplified to

$$P_{C_{ij,s}}^c = \mathbb{E}_{r_{ij,s}} \left[e^{-\mu_{ij}^s \sigma_n^2} \right]. \quad (4.29)$$

Next we consider a further simplified case, specifically a two-tier heterogeneous network, including one tier of small-cell BSs with UEs clustered around, and one tier of macrocell BSs; all links are LOS and the path loss exponent is $\alpha = 2$; and only noise is considered. Then, we can obtain the association probability and SNR coverage probability as in the following lemma.

Lemma 4.4. *In the above described simplified two-tier network model with LOS links, path loss exponent $\alpha = 2$, and no interference, we have the association and coverage probabilities given by the following:*

1) *Association probability:*

$$A_{10} = \frac{1}{2\sigma^2 C_0} = \frac{P_1 B_1}{P_1 + B_1 + 2\pi\sigma^2\lambda_1 P_1 B_1 + 2\pi\sigma^2\lambda_2 P_2 B_2} \quad (4.30)$$

$$A_{11} = \frac{\pi\lambda_1}{C_0} = \frac{2\pi\sigma^2\lambda_1 P_1 B_1}{P_1 B_1 + 2\pi\sigma^2\lambda_1 P_1 B_1 + 2\pi\sigma^2\lambda_2 P_2 B_2} \quad (4.31)$$

$$A_{12} = \frac{\pi\lambda_2}{C_2} = \frac{2\pi\sigma^2\lambda_2 P_2 B_2}{P_1 B_1 + 2\pi\sigma^2\lambda_1 P_1 B_1 + 2\pi\sigma^2\lambda_2 P_2 B_2} \quad (4.32)$$

2) SNR coverage probability:

$$P_{10} = \frac{1}{2\sigma^2(C_0 + \frac{T\sigma_n^2}{P_u G_0})A_{10}} \quad (4.33)$$

$$P_{11} = \frac{\pi\lambda_1}{\left(C_0 + \frac{T\sigma_n^2}{P_u G_0}\right)A_{11}} \quad (4.34)$$

$$P_{12} = \frac{\pi\lambda_2}{\left(C_2 + \frac{T\sigma_n^2}{P_u G_0}\right)A_{12}} \quad (4.35)$$

where λ_1 and λ_2 are the densities of small-cell BSs and macrocell BSs, respectively, σ^2 is the variance of the UE distribution, $C_0 = \frac{1}{2\sigma^2} + \pi\lambda_1 + \pi\lambda_2 \frac{P_2 B_2}{P_1 B_1}$, and $C_2 = \frac{P_1 B_1}{2\sigma^2 P_2 B_2} + \pi\lambda_1 \frac{P_1 B_1}{P_2 B_2} + \pi\lambda_2$.

Proof: See Appendix 13.

Results in (4.30) - (4.35) provide closed-form expressions for the association probabilities and SNR coverage probabilities as functions of the key system/network parameters, e.g., the standard deviation of the UE distribution σ , the transmit powers of the UEs and BSs, the densities of the BSs in each tier. From the expressions, we can directly identify the impact of these parameters on the network performance. For instance, we note that SNR coverage probability is a monotonically increasing function of P_u and G_0 , and a monotonically decreasing function of the SNR threshold T . Additionally, we see that when the UEs are more and more sparsely distributed (i.e., $\sigma \rightarrow \infty$), A_{10} and P_{10} approach 0.

Interference-Limited Scenario

In cases in which the interference power satisfies $I \gg \sigma_n^2$, the thermal noise can be ignored and the coverage probability of each tier can be expressed as

$$P_{C_{ij},s}^c = \mathbb{E}_{r_{ij},s} \left[\mathcal{L}_{I_{j0}}(\mu_{ij}^s) \prod_{k=1}^{K_u} \mathcal{L}_{I_{jk}}(\mu_{ij}^s) \right]. \quad (4.36)$$

In this interference-limited case, since the noise term $e^{-\mu_{ij}^s \sigma_n^2}$ is removed, expression (4.36) is relatively easier to compute than the general case given in (4.15).

Cluster Center Association Scenario

In the scenarios that the clusters are sparsely distributed, e.g. in rural areas, it is reasonable to require the UEs to be associated with their cluster center BSs. In such case, the coverage probability can be expressed as

$$P_{C_{i,s}} = \int_0^\infty e^{-\mu_i^s \sigma_n^2} \prod_{k=1}^{K_u} \mathcal{L}_{I_{ik}}(\mu_{i0}^s) f_{r_{i0}^s}(r_{i0}^s) dr_{i0}^s. \quad (4.37)$$

Additionally, in this case there is no need to find the association probabilities and the conditional PDFs of the distances from UEs to the associated BSs, since UEs are connected with their cluster centers BSs. The use of $f_{r_{i0}^s}(r_{i0}^s)$ makes (4.37) much easier to compute than (4.15).

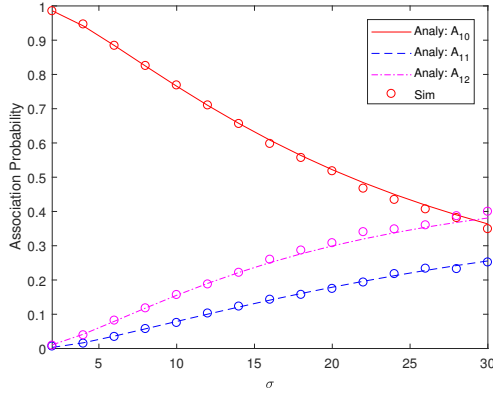
4.6 Numerical Results

In this section we present numerical and simulation results to confirm our analytical characterizations and further study the performance levels in the considered mmWave network model.

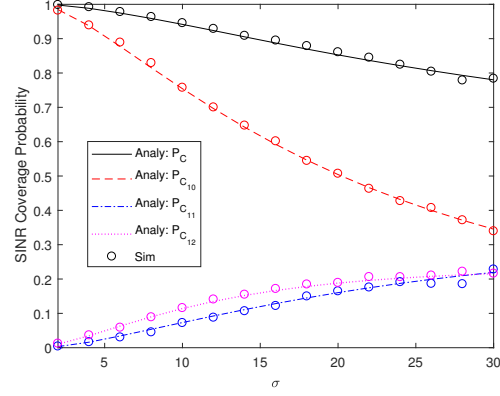
In the numerical evaluations and simulations, unless specified otherwise, we consider a two-tier heterogeneous network model in the uplink scenario. More specifically, BSs in the 1st tier are assumed to operate with relatively smaller transmit power but have larger density, and are regarded as small-cell BSs, while BSs in the 2nd tier are assumed to have larger transmit power but smaller density, and are regarded as macrocell BSs. Besides, UEs are considered to cluster around small-cell BSs. Some notations are defined as follows: A_{10} , $P_{C_{10}}$ are the association probability (AP) that a UE is served by its cluster center BS and the coverage probability (CP) of this link, respectively; A_{11} , $P_{C_{11}}$ are the AP that a UE is served by a small-cell BS from other clusters and the CP of this link, respectively; and A_{12} , $P_{C_{12}}$ are the AP that a UE is served by a macrocell BS the CP of this link, respectively. Parameter values are listed in Table 4.1 below.

Table 4.1: Parameters Table

Parameters	Values
P_0, P_1, P_2	30dBm, 30dBm, 46dBm [62]
P_u	23dBm [62]
B_0, B_1, B_2	1, 1, 1
ϵ	$\sqrt{2}/200$
$\alpha_d^{j,L}, \alpha_d^{j,N} \forall j, \forall d$	2, 4
$\lambda_1, \lambda_2, \lambda_u$	$10^{-4}, 10^{-5}, 5 \times 10^{-4} / \text{m}^2$
M, m, θ	10dB, -10dB, $\pi/6$
Career frequency F_c	28 GHz
$\kappa_L = \kappa_N$	$(F_c/4\pi)^2$
$\sigma_{n,j}^2 \forall j$	-174dBm/Hz + $10 \log_{10}(W) + 10\text{dB}$



(a) Association Probability.



(b) SINR coverage probability.

Fig. 4.3: APs and SINR CPs as a function of the standard deviation of UE distribution when $T = 10\text{dB}$.

4.6.1 Impact of the Cluster Size

In this section, we investigate the impact of the cluster size (i.e. the standard deviation σ of the UE distribution) on the system performance. In Fig. 4.3, we observe that the simulation results match with the analytical results when $\sigma \leq 30$, and hence we verify our analysis. Then we can say our analysis can be applied to practical PCP-based uplink mmWave networks, providing reliable and useful insights.

Association Probability (AP)

Fig. 4.3(a) shows the APs of each tier as a function of σ . When σ becomes larger, UEs are getting spread further away from their own cluster center and moving closer to other BSs, which can be either small-cell or macrocell BSs. As a result, small-cell BSs become less likely to serve their cluster members and more likely to serve UEs from other clusters. Macrocell BSs become more likely to serve a UE as well. Therefore, A_{10} is expected to decrease, and A_{11} and A_{12} to increase with the growing σ , and this is observed in Fig. 4.3(a).

On the other hand, initially when σ is small and therefore UEs are more tightly clustered around their cluster center, A_{10} is larger than both A_{11} and A_{12} . Also, since the macrocell BSs have much larger transmit power than small-cell BSs, A_{12} is larger than A_{11} .

Coverage Probability (CP)

Fig. 4.3(b) plots the SINR CP as a function of σ . Again, increasing σ implies that the UEs are more widely distributed. Thus, the path loss from a small-cell BS to its cluster member increases on average, while the path loss to other UEs as well as the path loss from a macrocell BS to a UE decrease. As a result, we observe in Fig. 4.3(b) decreasing $P_{C_{10}}$ and increasing $P_{C_{11}}$ and $P_{C_{12}}$. And since the decrease in $P_{C_{10}}$ is not compensated, the overall SINR CP diminishes as well.

A Three-Tier Heterogeneous Network

Fig. 4.4 plots the AP and SINR CP as a function of σ in a three-tier heterogeneous network. In this network, we add one more tier of small-cell BSs, referred to as the 2^{nd} tier with density $\lambda_2 = 10^{-5}$ /m² and UE transmission power $P_2 = 30$ dBm. The macrocell BSs are now referred to as the 3^{rd} tier. Again, increasing σ implies that the UEs are more widely distributed. In Fig. 4.4, we observe similar performances as in Fig. 4.3. Since the density and transmit power of the 2^{nd} tier small-cell BSs are not very large, the presence of this tier does not influence the performance significantly.

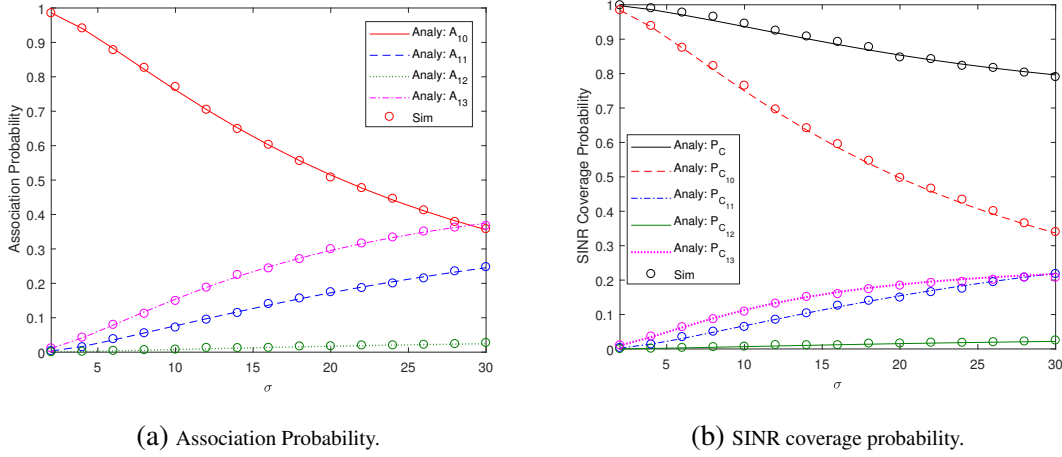


Fig. 4.4: APs and SINR CPs as a function of σ when $T = 10\text{dB}$ in a three-tier heterogeneous network.

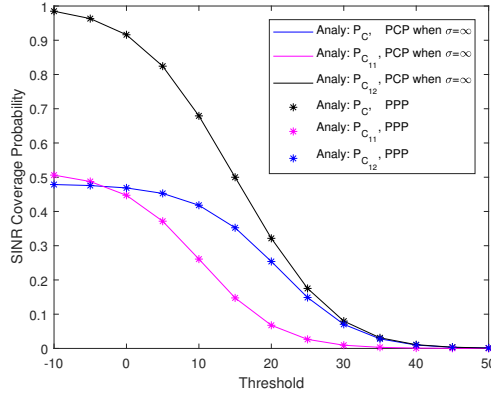


Fig. 4.5: SINR CPs as a function of threshold T .

Comparison with PPP

Fig. 4.5 shows the SINR CP of the considered network when $\sigma \rightarrow \infty$ ($P_{C_{10}} = 0$ is not shown in the figure) and SINR CP of the same network when the UEs are uniformly distributed according to a PPP. This figure demonstrates that as $\sigma \rightarrow \infty$ the performance of the considered network converges to the performance in the PPP-based model, indicating that our analysis can be specialized to determine the performance of the PPP-based model (where the density of UEs is $\phi_u^{i'} = \phi_i$) by setting $\sigma = \infty$.

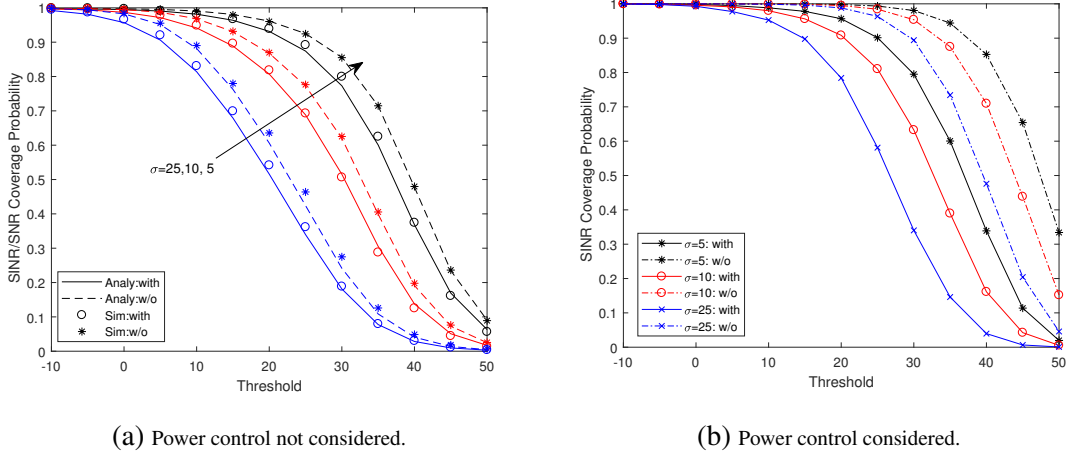


Fig. 4.6: SNR and SINR CPs as a function of threshold for different cluster size σ .

4.6.2 Impact of Interference and the Small-Scale Fading

Impact of Interference

We next investigate the influence of interference in the considered heterogeneous mmWave network. Fig. 4.6 exhibits the total SNR and SINR coverage probabilities of the entire network as a function of the threshold for different values of σ . While Fig. 4.6(a) is obtained without any power control (i.e., transmission power is fixed), fractional power control is employed in the performance results in Fig. 4.6(b). It is obvious that the interference has a significant impact on the coverage performance as shown in this figure. From Fig. 4.6(b) we observe that if path loss based fractional power control is used by the UEs, the impact of interference becomes more pronounced. Note that SINR CPs (described in the legend as “with” as in “with interference”) are lower than SNR CPs (denoted with “w/o”).

Impact of Small-Scale Fading

In Fig. 4.7, we compare the performances with different types of small-scale fading. In particular, we consider Rayleigh fading and Nakagami fading with parameters $N_L = 3$ for LOS and $N_N = 2$ for NLOS links. We observe from the figure that two types of small-scale fading lead to similar performance trends. However, since Nakagami fading implies more favorable channel conditions,

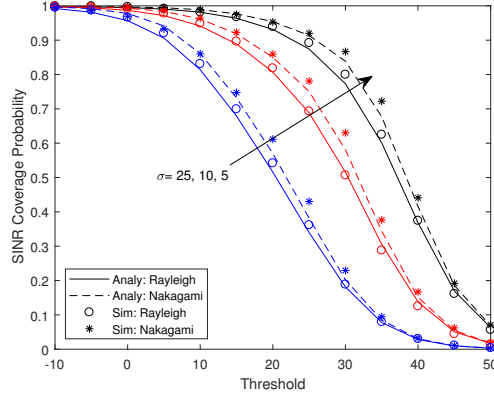


Fig. 4.7: SINR and SINR CPs as a function of threshold for different cluster size σ .

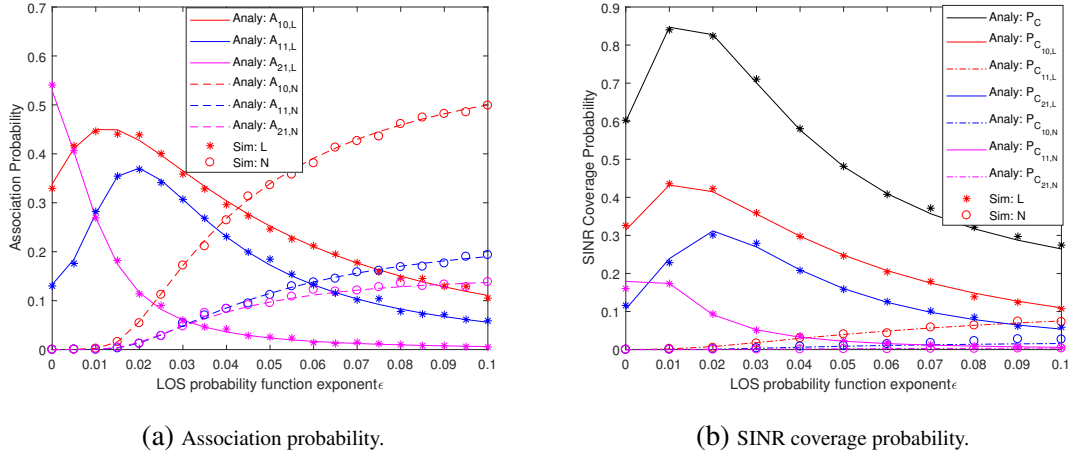


Fig. 4.8: APs and SINR CPs for different tier as a function of the LOS probability function exponent ϵ when $\sigma = 25$ and $T = 10\text{dB}$.

higher CP is achieved with Nakagami fading.

4.6.3 Impact of the LOS Probability Exponent ϵ

In this subsection, we investigate the impact of the LOS probability exponent ϵ . Note that the smaller ϵ is, the sparser the environment will be, leading to higher LOS probabilities. And we aim to obtain insights on how the building deployments influence the system performance.

Association Probability

Fig. 4.8(a) shows the AP as a function of ϵ . When $\epsilon = 0$, all links are LOS and the signals are not attenuated significantly during transmission. Since macrocell BSs provide larger transmit power, we can observe from the figure that $A_{12,L} > A_{10,L} > A_{11,L}$. When ϵ is increased, more links become NLOS. Thus $A_{12,L}$ decreases dramatically. In the meantime, small-cell BSs have more chance to serve the UEs, and we notice increasing $A_{10,L}$ and $A_{11,L}$ initially. When we increase ϵ further, more and more links become NLOS. Consequently, we have increasing $A_{10,N}$, $A_{11,N}$ and $A_{12,N}$, as well as decreasing $A_{10,L}$, $A_{11,L}$ and $A_{12,L}$. Additionally, when more links are NLOS, signals are attenuated considerably during transmission. And since the distance between UEs and their cluster center BSs are relatively smaller, $A_{10,N}$ increases more than $A_{11,N}$ and $A_{12,N}$.

Coverage Probability

Fig. 4.8 (b) plots the SINR CP as a function of ϵ . The first observation shown in the figure is that similar to the performance trends with respect to AP, with increasing ϵ , we have increasing $P_{C_{10,N}}$, $P_{C_{11,N}}$ and $P_{C_{12,N}}$. In addition, $P_{C_{10,L}}$ and $P_{C_{11,L}}$ increase initially and then start diminishing, while $P_{C_{12,L}}$ decreases continuously. The second observation is that $P_{C_{10,s}} > P_{C_{11,s}} > P_{C_{12,s}}$ is always satisfied. This is due to the following reasons: 1) no matter which BS the UE is associated with depending on the averaged received power of the UE, in the uplink phase, UE is transmitting information to BSs with the same transmit power; 2) the distance between the UEs and their cluster center BS is generally smaller than to other small-cell BSs and macrocell BSs, leading to the conditional CP of the cluster center being much larger than those of other BSs. The third observation is that the total CP increases at the beginning and then decreases. This is because that $P_{C_{10,L}}$ and $P_{C_{11,L}}$ increase initially, and then the increase in the coverage with NLOS Links cannot compensate the decrease in the coverage with LOS links.

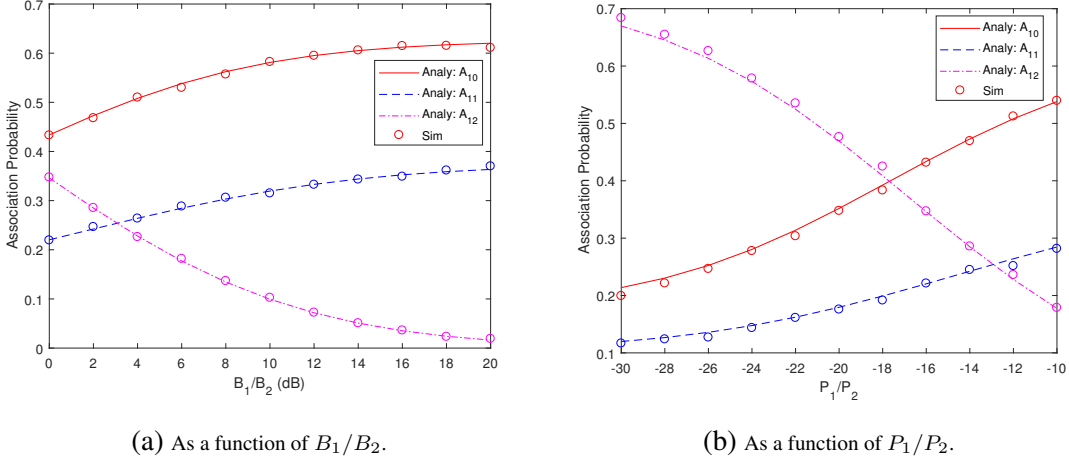


Fig. 4.9: APs as a function of the biasing factor ratio B_1/B_2 and the BS transmit power ratio P_1/P_2 when $\sigma = 25$ and $T = 10$ dB.

4.6.4 Impact of the Biasing Factor and Transmit Power

Association Probability

Fig. 4.9(a) displays the AP as a function of the biasing factor ratio B_1/B_2 in dB, where B_1 and B_2 are the biasing factors of the small-cell BSs and the macrocell BSs, respectively. When $B_1 = B_2$, we have $A_{10} > A_{11} > A_{12}$ since UEs are relatively closer to the cluster centers. On the other hand, when we fix $B_2 = 1$ and increase B_1 , we observe, as expected, that A_{10} and A_{11} grow, while A_{12} diminishes.

Fig. 4.9(b) shows the AP as a function of the transmit power ratio P_1/P_2 in dB. At the beginning, since P_2 is much larger than P_1 , even though the distance between the macrocell BSs and UEs are large, the macrocell BSs still have a high probability to connect with the UEs. When we fix P_2 and increase P_1 , the small-cell BSs start having larger transmit power, and as a result A_{10} and A_{11} increase.

Coverage Probability

Due to their impact on the association probabilities, biasing factor ratio and the BS transmit power ratio influence the choice of the associated reference BS, and consequently affect the SINR coverage probability of each reference BS. Fig. 4.10 plots the conditional SINR coverage probabil-

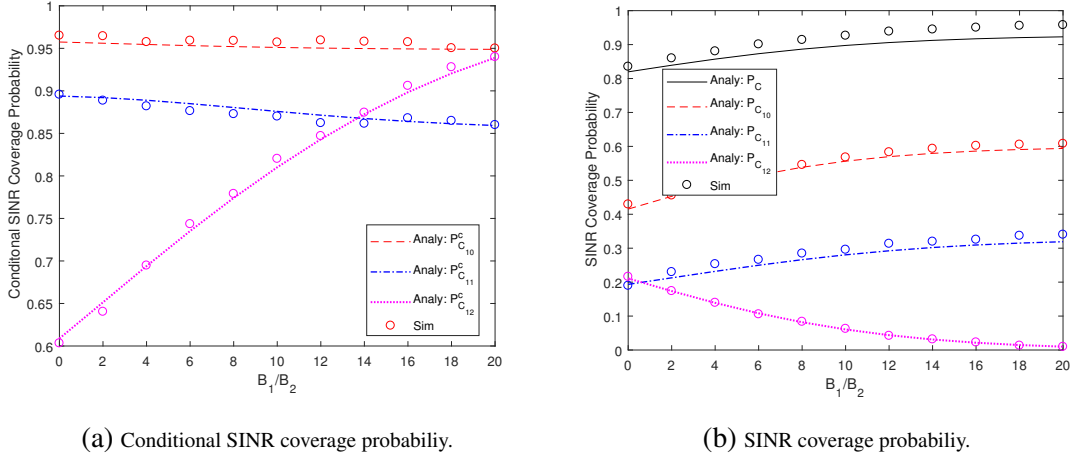


Fig. 4.10: SINR CP as a function of B_1/B_2 when $\sigma = 25$ and $T = 10\text{dB}$.

ity ($P_{C_{ij}}^c$) of each tier of reference BSs, and the SINR coverage probability of each tier ($P_{C_{ij}} = P_{C_{ij}}^c A_{ij}$). From Fig. ??(a), we can observe that the conditional SINR coverage probability of the cluster center BSs $P_{C_{10},s}^c$ and other small-cell BSs $P_{C_{11},s}^c$ decrease, while that of the macrocell BSs $P_{C_{12},s}^c$ increases with increasing B_1/B_2 . The reason is that, as B_1/B_2 gets large, UEs increasingly prefer to associate with small cell BSs, and consequently the small-cell BSs start having larger association priority, while the macrocell BSs have small association priority. In this case, if the typical UE is still associated with a macrocell BS, then that link should be in really good condition, and hence has large coverage probability. Therefore, with increasing B_1/B_2 , given that the typical UE is associated to the macrocell BS, the macrocell BS should provide strong power and have larger coverage probability, leading to increasing $P_{C_{12},s}^c$. Conversely, for large B_1/B_2 , small-cell BSs, which do not need large power to get associated to UEs, have smaller coverage.

On the other hand, due to the variations in the association probability of each tier shown in Fig. 4.9(a), we have the performance in Fig. 4.10(b). In particular, we note that $P_{C_{10}}$ and $P_{C_{11}}$ both increase, because A_{10} and A_{11} grow significantly with increasing B_1/B_2 . Since the increment in $P_{C_{10}}$ and $P_{C_{11}}$ is larger than the decrease in $P_{C_{12}}$, we have a growing total network CP. Therefore, total SINR CP of the network is an increasing function of B_1/B_2 . Regarding the transmit power, if we increase the transmit power of small-cell BSs, the total CP of the network will also increase.

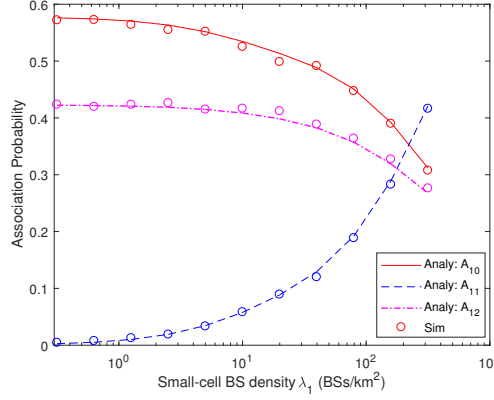


Fig. 4.11: APs as a function of the density of small-cell BSs λ_1 , when $\sigma = 25$ and $T = 10\text{dB}$.

4.6.5 Impact of the Density of BSs

Association Probability

Fig. 4.11 shows the AP as a function of λ_1 when $\lambda_2 = 10 / \text{km}^2$ and $\sigma_u = 25$. Initially, the density of small-cell BSs is small, UEs are still clustered around them, and the macrocell BSs are not densely distributed. Hence, the UEs are likely to be served by their cluster center BSs, i.e. $A_{10} > A_{12} > A_{11}$. When we increase λ_1 , more and more small-cell BSs are deployed. The distance between the UEs and their cluster center BS does not change, while the distance from the UEs to other small-cell BSs becomes smaller. Hence, the USs become more and more likely to be served by other small-cell BSs. In other word, A_{11} increases, while A_{10} and A_{12} both decrease.

Coverage Probability

Fig. 4.12(a) shows the SINR CP as a function of λ_1 . Via the CP of each tier, we can observe that with an increasing λ_1 , P_{C10} and P_{C12} diminish, while P_{C11} grows. Initially, the increase in P_{C11} is larger than the decrease in P_{C10} and P_{C12} , leading to the result that total CP increases. As we increase λ_1 further since the interference grows, the increase in P_{C11} cannot compensate the decrease in P_{C10} and P_{C12} , and consequently the total CP decreases.

Fig. 4.12(b) plots the SINR CP vs. small-cell BS density λ_1 for different densities λ_2 of the macrocell BSs. From the figure, we observe that when $\lambda_1 = 1 \text{ BS/km}^2$ which is small, increas-

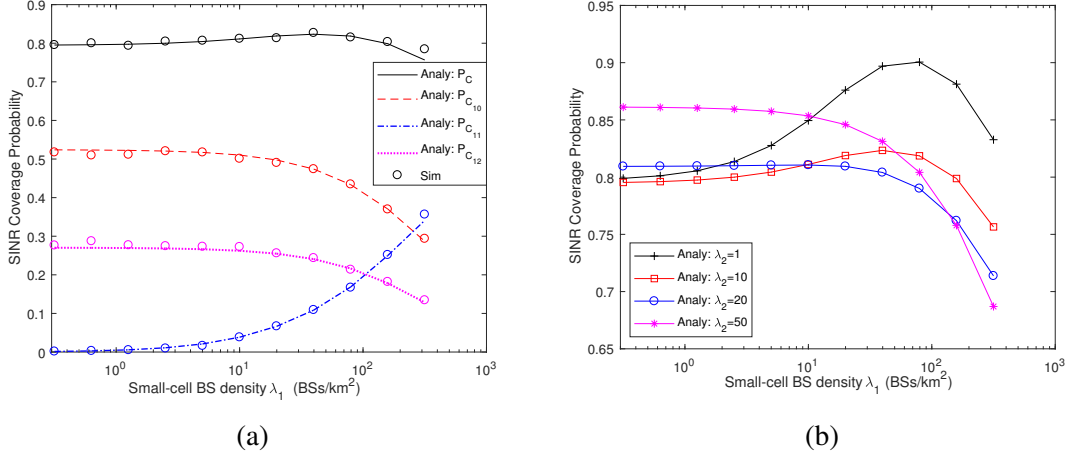


Fig. 4.12: SINR CPs of each tier and the entire network as a function of the density of small-cell BSs λ_1 , when $\sigma = 25$ and $T = 10$ dB.

ing λ_2 improves the total network coverage. This is expected since we have a sparse network and interference can be ignored, and increasing the number BSs results in network performance improvement. On the other hand, when $\lambda_1 = 100$ BSs/km², increasing λ_2 lowers the SINR CP performance. In this case, the network have more small-cell BSs, including the cluster center BSs and other small-cell BSs, which together can provide good coverage. Increasing the macrocell BS density will lead to more interference, and also will result in UEs getting connected to macrocell BSs with potentially larger link distances. Thus, in this case, the total SINR coverage generally diminishes when λ_2 is increased.

These two figures give us the following useful insights: 1) when the macrocell BSs are sparsely deployed (e.g., $\lambda_2 \leq 10$ BSs/km²), there is an optimal density of small-cell BSs to maximize the uplink SINR CP of the entire network; while when the macrocell BSs are densely deployed, increasing the small-cell BS density will lead to smaller uplink SINR CP; 2) when the small-cell BSs are sparsely deployed, increasing the density of macro BS will improve the uplink CP; while the opposite will happen for densely deployed small-cell BS networks.

CHAPTER 5

MULTI-AGENT DOUBLE DEEP

Q-LEARNING FOR BEAMFORMING IN

MMWAVE MIMO NETWORKS

5.1 System Model

In this section, we describe the considered mmWave MIMO network.

5.1.1 System Model

We consider multi-BS multi-UE MIMO networks, where J BSs are simultaneously serving K mobile UEs. Each BS is equipped with N_t antennas and N_{RF} RF chains. We assume that the BSs apply analog-only beamforming using networks of phase shifters, and each RF chain is fully-connected with each antenna.

In this analog-only beamforming network, the BS up-converts the data stream to the carrier frequency by passing it through N_{RF} RF chains. Following this, the BS uses an $N_t \times N_{\text{RF}}$ RF precoder \mathbf{V}_{RF} , which is implemented using analog phase shifters, i.e., with $|\mathbf{V}_{\text{RF}}(a, b)|^2 = \frac{1}{N_t}$, to construct the final transmitted signal. Note that $\mathbf{V}_{\text{RF}}(a, b) = \frac{1}{\sqrt{N_t}} e^{j\phi_{ph}}$ where ϕ_{ph} is the phase shift

angle. For the k -th user, the received signal can be modeled as

$$\mathbf{y}_k = \sum_{j=1}^J \mathbf{H}_{kj} \mathbf{V}_{\text{RF}j} \mathbf{s}_{kj} + \mathbf{n}_{kj} \quad (5.1)$$

where \mathbf{s}_{kj} is the data stream vector for the k -th UE from the j -th BS. We assume that $\mathbb{E}[\mathbf{s}_{kj} \mathbf{s}_{kj}^H] = P_j \mathbf{I}_{N_s}$, and the noise factor $\mathbf{n}_{kj} \sim \mathcal{CN}(0, \sigma^2 \mathbf{I}_{N_t})$. \mathbf{H}_{kj} is the channel response from the j^{th} BS to the k^{th} UE. $\mathbf{V}_{\text{RF}j}$ is the RF precoder of the j^{th} BS.

5.1.2 Channel Model

We adopt a channel model with L paths. L is a small number for mmWave communications, and we assume $L = 1$ for LOS links. Now, the mmWave MIMO channel \mathbf{H} can be expressed as

$$\mathbf{H} = \sqrt{\frac{N_t N_r}{L}} \sum_{l=1}^L \frac{\alpha_l}{p_l} \mathbf{a}_r(\phi_r^l) \mathbf{a}_t^H(\phi_t^l) \quad (5.2)$$

where α_l and p_l are the complex gain and the path loss of path l , respectively. \mathbf{a}_t and \mathbf{a}_r are the array response vectors at the BS and the UE sides, respectively. ϕ_t^l and ϕ_r^l are the angles of departure and arrival of the l^{th} path, respectively.

Array response

While the algorithms introduced in this paper can be applied to arbitrary antenna arrays, we provide the following two illustrative examples of commonly-used antenna arrays. For an N element uniform linear array (ULA) on the y -axis, the array response vector can be written as [189]

$$\mathbf{a}_{\text{ULA}_y}(\phi) = \frac{1}{\sqrt{N}} [1, e^{jkd \sin(\phi)}, \dots, e^{j(N-1)kd \sin(\phi)}] \quad (5.3)$$

where $k = \frac{2\pi}{\lambda}$, λ is the wavelength, and d is the inter-element spacing. In the case of a uniform planar array (UPA) in the yz -plane with W and H elements on the y and z axes respectively, the

array response vector is given by

$$\mathbf{a}_{UPA}(\phi, \theta) = \frac{1}{\sqrt{N}} \left[1, \dots, e^{jkd(m \sin(\phi) \cos(\theta) + n \sin(\phi) \sin(\theta))}, \dots, e^{jkd((W-1) \sin(\phi) \cos(\theta) + (H-1) \sin(\phi) \sin(\theta))} \right] \quad (5.4)$$

where $0 < m < W$ and $0 < n < H$ are the y and z indices of an antenna element respectively and the antenna array size is $N = WH$. In this paper, we primarily concentrate on ULA.

Path Loss

Link between a UE and a BS can be either LOS or NLOS. The path loss model is formulated as

$$p_l(r) = \begin{cases} \kappa^{los} r^{\alpha^{los}}(r) & \text{with prob. } p^{los}(r) \\ \kappa^{nlos} r^{\alpha^{nlos}}(r) & \text{with prob. } p^{nlos}(r) = (1 - p^{los}(r)) \end{cases} \quad (5.5)$$

where r is the two-dimensional distance between the UE and BS. $\alpha^{los}, \alpha^{nlos}$ are the path loss exponents for LOS and NLOS links, respectively, $\kappa^{los}, \kappa^{nlos}$ are the intercepts of the LOS and NLOS path loss formulas, respectively, and $p^{los}(r)$ is the probability that the link has a LOS transmission at distance r .

Following the 3GPP standards described in [190], we express the probability of LOS link between the BSs and the UEs as

$$p^{los}(r) = \min(18/r, 1) \times (1 - \exp(-r/63)) + \exp(-r/63). \quad (5.6)$$

Shadowing is also taken into account in the channel model, and is modeled as a log-normal random variable, i.e., $10 \log v \sim \mathcal{N}(\mu_v, \sigma_v^2)$ with μ_v and σ_v^2 being the mean and variance of the channel power under shadowing, respectively.

5.1.3 Achievable Rate

In the multi-BS multi-UE mmWave MIMO network, beside the serving BS, other BSs inflict interference to the UEs. We can express the rate of the k -th UE when associated with the j -th BS as [85] [191] [192]

$$R_k = \log_2 \left(1 + \frac{P_j |\mathbf{H}_{kj} \mathbf{V}_{\text{RF}_j} \mathbf{V}_{\text{RF}_j}^H \mathbf{H}_{kj}^H|}{\sigma^2 + \sum_{i=1, i \neq j}^J P_i |\mathbf{H}_{ki} \mathbf{V}_{\text{RF}_i} \mathbf{V}_{\text{RF}_i}^H \mathbf{H}_{ki}^H|} \right) \quad (5.7)$$

where superscript H and $|\cdot|$ denote the conjugate transpose and the determinant of a matrix, respectively. Then, the sum-rate of all UEs is $R_{\text{sum}} = \sum_{k=1}^K R_k$.

Our goal is to maximize the sum-rate of all UEs, and therefore we consider the following optimization problem:

$$\max_{\mathbf{V}_{\text{RF}_j}, j \in J} \sum_{k=1}^K R_k \quad (5.8)$$

$$\text{subject to} \quad |\mathbf{V}_{\text{RF}_j}(a, b)|^2 = \frac{1}{N_t} \forall j, \quad (8a)$$

where \mathbf{V}_{RF_j} is the analog beamforming vector of the j -th BS.

5.2 Distributed multi-agent DDQN for mmWave MIMO networks

The algorithm of the distributed multi-agent DDQN for mobile UEs is provided in Algorithm 1. Before providing the definitions of states, actions, and rewards, the environment should be introduced first. In the environment \mathcal{E} , BSs are located with a certain distance in between. UEs move from different initial locations in different directions with different speeds. In each episode, UEs do not change their speed and direction until they move out of the coverage region of all

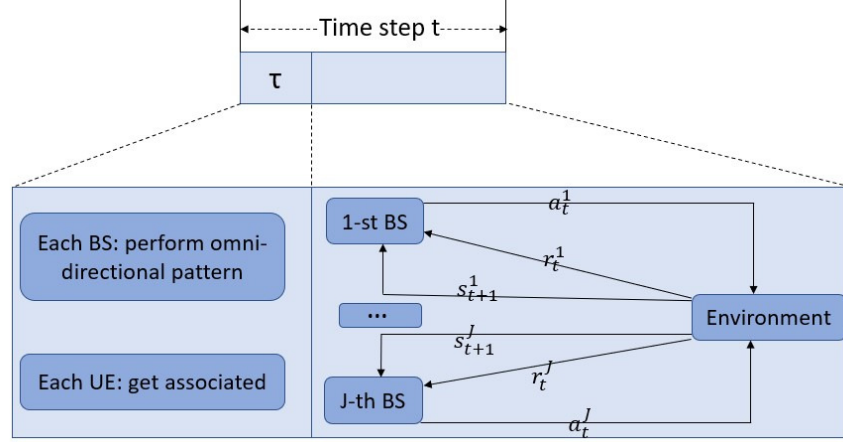


Fig. 5.1: An illustration of the procedure in one time step.

BSs, and the episode ends. In each episode, at each time step, UEs move to new locations. We assume that at the beginning of each time step, in a very short time slot τ , each BS uses an omni-directional antenna pattern, and transmits pilot signals to all UEs. Therefore, each UE receives pilot signals from all BSs, and chooses to associate with the BS providing the strongest pilot signal, and computes the immediate rate under the omni-directional pattern, and sends it to the serving BS, indicating the association condition with itself. It is assumed that each UE is equipped with a memory containing prior information (e.g., the location history, the omni-directional rate in the last T_m time steps), and each UE can send this information to the associated BS as well. Subsequently, the BS performs beamforming according to our algorithm, and serves the associated UEs. Then the UEs learn the immediate rate achieved with beamforming, and feed this information back to the serving BS. The procedure in one time step is illustrated in Fig. 5.1.

In the multi-agent DDQN model, each BS is an agent and the state, action, and reward tuple of the j -th BS is denoted by (s_t^j, a_t^j, r_t^j) . These states, actions and rewards are described in detail below:

5.2.1 State

At each time step, each BS serves multiple UEs, and is able to obtain the information in the memory of each UE. This information of all associated UEs constitute as state at time t , noted as s_t^j for the

Algorithm 1: Distributed multi-agent DDQN

Require:

- 1: Initialize replay memory D^j of DDQN, $j \in J$, to capacity N for every BS.
- 2: Initialize online network with random parameter ξ^j , $j \in J$.
- 3: Initialize target network with parameter $\xi^{j-} = \xi^j$, $j \in J$.

Ensure:

- 4: **for** episode = 0: total episode **do**
 - 5: Reset environment \mathcal{E} .
 - 6: Initialize s_1^j for $j \in J$.
 - 7: **for** $t = 1 : T$ **do**
 - 8: **for** $j = 1 : J$ **do**
 - 9: Obtain association condition and the sum-rate of all associated UEs R_t^{oj} by association procedure.
 - 10: Sample c from Uniform (0,1)
 - 11: **if** $c \leq \epsilon$ **then**
 - 12: Select an action (beamforming vector index) randomly from the codebook \mathcal{F} .
 - 13: **else**
 - 14: Select the action $a_t^j = \operatorname{argmax}_a Q_j^*(s_t^j, a; \xi_t^j)$.
 - 15: **end if**
 - 16: Execute action a_t^j , i.e. apply the selected beamforming vector on the antenna arrays of j -th BS.
 - 17: Observing the resulting state s_{t+1}^j and the immediate sum-rate of all associated UEs R_t^j .
 - 18: Compute the immediate reward r_t^j , i.e. $\frac{R_t^{oj}}{R_t^j} \times 100\%$.
 - 19: Store the experience tuple $(s_t^j, a_t^j, r_t^j, s_{t+1}^j)$ in D^j .
 - 20: Sample random minibatch of experience $(s_\tau^j, a_\tau^j, r_\tau^j, s_{\tau+1}^j)$ from D^j .
 - 21: Update

$$y_\tau^j = \begin{cases} r_\tau^j & \text{if episode terminates at step } \tau + 1 \\ r_\tau^j + \gamma Q(s_{\tau+1}^j, \operatorname{argmax}_{a'} Q(s_{\tau+1}^j, a'; \xi_\tau^j); \xi_\tau^{j-}) & \text{otherwise} \end{cases}$$
 - 22: Perform a gradient descent step on $(y_\tau^j - Q(s_\tau^j, a; \xi_\tau^j))^2$ with respect to the network parameters ξ_τ^j
 - 23: For every N_n steps reset target network parameter $\xi^{j-} = \xi^j$
 - 24: **end for**
 - 25: **end for**
 - 26: **end for**
-

j -th BS. Assume that the length of history in each memory is T_m , and there are K UEs in this network, then the state $s_t^j = [m_{t-T_m}^0, m_{t-T_m+1}^0, \dots, m_{t-1}^0, \dots, m_{t-1}^K]$. It is worth noting that for UEs not associated with the j -th BS, m_{t-*}^* is set to be 0. In other words, the BSs only need information from the associated UEs. In this paper, we denote the rate achieved with the omni-directional antenna pattern as m_{t-*}^* . If the location information of each UE is also available, we denote the omni-directional pattern rate and the location information together as state s_t^j . In Section IV, we provide performance results with and without location information.

5.2.2 Action

At each time step, each BS chooses an analog beamforming vector \mathbf{V}_{RF} . Due to the constraints on the RF hardware, such as the availability of only certain quantized angles for the RF phase shifters, the analog beamforming vectors can take only certain values. Hence, finite-size codebooks for the candidate beamforming vectors are needed. In practice, the beamforming vectors are spatial matched filters for the single-path channels [192]. Thus, they have the same form of the array response vector and can be parameterized by a simple angle. While the algorithm in this paper can be applied to arbitrary finite-size codebooks, we adopt the codebook, denoted by \mathcal{F} , consisting of the steering vectors $\mathbf{a}_t(\phi_Q)$ where ϕ_Q is the quantized angle. The beamforming vector index in the codebook is defined as the action a_t^j .

5.2.3 Reward

As noted before, at the beginning of each time step, each BS learns the immediate rate, R_t^{oj} , provided to all associated UEs with the omni-directional antenna radiation pattern. After performing beamforming, each BS also learns the immediate rate R_t^j achieved with beamforming. We regard the ratio of two rates, $\frac{R_t^j}{R_t^{oj}}$ as the immediate reward r_t^j of the j -th BS when this BS takes action a_t^j in state s_t^j .

Setting the analog beamforming vector codebook \mathcal{F} , the optimization problem can be refor-

mulated as

$$\max_{\mathbf{V}_{\text{RF}_j}[t], j \in J} \sum_{k=1}^K R_k[t] \quad (5.9)$$

$$\text{subject to} \quad \mathbf{V}_{\text{RF}_j}[t] \in \mathcal{F}, \forall j, \quad (12a)$$

where $\mathbf{V}_{\text{RF}_j}[t]$ is the analog beamforming vector of the j^{th} BS at time t .

5.3 Performance Evaluation

In this section, we provide simulation results and evaluate the performance of the proposed multi-agent DDQN for mmWave MIMO beamforming.

5.3.1 Environment Setting

The considered environment is illustrated in Fig. 5.2. As shown in the figure, we have two intersecting streets. The BSs are located along the streets, while the UEs are moving from the beginning of either street in either direction. UEs move at random speeds. The length of each street is set as 100m, starting from -50m to 50m on each axis. The width of the road is set as 8m, i.e., (-4m, 4m). The speed of the UEs can be between 2 to 5 m/s. The locations of BSs are set at the coordinates of [(5,-5),(-25,-5)]. In addition, the number of antennas at the base stations and the UEs are set, respectively, as $N_t = 16$, $N_r = 1$. Finally, the number of RF chains is $N_{\text{RF}} = 2$.

5.3.2 Hyperparameters

In our experiment, we construct the DDQN via three-layered neural networks using Adam optimizer to evaluate the gradient descent of the evaluated and target networks. Our input size depends on the number of UEs in the environment, i.e., the input size is KT_m when K is the number of UEs and T_m is the length of historic/prior information at of each UE, and is set to be 8 in the simulation. The output size should be the size of the action notebook \mathcal{F} . The number of neurons

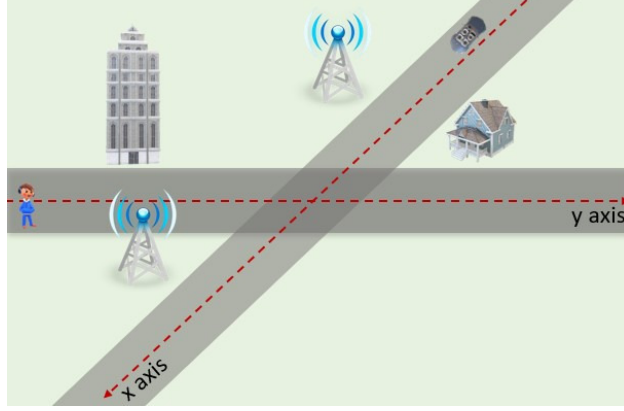
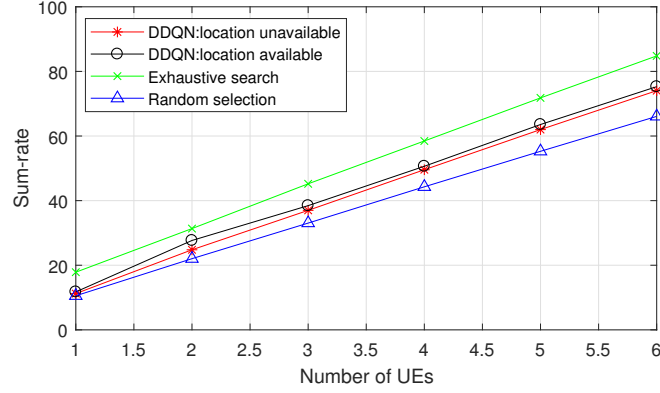


Fig. 5.2: An illustration of the simulation environment.

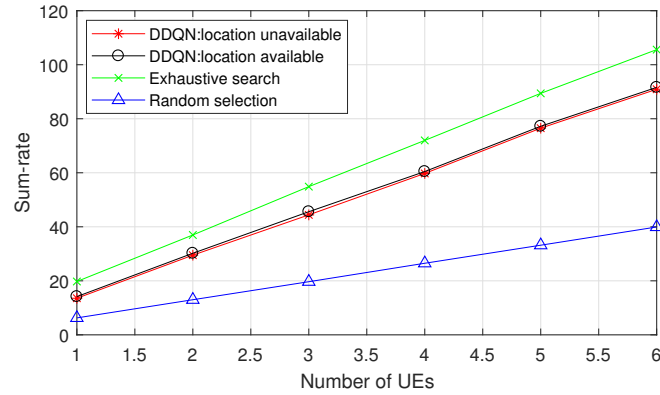
of the three layers are $12K$, $8K$ and 8 , respectively. The discount factor is 0.95 , batch size is 32 , and the learning rate for two BSs are 0.0001 and 0.005 , respectively. We also use ϵ -greedy policy and the maximum value of ϵ is 0.9 and the minimum is 0.1 .

5.3.3 Experiment results

Fig. 5.3 plots the sum-rate as a function of the number of UEs for different number of BSs. Results from exhaustive search among all possible beamforming directions and also random selection are provided as two benchmark results. Note that the exhaustive search requires perfect channel state information (CSI), and in random selection the BSs randomly choose actions from the codebook. Figs. 5.3(a) and 5.3(b) (in which we consider the cases of a single BS and two BSs, respectively) show that DDQN can achieve better performance than random selection, and comparable results with exhaustive search which has high computational complexity and incurs potentially large delays especially in mobile scenarios. In addition, in both figures, we provide the performance curves when the location information is available and unavailable. The performance with location information given is only slightly better, indicating that such information is not critical for our algorithm. Furthermore, when the number of UEs increases, the sum-rate grows almost linearly, demonstrating that the proposed algorithm can handle multiple UEs without much decrease in the data rate experienced at each UE. On the other hand, when we compare Figs. 5.3(a) and 5.3(b), we notice that for the same number of UEs, two BSs can provide higher sum-rate than



(a) Single Base Station.



(b) Two Base Stations.

Fig. 5.3: Sum-rate as a function of number of UEs for different number of BSs.

in the case of a single BS. Even though there is interference when there are multiple BSs, two BSs can provide larger coverage, leading to higher SINR levels and rates with effective beamforming. We also notice that random selection performs rather poorly especially in the presence of two BSs.

Fig. 5.4 displays the sum-rate performances during testing, when the DDQN is trained for the exact number of UEs used in the tests and also when DDQN is trained considering 6 UEs regardless of how many UEs we have in the test period. When the DDQN is trained for 6 UEs, if the real number of UEs is less than 6 in the testing, we need to do zero padding in the input of the DDQN; if the actual number of UEs is more than 6, we just randomly choose 6 UEs and make a decision. From Fig. 5.4, we observe that when the DDQN is trained for the actual number of UEs, the testing performance is slightly better than that of the other case, indicating that the pre-trained model does not need to be restricted to a certain number of UEs and can be applied to scenarios in

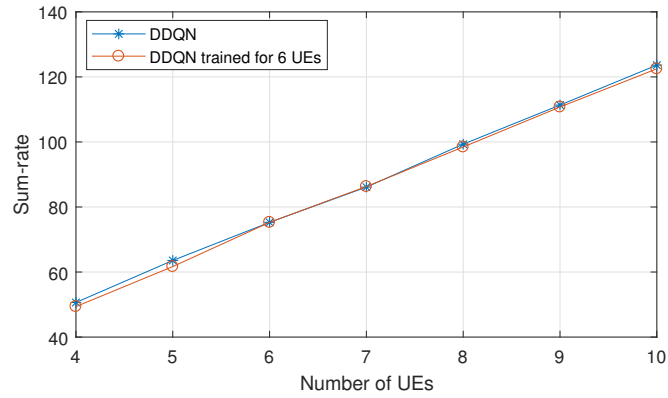


Fig. 5.4: A performance comparison of testing results, when the DDQN is trained for the exact number of UEs and the DDQN is trained for 6 UEs. The number of BS is one.

which the number of UEs in the test is different from that in the training period.

CHAPTER 6

COVERAGE IN NETWORKS WITH HYBRID TERAHERTZ, MILLIMETER WAVE, AND MICROWAVE TRANSMISSIONS

6.1 System Model

In this section, distributions of BSs and UEs, and the key features of transmission in different frequency bands are introduced.

6.1.1 Deployment Model

We assume that there are three tiers of BSs, including a tier of access points (APs), denoted as the 1st tier, a tier of small-cell BSs (SBSs), denoted as the 2nd tier, and a tier of macrocell BSs (MBSs), denoted as the 3rd tier. The APs are assumed to be transmitting in the THz frequency bands, SBSs transmit in the mmWave frequency bands, while the MBSs transmit in conventional microwave frequency bands. BSs in the j^{th} ($j \in \{1, 2, 3\}$) tier are assumed to be distributed according to the Poisson point processes Φ_j with density λ_j . The APs, SBSs and MBSs are assumed to have heights H_1 , H_2 and H_3 , respectively. Since THz APs are expected to be placed at much lower heights (due

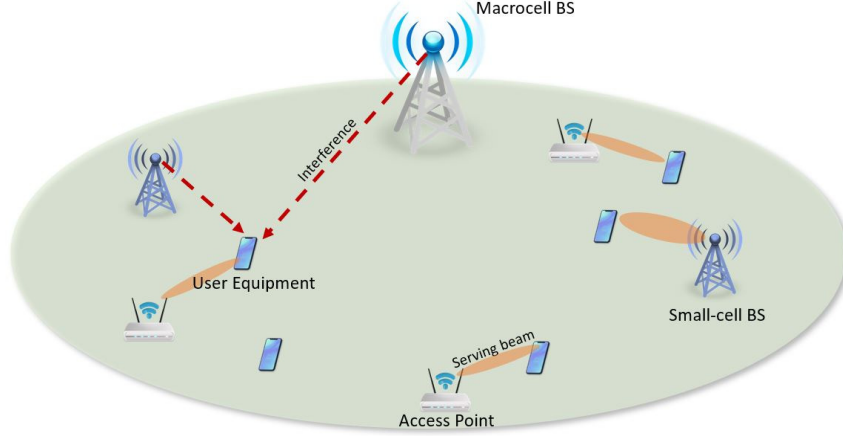


Fig. 6.1: An illustration of a three-tier HetNet.

to the limited range of THz transmissions), we approximate $H_1 = 0$. BSs in the j^{th} tier are also distinguished by their transmit power P_j .

The UEs are assumed to be distributed according to a stationary Poisson point process Φ_U with density λ_U , which is independent of the distributions of the BSs in the network. In this chapter, we focus on the analysis of the outdoor networks. The UEs are assumed to be located outdoors, and the indoor-to-outdoor penetration loss is assumed to be strong enough so that the UEs cannot receive signal or interference from the indoor BSs.

An illustration of the considered three-tier heterogeneous network (HetNet) is provided in Fig. 6.1.

6.1.2 Channel Modeling

Different path loss laws are applied to LOS and NLOS links from BSs in each tier to the UEs. The blockage model and path gain are provided in 2.2.1. Nakagami- m fading is adopted in this chapter. It is assumed that the UEs used omni-directional antenna pattern with gain 0dB.

THz APs

Antenna arrays are deployed at the APs to perform directional beamforming. For tractability of the analysis, the actual antenna array pattern is approximated by a cone-shaped model, which has

been widely used in THz communication networks [4] [8] [6] [7]. In this cone-shaped model, the array gains are assumed to be a constant G_1^{max} for all angles in the main lobe, and to be a smaller constant G_1^{min} for all angles in the side lobe. The antenna gain can be mathematically expressed as in (2.22), and denoted by G_1 with θ_1 being the half power beamwidth of the APs' antennas.

SBSs

According to [168], the 3D antenna pattern from the SBSs to the UE can be divided into horizontal and vertical components. The vertical antenna gain can be written as (2.24), and denoted by $G_2^v(x) = 10^{-1.2 \left(\frac{\arctan(\frac{H_2}{x}) - \phi_2^{etilt}}{\phi_2^{3dB}} \right)^2}$. The horizontal antenna pattern is assumed to be cone-shaped, and denoted by G_2^h with θ_2 being the horizontal half power beamwidth of the SBSs' antennas. Therefore, the antenna gain can be expressed as

$$G_2(x) = \begin{cases} G_2^{max} 10^{-1.2 \left(\frac{\arctan(\frac{H_2}{x}) - \phi_2^{etilt}}{\phi_2^{3dB}} \right)^2}, & \text{w.p. } p_2^{max}, \\ G_2^{min} 10^{-1.2 \left(\frac{\arctan(\frac{H_2}{x}) - \phi_2^{etilt}}{\phi_2^{3dB}} \right)^2}, & \text{w.p. } p_2^{min}. \end{cases} \quad (6.1)$$

MBSs

MBSs will be essential in providing umbrella coverage to guarantee consistent service to UEs [193], and therefore omni-directional antenna pattern is considered at MBSs, i.e., $G_3 = 1$.

To parameterize the antenna models, we need to provide the antenna gain G_j^{max} for the main lobe with beamwidth θ_j , and G_j^{min} for the side lobe gain with beamwidth $2\pi - \theta_j$. Introducing $g_j = G_j^{max}/G_j^{min}$, according to [7], we have

$$\begin{cases} G_j^{max} = 2[(1 - \cos(\theta_j/2)) + g_j(1 + \cos(\theta_j/2))]^{-1}, \\ G_j^{min} = g_j G_j^{max}. \end{cases} \quad (6.2)$$

We now have the relations to specify the antenna gain of the main lobe and the side lobe as a function of θ_j and g_j in such a way that the total transmit power does not change with the antenna

directivity. Then, we can have a fair comparison of the impact of the system parameters. It is also assumed that, after association, the APs and the SBSs can steer their horizontal antenna array directions to the UEs they serve so that the UEs can obtain maximum horizontal antenna gain G_j^{max} .

6.2 Path Loss Based Association

In the considered three-tier HetNet, BSs in each tier have different transmit power levels, and their transmissions experience different path loss. Therefore, we adopt the path loss based association criterion for the UEs. First, we introduce the characterization of the nearest distance from a typical UE to the nearest BS in each tier. Subsequently, we provide the association criterion, and determine the association probability.

6.2.1 Characterization of the Nearest 2D Distance

Note that considering the LOS/NLOS links, the original PPP of APs and SBSs can be thinned into two independent PPPs Φ_j^s with density $\lambda_j p_j^s(x)$ for $j = 1, 2$ and $s \in \{\text{LOS}, \text{NLOS}\}$. Without loss of generality, we randomly choose a UE as the typical UE, and assume that it is located at the origin. With this, the CCDF and the PDF of the distance from this typical UE to the nearest LOS/NLOS j^{th} ($j = 1, 2$) tier BS can be given as (4.3) and (4.4). The CCDF and PDF of distance from the typical UE to the nearest 3^{rd} tier BS are given by (2.4) and (2.5).

6.2.2 Association Criterion

By adopting the path loss based association criterion, the UEs are assumed to be associated with the BS providing the largest received power $P_j l_j^s$. This criterion can be formulated as

$$\{j^*, s^*\} = \underset{\substack{j=1,2,3 \\ s=L,N}}{\operatorname{argmax}} P_j l_j^s. \quad (6.3)$$

6.2.3 Association Probabilities

Since the path loss depends on the link distance that is a random variable, we characterize the association to each tier statistically. More specifically, the association probability of each tier is defined as the probability that the typical UE is served by a BS in that tier, i.e.

$$A_j^s = \mathbb{P}(j^* = j, s^* = s). \quad (6.4)$$

Theorem 6.1. *The probabilities of associating with a BS in the 1st, 2nd and 3rd tiers are given, respectively, by*

$$A_1 = \sum_{s=L,N} A_1^s = \sum_{s=L,N} \mathbb{E}_{R_1^s}[A_1^{ins}(x)] \quad (6.5)$$

$$A_2 = \sum_{s=L,N} A_2^s = \sum_{s=L,N} \mathbb{E}_{R_2^s}[A_2^{ins}(x)] \quad (6.6)$$

$$A_3 = \mathbb{E}_{R_3}[A_3^{in}(x)] \quad (6.7)$$

where \mathbb{E}_R is the expectation with respect to R , and \overline{F}_R is the CCDF of R provided in Section III.A, $\mathcal{N}_{jk}^{sb}(x) = \left(\left(\frac{P_k \kappa_k^b}{P_j \kappa_j^s} (x^2 + H_j^2)^{\frac{\alpha_j^s}{2}} \right)^{\frac{2}{\alpha_k}} - H_k^2 \right)^{\frac{1}{2}}$, and

$$A_1^{ins}(x) = \overline{F}_{R_1^{s'}}[\mathcal{N}_{11}^{ss'}(x)] \overline{F}_{R_2^L}[\mathcal{N}_{12}^{sL}(x)] \overline{F}_{R_2^N}[\mathcal{N}_{12}^{sN}(x)] \overline{F}_{R_3}[\mathcal{N}_{13}^{sL}(x)],$$

$$A_2^{ins}(x) = \overline{F}_{R_2^{s'}}[\mathcal{N}_{22}^{ss'}(x)] \overline{F}_{R_1^L}[\mathcal{N}_{21}^{sL}(x)] \overline{F}_{R_1^N}[\mathcal{N}_{21}^{sN}(x)] \overline{F}_{R_3}[\mathcal{N}_{23}^{sL}(x)],$$

$$A_3^{in}(x) = \overline{F}_{R_1^L}[\mathcal{N}_{31}^{LL}(x)] \overline{F}_{R_1^N}[\mathcal{N}_{31}^{LN}(x)] \overline{F}_{R_2^L}[\mathcal{N}_{32}^{LL}(x)] \overline{F}_{R_2^N}[\mathcal{N}_{32}^{LN}(x)].$$

Proof : Appendix 14.

We note that in the derivation of the characterizations in Theorem 6.1, we have neglected the exponential term in the path loss given in (2.14) as a simplifying assumption whose accuracy is demonstrated via numerical and simulation results.

6.2.4 Conditional PDF of the Distance of the Main Link

Given that the typical UE is served by a j^{th} tier BS and the link is in $s \in \{\text{LOS}, \text{NLOS}\}$ transmission for $j = 1, 2$, the conditional PDF of the distance from the typical UE to its serving BS can be expressed as

$$\hat{F}_{R_j^s}(x) = \mathbb{P}(r < x | j, s) = \frac{\mathbb{P}(r < x, j, s)}{\mathbb{P}(j, s)} = \frac{\mathbb{P}(r < x, j, s)}{A_j^s}. \quad (6.8)$$

Following the similar approach as in the analysis of the association probability, we obtain the conditional PDF as

$$\hat{f}_{R_j^s}(x) = \frac{d\hat{F}_{R_j^s}(x)}{dx} = \begin{cases} f_{R_j^s}(x) A_j^{ins}(x) / A_j^s, & j = 1, 2, \\ f_{R_3}(x) A_3^{in}(x) / A_3, & j = 3. \end{cases} \quad (6.9)$$

6.3 Coverage Analysis

To evaluate the performance of the HetNet, we in this section determine the CCDF of the received signal power from the serving BS, the Laplace transform of the aggregated interference, and the SINR coverage probability experienced at the typical UE.

6.3.1 Distribution of the Received Signal Power

By combining the path gain, small-scale fading, and the antenna gain, the received signal power experienced at the typical UE from its serving BS in the j^{th} tier with a $s \in \{\text{LOS}, \text{NLOS}\}$ link can be expressed as

$$P_j^{ms} = P_j G_j^m h^s l_j^s(r) \quad (6.10)$$

where r is the 2D distance from the UE to its serving BS. P_j is the transmit power, $G_j^m(r)$ denotes the antenna gain of the main link, h^s is the small-scale fading, and $l_j^s(r)$ is the path gain of the main

link.

Theorem 6.2. *The CCDF of the received signal power of the main link can be expressed as*

$$M(T) = \sum_{j=1,2,3} M_j(T) = \sum_{j=1,2,3} \sum_{s=L,N} M_j^s(T) A_j^s \quad (6.11)$$

where M_j^s is the CCDF of P_j^{ms} , given that the typical UE is associated with a j^{th} tier BS and the link is in $s \in \{LOS, NLOS\}$ transmission, and

$$\begin{aligned} M_j^s(T) &= \mathbb{P}(P_j^{ms} > T) = \mathbb{E}_r[\mathbb{P}(P_j^{ms} > T|r)] \\ &= \sum_{n=1}^{N^s} (-1)^{n+1} \binom{N^s}{n} \int_0^\infty e^{-\frac{n\xi_s N^s T}{P_j G_j^m I_j^s(r)}} \hat{f}_{R_j^s}(r) dr \end{aligned} \quad (6.12)$$

where $\xi_s = N^s(N^s!)^{\frac{1}{N^s}}$, and $\hat{f}_{R_j^s}(x)$ is given in (6.9).

Proof : Appendix 15.

6.3.2 Laplace Transform of the Aggregate Interference

Besides the received power from the serving BS, the typical UE also receives interfering signals from other BSs. The interference from the i^{th} BS in the k^{th} tier can be formulated as

$$I_k^i = P_k G_k^i h^i l_k(r_i) \quad (6.13)$$

where r_i is the 2D distance from the typical UE to the interfering BS. Given that the distance of the main link is r , there is an exclusive disc $\mathbb{Q}(0, R)$ in which no interferer exists. If the serving BS is from the j^{th} tier and the interferers are from the k^{th} tier, the radius of the disc can be expressed as $R = \mathcal{N}_{jk}^{sa}(r)$, where $s, a \in \{LOS, NLOS\}$ denote the LOS/NLOS connectivity for the main link and the interfering link, respectively. If $j, k \in \{1, 2\}$, we have $s, a \in \{LOS, NLOS\}$, and if $j = 3$

or $k = 3$, we have $s = \text{LOS}$ or $a = \text{LOS}$. Therefore, the aggregate interference is expressed as

$$I_k = \sum_{s=L,N} \sum_{i \in \Phi_k^s \setminus \mathbb{Q}} P_k G_k^i h^i l_k^s(r_i). \quad (6.14)$$

To evaluate the aggregated interference, we analyze the Laplace transform of the interference, which can be formulated as

$$\mathcal{L}_{I_k}(\mu) = \mathbb{E}[e^{-\mu I_k}] \quad (6.15)$$

Theorem 6.3. *The Laplace transform of the interference from the k^{th} tier evaluated at μ can be expressed as*

$$\mathcal{L}_{I_k}(\mu) = \exp \left(- \sum_{s=L,N} \sum_G \int_{R_c(r)}^{\infty} (1 - (1 + \mu P_k G_k^G(x) l_k^s(x) N^s)^{-N^s}) p_k^s(x) p_k^G(x) \lambda_k 2\pi x dx \right) \quad (6.16)$$

Proof : Appendix 16.

6.3.3 SINR Coverage Probability

Given that the typical UE is associated with a j^{th} tier BS and the link is in $s \in \{\text{LOS}, \text{NLOS}\}$ transmission, the SINR experienced at the typical UE can be expressed as

$$\text{SINR}_j^s = \frac{P_j G_j^m h^s l_j^s(r)}{N + \sum_{i \in \Phi_j \setminus \mathbb{Q}(r)} P_j G_j^i h^i l_j^s(r_i)} \quad (6.17)$$

where N is the noise power.

The SINR coverage probability is defined as the SINR experienced at the UE being larger than a certain threshold T . Since in this heterogeneous network, UEs are possible to be associated with

BS from each tier, the SINR coverage probability of the network can be written as

$$C = \sum_{j=1,2,3} C_j = \sum_{j=1,2,3} \sum_{s=L,N} C_j^s A_j^s \quad (6.18)$$

where C_j is the SINR coverage probability of the j^{th} tier, C_j^s is the conditional SINR coverage probability given that the UE is associated with a BS in the j^{th} tier and the link is in s transmission.

Theorem 6.4. *Given that the UE is served by an $s \in \{LOS, NLOS\}$ BS in the j^{th} tier, the conditional SINR coverage probability can be formulated as*

$$C_j^s = \sum_{n=1}^{N^s} (-1)^{n+1} \binom{N^s}{n} \int_0^\infty e^{-\frac{n\xi_s N^s T N}{P_j G_j^m l_j^s(r)}} \mathcal{L}_{I_j} \left(\frac{n\xi_s N^s T}{P_j G_j^m l_j^s(r)} \right) \hat{f}_{R_j^s}(r) dr \quad (6.19)$$

where r is the distance from a UE to its serving BS, the PDF of which is $\hat{f}_{R_j^s}(r)$ given in (6.9), and N^s is the Nakagami fading parameter.

Proof : Appendix 17.

6.4 Numerical Results

In this section, we elaborate on the analysis of the CCDF of the received signal power and the SINR coverage probability in the HetNet. Simulation results with Monte-Carlo methods are provided to validate the numerical evaluations of the derived expressions. Unless stated otherwise, the used parameters values are listed in Table 6.1 below. In the figures, we depict the performance by analyzing 1) the conditional CCDF of the received signal power M_j^s and the conditional SINR coverage probability C_j^s , given the typical UE is associated with a BS in the j^{th} tier with $s \in \{LOS, NLOS\}$ connectivity; 2) the CCDF of the received power of each tier M_j and the entire network M ; and 3) the SINR coverage probability of each tier C_j and the entire network C .

Table 6.1: Table of Parameters

Parameters	Values
P_1, P_2, P_3	20dBm, 24dBm, 43dBm [168]
$\lambda_2, \lambda_3, \lambda_U$	$10^{-4}/\text{m}^2, 10^{-6}/\text{m}^2, 10^{-2}/\text{m}^2$
H_1, H_2, H_3	0m, 10m, 32m [168]
$\alpha_1^L, \alpha_1^N, \kappa_1^L, \kappa_1^N$	2, 4, 0.1, 0.1
$\alpha_2^L, \alpha_2^N, \kappa_2^L, \kappa_2^N$	2, 4, 1, 1
$\kappa, \beta, \alpha_3, R_B$	0.01 [7], 1/141.4 [160], 3, 0.3m
$\phi_2^{etilt}, \phi_2^{3dB}, \theta_2$	15° [168], $30^\circ, 30^\circ$
g_1, g_2	0.05, 0.1
N^L, N^N, N	3, 2, 10^{-8} dB

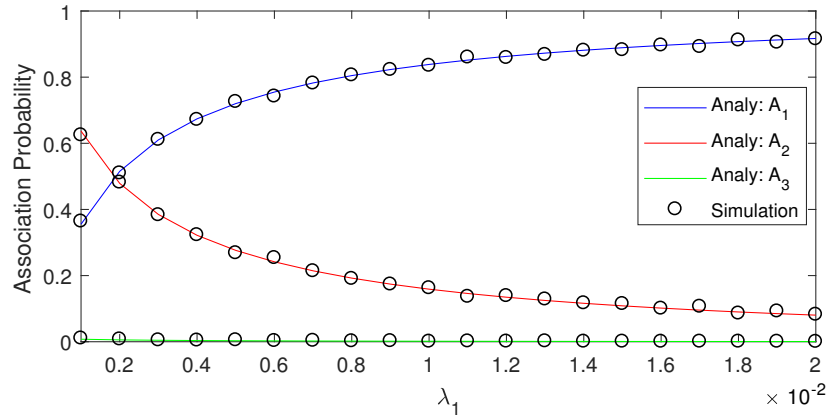
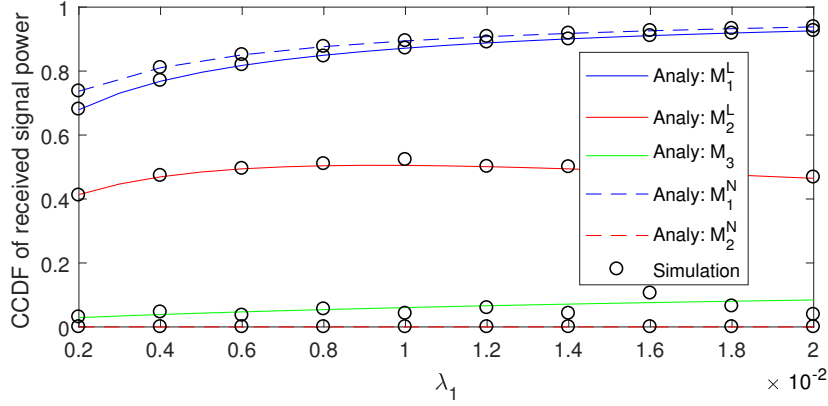


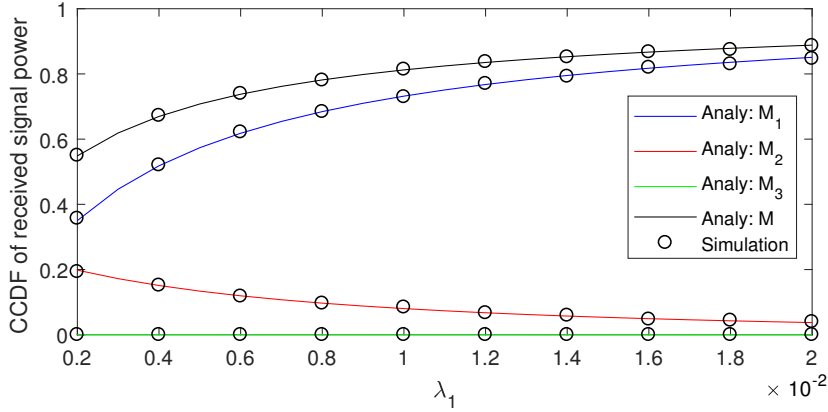
Fig. 6.2: Association probability as a function of the density of the APs.

6.4.1 Impact of the Density of THz APs

Fig. 6.2 shows the association probabilities A_j of each tier as functions of the density λ_1 of the THz APs. We observe that as λ_1 increases, the association probability of the APs increases, while those of the other two tiers decrease. It is worth noting that, in the simulations, we use the true path loss to find the association. And the simulation results match with association probabilities in (6.5)-(6.7), although in the derivation we have neglected the exponential term in the path loss. This indicates that the approximation is accurate and does not lead to much difference in the system performance analysis. In addition, in Fig. 6.2, we see that the association probabilities of the APs and SBSs are much larger than that of the MBSs, due to the much larger link distances from a MBS to the typical UE and the resulting much smaller path gain. The numerical results also show



(a) Conditional CCDF of the received singal power.



(b) CCDF of the received singal power.

Fig. 6.3: CCDF of the receive signal power as a function of the density of APs, when $T = -30$ dB and $\theta_1 = 15^\circ$.

that the association probability of the NLOS BSs are close to zero, i.e. $A_j \approx A_j^L$. Due to this, we have not separately plotted A_j^L and A_j^N .

Fig. 6.3 shows the CCDF of the received signal power as a function of λ_1 . As we increase λ_1 , there are more APs in the network, and the average distance between the typical UE and the APs decreases, leading to increasing path gain for both LOS and NLOS APs. Thus, we can observe increasing M_1^L and M_1^N . However, since there are more APs in the network, SBSs and MBSs need to be more appealing to the typical UE so that they can be associated with the UEs. In other words, they need to provide larger signal to the typical UE. Thus, if the typical UE is associated with a SBS or MBS, the received signal power is also increased with an increasing λ_1 . Therefore, M_1^L , M_1^N ,

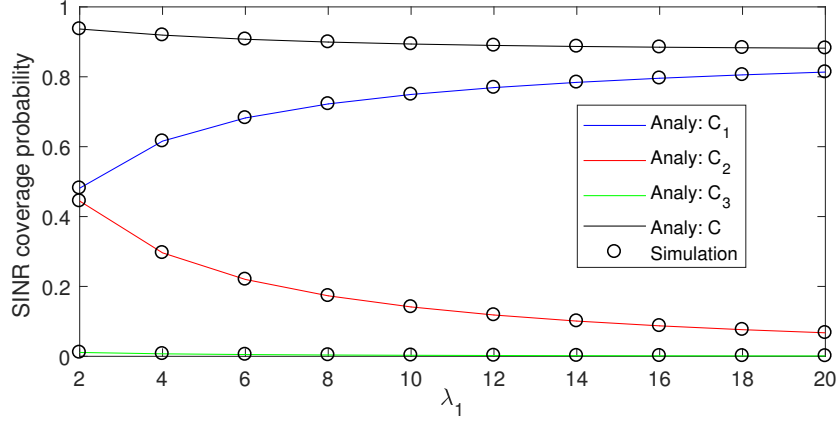


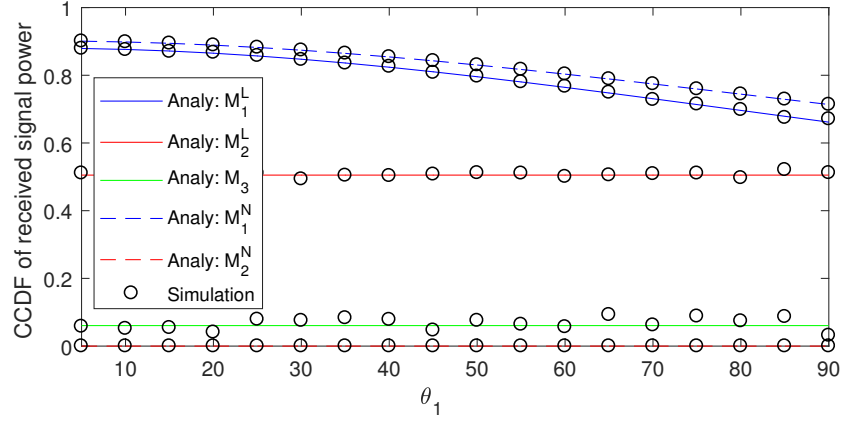
Fig. 6.4: SINR coverage probability as a function of the density of APs, when $T = -5$ dB and $\theta_1 = 15^\circ$.

M_2^L , and M^3 increase in Fig. 6.3(a). Since the received signal power of the NLOS SBSs is really small, M_2^N is close to zero when $T = -30$ dB. Combined with the association probability, we can observe in Fig. 6.3(b) that M_1 increases, M_2 decreases, while M_3 is zero, since the association probability also plays an important role. Due to the reason that the increase in M_1 can make up the decrease in M_2 , the received signal power experienced at the typical UE M increases.

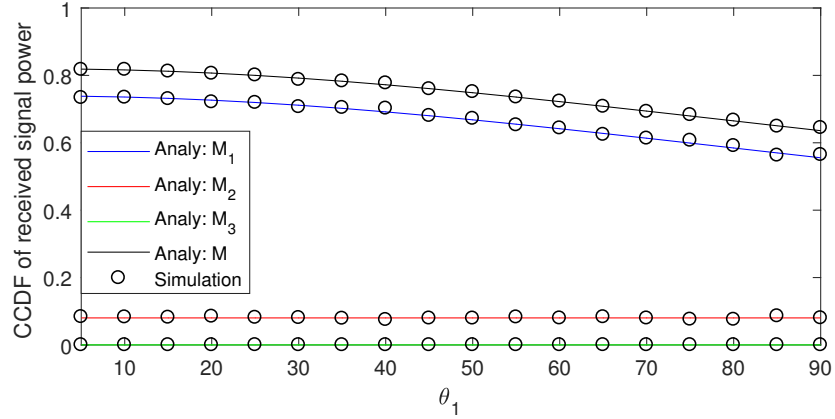
Fig. 6.4 shows the SINR coverage probability as a function of λ_1 . When there are more APs in the network, the interference from the APs increases. Even through the received signal power of the APs M_1^s also grows substantially, the increase in the interference is greater than that of M_1^s . However, as λ_1 increases, more and more UEs are served by the APs. Therefore, the SINR coverage probability of the APs C_1 increases. On the other hand, the interference from the APs does not impact the coverage of SBSs and MBSs greatly, but due to the decreases in A_2 and A_3 , both C_2 and C_3 decrease. Since the ascent in C_1 can not compensate the descent in C_2 and C_3 , the SINR coverage probability of the network decreases with an increasing λ_1 .

6.4.2 Impact of the Beamwidth of the Main Lobe at the THz APs

Fig. 6.5 shows the CCDF of the received signal power as a function of the beamwidth θ_1 of the main lobe at the APs. Since the total antenna gain is fixed to be 1, the antenna gain of the main lobe G_1^{max} will decrease if we increase θ_1 . Therefore, the received signal power of the APs M_1^s



(a) Conditional CCDF of the received signal power.



(b) CCDF of the received signal power.

Fig. 6.5: CCDF of the receive signal power as a function of beamwidth of the main lobe at the APs, when $T = -30$ dB and $\lambda_1 = 10^{-2}/\text{m}^2$.

decreases, while M_2^L and M_3 do not change. The antenna gain does not influence the association probability, and hence the association probability does not change with increasing θ_1 . As a result, M_j displays the same performance trends in Fig. 6.5(b) as M_j^s . And M decreases with increasing θ_1 since UEs are mostly served by the APs and M_1 increases.

Fig. 6.6 shows the SINR coverage probability as a function of θ_1 . As θ_1 is initially increased, the beamwidth of the main lobe at APs grows, and more interferers will generate interference with the main lobe gain G_1^{max} . Thus, the interference from APs increases. Since the received signal power from APs M_1 decreases, the SINR coverage probability of APs C_1 decreases. On the other hand, the change in θ_1 does not influence the coverage of SBSs and MBSs. Therefore, the SINR

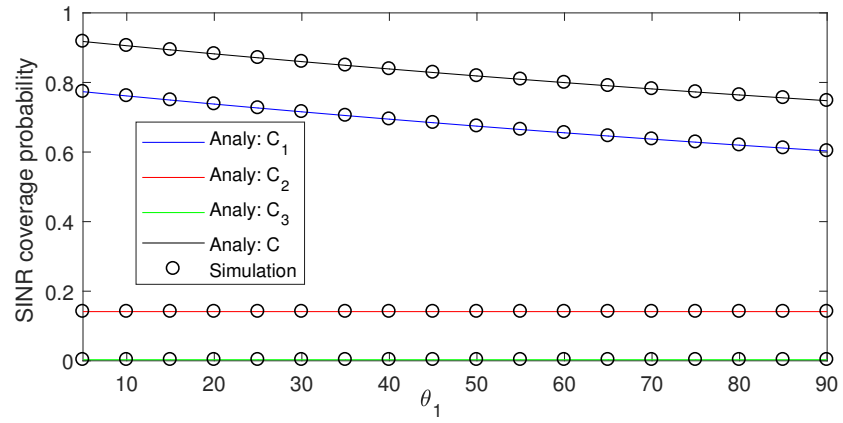


Fig. 6.6: SINR coverage probability as a function of beamwidth of the main lobe at the APs, when $T = -5$ dB and $\lambda_1 = 10^{-2}/\text{m}^2$.

coverage probability of the network decreases with an increasing θ_1 .

CHAPTER 7

COVERAGE ANALYSIS FOR

ENERGY-HARVESTING UAV-ASSISTED

MMWAVE CELLULAR NETWORKS

7.1 System Model

In this section, we describe the considered UAV-assisted mmWave cellular network with PCP distributed UEs.

7.1.1 BS and UE Deployment

UAV and GBS Modeling

The UAVs and GBSs are assumed to be distributed according to homogeneous PPPs Φ_U and Φ_G with densities λ_U and λ_G , respectively. All UAVs and GBSs are assumed to be transmitting in a mmWave frequency band and have transmit powers P_U and P_G , biasing factors to UEs B_U and B_G , respectively. The biasing factor indicates the association preference of the tier, i.e. when we increase the B of a tier, the UEs becomes more likely to be associated with the BS in that tier. All

UAVs are assumed to be located at the same height H . We assume that all UAVs have enough energy resources to arrive at its 3D position in the air, communicate with UEs, and fly back.

UE Modeling

The locations of the UEs are assumed to form a PCP denoted by Φ_u , and the ground projections of the UAVs are the parent nodes. In this chapter, we also adopt two particular PCPs: Thomas cluster processes and Matérn cluster processes.

Without loss of generality, in the downlink phase a random UE from a random cluster is chosen to be the typical UE and is assumed to be at the origin. To differentiate the distance from the typical UE to its cluster center UAV and the distance to other UAVs, we denote the cluster center as the 0^{th} tier UAV to the typical UE, and other UAVs and GBSs are the 1^{st} and 2^{nd} tier BSs, respectively. In the uplink phase, a UAV from a random cluster is chosen to be the typical BS. The descriptions of different tiers in the downlink phase are provided below in Table 7.1.

Table 7.1: Tiers in the Network

Downlink phase	
0^{th} tier	The cluster center UAV of the typical UE
1^{st} tier	Other PPP-distributed UAVs
2^{nd} tier	The PPP-distributed GBSs
$\mathcal{K} = \{0, 1, 2\}$	The set of all tiers of UAVs and GBSs

7.1.2 Downlink and Uplink Transmission

In this chapter, we jointly consider downlink and uplink transmissions, where the UEs harvest energy and decode information from its downlink associated BS during downlink phase, and then send data to its cluster center UAV during uplink phase. The total time duration for downlink and uplink is assumed to be T (seconds). As shown in Fig. 7.1, each time frame of T seconds is divided into downlink and uplink time slots with durations τ and $(T - \tau)$, respectively. In the downlink phase, SWIPT scenario is considered, and more specifically the power splitting technique is used. Employing this technique, the UEs can harvest energy and decode the information by splitting the

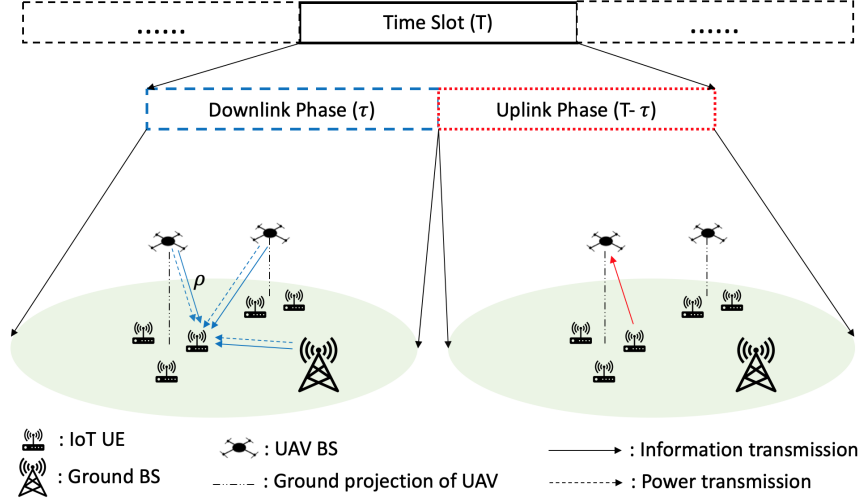


Fig. 7.1: An illustration of the system model of a UAV-assisted mmWave cellular network.

received signal into two streams. The power splitting parameter that represents the power fraction used for information processing is denoted by ρ . It's assumed the UEs have enough battery storage to store the harvested energy. In the uplink phase, UEs use the harvested energy to send data to their cluster center UAVs. It is worth noting that when $\tau = T$, our model specializes to a downlink SWIPT network. Additionally, when $\rho = 0$, we recover the network model with downlink energy harvesting and uplink data transmission (i.e. the WPCN scenario).

7.1.3 Path Loss Modeling

The path loss model is formulated as in (2.13), and denoted by $L_j^s(r)$ ($j \in \mathcal{K}$ and $s \in \{\text{LOS}, \text{NLOS}\}$).

Air-to-Ground

We formulate the probability of the LOS link between the UAVs and the UEs as (2.17), and denoted by $p_U^L(r) = \frac{1}{1+C \exp(-B(\theta-C))}$. Note that since the 0^{th} and 1^{st} tier BSs are UAVs, we have $p_0^L(r) = p_1^L(r) = p_U^L(r)$.

Ground-to-Ground

We can formulate the probability of LOS link between the GBSs and the UEs as in (2.11), and denoted by $p_2^L(r) = p_G^L(r) = e^{-\epsilon r}$.

It's worth noting that since we distinguish the links between the UEs to the GBS as either LOS or NLOS, we assume the BSs in the 1st and 2nd tiers are divided into two independent PPPs Φ_j^s for $s \in \{\text{LOS}, \text{NLOS}\}$.

7.1.4 Antenna Gain

The sectored antenna model given in (2.22) is considered in this chapter.

7.1.5 Small-Scale Fading

Nakagami- m fading is adopted in this chapter, and N_l, N_n are the Nakagami fading parameters for LOS and NLOS links, respectively, and are assumed to be positive integers.

7.2 Distance Distributions

In this section, we characterize the CCDF and the PDF of the distance from the typical UE to UAVs and GBSs in each tier. Fig. 7.2 provides an illustration of different distances.

7.2.1 The Distance R_0 from the Typical UE to the 0th Tier UAV

The distance from the typical UE to the projection of its cluster center UAV on the ground is denoted as D . Then the distribution of D can be expressed for different PCPs is given in 2.8 and 2.10.

Lemma 7.1. *Given that the link between the typical UE and its cluster center UAV is in $s \in \{\text{LOS}, \text{NLOS}\}$ transmission, the CCDF and PDF of R_0^s can be expressed as follows:*

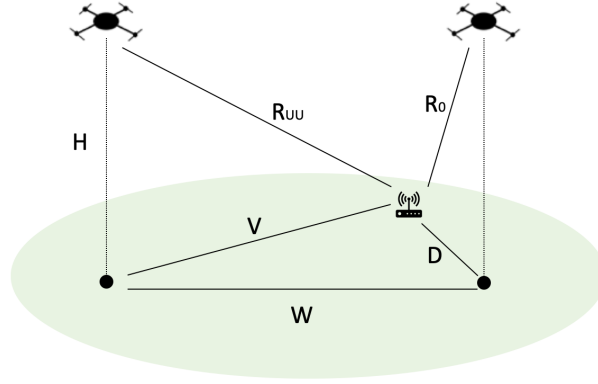


Fig. 7.2: An illustration of difference distance in the network.

(i) *Thomas cluster process:*

$$CCDF: \quad \bar{F}_{R_0^s}(x) = \int_{\sqrt{x^2-H^2}}^{\infty} p_U^s(\sqrt{d^2+H^2}) f_D(d) dd / D_0^s, \quad (x \geq H) \quad (7.1)$$

$$PDF: \quad f_{R_0^s}(x) = \frac{x p_U^s(x)}{\sigma^2 D_0^s} \exp\left(\frac{H^2 - x^2}{2\sigma^2}\right) \quad (x \geq H), \quad (7.2)$$

(ii) *Matérn cluster process:*

$$CCDF: \quad \bar{F}_{R_0^s}(x) = \int_{\sqrt{x^2-H^2}}^{R_c} p_U^s(\sqrt{d^2+H^2}) f_D(d) dd / D_0^s, \quad (H \leq x \leq \sqrt{H^2 + R_c^2}), \quad (7.3)$$

$$PDF: \quad f_{R_0^s}(x) = \frac{2x p_U^s(x)}{R_c^2 D_0^s}, \quad (H \leq x \leq \sqrt{H^2 + R_c^2}), \quad (7.4)$$

where $D_0^s = \int_0^\infty p_U^s(\sqrt{d^2+H^2}) f_D(d) dd$ is the probability that the link is in $s \in \{LOS, NLOS\}$ transmission.

Proof: See Appendix 18.

Therefore, we can obtain the CCDF and PDF of R_0 as follows:

$$\begin{aligned} \bar{F}_{R_0}(x) &= \sum_s D_0^s \bar{F}_{R_0^s}(x) \\ &= \begin{cases} \exp\left(\frac{H^2 - x^2}{2\sigma^2}\right) & (x \geq H) & \text{for Thomas cluster process,} \\ 1 - \frac{x^2 - H^2}{R_c^2} & (H \leq x \leq \sqrt{H^2 + R_c^2}) & \text{for Matérn cluster process,} \end{cases} \end{aligned} \quad (7.5)$$

$$\begin{aligned}
f_{R_0}(x) &= -\frac{d\bar{F}_{R_0}(x)}{dx} \\
&= \begin{cases} \frac{x}{\sigma^2} \exp\left(\frac{H^2 - x^2}{2\sigma^2}\right) & (x \geq H) & \text{for Thomas cluster process,} \\ \frac{2x}{R_c^2} & (H \leq x \leq \sqrt{H^2 + R_c^2}) & \text{for Matérn cluster process.} \end{cases}
\end{aligned} \tag{7.6}$$

7.2.2 The Distance R_U^s from the Typical UE to the Nearest LOS/NLOS UAV from the 1st Tier

Given that the typical UE can observe at least one LOS/NLOS UAV in the 1st tier, the CCDF and PDF of R_U^s can be expressed as follows:

$$\text{CCDF: } \bar{F}_{R_U^s}(x) = e^{-2\pi\lambda_U \int_H^x tp_U^s(t)dt} / D_U^s, \tag{7.7}$$

$$\text{PDF: } f_{R_U^s}(x) = 2\pi\lambda_U x p_U^s(x) e^{-2\pi\lambda_U \int_H^x tp_U^s(t)dt} / D_U^s, \tag{7.8}$$

where $x \geq H$, $D_U^s = 1 - e^{-2\pi\lambda_U \int_H^\infty tp_U^s(t)dt}$ is the probability that the typical UE has at least one LOS/NLOS UAV around.

7.2.3 The Distance R_G^s from the Typical UE to the Nearest LOS/NLOS GBS from the 2nd Tier

Given that the typical UE can observe at least one LOS/NLOS BS in the 2st tier, the CCDF and PDF of R_G^s can be given as (4.3) and (4.4)

7.2.4 The Distance R_{UU} from a UE to the Other Cluster Center UAV

For Thomas cluster process, the PDF of the distance V from a UE to the ground projection of other cluster center UAV, given the distance W from the UE's cluster center UAV to the corresponding

UAV, can be expressed as [74]

$$f_V(v|w) = \frac{v}{\sigma^2} \exp\left(-\frac{v^2 + w^2}{2\sigma^2}\right) I_0\left(\frac{vw}{\sigma^2}\right), \quad (7.9)$$

where $I_0(\cdot)$ is the modified Bessel function with order zero. For Matérn cluster process, the PDF can be expressed as [194]

$$f_V(v|w) = \frac{2v}{\pi R_c} \arccos \frac{v^2 + w^2 - R_c^2}{2vw} \mathbb{1}(|R_c - w| \leq v \leq R_c + w) + \frac{2v}{R_c^2} \mathbb{1}(v < R_c - w). \quad (7.10)$$

Then the PDF of R_{UU} can be obtained as

$$f_{R_{UU}}(x|w) = \frac{x}{\sqrt{x^2 - H^2}} f_V(\sqrt{x^2 - H^2}|w). \quad (7.11)$$

7.3 User Association

In this section, we focus on the downlink and uplink UE association, and also provide the downlink association probability of each tier, from which we can determine how the UEs connect with the UAVs and GBSs.

7.3.1 Downlink Association

In the downlink phase, UEs need to harvest energy and decode the information from the associated BS (e.g., a UAV or a GBS). The strongest biased average power association criterion [179] [195] is utilized, i.e. the UEs are assumed to be associated with the BS providing the strongest long-term biased average received power. Since the antenna gain of the main link is assumed to achieve the maximum value G_0 , the received power of the main link can be expressed as

$$P_m = \operatorname{argmax}_{j \in \mathcal{K}, i \in \Phi} P_j G_0 B_j L_{ji}^{-1} \stackrel{(a)}{=} \operatorname{argmin}_{j \in \mathcal{K}, s} P_j G_0 B_j (\kappa_j^s (r_j^s)^{\alpha_j^s}) \quad (7.12)$$

where r_j^s is the distance from the typical UE to the nearest LOS/NLOS BS in the j^{th} tier, and (a) follows from the fact that in each tier the transmit power and the biasing factor are the same, and therefore the maximum received power is from the nearest LOS/NLOS BS.

Lemma 7.2. *The probability that the typical UE is associated with a LOS/NLOS BS in the j^{th} tier is given by*

$$A_{j,s} = \begin{cases} \mathbb{E}_{R_0^s} \left[D_0^s \prod_k \prod_b D_k^b \bar{F}_{R_k^b} (Q_{k0}^{sb}(r_0)) \right], & \text{for } j = 0, \\ D_j^s \mathbb{E}_{R_j^s} \left[D_j^{s'} \bar{F}_{R_j^{s'}} (Q_{jj}^{ss'}(r_j)) \left(\sum_b D_0^b \bar{F}_{R_0^b} (Q_{0j}^{sb}(r_j)) \right) \prod_b D_k^b \bar{F}_{R_k^b} (Q_{kj}^{sb}(r_j)) \right], & \text{for } j = 1, 2, \end{cases} \quad (7.13)$$

where $s, s', b \in \{LOS, NLOS\}$, $s' \neq s$, $k = 1, 2$, $Q_{kj}^{sb}(r) = \left(\frac{P_k B_k \kappa_j^s}{P_j B_j \kappa_k^b} r^{\alpha_j^s} \right)^{\frac{1}{\alpha_k^b}}$, D_j^s and $\bar{F}_{R_j^s}(x)$ are given in section 7.2.

Proof: See Appendix 19.

Remark 7.1. *In order to characterize the link level performance of the UAV-assisted network, we will need to find the distance distribution give that link. Therefore, given that the typical UE is associated with a LOS/NLOS BS in the j^{th} tier, the PDFs of the distances from the typical UE to the associated BS can be expressed as follows:*

$$\hat{f}_{R_j^s}(x) = \begin{cases} \frac{f_{R_0^s}(x)}{A_{0,s}} D_0^s \prod_k \prod_b D_k^b \bar{F}_{R_k^b} (Q_{k0}^{sb}(x)), & \text{for } j = 0, \\ \frac{f_{R_j^s}(x)}{A_{j,s}} D_j^s D_j^{s'} \bar{F}_{R_j^{s'}} (Q_{jj}^{ss'}(x)) \left(\sum_b D_0^b \bar{F}_{R_0^b} (Q_{0j}^{sb}(x)) \right) \prod_b D_k^b \bar{F}_{R_k^b} (Q_{kj}^{sb}(x)), & \text{for } j = 1, 2. \end{cases} \quad (7.14)$$

And the proof follows the same way as the association probability in Appendix 19.

7.3.2 Uplink Association

In the uplink phase, each UAV aims to collect data from one cluster, and hence the UAV is assumed to communicate with its own cluster member UEs. It is further assumed that different UEs in one cell are served using orthogonal resources, and hence no intra-cell interference exists. UEs from other clusters can inflict interference. It is worth noting that UEs may not be associated with the same BSs in downlink and uplink phases, due to the adoption of the strongest biased average power association criterion in the downlink phase.

7.4 Downlink Coverage Analysis

In this section, we first investigate the interference in the downlink phase, then analyze the network performance by the energy coverage and SINR coverage of each tier. Finally, we provide a successful transmission probability which can jointly consider both energy coverage and SINR coverage and can represent the downlink performance of the UAV-assisted cellular network.

7.4.1 Interference

Since the typical UE is assumed to be served by a BS which provides the largest biased received power P_m , then if a UE is associated with a LOS/NLOS BS from the j^{th} tier at distance r , there exists an exclusive disc $q(0, Q_{kj}^{sb}(r))$ in which no interfering BS exists. Therefore, the experienced interference at the typical UE can be expressed as follows:

$$I = I_0 + I_1 + I_2 \quad (7.15)$$

$$I_0 = P_0 G h_0 (\kappa_U^b r_0^{\alpha_U^b})^{-1} \quad (7.16)$$

$$I_k = \sum_b \sum_{i \in \Phi_k^b \setminus q} P_k G_i h_k (\kappa_k^b r_{k,i}^{\alpha_k^b})^{-1} \quad (7.17)$$

where $b \in \{\text{LOS}, \text{NLOS}\}$, $k = 1, 2$, r_0 denotes the distance from the UE to its cluster center, and $r_{k,i}$ stands for the distance from the UE to the i^{th} BS in the k^{th} tier. It is worth noting that when

the serving BS is from the 0^{th} tier, we have $I_0 = 0$, since there's only one BS in this tier.

7.4.2 Harvested Energy and Signal to Interference Plus Noise Ratio

Since power splitting technique is employed with parameter ρ , the total harvested energy of the typical UE in the downlink phase can be expressed as

$$E_{j,s}^{hv} = \tau(1 - \rho)(P_m + I) \quad (7.18)$$

where τ is the time duration used for downlink phase, and $P_m = P_j G_0 h_j (\kappa_j^s r^{\alpha_j})^{-1}$ denotes the received power of the main link from the serving BS. We neglect the additive white Gaussian noise (AWGN) term in energy harvesting. It is worth noting that we assume linear energy harvesting, and the case of non-linear energy harvesting remains as future work.

Moreover, the experienced SINR at the typical UE can be expressed as

$$\text{SINR}_{j,s} = \frac{\rho P_m}{\sigma_c^2 + \rho(\sigma_n^2 + I)} = \frac{P_m}{\frac{\sigma_c^2}{\rho} + \sigma_n^2 + I} \quad (7.19)$$

where σ_n^2 is the variance of the Gaussian thermal noise component and σ_c^2 is the noise factor due to the conversion of the received bandpass signal to baseband.

7.4.3 Energy Coverage Probability

The energy coverage probability can be defined as the probability that the harvested energy is larger than a certain threshold $\gamma_E > 0$. Therefore, given the event $S_{j,s} = \{\text{The typical UE is associated with a LOS/NLOS BS in the } j^{th} \text{ tier}\}$, the conditional energy coverage can be expressed as

$$P_{E_{j,s}}^c(\rho, \tau, \gamma_E) = \mathbb{P}(E_{j,s}^{hv} > \gamma_E | S_{j,s}). \quad (7.20)$$

Hence, the energy coverage probability of the entire network can be obtained by

$$P_E(\rho, \tau, \gamma_E) = \sum_{j \in \mathcal{K}} P_{E_j}(\rho, \tau, \gamma_E) = \sum_{j \in \mathcal{K}} \sum_s P_{E_{j,s}}^c(\rho, \tau, \gamma_E) A_{j,s} \quad (7.21)$$

where $A_{j,s}$ is the association probability given in (7.13), and

$P_{E_j}(\rho, \tau, \gamma_E) = \sum_s P_{E_{j,s}}^c(\rho, \tau, \gamma_E) A_{j,s}$ is the energy coverage of tier j .

Theorem 7.1. *Conditioned on that the typical UE is associated with a LOS/NLOS BS in the j^{th} tier, the energy coverage probability can be expressed as follows:*

$$P_{E_{j,s}}^c(\rho, \tau, \gamma_E) = \begin{cases} \sum_{n=0}^N (-1)^n \binom{N}{n} \int_H^\infty \zeta_{j,s}^{G_0}(r) \hat{f}_{R_0^s}(r) \prod_k \mathcal{L}_{I_k}(\hat{a}) dr & \text{for } j = 0, \\ \sum_{n=0}^N (-1)^n \binom{N}{n} \int_{B_{d1}}^\infty \zeta_{j,s}^{G_0}(r) \hat{f}_{R_j^s}(r) \mathcal{L}_{I_0}(\hat{a}) \prod_k \mathcal{L}_{I_k}(\hat{a}) dr & \text{for } j = 1, 2, \end{cases} \quad (7.22)$$

where $s, b \in \{\text{LOS}, \text{NLOS}\}$, $\hat{a} = \frac{a n \tau (1-\rho)}{\gamma_E}$, $a = N(N!)^{-\frac{1}{N}}$, $B_{d1} = H$ for $j = 1$, $B_{d1} = 0$ for $j = 2$, $\zeta_{j,s}^G(r) = (1 + \hat{a} P_j G(\kappa_j^s r^{\alpha_j^s} N_s)^{-1})^{-N_s}$, and $\hat{f}_{R_j^s}(r)$ is the conditional PDF of distances given in (7.14). The Laplace transforms of the interference can be expressed as follows:

$$\mathcal{L}_{I_0}(\hat{a}) = \sum_G \sum_b \int_{\max\{H, Q_{0j}^{sb}(r)\}}^\infty \frac{p_G \hat{f}_{R_0^b}(r_0) dr_0}{\left(1 + \hat{a} P_0 G(\kappa_0^b r_0^{\alpha_0^b} N_b)^{-1}\right)^{N_b} \bar{F}_{R_0^b}(Q_{0j}^{sb}(r))} \quad (7.23)$$

$$\mathcal{L}_{I_k}(\hat{a}) = \prod_G \prod_b e^{-2\pi \lambda_k p_G \int_{B_{d2}}^\infty \left(1 - \left(1 + \hat{a} P_k G(\kappa_k^b r_k^{\alpha_k^b} N_b)^{-1}\right)^{-N_b}\right) p_k^b(r_k) r_k dr_k} \quad (7.24)$$

where $B_{d2} = \max(H, Q_{kj}^{sb}(r))$ for $k = 1$, and $B_{d2} = Q_{kj}^{sb}(r)$ for $k = 2$.

Proof: See Appendix 20.

Remark 7.2. We note that the provided analysis and expressions are general. To find the energy coverage probability of the Thomas cluster process and Matérn cluster process, we only need to substitute the corresponding PDFs and CCDFs in Section III for each cluster process in (7.22).

Remark 7.3. Since the harvested energy is a linear function of the downlink duration τ , the energy

coverage is a monotonically increasing function of τ . On the other hand, the energy coverage probability is monotonically decreasing function of the power splitting parameter ρ .

7.4.4 SINR Coverage Probability

The SINR coverage probability is defined as the probability that the received SINR is larger than a certain threshold $\gamma_{sinr} > 0$. Therefore, given the event $S_{j,s}$, the conditional SINR coverage probability of each tier can be determined using [195, Theorem 1] and expressed as follows:

$$P_{SINR_{j,s}}^c(\rho, \tau, \gamma_{sinr}) = \mathbb{P}(\text{SINR}_{j,s} > \gamma_{sinr} | S_{j,s}) = \begin{cases} \sum_{n=1}^{N_s} (-1)^{n+1} \binom{N_s}{n} \int_H^{\infty} \hat{f}_{R_0^s}(r) e^{-\mu_j^s \left(\frac{\sigma_c^2}{\rho} + \sigma_n^2 \right)} \prod_k \mathcal{L}_{I_k}(\mu_j^s) dr & \text{for } j = 0, \\ \sum_{n=1}^{N_s} (-1)^{n+1} \binom{N_s}{n} \int_{B_{d1}}^{\infty} \hat{f}_{R_j^s}(r) e^{-\mu_j^s \left(\frac{\sigma_c^2}{\rho} + \sigma_n^2 \right)} \mathcal{L}_{I_0}(\mu_j^s) \prod_k \mathcal{L}_{I_k}(\mu_j^s) dr & \text{for } j = 1, 2, \end{cases} \quad (7.25)$$

where $\mu_j^s = \frac{n\eta_s \gamma_{sinr} \kappa_j^s r^{\alpha_j^s}}{P_j G_0}$, $\eta_s = N_s(N_s!)^{-\frac{1}{N_s}}$, N_s is the Nakagami fading parameter.

Remark 7.4. From the downlink SINR expression, we can conclude that the SINR coverage probability is independent of τ . On the other hand, it is a monotonically increasing function of ρ .

7.4.5 Successful Transmission Probability

In general, the transmission is successful if the UE can both harvest enough energy to charge itself and has sufficient SINR levels for information decoding. Therefore, we define the successful transmission probability (STP) as follows.

Definition 7.1. Given that the typical UE is associated with a LOS/NLOS BS from the j^{th} tier, the conditional successful transmission probability is defined as

$$P_{ST_{j,s}}^c(\rho, \tau, \gamma_E, \gamma_{sinr}) = \mathbb{P}(E_{j,s}^{hv} > \gamma_E, \text{SINR}_{j,s} > \gamma_{sinr} | S_{j,s}). \quad (7.26)$$

Therefore, the total STP of the UAV-assisted mmWave network can be expressed as

$$P_{ST}(\rho, \tau, \gamma_E, \gamma_{sinr}) = \sum_{j \in \mathcal{K}} P_{ST_j}(\rho, \tau, \gamma_E, \gamma_{sinr}) = \sum_{j \in \mathcal{K}} \sum_s P_{ST_{j,s}}^c(\rho, \tau, \gamma_E, \gamma_{sinr}) A_{j,s}. \quad (7.27)$$

Theorem 7.2. Given that the typical UE is associated with a LOS/NLOS BS from the j^{th} tier, the conditional successful transmission probability of each tier can be expressed as

$$P_{ST_{j,s}}^c(\rho, \tau, \gamma_E, \gamma_{sinr}) = P_{E_{j,s}}^c(\rho, \tau, \gamma_E)(1 - \hat{F}_I(\omega)) + P_{SINR_{j,s}}^c(\rho, \tau, \gamma_{sinr})\hat{F}_I(\omega) \quad (7.28)$$

where $\omega = \frac{1}{1+\gamma_{sinr}} \left(\frac{\gamma_E}{\tau(1-\rho)} - \gamma_{sinr} \left(\frac{\sigma_c^2}{\rho} + \sigma_n^2 \right) \right)$, $P_{E_{j,s}}^c(\rho, \tau, \gamma_E)$ is the conditional energy coverage probability given in (7.22), $P_{SINR_{j,s}}^c(\rho, \tau, \gamma_{sinr})$ is the conditional SINR coverage probability given in (7.25), and $\hat{F}_I(x)$ is the CCDF of I given event $S_{j,s}$, whose expression is as follows:

$$\hat{F}_I(x) = \begin{cases} \sum_{n=0}^N (-1)^n \binom{N}{n} \int_H^\infty \hat{f}_{R_0^s}(r) \prod_k \mathcal{L}_{I_k}(\hat{a}') dr & \text{for } j = 0, \\ \sum_{n=0}^N (-1)^n \binom{N}{n} \int_{B_{d1}}^\infty \hat{f}_{R_j^s}(r) \mathcal{L}_{I_0}(\hat{a}') \prod_k \mathcal{L}_{I_k}(\hat{a}') dr & \text{for } j = 1, 2, \end{cases} \quad (7.29)$$

where $\hat{a}' = \frac{an}{x}$.

Proof: See Appendix 21.

7.5 Uplink Coverage Analysis

In the uplink phase, UEs use the energy harvested in the downlink phase to transmit data to the cluster center UAVs. We assume all UEs transmit at the fixed power level of P_t^{UL} . Then, for successful uplink transmission, the harvested energy E^{hv} for a UE should satisfy

$$E^{hv} \geq (T - \tau) P_t^{UL}. \quad (7.30)$$

If this condition is not satisfied, then the UE is assumed to be in inactive mode in the uplink phase, i.e. the UE is not able to transmit; otherwise the UE is in active mode. Therefore, we can obtain the probability that the UE is in active mode from the energy coverage probability derived in the previous section as follows:

$$p_{active} = P_E((T - \tau)P_t^{UL}). \quad (7.31)$$

7.5.1 Uplink SINR Coverage

A UAV from a random cluster is chosen as the typical BS, and a random active UE from the cluster is selected to be the transmitting UE. Note that the active UEs from other clusters will cause interference. Since the links between the typical UAV and the interfering UEs can also be LOS or NLOS, and at most one UE from one cluster inflicts interference, UE can be divided into groups of UEs with LOS and NLOS links, and these groups form PPPs Φ_{user}^L and Φ_{user}^N with densities $\lambda_{user}^L = p_{active}p_U^L\lambda_U$ and $\lambda_{user}^N = p_{active}p_U^N\lambda_U$, respectively. Therefore, the experienced SINR at the typical UAV can be expressed as

$$\text{SINR}^{UL} = \frac{P_t^{UL}G_0h_0(k_U^s r_0^{\alpha_U^s})^{-1}}{\sigma_n^2 + \sum_b \sum_{i \in \Phi_{user}^b} P_t^{UL}G_i h_i(\kappa_U^b r_i^{\alpha_U^b})^{-1}}. \quad (7.32)$$

where $b \in \{\text{LOS}, \text{NLOS}\}$. The uplink SINR coverage probability, given the serving UE is in active mode, can be expressed as

$$P_{SINR}^{UL}(\gamma^{UL}) = \mathbb{P}(\text{SINR}^{UL} \geq \gamma^{UL} | \text{active}). \quad (7.33)$$

Theorem 7.3. *Given that the serving UE is in active mode, then the uplink SINR coverage probability of the network can be expressed as*

$$P_{SINR}^{UL}(\gamma_{UL}) = \sum_{n=0}^{N_s} (-1)^{n+1} \binom{N_s}{n} \int_H^\infty e^{-\mu_s^{UL} \sigma_n^2} \mathcal{L}_{I_{user}^L}(\mu_s^{UL}) \mathcal{L}_{I_{user}^N}(\mu_s^{UL}) f_{R_0^s}(r_0) dr_0 \quad (7.34)$$

where $\mu_s^{UL} = \frac{n\eta_s\gamma^{UL}r_0^{\alpha_U^s}}{P_t^{UL}G_0k_U^s}$. $\mathcal{L}_{I_{user}^b}(\mu_s^{UL})$ is the Laplace transform expression which can be expressed as follows:

$$\mathcal{L}_{I_{user}^b}(\mu_s^{UL}) = \prod_G e^{-2\pi p_G \lambda_{user}^b \int_0^\infty \left(1 - \int_0^\infty \left(1 + \mu_s^{UL} P_t^{UL} G_i(\kappa_U^b (v^2 + H^2)^{\frac{\alpha_U^b}{2}} N_b)^{-1}\right)^{-N_b} f(v|w) dv\right) w dw} \quad (7.35)$$

Proof: See Appendix 22.

Remark 7.5. If the small-scale fading h_i of the interfering links are assumed to be Rayleigh distributed, i.e., $N_b = 1$, by utilizing the Rician property $\int_0^\infty f(v|w) w dw = v$ (when Thomas cluster processes are considered), the Laplace transform can be expressed as

$$\mathcal{L}_{I_{user}^b}(\mu_s^{UL}) = \prod_G \exp \left(-2\pi \int_0^\infty \frac{p_G \lambda_{user}^b}{1 + (\mu_s^{UL} P_t^{UL} G)^{-1} \kappa_U^b (v^2 + H^2)^{\frac{\alpha_U^b}{2}}} v dv \right). \quad (7.36)$$

7.5.2 Average Throughput

The average uplink throughput of the network can be expressed as

$$\begin{aligned} R^{UL} &= \mathbb{E} [(T - \tau) W \log(1 + \gamma^{UL}) \mathbb{1}(\text{SINR}^{UL} \geq \gamma^{UL}) p_{active}] \\ &= (T - \tau) W \log(1 + \gamma^{UL}) P_{SINR}^{UL}(\gamma^{UL}) p_{active} \end{aligned} \quad (7.37)$$

where W is the bandwidth of each channel. It is also worth noting that p_{active} is related to the energy coverage probability in the downlink phase, and therefore the average uplink throughput has dependence also on the downlink phase. With this, we formulate the following optimization problem to maximize R^{UL} subject to a lower bound constraint on the downlink throughput

$$\begin{aligned} \max_{\tau} \quad & (T - \tau) W \log(1 + \gamma^{UL}) P_{SINR}^{UL}(\gamma^{UL}) p_{active} \\ \text{s.t.} \quad & R^{DL} \geq R_{\min} \end{aligned} \quad (7.38)$$

where $R^{DL} = \tau W \log(1 + \gamma^{UL}) P_{SINR}(\gamma_{sinr})$ is the average downlink throughput, R_{\min} is the minimum average throughput requirement for the downlink transmission. We numerically solve this problem in the Section VIII.

7.6 Generalizations and Special Cases

While we have assumed in the previous sections that the UAVs fly at the same height, our analysis and approach are relatively broad. To demonstrate this, we extend our analysis to a multi-tier multi-height model in this section. Additionally, we address the special case of the noise-limited network and derive closed-form characterizations with practical implications.

7.6.1 Multi-Tier Multi-Height Model

In practice, UAVs can fly at different heights depending on the applications and regulations. For instance, UAV heights may differ in urban areas with high-rise buildings compared to suburban environments. With this motivation, we consider a multi-tier multi-height model, in which we have multiple tiers of UAVs and UAVs in the j^{th} tier are distinguished with their density λ_j , transmit power P_j , biasing factor B_j and height H_j . Next, we discuss how our previous analysis can be adapted to this model.

Suppose we have $\mathcal{K}_U = \{1, 2, \dots, K\}$ tiers of UAVs. Then we introduce two notations: $\mathcal{K}_G = \{GBS\} \cup \mathcal{K}_U$ and $\mathcal{K} = \{0\} \cup \{GBS\} \cup \mathcal{K}_U$. Since we still use the same downlink association criterion, the received power can be re-expressed as

$$P_m = \operatorname{argmin}_{j \in \mathcal{K}, s} P_j G_0 B_j (\kappa_j^s (r_j^s)^{\alpha_j^s}). \quad (7.39)$$

Now, the probability that the typical UE is associated with a LOS/NLOS BS in the j^{th} tier can be modified from (7.13) as

$$A_{j,s} =$$

$$\begin{cases} \mathbb{E}_{R_0^s} \left[D_0^s \prod_{k \in \mathcal{K}_G} \prod_b D_k^b \overline{F}_{R_k^b} (Q_{k0}^{sb}(r_0)) \right], & \text{for } j = 0, \\ D_j^s \mathbb{E}_{R_j^s} \left[D_j^{s'} \overline{F}_{R_j^{s'}} (Q_{jj}^{ss'}(r_j)) \left(\sum_b D_0^b \overline{F}_{R_0^b} (Q_{0j}^{sb}(r_j)) \right) \prod_{\substack{k \in \mathcal{K}_G \\ k \neq j}} \prod_b D_k^b \overline{F}_{R_k^b} (Q_{kj}^{sb}(r_j)) \right], & \text{for } j \in \mathcal{K}_1. \end{cases} \quad (7.40)$$

Similarly, the energy coverage, SINR coverage and the successful transmission probabilities can be modified from (7.22), (7.25) and (7.28), respectively, by letting $k \in \mathcal{K}_G$. The CCDFs and PDFs of the distances remain the same.

7.6.2 Noise-Limited Model

In this subsection, we investigate the network performance metrics when the interference is negligible. When interference $I \approx 0$, the energy coverage and SINR coverage probabilities can be simplified by removing the Laplace transform terms in (7.22) and (7.25), respectively. With this, the STP specializes to

$$\begin{aligned} P_{ST_{j,s}}^c(\rho, \tau, \gamma_E, \gamma_{sinr}) = \\ P_{E_{j,s}}^c(\rho, \tau, \gamma_E) \mathbb{1}(F(\rho, \tau, \gamma_E, \gamma_{sinr}) \geq 0) + P_{SINR_{j,s}}^c \mathbb{1}(F(\rho, \tau, \gamma_E, \gamma_{sinr}) < 0) \end{aligned} \quad (7.41)$$

where $F(\rho, \tau, \gamma_E, \gamma_{sinr}) = \frac{\gamma_E}{\tau(1-\rho)} - \gamma_{sinr} \left(\frac{\sigma_c^2}{\rho} + \sigma_n^2 \right)$. The partial derivative of F with respect to ρ can be expressed as

$$\frac{\partial F}{\partial \rho} = \frac{\gamma_E}{\tau(1-\rho)^2} + \frac{\gamma_{sinr} \sigma_c^2}{\rho^2} > 0. \quad (7.42)$$

Hence F is a monotonically increasing function of ρ . Therefore, depending on the values of τ , γ_E and γ_{sinr} , there are three cases: 1) if $F_{\max} < 0$, $P_{ST_{j,s}}^c = P_{SINR_{j,s}}^c$; 2) if $F_{\min} > 0$, $P_{ST_{j,s}}^c = P_{E_{j,s}}^c$; 3) if $F_{\max} > 0$ and $F_{\min} < 0$, then in region of $F < 0$ we have $P_{ST_{j,s}}^c = P_{SINR_{j,s}}^c$, which is a

monotonically increasing function of ρ , while in region of $F > 0$ we have $P_{ST_{j,s}}^c = P_{E_{j,s}}^c$, which is a monotonically decreasing function of ρ , therefore, with increasing ρ , $P_{ST_{j,s}}^c$ first increases then decreases, and $F = 0$ gives the maximum of $P_{ST_{j,s}}^c$, i.e. when

$$\rho^* = \frac{-(\gamma_E + \tau\gamma_{sinr}\sigma_c^2 - \tau\gamma_{sinr}\sigma_n^2) + \sqrt{(\gamma_E + \tau\gamma_{sinr}\sigma_c^2 - \tau\gamma_{sinr}\sigma_n^2)^2 - 4\tau^2\gamma_{sinr}^2\sigma_c^2\sigma_n^2}}{2\tau\gamma_{sinr}\sigma_n^2}. \quad (7.43)$$

When we further assume that the uplink between the typical UAV and its cluster member UE is in LOS, and the path-loss exponent is $\alpha_U^L = 2$ and the small-scale fading is Rayleigh fading, the uplink SNR coverage probability admits the following simpler expression:

$$P_{SINR}^{UL}(\gamma^{UL}) = \begin{cases} \frac{e^{-C'H^2}}{1+2C'\sigma^2} & \text{for Thomas cluster process,} \\ \frac{e^{-C'H^2}}{C'R_c^2} (1 - e^{-C'R_c^2}) & \text{for Matérn cluster process,} \end{cases} \quad (7.44)$$

where $C' = \frac{\gamma^{UL}\sigma_n^2}{P_t^{UL}G_0k_U^L}$.

7.7 Extensions to UAV-assisted IoT Networks with 3D Antenna Patterns

The analysis can be extended to consider 3D antenna patterns in the downlink transmission.

7.7.1 3D Antenna Pattern

We adopt a doughnut-shaped antenna radiation pattern, using an ultra-wideband transmitter at the UAV. The antenna gain at the UAV can be expressed as in (2.27). 3D antenna pattern are adopted at the GBSs as in (2.25). Similarly as in [102], we assume $G_m = \infty$ and $G_H(\phi) = 0$ dB to simplify the analysis. Then, we can rewrite the 3D antenna gain as

$$G_G(r) = G_G^0 - G_V(\theta_G)(\text{dB}) = G_G^0 10^{-1.2\left(\frac{\theta_G - \theta_{\text{tilt}}}{\theta_{3\text{dB}}}\right)^2}$$

$$= G_G^0 10^{-1.2 \left(\frac{\arcsin(H/r) - \theta_{\text{etilt}}}{\theta_{3dB}} \right)^2}. \quad (7.45)$$

7.7.2 Association analysis

With the 3D antenna patterns, the association probability are modified in the following Lemma.

Lemma 7.3. *The probability that the typical UE is associated with a LOS/NLOS BS in the j^{th} tier is given by*

$$A_{j,s} = \begin{cases} \mathbb{E}_{R_0^s} \left[D_0^s \prod_b D_U^b \bar{F}_{R_U^b} (Q^{sb}(r_0)) D_G^b F_{20}^{sb}(r_0) \right], & \text{for } j = 0, \\ \mathbb{E}_{R_U^s} \left[D_U^s D_U^{s'} \bar{F}_{R_U^{s'}} (Q^{ss'}(r_U)) \prod_b D_G^b F_{21}^{sb}(r_U) \left(\sum_b D_0^b \bar{F}_{R_0^b} (Q^{sb}(r_U)) \right) \right], & \text{for } j = 1, \\ \mathbb{E}_{R_G^s} \left[D_G^s D_G^{s'} F_{22}^{ss'}(r_G) \left(\sum_b D_0^b F_{02}^{sb}(r_G) \right) \prod_b D_U^b F_{12}^{sb}(r_G) \right], & \text{for } j = 2, \end{cases} \quad (7.46)$$

where $s, s', b \in \{\text{LOS}, \text{NLOS}\}$, $s \neq s'$, $Q^{sb}(r) = \left(\frac{\kappa_U^s}{\kappa_U^b} r^{\alpha_U^s + 1} \right)^{\frac{1}{\alpha_U^b + 1}}$, D_j^s , $\bar{F}_{R_U^s}(x)$ and $\bar{F}_{R_G^s}(x)$ are given in Section III, $C_{kj}^{sb} = \frac{P_k B_k \kappa_j^s}{P_j B_j \kappa_k^b}$, G_k is the antenna gain of the BSs in the k^{th} tier, and

$$F_{kj}^{sb}(x) = \int_{H_k}^{\infty} f_{R_k^b}(t) \mathbb{1} \left(G_k^{-1}(t) t^{\alpha_k^b} > C_{kj}^{sb} G_j^{-1}(x) x^{\alpha_j^s} \right) dt. \quad (7.47)$$

Given that the typical UE is associated with a LOS/NLOS BS in the j^{th} tier, the PDFs of the distances are given as

$$\hat{f}_{R_j^s}(x) = \begin{cases} \frac{f_{R_0^s}(x)}{A_{0,s}} D_0^s \prod_b D_U^b \bar{F}_{R_U^b} (Q^{sb}(r_0)) D_G^b F_{20}^{sb}(r_0), & \text{for } j = 0, \\ \frac{f_{R_U^s}(x)}{A_{1,s}} D_U^s D_U^{s'} \bar{F}_{R_U^{s'}} (Q^{ss'}(r_U)) \prod_b D_G^b F_{21}^{sb}(r_U) \left(\sum_b D_0^b \bar{F}_{R_0^b} (Q^{sb}(r_U)) \right), & \text{for } j = 1, \\ \frac{f_{R_G^s}(x)}{A_{2,s}} D_G^s D_G^{s'} F_{22}^{ss'}(r_G) \left(\sum_b D_0^b F_{02}^{sb}(r_G) \right) \prod_b D_U^b F_{12}^{sb}(r_G), & \text{for } j = 2. \end{cases} \quad (7.48)$$

7.7.3 Successful Transmission Probability

The analysis of the energy and SINR coverage probabilities of the proposed system and the successful transmission probability are similar as in (7.4).

7.8 Numerical Results

In this section, we provide numerical results to evaluate the performance of the considered UAV-assisted mmWave cellular network and identify the impact of key network parameters on the performance. Unless stated otherwise, the parameter values are listed in Table 7.2.

Table 7.2: Table of Parameter Values

Notations	Description
P_u, P_G, P_t^{UL}	24 dBm [23], 34 dBm, 1 dBm
λ_U, λ_G	$10^{-4} / \text{m}^2, 10^{-5} / \text{m}^2$
H, C, B	50 m, 11.95, 0.136 [23] [196]
$\kappa_j^L, \kappa_j^N, \alpha_j^L, \alpha_j^N$	$10^{3.08}, 10^{0.27}, 2.09, 3.75$ [23] [196]
$1/\beta$	141.4 [160] [197]
Carrier frequency, W	28 GHz, 100 MHz [160] [197]
σ_n^2, σ_c^2	-174 dBm/Hz+ $10\log_{10}(W)$ +10 dB, -80 dB [160] [197]
N_L, N_N	2, 3
T	1 s

7.8.1 Impact of the Cluster Size

First we investigate the influence of the cluster size on the network performance. The cluster size here is the spatial size of the cluster. More specifically, for the Thomas cluster process, 68.27% of UEs are located inside a circular region with radius σ , and 95.45% of UEs are located inside a circular region with radius 2σ , and we choose σ as the cluster size. For Matérn cluster process, R_c is the cluster size.

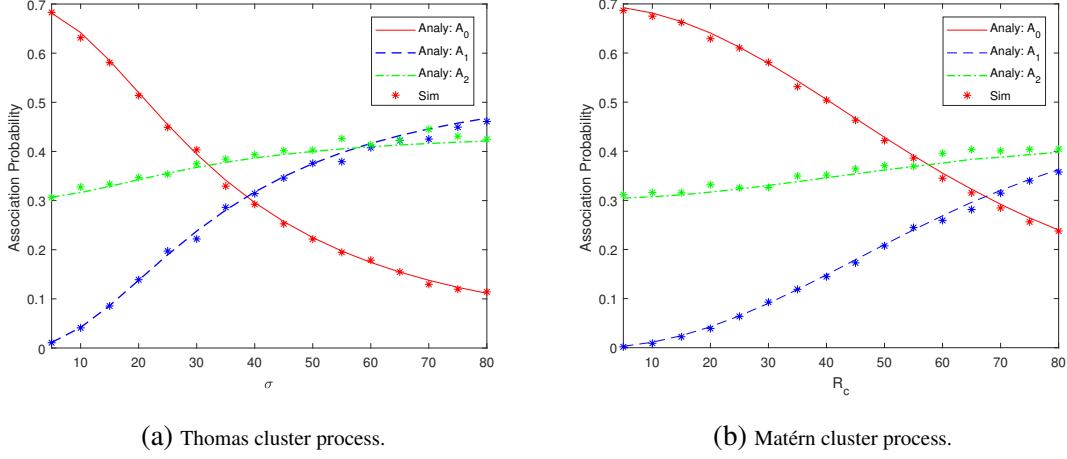


Fig. 7.3: Association probability as functions of the cluster size with parameter values listed in Table 7.2.

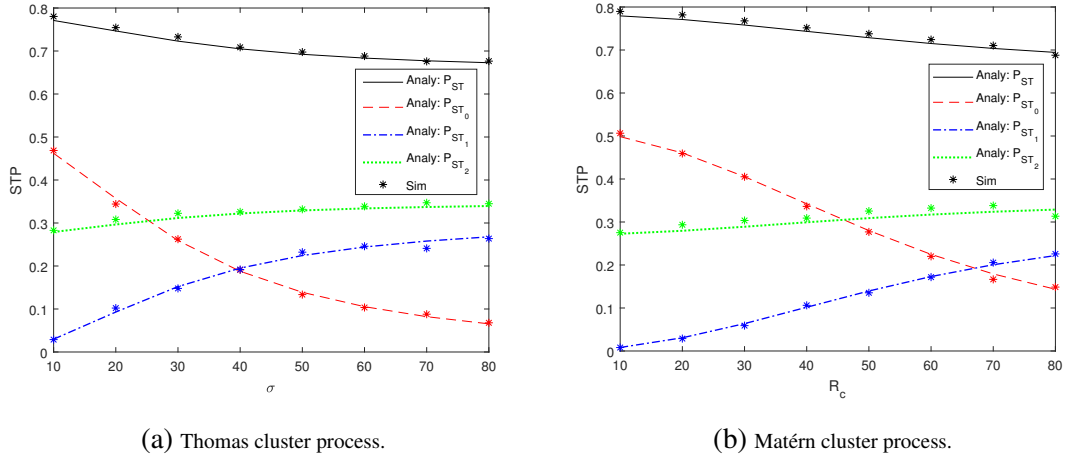


Fig. 7.4: STP of the network and each tier BSs as a function of the cluster size when $\tau = T$, $\gamma_E = -40$ dB, $\gamma_{sinr} = 0$ dB and $\rho = 0.5$.

Downlink Association Probability

Fig. 7.3 shows the association probability (AP) as a function of the cluster size in the downlink phase. As shown in the figure, when we increase σ and R_c , A_0 decreases while A_1 and A_2 increase. As σ and R_c increase, the UEs move further away from the projection of the cluster center UAV and hence are more spread away. As a result, the UEs move closer to other UAVs and GBSs. Therefore, A_0 decreases. On the other hand, because of the LOS probability function, the link between the UE and the UAVs are more likely to be LOS, and consequently the UEs prefer to be served by UAVs with higher probability. For this reason, A_1 increases faster than A_2 . We also

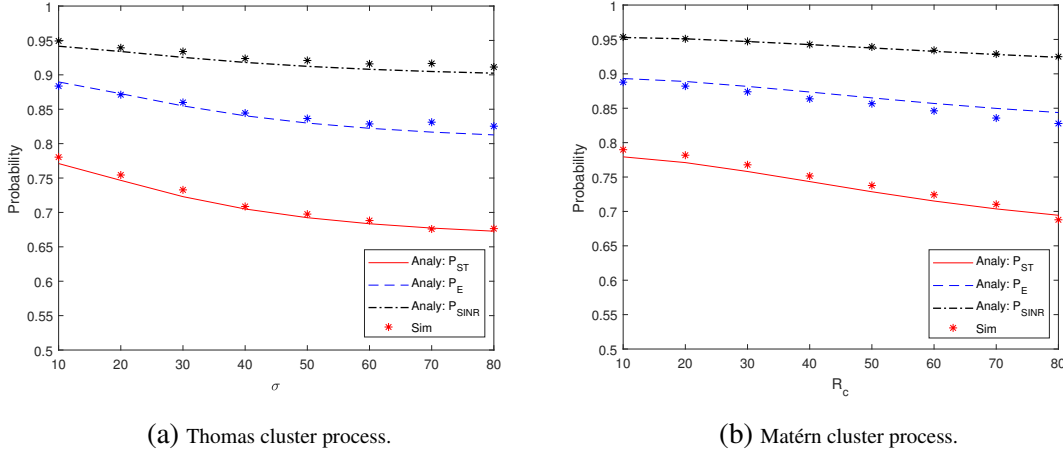


Fig. 7.5: STP, EC and SINRC probabilities as functions of the cluster size when $\tau = T$, $\gamma_E = -40$ dB, $\gamma_{sinr} = 0$ dB. And $\rho = 0.5$ for the SWIPT scenario.

note that in Fig. 7.3 (and in the subsequent figures in this section), simulation results are plotted with * markers and we generally observe excellent agreements with the analytical results, further confirming, for instance, our characterizations in Lemma 7.2 in this case.

Downlink Coverage Probabilities

Fig. 7.4 shows the successful transmission probability (STP) as a function of the cluster size. Since the STP, energy coverage (EC), SINRC coverage (SINRC) performances of each tier BS are similar, we evaluate the STP performance of each tier in the figure. In this figure, total STP decreases with increasing σ and R_c . As expected, when σ and R_c become larger, P_{ST_0} (i.e., the successful transition probability in tier 0) diminishes while P_{ST_1} and P_{ST_2} increase. However, since the cluster center UAV can provide the maximum conditional coverage, the increase in P_{ST_1} and P_{ST_2} is not able to compensate the decrease in P_{ST_0} , leading to the decrease in total STP.

In Fig. 7.5, we observe that STP, EC and SINRC are all monotonically decreasing functions of σ and R_c . Additionally, we note that since we consider the SWIPT scenario with $\rho = 0.5$, we divide the received power of the typical UE into two streams, one for energy harvesting and the other for information decoding. Due to this, the STP performance is lower compared to only EC or SINRC, where it is assumed that entire received power is used for energy harvesting or information

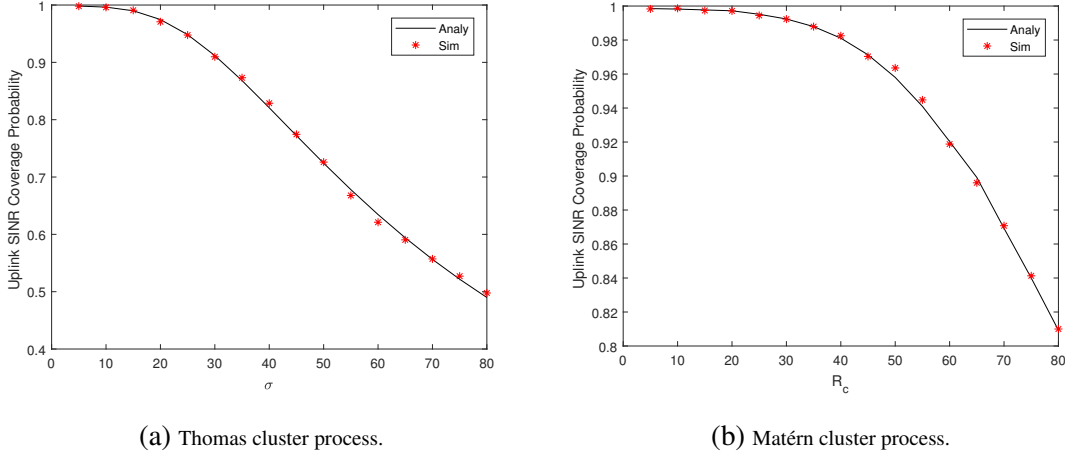


Fig. 7.6: Uplink SINR coverage probability as a function of the cluster size when $\tau = 0.5T$, $\rho = 0$, $\gamma^{UL} = -20\text{dB}$, and $\sigma = 10$.

decoding only.

Uplink Coverage Probability

We observe from Fig. 7.6 that the uplink SINRC is a monotonically decreasing function of the cluster size, similarly as in the downlink phase. When compared with the downlink SINRC (blue dashed line) in Fig. 7.5, we notice in Fig. 7.6 that the uplink SINRC drops faster than the downlink SINRC for larger thresholds. This is due to the different association criteria in different phases. In the downlink phase, because of the strongest long-term averaged received power association criterion, when the UEs are more spread away from their cluster center UAVs, they can get associated with other UAVs and GBSs to get the strongest received power. But in the uplink phase, UAVs are receiving information from their cluster member UEs, and therefore when the UEs are far away, the uplink SINRC decreases substantially.

Again, we note that simulation results are also provided in all the figures using markers, and these results match with the analytical results, further validating the accuracy of our coverage analysis. Additionally, we observe in the numerical results that Thomas cluster processes and Matérn cluster processes generally lead to similar network performance trends, which gives us the insight that considering PCP rather than PPP is the key to capture the UE distribution. Therefore,

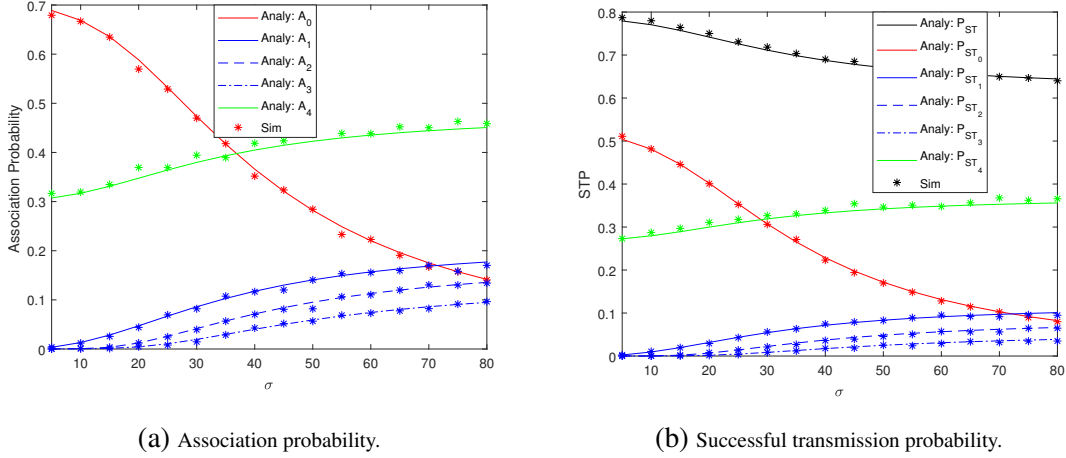


Fig. 7.7: Association probability and STP as a function of σ for Thomas cluster process, when $\gamma_E = -40$ dB, $\gamma_{sinr} = 0$ dB, $\rho = 0.5$ and heights for 0^{th} - 3^{rd} tier UAVs are 50m, 50m, 60m, and 70m, respectively. The GBS is regarded as the 4^{th} tier.

for brevity, we will just provide numerical results considering Thomas cluster processes in the following subsections.

Multi-Tier Multi-Height Model

In this part, we assume there are three tiers of UAVs with heights 50m, 60m, and 70m, respectively, and density $3 \times 10^{-5}/\text{m}^2$. And all UAVs have their own clustered UEs on the ground. There is a tier of GBSs with parameter values listed in Table III. We randomly choose a UE from a cluster of the 50m-high UAVs, and provide the association probability and STP in Figs. 7.7(a) and 7.7(b), respectively. In Fig. 7.7(a), we observe that the association probability of the GBS does not change much when compared with the one-tier UAV model. And as σ increases, the association probabilities of 1^{st} , 2^{nd} and 3^{rd} tier UAVs increase. Fig. 7.7(b) shows the similar performance levels as in Fig. 7.4. And the STP of the 1^{st} , 2^{nd} and 3^{rd} all increase with increasing σ .

7.8.2 Impact of the Interference

In this section, we investigate the impact of the interference. In Fig. 7.8, we plot the EC, coverage probability and STP as a function of the threshold in the downlink phase. Since the GBSs with

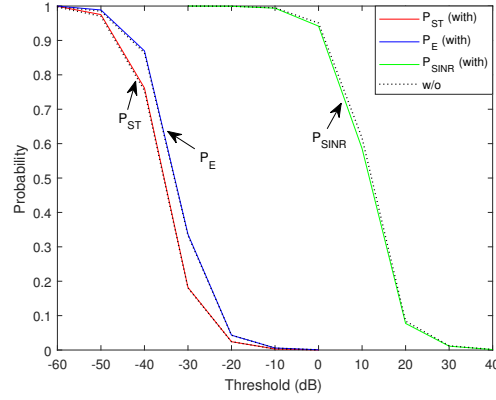


Fig. 7.8: STP, EC and SINRC as a function of the threshold when $\sigma = 10$, $\tau = T$ and $\rho = 0.5$ for the SWIPT scenario.

large transmit power are relatively far from the typical UE and the UAVs which are relatively denser and closer but with low transmit power, the interference is negligible. Thus the interference has little impact on the uplink SINRC. Therefore, as expected the interference does not lead to a significant difference on the probabilities. In the uplink phase, the interference from the UEs is small and has unnoticeable impact on the uplink SINRC.

7.8.3 Impact of the UAV Height

In this subsection, we investigate the impact of the UAV height on the network performance.

Downlink Association Probability

Fig. 7.9 depicts the AP of each tier BS as a function of H . When $H = 0$, the UAVs are located on the ground. Since the UAVs are more densely distributed than the GBSs, we have $A_0 > A_2 > A_1$. Also because p_U^L is a monotonically increasing function of H , the LOS probability of UAVs increases with increasing H . Therefore, as H becomes slightly larger, AP with the cluster center UAV, A_0 , and AP with other UAVs, A_1 , increase while AP with GBSs, A_2 , decreases. On the other hand, when we increase H substantially (e.g., beyond approximately 20m), the UAVs start being high above the sky. Therefore, even though the LOS probabilities have grown, the distances between the UAVs and UEs have increased as well (increasing the path loss), while the distance

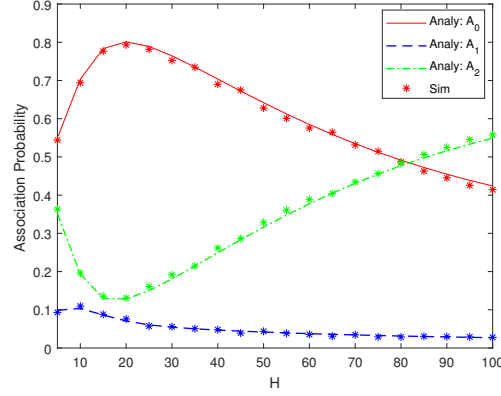


Fig. 7.9: Association probability as a function of the UAV height with parameter values listed in Table 7.2.

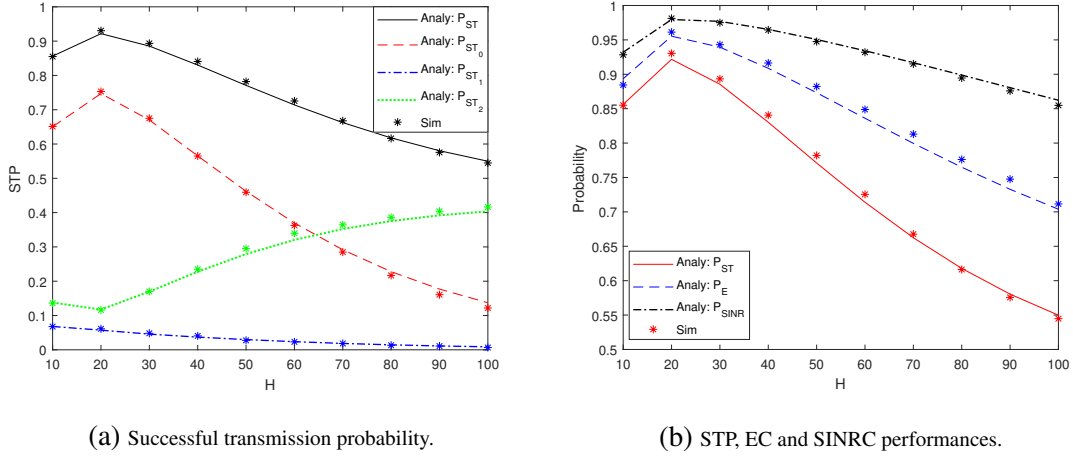


Fig. 7.10: STP, EC and SINRC as functions of the UAV height H when $\sigma = 10$, $\tau = T$, $\gamma_E = -40$ dB, $\gamma_{sinr} = 0$ dB. And $\rho = 0.5$ for the SWIPT scenario.

between the UEs and GBSs have not changed. Due to this, we observe that A_0 and A_1 decrease whereas A_2 starts increasing.

Downlink Coverage Probabilities

The STP performance curves of each tier BS shown in Fig. 7.10(a) demonstrate the same trends as the association probability in Fig. 7.9. In addition, the total STP initially grows, achieves its maximum around $H \approx 20$ m, and then decreases because of the increased distance between the UEs and UAVs when the UAV height H becomes larger. At these larger height levels, the increase in P_{ST_2} cannot compensate the decrease in P_{ST_0} and P_{ST_1} . Fig. 7.10(b) shows that the EC and

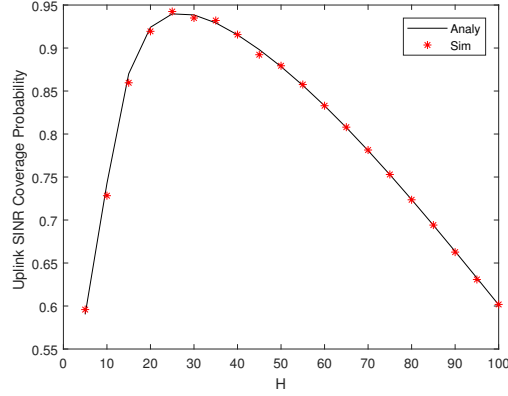


Fig. 7.11: Uplink SINR coverage probability as a function of the UAV height, when $\tau = 0.5T$, $\rho = 0$, $\gamma^{UL} = -20$ dB, and $\sigma = 10$.

SINRC performances follow the same trends as for STP.

Uplink Coverage Probability

In the uplink phase, the UAVs are receiving data from their cluster member UEs. When UAVs are at relatively lower height, the transmission are NLOS with high probability because of the blockage from buildings and other large objects. Since the blockage becomes less when we increase the UAV height, the SINRC increases. However, above a certain height, the distance between the UAV and the serving UEs becomes large enough that the path loss starts dominating and as a result, SINRC diminishes. Therefore, as shown in Fig. 7.11, SINRC increases at first and then decreases, and there exists an optimal height, which is not the same but very close to the optimal height in the downlink phase.

7.8.4 Impact of the Power Splitting Component

In this subsection, we investigate the impact of the power splitting parameter ρ on the network performance. From Fig. 7.12, we can conclude that EC is a monotonically decreasing function of ρ and SINRC is an increasing function of ρ , due to the facts that larger ρ means that more power is used for harvesting energy and less power for information decoding. Using the given set of parameter values, we observe that there exists an optimal ρ value that maximizes the system

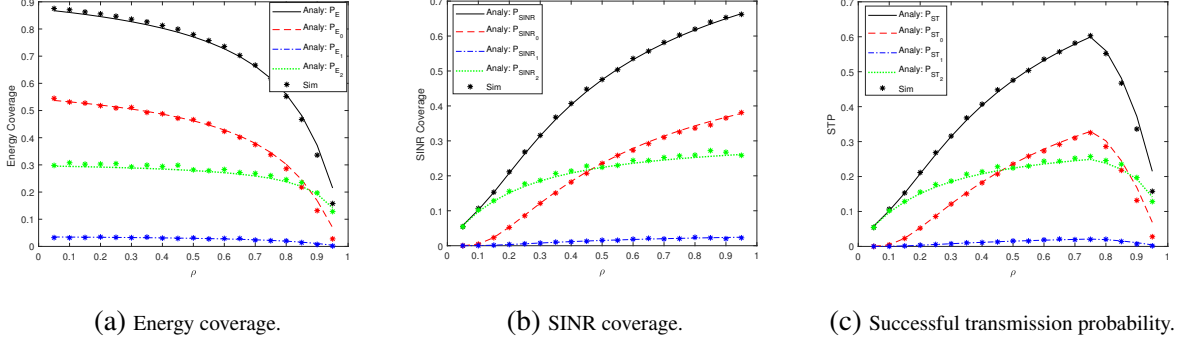


Fig. 7.12: STP, EC and SINRC as functions of the power splitting parameter ρ when $\sigma = 10$, $\tau = T$, $\gamma_E = -40$ dB, $\gamma_{sinr} = -15$ dB. To show the impact of ρ , we use $\sigma_c = -10$ dB in this figure .

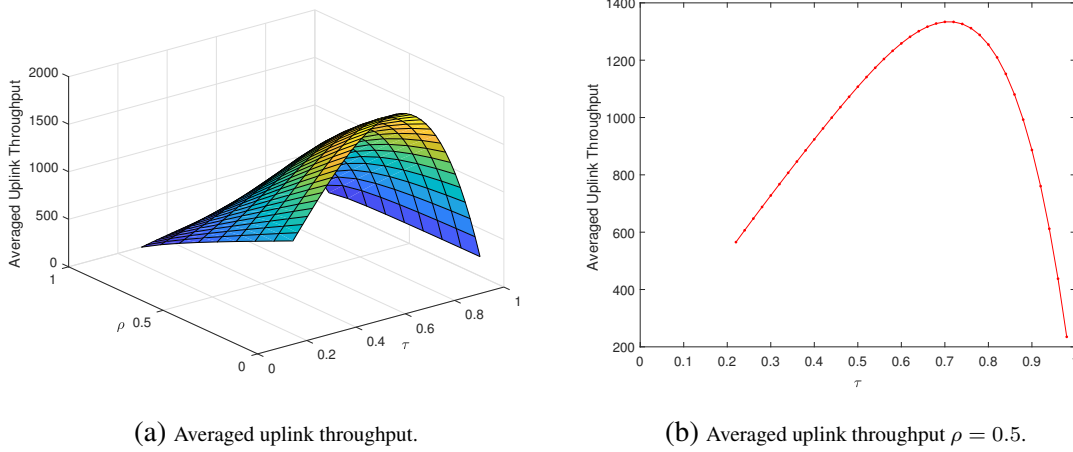


Fig. 7.13: Averaged uplink throughput as a function of τ and ρ for Thomas cluster process, when $\gamma_E = -40$ dB, $\gamma_{sinr} = 0$ dB, $\gamma^{UL} = -20$ dB, and $\sigma = 10$.

downlink performance. Since in this model, the interference is negligible, we can use (7.43) to approximately find the optimal value of ρ . By substituting the parameter values provided in (7.43), we obtain $\rho = 0.7603$ and this is consistent with what we have from the numerical result.

7.8.5 Impact of the τ

In this section, we investigate the effect of the time duration τ allocated to the downlink phase. Fig. 7.13 shows the average uplink throughput as a function of τ and ρ under the constraint that the average downlink throughput R^{DL} is larger than R_{\min} (addressing the optimization problem in (7.38)). As shown in Fig. 7.13(a), R^{UL} decreases with increasing ρ , since larger ρ means less

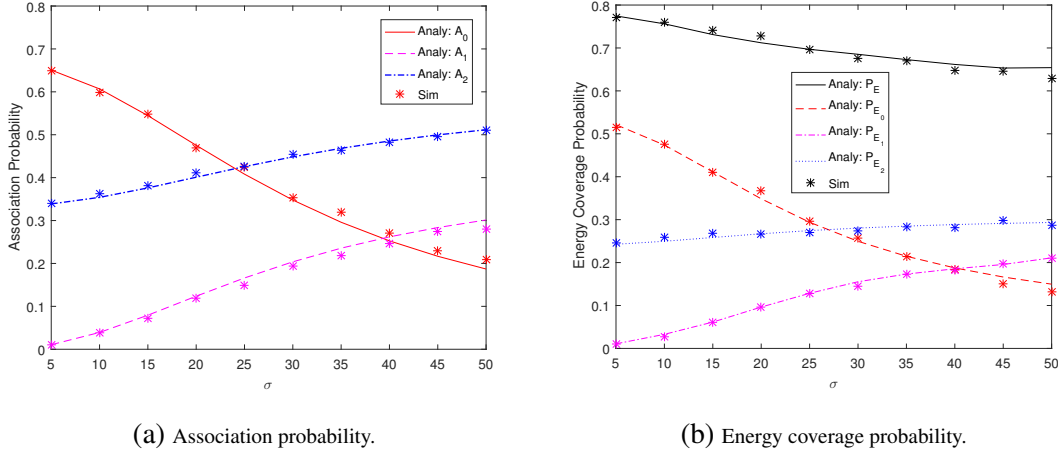


Fig. 7.14: AP, EC as a function of cluster size σ , when $H = 50\text{m}$, $\gamma_E = -80\text{ dB}$ and $\gamma_{\text{sinr}} = -40\text{ dB}$.

power for energy harvesting. On the other hand, since R^{DL} is a monotonically increasing function of τ , if we want to satisfy the minimum throughput requirement, there is a minimum value of τ . Therefore, as shown in Figs. 7.13 (a) and (b), when τ is smaller than a certain value, the minimum downlink throughput constraint cannot be satisfied and the optimization problem in (7.38) is not feasible. When τ increases, the downlink constraint is satisfied, and we note that there is an optimal τ that maximizes the average uplink throughput.

7.8.6 Numerical Results when Considering 3D Antenna Patterns

First, we investigate the impact of the cluster size σ on the network performance with 3D antenna patterns. Fig. 7.14(a) shows the AP as a function of the cluster size, i.e., the standard deviation of the UE distribution in Thomas cluster processes. As shown in the figure, when σ becomes larger, the A_0 (i.e. the AP of the cluster center UAV) decreases while A_1 and A_2 increase. This is because that, as σ increases, the UEs move further away from the projection of the cluster center UAV and hence are more spread away. As a result, the UEs move closer to other UAVs and GBSs.

Fig. 7.14(b) shows the EC probability as a function of the cluster size. In the figure, total EC decreases with increasing σ . As expected, when σ becomes larger, P_{E_0} diminishes while P_{E_1} and P_{E_2} increase. However, since the cluster center UAV generally provides the maximum conditional coverage, the increase in P_{E_1} and P_{E_2} is not able to compensate the decrease in P_{E_0} , leading to

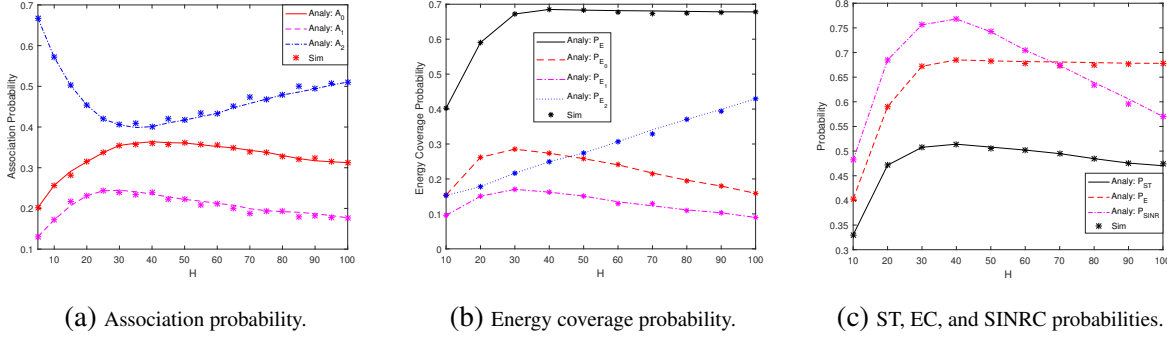


Fig. 7.15: AP, EC and SINRC as a function of UAV height H , when $\sigma = 30$, $\gamma_E = -80$ dB and $\gamma_{sinr} = -40$ dB.

the decrease in total EC. We finally note that the simulation results are depicted by markers * in Fig. 4. The generally excellent agreements with the dashed and dotted curves obtained using our analytical characterizations in the paper further confirm our analysis and theoretical results.

Then, we investigate the impact of the UAV height H on the network performance with 3D antenna patterns. Fig. 7.15(a) depicts the association probability of each tier BS as a function of the UAV height H . When H is small, the UAVs are located close to the ground. Since $\sigma = 30$, i.e. the UEs are spread away, the links between UAVs and UEs are more likely to be in NLOS. Also note that the GBS transmission power is larger than that of the UAVs. Therefore, we have $A_2 > A_0 > A_1$. We further note that since p_U^L is a monotonically increasing function of H , the LOS probability of UAVs increases with increasing H . Therefore as H becomes larger, A_0 and A_1 increase while A_2 decreases. In addition, when we slightly increase H , the link to the cluster center UAV is LOS with higher probability, while the link to other UAVs is more likely to be NLOS because the signal can be obstructed by buildings. Consequently, A_0 tends to be greater than A_1 . When we increase H substantially, the UAVs are high above the sky and path loss becomes large between the UAVs and UEs, leading to decreasing A_0 and A_1 and an increasing A_2 .

The EC performance curves of each tier BS are shown in Fig. 7.15 (b). The total EC increases at the beginning due to the increase in P_{E_0} and P_{E_1} (which are the conditional energy coverage probabilities of cluster center UAV and other UAVs, respectively, multiplied with the corresponding association probability). As the height is further increased, both P_{E_0} and P_{E_1} start decreasing

while P_{E_2} keeps on increasing, following the performance in Fig. 7.15(a). However, because the increase in P_{E_2} just falls short of compensating the decrease in P_{ST_0} and P_{ST_2} , we have a slightly decreasing EC. Fig. 7.15(c) shows that the SINRC and STP follow similar performance trends as for EC. Additionally, we note that since we consider the SWIPT scenario with $\rho = 0.5$, we divide the received power of the typical UE into two streams, one for energy harvesting and the other for information decoding. Due to this, the STP performance is lower compared to only EC or SINRC, where it is assumed that entire received power is used for energy harvesting or information decoding only. Finally, we again observe excellent agreements between the analytical and simulation results.

CHAPTER 8

COVERAGE ANALYSIS FOR

CELLULAR-CONNECTED UAVS WITH 3D

ANTENNA PATTERNS

8.1 System Model

We consider a cellular network composed of GBSs and UAVs as the aerial UEs. The GBSs are randomly distributed according to a homogeneous PPP Φ with density λ . GBSs are assumed to have transmit power P_U and height H_G . Without loss of generality, a random UAV is chosen as the typical UAV, and is assumed to be located above the origin at altitude H_U .

8.1.1 Ground-to-Air Channel Model

Link between a UAV and a GBS can be either LOS or NLOS. The path loss model is formulated as

$$L_j^s(x) = \begin{cases} \kappa^L(H^2 + x^2)^{\alpha^L/2} & \text{w.p. } p^L(x) \\ \kappa^N(H^2 + x^2)^{\alpha^N/2} & \text{w.p. } p^N(x) = (1 - p^L(x)) \end{cases} \quad (8.1)$$

where $H = |H_U - H_G|$, x is the horizontal distance from the UAV to the GBS, α^L, α^N are the path loss exponents for LOS and NLOS links, respectively, κ^L, κ^N are the intercepts of the LOS and NLOS path loss formulas, respectively, and $p^L(x)$ is the probability that the link has a LOS transmission at distance x , and is given in (2.17).

In addition, we assume that all links experience independent Nakagami-m fading. Thus, the small-scale fading gain h follows a Gamma distribution $h \sim \Gamma(N_s, 1/N_s)$ where $s \in \{\text{LOS}, \text{NLOS}\}$, and N_s is the Nakagami fading parameter.

8.1.2 3D Antenna Patterns for GBSs/UAVs

3D antenna patterns are adopted for the GBSs and UAVs. For GBSs, the antenna gain can be formulated as in (2.25). When assuming $G_m = \infty$ and $G_H(\phi) = 0$ dB to simplify the analysis, 3D antenna gain can be rewrite as

$$G_G(r) = G_G^0 10^{-1.2 \left(\frac{\arcsin(H/r) - \theta_{etilt}}{\theta_{3dB}} \right)^2}. \quad (8.2)$$

For the UAVs, the antenna gain can be formulated as in (2.26) (2.27) (2.28) and (2.29). The antenna gain of the GBS-to-UAV link can be written as $G(x) = G_G(x)G_U(x)$.

8.2 SINR Coverage Analysis

In this section, we first provide the formulation of the distance from the UAV to GBSs. Then, we analyze the SINR coverage probability and provide general expressions.

8.2.1 SINR Coverage Probability

The SINR coverage probability P_C is defined as the probability that the SINR experienced at the typical UAV is larger than a threshold $\gamma > 0$. Then, we can derive P_C as follows:

$$\begin{aligned}
 P_C(\gamma) &= \mathbb{P}(\text{SINR} > \gamma) \\
 &= \mathbb{E}_{D_0} [\mathbb{P}(\text{SINR} > \gamma | D_0)] \\
 &= \mathbb{E}_{D_0} [\mathbb{P}(\text{SINR} > \gamma | D_0, \text{LOS}) D^{\text{LOS}} + \mathbb{P}(\text{SINR} > \gamma | D_0, \text{NLOS}) D^{\text{NLOS}}] \\
 &= \mathbb{E}_{D_0} [\mathbb{P}(\text{SINR} > \gamma | D_0, \text{LOS})] D^{\text{LOS}} + \mathbb{E}_{D_0} [\mathbb{P}(\text{SINR} > \gamma | D_0, \text{NLOS})] D^{\text{NLOS}} \\
 &= P_C^{\text{LOS}} D^{\text{LOS}} + P_C^{\text{NLOS}} D^{\text{NLOS}}
 \end{aligned} \tag{8.3}$$

where D^s is the probability that the UAV has at least one s -GBS around, P_C^s is the conditional coverage probability given D_0 and the link is in $s \in \{\text{LOS}, \text{NLOS}\}$ transmission, and can be formulated as follows:

$$\begin{aligned}
 P_C^s(\gamma) &= \mathbb{E}_{D_0} [\mathbb{P}(\text{SINR} > \gamma | D_0, \text{LOS})] = \mathbb{P} \left(\frac{PG_0 h_0 \kappa_s^{-1} (H^2 + d_0^2)^{-\frac{\alpha_s}{2}}}{\sigma_n^2 + I} > \gamma \right) \\
 &= \mathbb{E}_{D_0^s} \left[\mathbb{P} \left(h_0 > \frac{\gamma \kappa_s (H^2 + d_0^2)^{\frac{\alpha_s}{2}} (\sigma_n^2 + I)}{PG_0} \right) \right] \\
 &\stackrel{(a)}{=} \mathbb{E}_{D_0^s} \left[\sum_{n=1}^{N_s} (-1)^{n+1} \binom{N_s}{n} e^{-\mu_s \sigma_n^2} e^{-\mu_s I^L} e^{-\mu_s I^N} \right]
 \end{aligned} \tag{8.4}$$

where $\mu_s = \frac{n \eta_s \gamma \kappa_s (H^2 + d_0^2)^{\frac{\alpha_s}{2}}}{PG_0}$, $\eta_s = N_s (N_s!)^{-\frac{1}{N_s}}$ and

$$\begin{aligned}
 \mathcal{L}_{I^a}(\mu_s) &= E_{D_0^s} [e^{-\mu_s I^a}] \\
 &\stackrel{(b)}{=} e^{-2\pi \int_{d_0}^{\infty} \left(1 - E_{h_i} \left[\mu_s PG_i h_i \kappa_a^{-1} (H^2 + d_i^2)^{-\frac{\alpha_a}{2}} \right] \right) \lambda p^a(d_i) d_i dd_i} \\
 &= e^{-2\pi \int_{d_0}^{\infty} \left(1 - \left(1 + \mu_s PG_i \kappa_a^{-1} (H^2 + d_i^2)^{-\frac{\alpha_a}{2}} N_a^{-1} \right)^{-N_a} \right) \lambda p^a(d_i) d_i dd_i}
 \end{aligned} \tag{8.5}$$

where $a \in \{\text{LOS}, \text{NLOS}\}$, (a) is due to the use of the moment generating function of the Gamma random variable and the interfering GBSs being divided into two independent PPPs Φ_s with density λp^s for $s \in \{\text{LOS}, \text{NLOS}\}$, and (b) follows by computing the moment generating functional of a PPP.

8.3 Numerical Results

In this section, we evaluate the performance of the considered cellular-connected UAV network. We also use Monte Carlo simulations to validate the models and confirm the accuracy of the analysis. The simulation parameters are listed below in Table I.

Table 8.1: Table of Parameter Values

Parameters	Values
P, λ	43 dBm [168], 10 /km ²
H_U	50 m
H_G, a, b, c	32, 1, 6.581, 1 @suburban; 19, 1, 0.151, 1 @urban [95]
$\alpha^L, \alpha^N, \kappa^L, \kappa^N$	2.09, 3.75, 10 ^{4.11} , 10 ^{3.29} [190]
G_U^0, G_G^0	5 dB, 15 dB
$\theta_{\text{tilt}}, \theta_{3\text{dB}}, \psi_w$	15°, 10° [168], 15°
σ_n^2, N_L, N_N	-44 dB, 2, 3

The impact of the UAV altitude is depicted in Fig. 8.1. Overall, we first observe that there exists an optimal altitude H_U^{opt} for the UAV. This is because the antenna of the GBS is tilted down with θ_{tilt} , and when the elevation angle of the link between the UAV and the serving GBS $\theta = \theta_{\text{tilt}}$, the UAV receives the maximum antenna gain provided by the GBS, which is much larger than the interference. Thus, we have an optimal altitude for the UAV. In different environments (i.e. suburban, urban), since H_G is different, the H_U^{opt} is different. Second, when we compare Figs. 8.1(a) and 8.1(b), we observe that better SINR coverage can be achieved in a suburban environment than in the urban environment. This is due to the fact that in suburban environments more links are in LOS, which in turn leads to larger received power over the main link, and hence larger SINR levels. In addition, in Figs. 8.1(a) and 8.1(b), we compare the performances of different antenna

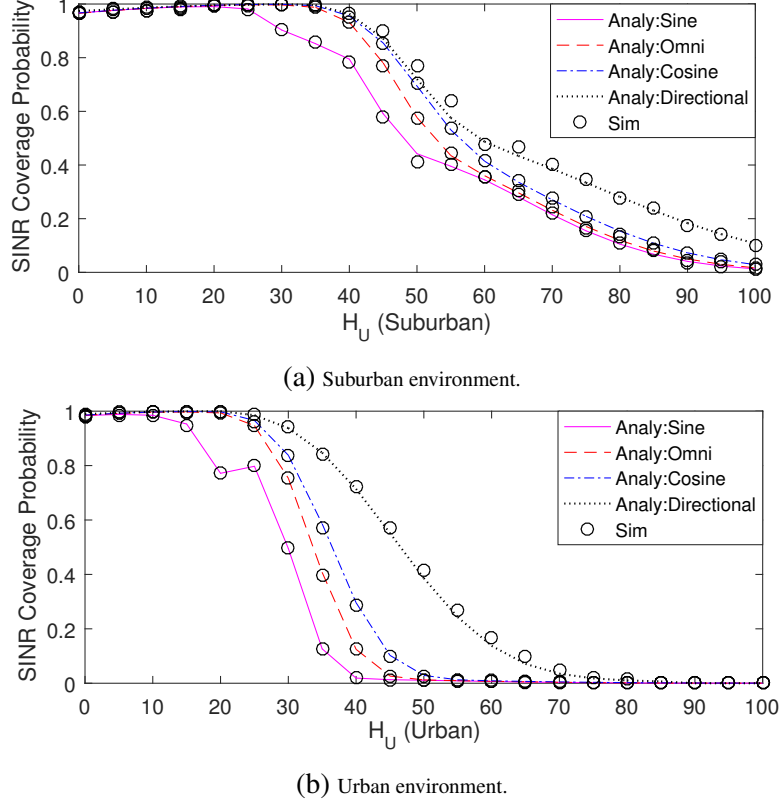


Fig. 8.1: SINR coverage probability as a function of the UAV altitude in a suburban and urban environments.

patterns. It is observed that the observed antenna pattern with tilting angle toward the serving GBS has the best performance, since this antenna pattern can provide the maximum antenna gain over the main link and narrow beamwidth can reduce the amount of interference. On the other hand, sine pattern results in the worst performance in this network.

Fig. 8.2 shows the influence of the tilting angle of the GBS. Since the UAV is higher than the GBSs, when θ_{tilt} becomes larger, the decrease in the antenna gain of the main link is larger than the decrease in the interference, and therefore, we have a diminishing SINR coverage probability. On the other hand, for the ground UEs, when $\theta_{tilt} = 0$, the antenna is not tilting down, and therefore the antenna gain for the ground UEs is small. When we increase θ_{tilt} , the ground UE experiences a higher antenna gain from the serving GBS, and as a result, the coverage probability increases accordingly. As we keep increasing θ_{tilt} further, the ground UE (unless it is very close to the GBS) experiences lower antenna gains and consequently, the SINR coverage probability of the ground

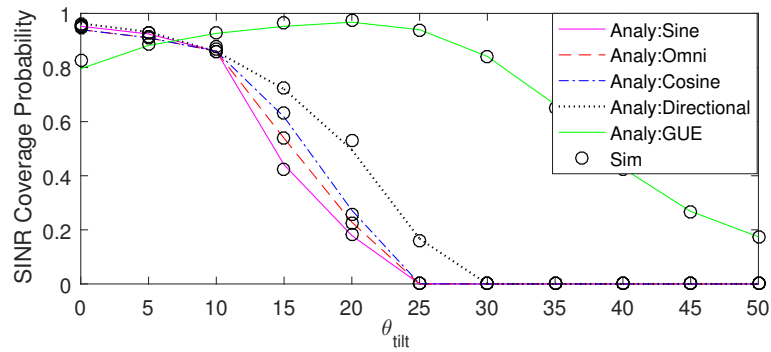


Fig. 8.2: SINR coverage probability as a function of the GBS tilting angle in degrees.

UE starts decreasing after reaching its peak value. We finally note that the simulation results (shown with circle-markers) have excellent agreements with the analytical results in both Figs. 8.1 and 8.2.

CHAPTER 9

LEARNING-BASED TRAJECTORY OPTIMIZATION FOR CELLULAR-CONNECTED UAVS

9.1 Learning-Base UAV Trajectory Optimization with Collision Avoidance and Connectivity Constraints

9.1.1 System Model

In this section, we introduce the system model of the multi-UAV and multi-GBS cellular networks in detail. Note that in this section, unless specified otherwise, we remove the time index e.g., in the position vector $\mathbf{p}(t) \rightarrow \mathbf{p}$, and the index for UAVs or GBSs, e.g., $\mathbf{p}_i \rightarrow \mathbf{p}$.

Deployment

We consider multi-UAV multi-GBS cellular networks as displayed in Fig. 9.1, in which J UAVs, with potentially different missions, need to fly from starting locations to destinations over an area containing K GBSs. Without loss of generality, we assume that the area of interest is a cubic

volume, which can be specified by $C : \mathcal{X} \times \mathcal{Y} \times \mathcal{Z}$ and $\mathcal{X} \triangleq [x_{\min}, x_{\max}]$, $\mathcal{Y} \triangleq [y_{\min}, y_{\max}]$, and $\mathcal{Z} \triangleq [z_{\min}, z_{\max}]$. Each UAV is modeled as disc-shaped with radius r . Let $\mathbf{p} = [p_x, p_y, H_V]$ denote the 3D position of the UAV, which is the center of the disc. H_V is the altitude of the UAVs which is assumed to be fixed for all UAVs. $\mathbf{p}^S = [p_{sx}, p_{sy}, H_V] \in \mathbb{R}^3$ and $\mathbf{p}^D = [p_{gx}, p_{gy}, H_V] \in \mathbb{R}^3$ are used to denote the coordinates of the starting points and destinations.

Each UAV's state is composed of an observable information vector and an unobservable (hidden) information vector, $\mathbf{s} = [\mathbf{s}^o, \mathbf{s}^h]$, where the observable state can be observed by other UAVs, while the unobservable state can not. In the global frame, observable state includes the UAV's position, velocity $\mathbf{v} = [v_x, v_y]$, and radius r , i.e., $\mathbf{s}^o = [\mathbf{p}, \mathbf{v}, r] \in \mathbb{R}^6$. The unobservable state consists of the destination \mathbf{p}^D , maximum speed v_{\max} , and orientation ϕ , i.e., $\mathbf{s}^h = [\mathbf{p}^D, v_{\max}, \phi] \in \mathbb{R}^5$. It is worth noting that the UAVs do not communicate with other UAVs. Hence, we address a more challenging non-communicating scenario.

In this cellular network, there are K GBSs providing wireless coverage simultaneously. The k^{th} GBS has transmit power P_{B_k} , and it is located at position $\mathbf{p}_{B_k} = [p_{x_{B_k}}, p_{y_{B_k}}, H_B]$, where H_B is the height of the GBS and is assumed to be the same for all GBSs.

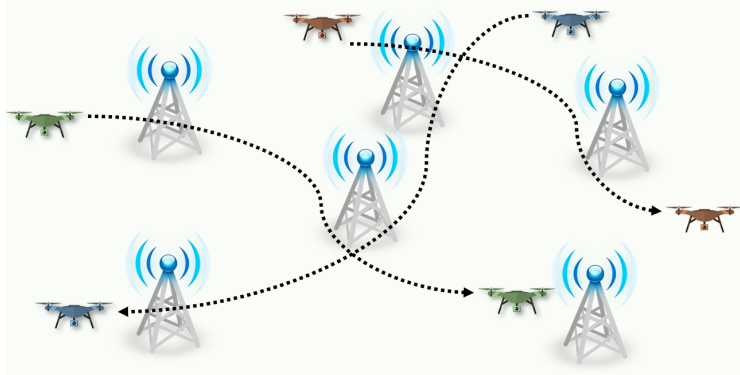


Fig. 9.1: An illustration of multi-UAV multi-GBS cellular networks.

Channel Modeling

For cellular-connected UAVs, due to high UAV altitude, UAV-to-GBS channels usually constitute strong LOS links, and LOS links are dominant [19, 198]. In addition, if the UAV altitude H_V

is greater than a threshold, 3GPP specifications suggest a LOS link with probability one. For example, in the 3GPP specifications in [199], the altitude threshold is suggested to be 40m for RMa (Rural Macro) deployment, and 100m for UMa (Urban Macro) deployment. Therefore, we assume that all links between the UAVs and GBSs are LOS. The path loss can be expressed as

$$L(d) = (d^2 + (H_B - H_V)^2)^{\alpha/2} \quad (9.1)$$

where α is the path loss exponent.

The 3D antenna gain at the GBSs and UAVs are modeled as 2.25 and 2.27, respectively. We assume that the antenna elements of the GBSs are only directional along the vertical dimension but omni-directional horizontally [19]. Therefore, the antenna gain can be expressed as [168]

$$G_B(d) = G_h + G_v \text{ (dB)} = 10^{-\min\left(-1.2\left(\frac{\arctan(\frac{H_B-H_V}{d})-\theta^{tilt}}{\theta^{3dB}}\right)^2, \frac{G_m}{10}\right)} \quad (9.2)$$

where

$$G_h = 0 \text{ (dB)} \quad (9.3)$$

$$G_v(d) = -\min\left(12\left(\frac{\arctan(\frac{H_B-H_V}{d})-\theta^{tilt}}{\theta^{3dB}}\right)^2, G_m\right) \text{ (dB)}. \quad (9.4)$$

SINR and Connectivity

The UAVs receive signals from all GBSs, among one of which is the serving BS, and others contribute to the interference. The received signal from the k^{th} GBS to the i^{th} UAV can be expressed as $P_k G_{B_k}(d_{ik}) G_{V_i}(d_{ik}) L^{-1}(d_{ik})$. The experienced SINR at the i^{th} UAV if it is associated with the k^{th} GBS can be expressed as

$$S_{r_{i,k}} \triangleq \frac{P_k G_{B_k}(d_{ik}) G_{V_i}(d_{ik}) L^{-1}(d_{ik})}{\mathcal{N}_s + \sum_{k' \neq k} P_{k'} G_{B_{k'}}(d_{ik'}) G_{V_i}(d_{ik'}) L^{-1}(d_{ik'})} \quad (9.5)$$

where \mathcal{N}_s is the noise power. If the experienced SINR at a UAV is larger than a threshold \mathcal{T}_s , then the UAV is regarded as connected with the cellular network, and disconnected otherwise.

SINR Measurement

Along the path to destination, UAVs interact with the cellular network, measure the raw signal from GBSs, and obtain the instantaneous SINR $S'_r([\mathbf{p}, \mathbf{s}_B]; h)$, where h includes the random small-scale fading coefficients with all GBSs, and \mathbf{p} and $\mathbf{s}_B = [\mathbf{p}_{B_k}, \forall k]$ are the position of the UAV and positions of all GBSs, respectively. These measurements can be obtained by leveraging the existing soft handover mechanisms with continuous reference signal received power (RSRP) and reference signal received quality (RSRQ) [115]. At each time t , over a very short time interval, during which the agents' locations can be approximately considered to be unchanged, it is assumed that the UAV performs N_m SINR measurements. Then the empirical SINR can be obtained as

$$\hat{S}_{r(t)} = \frac{1}{N_m} \sum_{n=1}^{N_m} S'_{r(t)}([\mathbf{p}(t), \mathbf{s}_B]; h_{(t),n}). \quad (9.6)$$

To average over the randomness arising from small-scale fading, we can consider large N_m and have $\lim_{N_m \rightarrow \infty} \hat{S}_{r(t)} = S_{r(t)}$ by applying the law of large numbers. Therefore, as long as the UAV performs signal measurements sufficiently frequently so that $N_m \gg 1$, $S_{r(t)}$ can be evaluated by its empirical value $\hat{S}_{r(t)}$.

9.1.2 Multi-UAV Trajectory Optimization

In this section, we first introduce the constraints and then formulate the multi-UAV trajectory optimization problem.

Constraints

- **Collision Avoidance:** Collision avoidance is central to many autonomous systems. During flight, the UAVs should not collide with others, which means that the distance between two

agents should be larger than their radius all the time, i.e.,

$$\|\mathbf{p}_i(t) - \mathbf{p}_j(t)\|_2 > r_i + r_j \quad \forall j \neq i, \forall t \quad (9.7)$$

where $\mathbf{p}_i(t)$ is the location of the i^{th} UAV at time t , and r_i is its radius. Note that this radius can also include a buffer zone in which no other UAV should be present.

- **Wireless Connectivity Constraint:** To support the command and control and also data flows, UAVs have to maintain a reliable communication link to the GBSs. To achieve this goal, we consider the connectivity constraint for the UAVs, i.e., the maximum continuous time duration that the UAV is disconnected should not be longer than \mathcal{T}_t time units. The maximum continuous disconnected time duration can be mathematically expressed as

$$T_O^{\max} = \max_{t \in [0, T]} t - T_L(t) \quad (9.8)$$

where T is the total travel time, and $T_L(t)$ is the last time that the UAV is connected with the cellular network before time t , i.e.,

$$\begin{aligned} T_L(t) = \max \quad & \tau \\ \text{s.t.} \quad & \tau \in [0, t] \\ & S_r(\tau) \geq \mathcal{T}_s. \end{aligned} \quad (9.9)$$

Therefore, the connectivity constraint can be written as

$$\left(\max_{t \in [0, T]} t - T_L(t) \right) \leq \mathcal{T}_t. \quad (9.10)$$

- **Initial and Final Locations:** Each UAV starts its mission from a given initial location and

completes its flight at a given destination, i.e.,

$$\mathbf{p}(0) = \mathbf{p}^S \text{ and } \mathbf{p}(T) = \mathbf{p}^D \quad (9.11)$$

- **Kinematic Constraint:** Kinematic constraints need to be considered for operating UAVs.

We impose the speed and rotational constraints as follows:

$$\mathbf{v}(t) = [v_s(t), \phi(t)] \quad (9.12)$$

$$\text{Speed limit: } v_s(t) \leq v_{\max} \quad (9.13)$$

$$\text{Rotation limit: } |\phi(t) - \phi(t - \Delta t)| \leq \Delta t \cdot \mathcal{T}_r \quad (9.14)$$

where $\mathbf{v}(t)$, $v_s(t)$ and $\phi(t)$ are the UAV's velocity, speed and orientation at time t . v_{\max} is the maximum of speed the UAV, and \mathcal{T}_r is the maximum angle that a UAV can rotate in unit time period. This constraint limits the direction that a UAV can travel at a given time.

- **Association Constraint:** Each UAV is associated with one GBS at a time, and the associated GBS is denoted by $a(t) \in \{1, \dots, K\}$. Largest received signal power based association is adopted in this paper, where

$$a(t) = \underset{k}{\operatorname{argmax}} P_k G_{B_k}(d_k(t)) G_V(d_k(t)) L^{-1}(d_k(t)). \quad (9.15)$$

Problem Formulation in Continuous Time Domain

The goal of this work is to find trajectories for all UAVs in the network such that the travel/flight time of each UAV between the initial and final locations is minimized, while the constraints are satisfied. In the considered decentralized setting, the trajectory optimization problem for the i^{th} UAV can be formulated as

$$(P0) : \underset{\{\mathbf{p}_i(t), \forall t\}}{\operatorname{argmin}} \quad T_i$$

$$\begin{aligned}
s.t. \quad & (9.7), (9.10), (9.11), (9.13), (9.14) \\
& a(t) \in \{1, \dots, K\}, \forall t
\end{aligned}$$

Problem Formulation in Discrete Time Domain

Since the UAV is not permitted to be disconnected continuously for more than \mathcal{T}_t time units, it is sufficient to consider $\Delta t = \mathcal{T}_t/n_t$ as one time step and address the problem every n_t time steps. If, at these specific time instances, the experienced SINRs at all UAVs are higher than \mathcal{T}_s , we can guarantee that the connectivity constraint is satisfied. Now, the optimization problem can be represented in discrete time domain as follows:

$$\begin{aligned}
(\text{P1}) : \underset{\{\mathbf{p}_{i,t}, \forall t\}}{\text{argmin}} \quad & T_i \\
s.t. \quad & \|\mathbf{p}_{i,t} - \mathbf{p}_{j,t}\|_2 > r_i + r_j, \forall j \neq i, \forall t & (\text{P1.a}) \\
& S_{r_{i,t}} \geq \mathcal{T}_s, \text{ if } t \mid n_t & (\text{P1.b}) \\
& \mathbf{p}_{i,0} = \mathbf{p}_i^S, \mathbf{p}_{i,T_i} = \mathbf{p}_i^D, \forall i & (\text{P1.c}) \\
& v_{s_{i,t}} \leq v_{\max_i}, \forall t & (\text{P1.d}) \\
& |\phi_{i,t} - \phi_{i,t-1}| \leq \Delta t \cdot \mathcal{T}_r, \forall t & (\text{P1.e}) \\
& a_t \in \{1, \dots, K\}, \forall t & (\text{P1.f})
\end{aligned}$$

where the integer-valued discrete time index t indicates time increments by Δt , and $t \mid n_t$ signifies that t is divisible by n_t .

The non-communicating multi-agent navigation task can be formulated as a sequential decision making problem in a reinforcement learning framework [170]. The objective then is to develop policies, $\{\pi_i : \mathbf{s}_{i,t}^{jn} \mapsto \mathbf{v}_{i,t}, \forall i\}$ that select actions to minimize the expected time to destination while satisfying all the constraints, where $\mathbf{s}_{i,t}^{jn}$ and $\mathbf{v}_{i,t}$ are the joint state and the action of the agent,

respectively. Now, the optimization problem can be reformulated as

$$\begin{aligned}
 (\text{P2}) : \underset{\pi_i}{\operatorname{argmin}} \quad & \mathbb{E}[T_i | \mathbf{s}_i^{jn}, \pi_j, \forall j \neq i] \\
 \text{s.t.} \quad & (\text{P1.a}) - (\text{P1.c}), (\text{P1.f}) \\
 & \mathbf{p}_{i,t} = \mathbf{p}_{i,t-1} + \Delta t \cdot \pi_i(\mathbf{s}_{i,t-1}^{jn}), \forall t
 \end{aligned} \tag{P2.d}$$

where the expectation in the objective function in (P2) is with respect to other agents' unobservable states and policies, and (P2.d) is the agent's kinematics, which satisfy the kinematic constraints in (P1.d) and (P1.e). Further, since the agents in the considered networks have the same objective function and constraints, we use the common assumption that each agent would follow the same policy [170, 200, 201], i.e., $\pi = \pi_i$.

9.1.3 Reinforcement Learning Based Approach

In this section, we first introduce reinforcement learning (RL) formulation for the multi-UAV navigation problem. Then, we present the approaches used to tackle the uncertainty in the UAVs' unobservable intents, and the interaction between the UAVs and the cellular network.

Reinforcement Learning Formulation

To estimate the high-dimensional, continuous value function, it is common to approximate it with a deep neural network (DNN) parameterized by weights and biases, ξ . For notational simplicity, we drop the DNN parameters from the value function notation, i.e., $\mathcal{V}(\mathbf{s}; \xi) = \mathcal{V}(\mathbf{s})$. And \mathbf{s} is the joint state of an agent which is also the input of the DNN, and $\mathcal{V}(\mathbf{s})$ is the output of the value network given \mathbf{s} .

By detailing each of these elements and relating to (P1.a)-(P1.c) and (P2.d), the following provides an RL formulation for the multi-UAV navigation problem. Each UAV is an independent agent, and in the discussions below, we use agent instead of UAV.

- **State Space:** In multi-agent multi-GBS cellular networks, the agents are able to observe the following information from the environment: 1) its own information vector $\mathbf{s}_{i,t}$ (for the i^{th} agent at time step t); 2) the observable state of the nearest $J_n < J$ agents $\mathbf{s}_{i,t}^{jno} = [\mathbf{s}_{j,t}^o : j \in \{1, 2, \dots, J_n\}]$; 3) the location information of the nearest $K_n \leq K$ GBSs, which is assumed to be observed by the agents, and is denoted by $\mathbf{s}_B^o = [\mathbf{p}_{B_k} : k \in \{1, \dots, K_n\}]$. All the information observed by the agent constitutes its joint state $\mathbf{s}_{i,t}^{jn} = [\mathbf{s}_{i,t}, \mathbf{s}_{i,t}^{jno}, \mathbf{s}_B^o], \forall t$.
- **Action Space:** The action space is a set of permissible velocity vectors. Ideally, the agent can travel in any direction at any time. However, in reality the kinematic constraints in (9.12)-(9.14) restrict the agent's movement and should be taken into account. Then, based on the agent's current speed, orientation $[v_{s,i,t}, \phi_{s,i,t}]$ and the kinematic constraints, permissible actions $\mathbf{v} = [v_s, \phi]$ are sampled to build the action space $\mathcal{A}_{i,t}$.
- **Reward Function:** Similar to the formulation of the reward function defined in [170], [202], and [171], we define a sparse reward function, which awards the agent for reaching its goal, and penalizes the agent for getting too close or colliding with other agents, and also penalizes for getting close to be disconnected or already being disconnected from the cellular network. The reward function consists of four parts: the reward, \mathcal{R}_c , that penalizes close encounters with other agents; the reward, \mathcal{R}_s , that encourages keeping connectivity with the cellular network; the reward, \mathcal{R}_d , that encourages arrival at the destination; and a step penalty, \mathcal{R}_t , that encourages fast arrival. For instance, at time step t , the reward functions for the i^{th} agent can be expressed as follows:

$$\mathcal{R}_{c_{i,t}}(\mathbf{s}_{i,t}^{jn}, \mathbf{v}_{i,t}) = \begin{cases} -\alpha_1, & \text{if } d_{t_{\min}} \leq r_i + r_j, \\ -\alpha_1 \times \left(1 - \frac{d_{t_{\min}} - r_i - r_j}{d_b}\right), & \text{if } r_i + r_j < d_{t_{\min}} \leq d_b + r_i + r_j, \\ 0, & \text{otherwise,} \end{cases} \quad (9.16)$$

$$\mathcal{R}_{s_{i,t}}(\mathbf{s}_{i,t}^{jn}, \mathbf{v}_{i,t}) = \begin{cases} -\alpha_2, & \text{if } t \mid n_t \text{ and } S_{r_{i,t+1}} < \mathcal{T}_s, \\ -\alpha_2/2, & \text{if } t \mid n_t \text{ and } \mathcal{T}_s \leq S_{r_{i,t+1}} < \mathcal{T}_s + S_{r_b}, \\ 0, & \text{otherwise,} \end{cases} \quad (9.17)$$

$$\mathcal{R}_{d_{i,t}}(\mathbf{s}_{i,t}^{jn}, \mathbf{v}_{i,t}) = \begin{cases} \alpha_3, & \text{if } \mathbf{p}_{i,t+1} = \mathbf{p}_i^D, \\ 0, & \text{otherwise,} \end{cases} \quad (9.18)$$

$$\mathcal{R}_t = -\alpha_4, \quad (9.19)$$

where $d_{t_{\min}}$ is the minimum distance to other agents within the next time step duration. $\alpha_{1 \sim 4}$ are position constants that can be varied to adjust the weight or emphasis of each reward term, d_b is a distance buffer between two agents, and S_{r_b} is an SINR buffer. Therefore, the overall reward function can be expressed as the sum

$$\mathcal{R}_{i,t}(\mathbf{s}_{i,t}^{jn}, \mathbf{v}_{i,t}) = \mathcal{R}_{c_{i,t}}(\mathbf{s}_{i,t}^{jn}, \mathbf{v}_{i,t}) + \mathcal{R}_{s_{i,t}}(\mathbf{s}_{i,t}^{jn}, \mathbf{v}_{i,t}) + \mathcal{R}_{d_{i,t}}(\mathbf{s}_{i,t}^{jn}, \mathbf{v}_{i,t}) + \mathcal{R}_t. \quad (9.20)$$

Estimation of the Agents' Unobservable Intents

The probabilistic state transition model is determined by the agents' kinematics as defined in (P2.d), other agents' hidden states, and the other agents' choices of action. Since the other agents' hidden intents are unknown, the system's state transition model is unknown as well. In addition, it is difficult to evaluate the integral, because the other agents' next state has an unknown distribution (that depends on their unobservable intents). We approximate this integral by assuming that the other agent would be traveling at a filtered velocity for a short duration Δt , which is regarded as a one-step lookahead procedure [170, 200, 203, 204]. This propagation step amounts to predicting the other agent's motion with a simple linear model, i.e., $\hat{\mathbf{v}}_{j,t} = \text{filter}(\mathbf{v}_{j,0:t})$. For the i^{th} agent, other agents' filtered velocities are included in the vector $\hat{\mathbf{v}}_{i,t}^{jno} = [\hat{\mathbf{v}}_{j,t} : j \in \{1, 2, \dots, J_n\}]$. Then, the

estimated next state of the i^{th} agent will be

$$\hat{\mathbf{s}}_{i,t+1,\mathbf{v}}^{jn} = [f(\mathbf{s}_{i,t}, \Delta t, \mathbf{v}), f(\mathbf{s}_{i,t}^{jno}, \Delta t, \hat{\mathbf{v}}_{j,t}^{jno}), \mathbf{s}_B^o] \quad (9.21)$$

where $f(\cdot)$ is the kinematic model. Then, we can select the action that has the highest value with respect to other agents' estimated state, which can be formulated as

$$\operatorname{argmax}_{\mathbf{v} \in A_{i,t}} R_{i,t}(\mathbf{s}_{i,t}^{jn}, \mathbf{v}) + \gamma V(\hat{\mathbf{s}}_{i,t+1,\mathbf{v}}^{jn}). \quad (9.22)$$

SINR Prediction

Model-free RL requires no prior knowledge about the environment. This usually leads to slow learning process and requires a large number of agent-environment interactions, which is typically costly or even risky to obtain [115]. Actually, each real experience obtained from the agent and cellular network interaction not only can be used to get reward and refine the value network, but also can be used for model learning in order to predict the agent's SINR experienced at certain positions. More specifically, when flying in the environment, agents interact with the cellular network and obtain the empirical SINR \hat{S}_r . Since there is no need to use the exact SINR for connectivity measurement, this work uses the quantized SINR level, $L_w(\hat{S}_r)$, to check the agent's connectivity. With a finite set of measurements $\{\langle \mathbf{s}_B^{jn}, L_w(\mathbf{s}_B^{jn}) \rangle\}$, where $\mathbf{s}_B^{jn} = [\mathbf{p}, \mathbf{s}_B^o]$, a DNN can be trained to predict the SINR level $L_w(\mathbf{s}_B^{jn})$.

A fully connected DNN with parameters ξ_w can be used to predict the agent's SINR level, i.e., ξ_w is trained so that $L_w(\mathbf{s}_B^{jn}) \approx \mathcal{L}_w(\mathbf{s}_B^{jn}; \xi_w)$. The data measurement $\langle \mathbf{s}_B^{jn}, L_w(\mathbf{s}_B^{jn}) \rangle$ only arrives incrementally as the agent flies to new locations and can be saved in a database (e.g., replay memory), and a minibatch is sampled at random from the database to update the network parameter ξ_w . Note that the prediction of SINR levels might be highly inaccurate initially, but can be continuously improved as more real experience is accumulated.

9.1.4 Decentralized Deep Reinforcement Learning Algorithm

In this section, we present the proposed decentralized deep reinforcement learning algorithm as a solution to multi-UAV navigation with collision avoidance and wireless connectivity constraints, including the SINR-prediction neural network. The proposed algorithm is presented in Algorithm 2, and is referred to as RLTCW-SP (RL for Trajectory optimization with Collision avoidance and Wireless connectivity constraint and with SINR Prediction).

Parametrization

Since the optimal policy should be invariant to any coordinate plane, we follow the agent-centric parameterization as in [170, 171, 202], where the agent is located at the origin and the x -axis is pointing toward the agent's destination. The states of the i^{th} agent after transformation is

$$\tilde{\mathbf{s}}_i = [d_{g_i}, v_{\max_i}, \tilde{v}_{x_i}, \tilde{v}_{y_i}, r_i, \tilde{\phi}_i] \quad (9.23)$$

$$\tilde{\mathbf{s}}_i^{jno} = [[\tilde{p}_{x_j}, \tilde{p}_{y_j}, H_V, \tilde{v}_{x_j}, \tilde{v}_{y_j}, r_j, d_j] : j \in \{1, 2, \dots, J_n\}] \quad (9.24)$$

where d_g is the agent's distance to the goal, d_j is the agent's distance to the j^{th} agent, and \tilde{p} denotes p in the new coordinate.

In addition, SINR experienced at an agent depends on the distance and the relative angular direction from the agent to the GBSs, while it does not depend on the positions in global coordinates. To remove this redundant dependence, the location information vector of all GBSs can be parameterized as

$$\tilde{\mathbf{p}}_{B_k} = [\tilde{p}_{x_{B_k}}, \tilde{p}_{y_{B_k}}, d_{B_k}, \phi_{B_k}, \theta_{B_k}] \quad (9.25)$$

$$\tilde{\mathbf{s}}_{B_i} = [\tilde{\mathbf{p}}_{B_k} : k \in \{1, \dots, K_n\}] \quad (9.26)$$

where $d_{B_k} = \|\mathbf{p}_{B_k} - \mathbf{p}_i\|$ is the distance from the agent to the k^{th} BS, ϕ_{B_k} and θ_{B_k} are the horizontal and vertical angles of the k^{th} BS with respect to the agent.

Algorithm 2: RLTCW-SP Algorithm

Input: State-value pairs D

- 1 Initialize state-value pairs D
- 2 Initialize location-SINR pairs D_w
- 3 Initialize value network ξ with D
- 4 Initialize SINR-prediction network ξ_w
- 5 **for** $episode = 0$: total episode **do**
- 6 **for** n random training cases **do**
- 7 Initialize $s_{i,0} \forall i$
- 8 **while** not all reached destinations **do**
- 9 **for** each agent i **do**
- 10 **if** not reached destination **then**
- 11 $s_{i,t}^{jn} \leftarrow \text{observeEnvironment}()$
- 12 $\mathcal{A}_{i,t} \leftarrow \text{sampleActionSpace}()$
- 13 $c \leftarrow \text{randomSample}(\text{Uniform}(0,1))$
- 14 **if** $c \leq \epsilon$ **then**
- 15 $\mathbf{v}_{i,t} \leftarrow \text{randomSample}(\mathcal{A}_{i,t})$
- 16 **else**
- 17 $\hat{\mathbf{v}}_{i,t}^{jno} \leftarrow \text{filter}(\mathbf{v}_{0:t-1}^{jn})$
- 18 $\hat{s}_{i,t+1}^{jno} \leftarrow \text{propagate}(s_{i,t}^{jno}, \hat{\mathbf{v}}_{i,t}^{jno})$
- 19 **for** every \mathbf{a} in $\mathcal{A}_{i,t}$ **do**
- 20 $\hat{s}_{i,t+1} \leftarrow \text{propagate}(s_{i,t}, \mathbf{a})$
- 21 $\hat{L}_{w_{i,t+1}} = \mathcal{L}_w(\hat{s}_{B_{i,t+1}}^{jn})$
- 22 $\mathcal{R}_{i,t} \leftarrow \text{getReward}(\hat{s}_{i,t+1}^{jn}, \hat{L}_{w_{i,t+1}})$
- 23 $V_p = \mathcal{R}_{i,t} + \gamma \mathcal{V}(\hat{s}_{i,t+1}^{jn})$
- 24 $\mathbf{v}_{i,t} \leftarrow \text{argmax}_{\mathbf{a} \in \mathcal{A}_{i,t}} V_p$
- 25 $\mathcal{R}_{i,t}, s_{i,t+1}, S_{r_{i,t+1}} \leftarrow \text{executeAction}(\mathbf{v}_{i,t})$
- 26 **for** each agent i **do**
- 27 $V_{i,0:T_i} \leftarrow \text{updateValue}(s_{i,0:T_i}^{jn}, \mathcal{R}_{i,0:T_i}, \xi)$
- 28 $L_{w_{i,0:T_i}} \leftarrow \text{getSINRlevel}(S_{r_{i,0:T_i}})$
- 29 Update state-value pairs D with $\langle s_{i,0:T_i}^{jn}, V_{i,0:T_i} \rangle$
- 30 Update location-SINR pairs D_w with $\langle s_{B_{i,0:T_i}}^{jn}, L_{w_{i,0:T_i}} \rangle$
- 31 Sample random minibatch from D , and update value network ξ by gradient descent.
- 32 Sample random minibatch from D_w , and update SINR-prediction network ξ_w by gradient descent.
- 33 **return** ξ, ξ_w

Therefore, the joint state of the i^{th} agent after transformation is

$$\tilde{\mathbf{s}}_i^{jn} = [\tilde{\mathbf{s}}_i, \tilde{\mathbf{s}}_i^{jno}, \tilde{\mathbf{s}}_{B_i}]. \quad (9.27)$$

And the input of the SINR-prediction network becomes

$$\tilde{\mathbf{s}}_{B_i}^{jn} = [[d_{B_k}, \phi_{B_k}, \theta_{B_k}] : k \in \{1, \dots, K_n\}]. \quad (9.28)$$

Initialization

The value network ξ can be first initialized with imitation learning using a set of experiences to accelerate the convergence. More specifically, in this work, we use optimal reciprocal collision avoidance (ORCA) [200] to generate a number of trajectories that contain a large set of state-value pairs $\{\langle \mathbf{s}^{jn}, V \rangle\}^{N_1}$, where $V = \gamma^{t_g}$ and t_g is the time to reach the destination. The experiences are saved in memory D (line 1 in Algorithm 2). Then, the value network is initialized by supervised training on D (line 3). The value network is trained by back-propagation to minimize a quadratic regression error

$$\xi = \underset{\xi'}{\operatorname{argmin}} \sum_{k=1}^{N_1} (V_k - \mathcal{V}(\mathbf{s}_k^{jn}; \xi')). \quad (9.29)$$

If a set of location-SINR experiences can be downloaded from the cloud, we can save the downloaded dataset in memory D_w (line 2), $\{\langle \mathbf{s}_B^{jn}, L_w \rangle\}^{N_2}$, where L_w is the scaled SINR level that the agent experienced. Then, the SINR-prediction network can be initialized with $\xi_w = \underset{\xi'}{\operatorname{argmin}} \sum_{k=1}^{N_2} (L_{w_k} - \mathcal{L}(\mathbf{s}_B^{jn}; \xi'))$, which is trained by back-propagation (line 4). If no dataset is available, D_w is initialized with an empty list, and the SINR-prediction network is initialized with random network parameters.

Refining Process

After initialization, a refining process is performed using RL. Particularly, a set of random training cases is generated in each episode (line 6). In each training case, each agent navigates around others to arrive its destination, while interacting with the cellular network (line 10- line 25). It is worth noting that the agents navigate simultaneously and with no communication among each other. At each time step t , each agent first observes the environment, obtains the observable states of other nearby agents and the location information of the GBSs, and then obtains its joint state \mathbf{s}_t^{jn} (line 11). Then, based on its current velocity and kinematic constraints, each agent builds an action space A_t (line 12). Using an ϵ -greedy policy, each agent selects a random action with probability ϵ from A_t (line 15), or follows the value network greedily otherwise (lines 17-24). When following the value network to choose actions, each agent performs the following: 1) estimate other nearby agents' motion by filtering their velocities, and estimate their observable states $\hat{\mathbf{s}}_{t+1}^{jno}$ following equation (9.21) (lines 17-18); 2) predict its next SINR level $\mathcal{L}_{w_{t+1}}$ using the SINR-prediction network ξ_w ; 3) choose the best action in A_t which has the maximum V_p .

When all agents have arrived their destinations in each training case, trajectories $\mathbf{s}_{i,0:T_i} \forall i$ are then processed to generate a set of state-value pairs $\langle \mathbf{s}_{i,0:T_i}^{jn}, V_{i,0:T_i} \rangle$, where

$$V_{i,t} = \begin{cases} \mathcal{R}_{i,t} + \gamma \mathcal{V}(\mathbf{s}_{i,1:t+1}^{jn}) & \text{if } t + 1 < T_i, \\ \mathcal{R}_{i,t} & \text{if } t + 1 = T_i, \end{cases}$$

and a set of location-SINR pairs $\langle [\mathbf{p}_{i,0:T_i}, \mathbf{s}_B^o], L_{w_{i,0:T_i}} \rangle$. The new pairs are used to update D and D_w .

Training

We first use ORCA [200] to generate a number of trajectories that contain a large set of state-value pairs $\{\langle \mathbf{s}^{jn}, V \rangle\}^{N_1}$, where $V = \gamma^{t_g}$ and t_g is the time to reach the destination. The experiences, as input of Algorithm 2, are saved in memory D , which will be refined during training. To train

the value network and SINR-prediction network, a set of training points is randomly sampled from the experience set, which contains state-value pairs for ξ or location-SINR pairs for ξ_w from many different trajectories. Then, the networks are finally updated by stochastic gradient descent (back-propagation) on the sampled subsets of experience.

Real-Time Navigation

With the trained value network and SINR-prediction network, agent can execute real-time navigation. This process is provided in Algorithm 3.

Algorithm 3: Real-Time Navigation

Input: ξ, ξ_w

- 1 Initialize \mathbf{s}_0
- 2 **while** not reached destination **do**
- 3 $\mathbf{s}_t^{jn} \leftarrow \text{observeEnvironment}()$
- 4 $\mathcal{A}_t \leftarrow \text{sampleActionSpace}()$
- 5 $\hat{\mathbf{v}}_t^{jn} \leftarrow \text{filter}(\mathbf{v}_{0:t-1}^{jn})$
- 6 $\hat{\mathbf{s}}_{t+1}^{jno} \leftarrow \text{propagate}(\mathbf{s}_t^{jno}, \hat{\mathbf{v}}_t^{jn})$
- 7 **for every** \mathbf{a} in \mathcal{A}_t **do**
- 8 $\hat{\mathbf{s}}_{t+1} \leftarrow \text{propagate}(\mathbf{s}_t, \mathbf{a})$
- 9 $\hat{L}_{w_{t+1}} = \mathcal{L}_w([\hat{\mathbf{p}}_{t+1}, \mathbf{s}_B])$
- 10 $\mathcal{R}_t \leftarrow \text{getReward}(\hat{\mathbf{s}}_{t+1}, \hat{\mathbf{s}}_{t+1}^{jno}, \hat{L}_{w_{t+1}})$
- 11 $V_p = \mathcal{R}_t + \gamma \mathcal{V}(\hat{\mathbf{s}}_{t+1}^{jn})$
- 12 $\mathbf{v}_t \leftarrow \text{argmax}_{\mathbf{a} \in \mathcal{A}_t} V_p$
- 13 $\mathbf{s}_{t+1} \leftarrow \text{executeAction}(\mathbf{v}_t)$
- 14 **return** $\mathbf{v}_{0:T-1}, \mathbf{s}_{0:T}$

9.1.5 Numerical Results

In this section, we present the numerical results to evaluate the performance of the proposed algorithms. In the illustrations of environment and trajectories in this section, the GBSs are marked by green triangles, and the yellow areas indicate the communication coverage zones where the agents are able to connect with the cellular network (i.e., $S_r \geq \mathcal{T}_s$). Agents' trajectories are displayed as a list of dots in different colors, and the destinations are marked with crosses. In each flight

trajectory, there are four possible outcomes for the agent/UAV: 1) success, if the agent arrives its destination successfully; 2) collision, if it collides with others; 3) disconnection, if the continuous disconnected time is larger than the threshold \mathcal{T}_t ; 4) stuck, if the agent freezes and stops moving and consequently does not reach the destination. In addition, we also compute the additional average time (referred to also as average more time) needed to reach the destination, when compared with the lower bound (attained when the UAV goes straight towards the destination at the maximum speed). Therefore, we use success rate (SR), collision rate (CR), disconnection rate (DR) and average more time (AMT) to show the performance of the algorithms.

Environment Setting and the Networks

Since the agents fly at the same altitude, the area of interest becomes two-dimensional. In the simulations, we consider an area with 12 GBSs deployed. The GBSs transmit with power $P_B = 1$ dBW, have a height of $H_B = 32$ m, and the antenna patterns are set with $\theta^{tilt} = 10^\circ$ and $\theta^{3dB} = 15^\circ$. The UAVs are assumed to fly at a fixed altitude of $H_V = 50$ m. The noise power is $\mathcal{N}_s = 10^{-6}$, and the SINR threshold is $\mathcal{T}_s = -3$ dB. Each UAV, as an independent agent, is able to observe the nearest 8 GBSs' locations and at most 2 other agents' observable states.

We construct the value network via a three-layered DNN of size (64,32,16). The exploration parameter ϵ linearly decays from 0.5 to 0.1. The replay memory capacity is 30000 for the 2-agent scenario and 100000 for scenarios with more than two agents. The SINR-prediction network is constructed via a three-layered DNN of size (32,16,8). A standardization layer is utilized after the input layer of both networks. ReLU activation function is used for the input layer and two hidden layer for both networks. Both networks use Adam optimizer, and have learning rate 0.01, batch size 200, and a regularization parameter 0.0001.

To build the action spaces $A_{i,t}$, based on the agent's current velocity $[v_{s,i,t}, \phi_{s,i,t}]$, 22 velocities are chosen, including: 1) combinations $[v_s, \phi_{s,i,t} + \phi]$, where $v_s \in \{0, \frac{1}{2}v_{\max}, v_{\max}\}$ and $\phi \in \{\pm\mathcal{T}_r, \pm\frac{2}{3}\mathcal{T}_r, \pm\frac{1}{3}\mathcal{T}_r, 0\}$; and 2) current velocity. The values for $\alpha_{1\sim 4}$, d_b and S_b in reward function are selected as follows: $\alpha_1 = 1, \alpha_2 = 1, \alpha_3 = 2, \alpha_4 = 0.1, d_b = 0.2$ and $S_{r_b} = 0.1$.

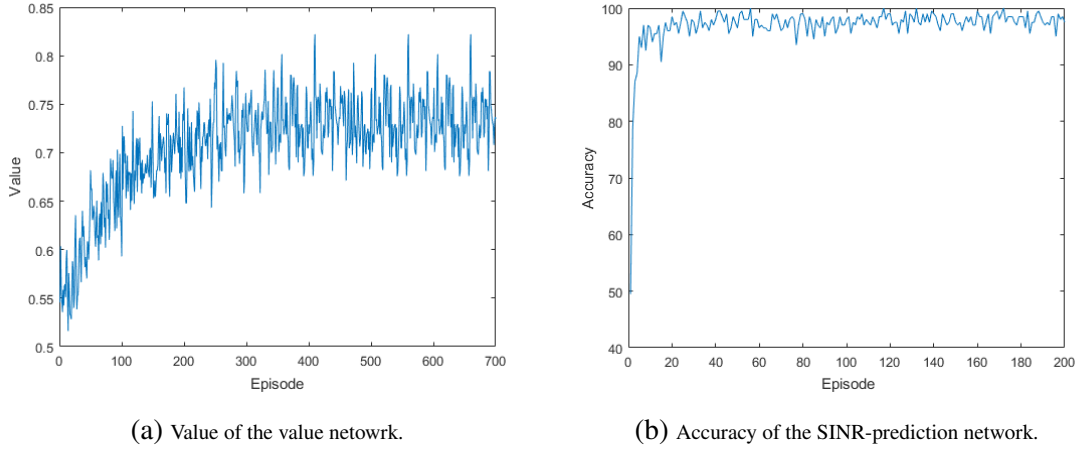


Fig. 9.2: Value of the value network and accuracy of the SINR-prediction network as functions of the number of episodes.

Convergence in Training

Fig. 9.2 shows the value of the value network and accuracy of the SINR-prediction network as functions of the number of episodes during training for a 2-agent scenario. Fig. 9.2(a) shows that the value converges after around 200 episodes. From Fig. 9.2(b), we can see that the accuracy converges after around 20 episodes, since in each episode 50 random trajectories are generated for each agent, during which more than 15000 location-SINR pairs are collected and used to train the SINR-prediction network.

The trajectory optimization process for two UAVs is displayed in Fig. 9.3. At episode 0, the SINR-prediction network is initialized with random weights and bias, and is not able to predict the accurate SINR level. Besides, the policy has not been refined by RL. As a result, the two agents are easily getting disconnected or stuck. After 100 episodes of training, the SINR-prediction network is well-trained and able to predict the SINR levels with 97% accuracy. Also, the value network is trained with refined state-value pairs. Thus, the agents can reach their destinations, but with long trajectories to avoid collisions and disconnection. As the training proceeds, the policy improves, leading to shorter expected trajectories.

After 700 episodes of training, the AMT (for the successful trajectories) is 0.2662s. Separately, we also compute the AMT in two different scenarios for comparison: 1) the connectivity constraint

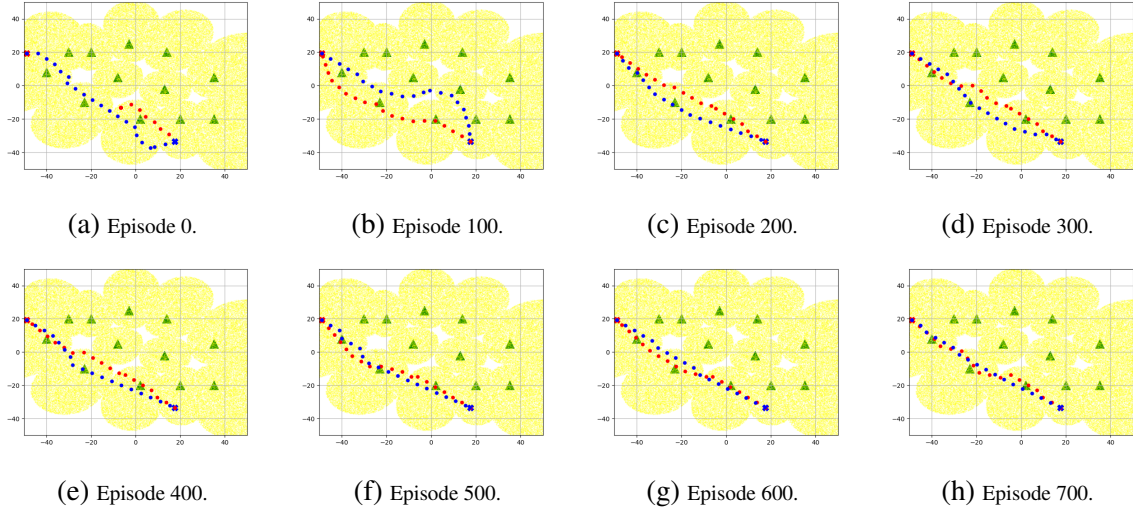


Fig. 9.3: Trajectory examples at different episodes during training.

is not considered for the two-agent trajectory design (CADRL [170]); and 2) the collision avoidance constraint is not considered if there is only one agent. The AMT in these two scenarios are 0.195s, and 0.204s, respectively.

Testing of Navigation in Different Environments

In the proposed RLTCW-SP algorithm, an SINR-prediction network is trained to predict the SINR level. In an ideal scenario, the antenna pattern information of GBSs may be available to the agents, and then the agents are able to predict the SINR with that information. In this subsection, we compare the performances of the following three algorithms: 1) the agents are able to get the antenna pattern information of the GBSs, and then predict the SINR directly (referred to as RLTCW-AW); 2) the proposed RLTCW-SP algorithm, which uses the location-SINR memory, and trains an SINR-prediction network to predict the SINR level; 3) the agents do not predict the SINR and only use the value network to make decisions (referred to as RLTCW). The navigation test is done in three types of environments: 1) the same environment as in the training; 2) the same environment but two BSs are not operational for the UAV (due to congestion, malfunction, resource allocation to ground users, or GBS activation schedule), an illustration of which is presented in Fig. 9.4(a); 3) different environment with different GBS deployment, illustrations of which are presented in Figs.

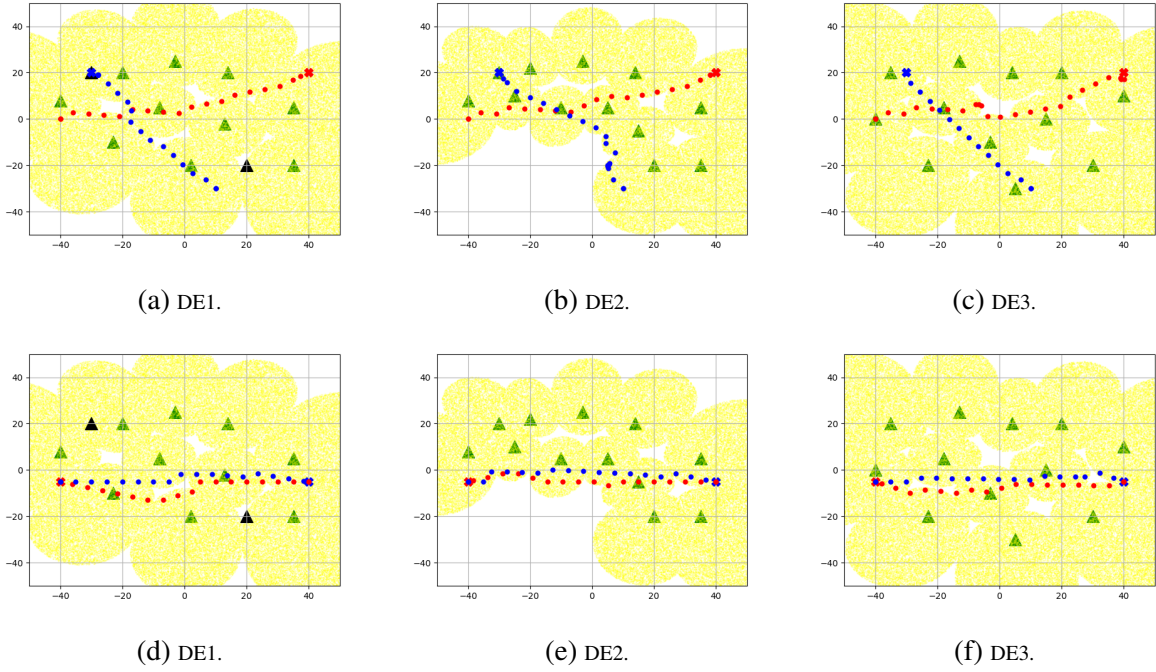


Fig. 9.4: Illustrations of different environments used in navigation testing, and trajectory examples when using proposed RLTCW-SP algorithm. In (a) and (d), the two BSs in black are not operational for the UAVs.

9.4(b) and 9.4(c). Fig. 9.4 also presents examples of trajectories that the agents perform using the proposed RLTCW-SP algorithm in a challenging scenario in which the destination of one UAV is the starting point of the other UAV. Environments displayed in Figs. 9.4 (a) (b) and (c) are referred as DE1, DE2 and DE3 (using DE as the abbreviation for different environment).

The performance of the three algorithms in different environments are presented in Table 9.1. As expected, the RLTCW-AW with the perfect knowledge of antenna patterns has the best performance, and the RLTCW-SP algorithm has slightly lower performance which is due to the potential inaccuracies in the SINR prediction, while the performance of RLTCW is substantially lower compared to the other two, due to very high DR (disconnection rate). In addition, the SR (success rate) performance of the proposed RLTCW-SP algorithm decreases only slightly in different environments, and how large the decrease is depends on which environment is used in testing. When there are large and wide out-of-coverage zones in the environment (as shown in Fig. 9.4(b)), the SR performance decreases relatively a bit more. The reason is that the wide out-of-coverage zones are

Table 9.1: Performance of different algorithms in different environments in terms of success rate (SR), collision rate (CR), and disconnection rate (DR) (**all rates are in %**).

	Same Environment			DE1		
	SR	CR	DR	SR	CR	DR
RLTCW-AW	99.15	0.85	0	98.95	0.95	0
RLTCW-SP	99.1	0.85	0.05	99.05	0.85	0.07
RLTCW	64.8	0.6	34.6	74.85	0.15	25
	DE2			DE3		
	SR	CR	DR	SR	CR	DR
RLTCW-AW	98.25	1.42	0.17	99.1	0.9	0
RLTCW-SP	98.08	1.5	0.42	99	0.92	0.08
RLTCW	60.7	0.8	38.5	69	0.33	30.67

more likely to make the agent get stuck at the edge and not be able to decide which direction to go. Overall, in the three different environments in testing, the proposed RLTCW-SP can achieve above 98% of SR in 2-agent scenarios.

Navigation in Different Settings

In this subsection, we present simulation results on the trajectories when the GBSs have different antenna patterns and when the UAVs fly at different heights. The SINR threshold is $\mathcal{T}_s = -4$ dB in this subsection. In Figs. 9.5 (a) and (d), we provide two different trajectory examples when we have $H_V = 50$ m, $\theta^{tilt} = 10^\circ$ and $\theta^{3dB} = 15^\circ$. In Figs. 9.5 (b) and (e), UAV altitudes are increased to $H_V = 100$ m, and we notice that due to larger path loss and smaller antenna gains, coverage zones shrink, which in turn potentially increases the length of the trajectories. In Figs. 9.5 (c) and (f), GBSs have larger downtilting angle and 3dB beamwidth of the main lobe. In this case, the UAVs experience smaller received power from the main link and potentially larger interference, leading to substantially smaller SINR levels. Therefore, the coverage zones in Figs. 9.5 (c) and (f) are smaller than those in Figs. 9.5 (a) and (d) and even Figs. 6 (b) and (e). In all cases, we note that UAVs successfully find different trajectories to meet the connectivity requirements and adapt to different coverage zones.

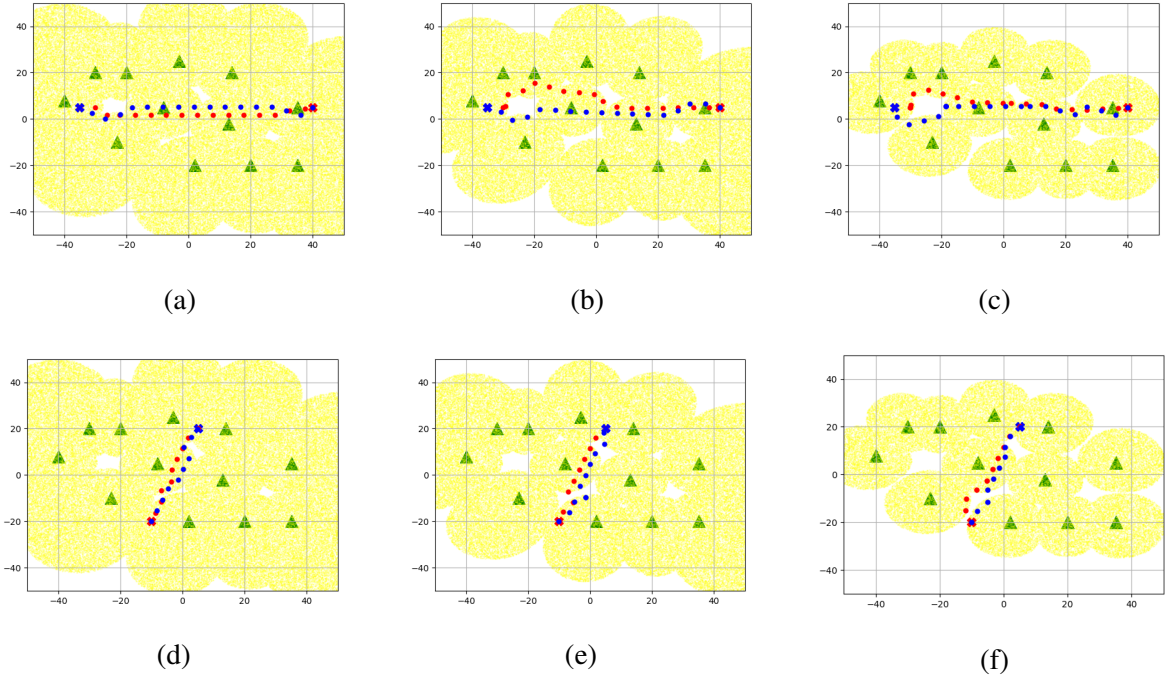


Fig. 9.5: Trajectory examples in environments with different settings, i.e., in (a) and (d), $H_V = 50$ m, $\theta^{tilt} = 10^\circ$ and $\theta^{3dB} = 15^\circ$; in (b) and (e), $H_V = 100$ m, $\theta^{tilt} = 10^\circ$ and $\theta^{3dB} = 15^\circ$; and in (c) and (f), $H_V = 50$ m, $\theta^{tilt} = 15^\circ$ and $\theta^{3dB} = 35^\circ$.

Navigation in Environments with Obstacles/No-Fly Zones

The proposed RLTCW-SP algorithm can also be used for navigation in environment with obstacles that are regarded as non-moving agents. For instance, the trained networks for the 2-agent scenario can be used for one agent navigation in an environment with obstacles or no-fly zones. More specifically, the agent can observe the nearest obstacle, and takes the obstacle's location in the joint state for choosing actions. Fig. 9.6 displays two illustrations. In this setting, obstacles can be considered as actual obstacles (e.g., tall buildings or structures) or they can model no-fly zones for the UAVs.

Navigation with More Than Two UAVs

Fig. 9.7 provides the illustrations for 8-agent, 12-agent, 16-agent navigation scenarios, respectively, where dotted lines are used to display the trajectories. The SR, CR, DR and AMT performances in scenarios with 2 to 20 agents are presented in Table 9.2, when the distance buffer is

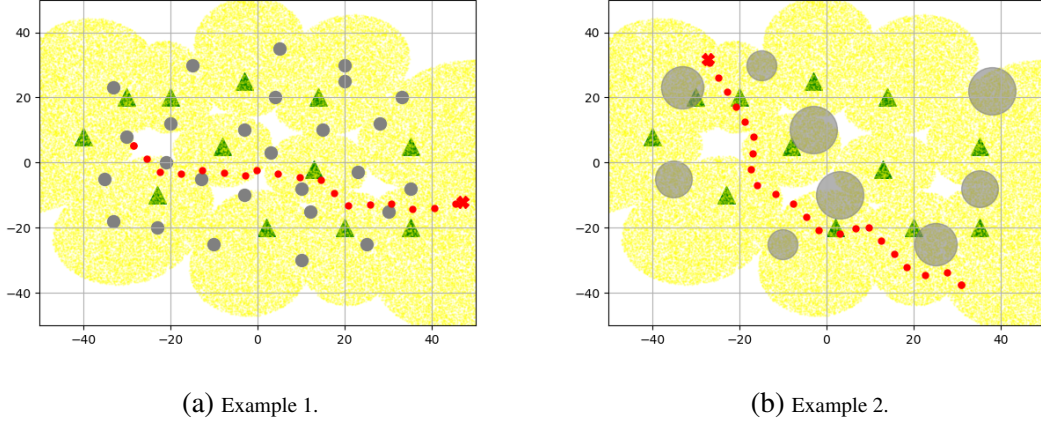


Fig. 9.6: Trajectory examples in environments with obstacles/no-fly zones.

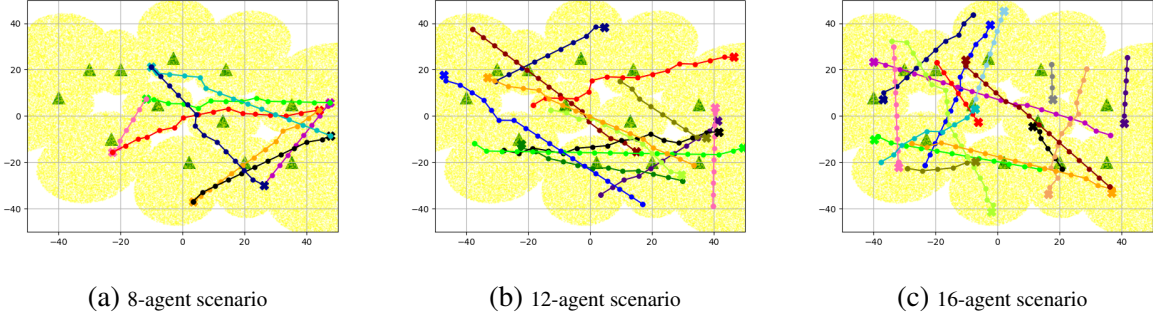


Fig. 9.7: Trajectory examples for multi-agent navigation.

$d_b = 0.2$ (default) or 1. We note that the CR increases when more agents are in the environment. As mentioned before, the agents can observe a maximum of 2 nearest agents in the environment. Therefore, for more crowded scenarios, several agents are non-observable and as a result the CR can increase when compared with scenarios involving smaller number of agents. Additionally, when there are more agents in the same area, the interactions become more complex, and challenging for the algorithm to handle. However, we note that the performance regarding the SR is still above 90% for the 20-agent scenario. Table 9.2 further shows that the agents need more time to reach their destinations when there are more agents in the environment. Moreover, when we compare the performances between the scenario with $d_b = 0.2$ and the scenario with $d_b = 1$, we have the following observations for larger d_b : 1) the CR is reduced, since larger d_b encourages the UAVs to stay relatively farther from each other and therefore leads to lower collision risk; and

Table 9.2: Performance for Multi-Agent Navigation

Number of agents		2	4	6	8	10	12	14	16	18	20
$d_b=0.2$	SR(%)	99.1	98.65	97.37	97	96.9	95.55	94.83	93.9	91.9	91.74
	CR(%)	0.85	1.32	2.18	2.73	3.68	4.38	5.12	6.31	7.06	8.18
	DR(%)	0.05	0.03	0.1	0.06	0.05	0.07	0.05	0.1	0.04	0.08
	AMT(s)	0.266	0.306	0.319	0.322	0.336	0.346	0.364	0.369	0.381	0.441
$d_b=1$	SR(%)	99.33	98.92	98.58	97.67	97.53	97.28	97	96.19	95.32	95
	CR(%)	0.56	1	1.25	2.17	2.13	2.67	2.5	3.62	4.37	4.7
	DR(%)	0.11	0.08	0.17	0.17	0.33	0.06	0.5	0.19	0.11	0.3
	AMT(s)	0.299	0.359	0.365	0.406	0.470	0.481	0.510	0.525	0.572	0.675

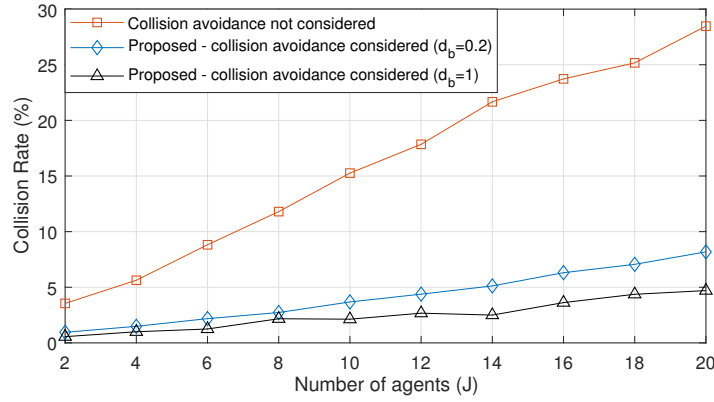


Fig. 9.8: Collision rate comparison between two methods: 1) the proposed approach, in which the collision avoidance is taken into account in training; 2) the approach in which collision with other UAVs is not considered in training.

2) the AMT is increased, since staying further away from each other leads to longer trajectories and correspondingly longer mission completion time. In addition, the CR is less than 5% for the 20-agent scenario when we set $d_b = 1$.

Fig. 9.8 compares the collision rates between the proposed algorithm (RLTCW-SP) and the trajectory optimization algorithm with connectivity constraint only, i.e., collision avoidance is not considered. It can be observed from the figure that as the number of agents in the environment grows, CR increases accordingly. If collision avoidance is not considered in the algorithm, CR is not only much higher (e.g., three to six times higher) but also increases much faster than the proposed algorithm, which takes into account the collision avoidance. Therefore, collision avoidance is critical in multi-UAV scenarios, especially in crowded environments, and the proposed algorithm can significantly decrease the collision risk and hence achieve much lower collision rates.

9.2 Jamming-Resilient Path Planning for Multiple UAVs via Deep Reinforcement Learning

9.2.1 System Model

A multi-UAV multi-GBS cellular network is considered, in which K GBSs provide wireless connectivity to the UAVs. There is also a jammer in the network that transmits jamming signals to interfere the links between the UAVs and their serving GBSs, and hence disrupts the communication. The location and the transmit power of the jammer can vary over time. An illustration of the cellular networks with multiple UAVs, multiple GBSs, and a jammer is provided in Fig. 9.9.

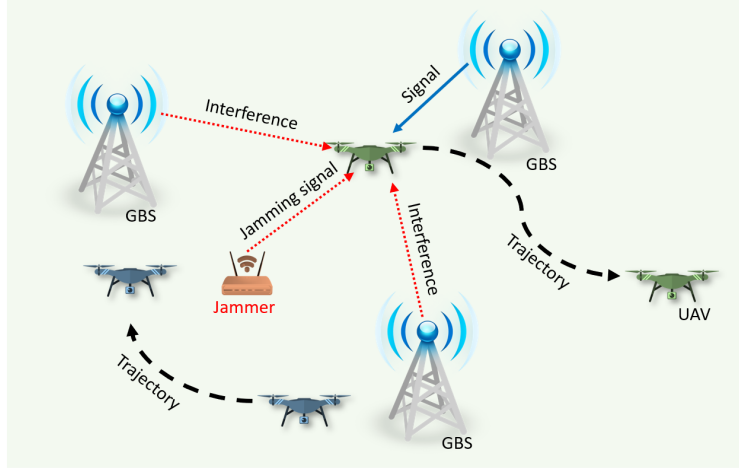


Fig. 9.9: An illustration of the cellular networks with multiple UAVs, multiple GBSs, and a jammer.

The UAVs receive desired signal from the serving GBS, interference from other GBSs and jamming signal from the jammer. Thus, the experienced SINR at a UAV can be expressed as

$$\mathcal{S}_{r_k} \triangleq \frac{P_k G_B(d_k) G_V(d_k) L^{-1}(d_k)}{\mathcal{N}_s + I_J(d_J) + \sum_{k' \neq k}^K P_{k'} G_B(d_{k'}) G_V(d_{k'}) L^{-1}(d_{k'})} \quad (9.30)$$

where \mathcal{N}_s is the noise power, P_k is the transmit power of the k^{th} GBS, d_k is the horizontal distance between the UAV and the k^{th} GBS. G_B is the 3D antenna gain at the GBSs. G_V is the 3D antenna

gain at the UAVs. L is the path loss

$$L(d) = (d^2 + (H_B - H_V)^2)^{\alpha/2} \quad (9.31)$$

where α is the path loss exponent. In addition, I_J is the interference from the jammer, which can be expressed as

$$I_J(d_J) = P_J (d_J^2 + (H_J - H_V)^2)^{\alpha/2} \frac{(H_V - H_J)}{\sqrt{d_J^2 + (H_V - H_J)^2}} \quad (9.32)$$

where P_J and H_J are the transmit power and height of the jammer, respectively, and d_J is the horizontal distance between the UAV and the jammer. If the SINR experienced at the UAV is smaller than a threshold \mathcal{T}_s , the UAV is regarded as disconnected from the network.

9.2.2 Proposed Algorithm

Problem Formulation

The goal of this work is to find policies to determine the trajectories for UAVs such that the mission completion time is minimized and the constraints are satisfied. Therefore, the problem can be formulated the same as in 9.1.2.

Algorithm

The proposed optimization problem is difficult to solve due to the non-convex constraints, lack of knowledge on the jammer, and the interactions among multiple UAVs. To overcome this difficulty, we can cast the problem into a sequential decision making problem that can be solved by RL. We propose a offline temporal-difference (TD) algorithm with online SINR mapping for multi-UAV path planning with jamming resiliency. The proposed algorithm consists of two modules: 1) offline value network training by TD method with standard experience replay; 2) online SINR mapping by supervised learning; and both modules will be introduced in detail in the following subsections.

Offline Value Network Training

This offline learning module can be implemented on a simulator, therefore reducing the collision risk. The environment can be modeled close to the reality, containing the following information: GBSs which are distributed according to the real deployment; the channel modeled according to real ray-tracing data; a dynamic jammer, which changes its location and transmit power periodically. TD learning is used to train the value network, and the MDP, i.e., $\langle \mathcal{S}, \mathcal{A}, \mathcal{R} \rangle$, formulation for the proposed problem is provided as follows:

- **State Space:** In multi-UAV cellular networks, the UAVs are able to observe the following information from the environment: 1) its own information vector $\mathbf{s}_{i,t}$ (for the i^{th} UAV at time step t); 2) the observable state of the nearest $J_n < J$ UAVs $\mathbf{s}_{i,t}^{jno} = [\mathbf{s}_{j,t}^o : j \in \{1, 2, \dots, J_n\}]$; 3) the experienced SINR $\mathcal{S}_{r_{i,t}}$. Since the policy should not be influenced by the choice of the coordinates, we choose an agent-centric coordinate plane, where the UAV's location is the origin. Then, we need to change the positions from the global frame to the chosen coordinates. In addition, the observed information can be parameterized to provide more information. Hence, the observations are transformed into

$$\begin{aligned}\tilde{\mathbf{s}}_i &= [v_{x_i}, v_{y_i}, \tilde{p}_{d_{x_i}}, \tilde{p}_{d_{y_i}}, d_{d_i}, a_{d_i}, r_i, v_{\max_i}, \phi_i] \\ \tilde{\mathbf{s}}_i^{jno} &= [[\tilde{p}_{x_j}, \tilde{p}_{y_j}, v_{x_j}, v_{y_j}, d_j, a_j] : j \in \{1, 2, \dots, J_n\}] \\ \tilde{\mathcal{S}}_{r_{i,t}} &= L_{w_{i,t}}\end{aligned}$$

where \tilde{p} denotes p in the new coordinates. d_{d_i} and a_{d_i} are the distance and azimuth angle from the typical UAV to its destination. d_j and a_j are the distance and azimuth angle to the j^{th} other UAV. $L_{w_{i,t}}$ is the quantized SINR level. All the information observed by the agent constitutes its joint state

$$\mathbf{s}_{i,t}^{jn} = [\tilde{\mathbf{s}}_{i,t}, \tilde{\mathbf{s}}_{i,t}^{jno}, \tilde{\mathcal{S}}_{r_{i,t}}], \forall t. \quad (9.33)$$

- Action space and the reward function are defined the same as in Section 9.1.3.

The offline value network training can be done using Algorithm 2.

Online SINR Mapping

Along the path to destination, UAVs interact with the cellular network, measure the raw signal from GBSs, and obtain the instantaneous SINR. The empirical instantaneous SINR can be processed to obtain the SINR in (9.30). UAVs with sensors can also observe the positions of the nearby GBSs $\mathbf{s}_B^{jn} = [\mathbf{p}_{B_k} : k \in \{1, \dots, K_n\}]$. Therefore, the UAVs with sensors are able to obtain measurements $\{\langle \mathbf{s}_B^{jn}, \mathcal{S}_r(\mathbf{s}_B^{jn}) \rangle\}$ along their paths.

It is assumed that there is a cloud computing center to where all UAVs in the area can upload their measurements, and the cloud will keep updating the recent measurements in its memory D_w . A DNN, denoted by ξ_w , can be designed to map the position information of nearby GBSs into the SINR level by supervised learning using the recent measurements in memory. The DNN is updated periodically based on how frequently the jammer varies.

- **Input:** The input of the DNN is the parameterized position information vector of the nearby GBSs. By changing the positions into the agent-centric coordinates and processing relative locations into distance and angles, the vector can be transformed into

$$\tilde{\mathbf{s}}_{B_i}^{jn} = [[\tilde{p}_{k_{x_k}}, \tilde{p}_{k_{y_k}}, d_{B_k}, \phi_{B_k}, \theta_{B_k}] : k \in \{1, \dots, K_n\}] \quad (9.34)$$

where d_{B_k} , ϕ_{B_k} , θ_{B_k} are the distance, elevation angle, azimuth angle from the UAV to the k^{th} nearby GBS.

- **Label:** The label of the supervised DNN is the quantized SINR level $L_w(\mathbf{s}_B^{jn})$.
- **Detection:** A simple jammer change detection method can be adopted. More specifically, the cloud can check the accuracy of the DNN periodically on the newly uploaded measurements. The accuracy dropping significantly indicates the changes in the jammer (either its location

or transmit power). Then, the DNN should be updated. From numerical results, this jammer change detection method takes less than 1s.

- **Training:** If the parameters of the DNN ξ_w need to be updated, training can be done by stochastic gradient descent (back-propagation) on mini-batches randomly sampled from D_w for a fixed number of episodes.

Real-Time Navigation

The UAVs can perform real-time navigation with the offline trained value network and online SINR mapping DNN downloaded from the computing cloud.

9.2.3 Numerical Results

In this section, we present the numerical results to evaluate the performance of the proposed algorithm. The environment setting and the construction of the neural networks are similar as that in 9.1.5.

Training

In the offline value network training module, the jammer changes its location or transmit power periodically. Fig. 9.10 shows the accumulated reward per episode during two distinct training. First, we can observe from the figure that the reward in two distinct training can converge to the same level. The relatively larger drops in the convergence phase (after 20000 episodes) are due to the significant changes in the jammer, and the value network can learn fast and recover the reward back to the converged level. Secondly, we can observe that our proposed algorithm can achieve comparable reward level to the upper bound. The upper bound in this figure (presented in green line with squared markers) is the accumulated reward if the UAVs fly straight to their destinations, ignoring the wireless connectivity (i.e. $R_{s_{i,t}} = 0$) and collision avoidance constraints (i.e. $R_{c_{i,t}} = 0$). Note that when these constraints are taken into account, the UAVs need to perform

turns or stops. Therefore, due to the negative reward R_t given to each step and the exploration strategy (i.e. $\epsilon_{\min} = 0.1$), the reward achieved in training is smaller than the upper bound.

In the online SINR mapping module, the DNN is updated periodically using the latest uploaded SINR measurements. Fig. 9.11 presents the accuracy during the online training period. It can be observed that the DNN can adapt fast to the new location/transmit power of the jammer with very high SINR mapping accuracy.

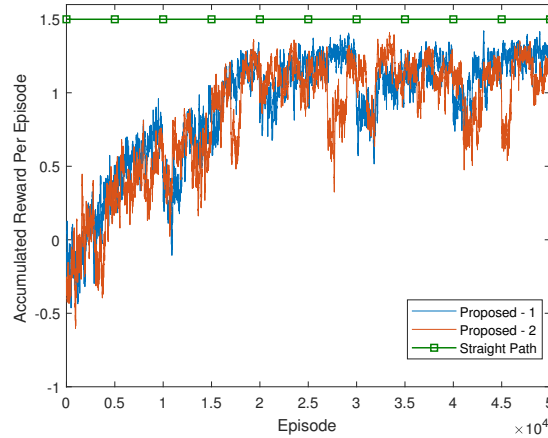


Fig. 9.10: Accumulated reward per episode for two distinct training cases and the straight path scenario, as functions of episode.

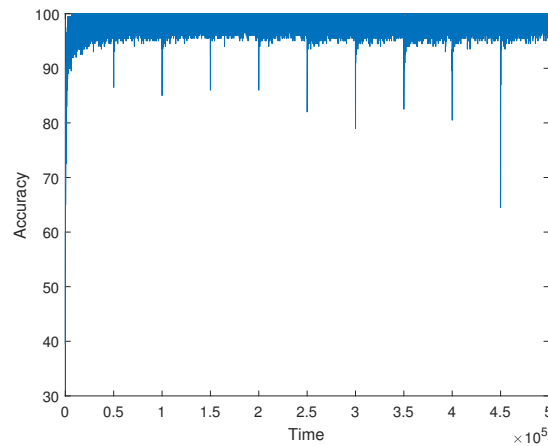


Fig. 9.11: Accuracy of the SINR mapping DNN as a function of training time.

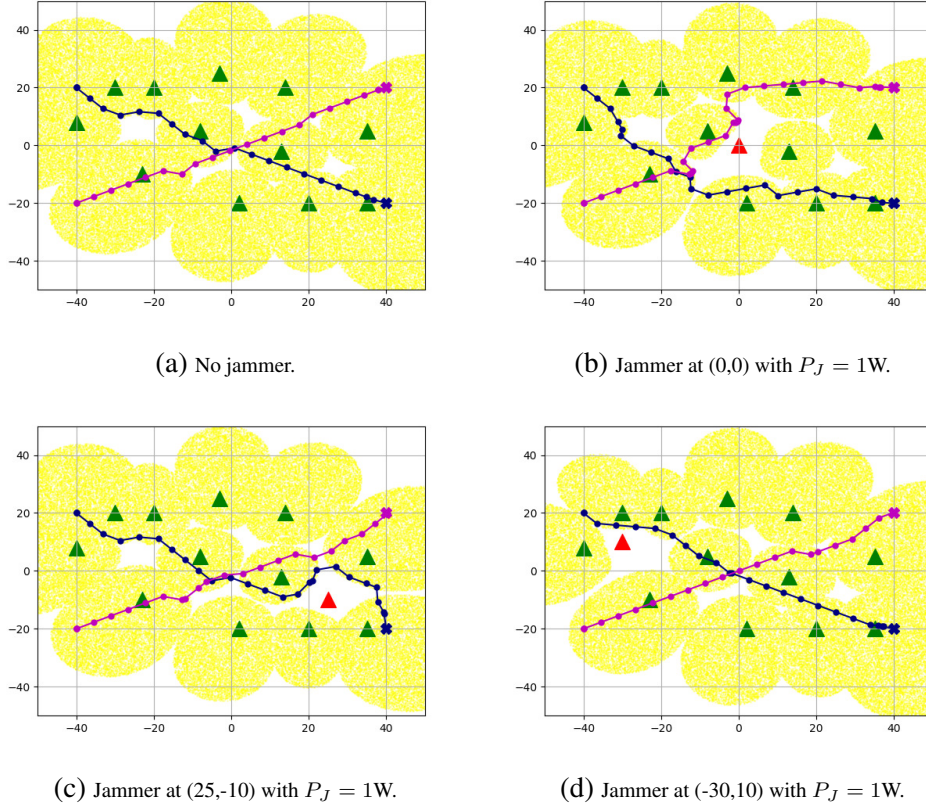


Fig. 9.12: Illustrations of trajectories in environments, where jammer does not exit or the jammer is located at different positions.

Real-Time Navigation

Fig. 9.12 displays the illustrations of real-time navigation trajectories, while also depicting the trajectory changes due to the presence of jammers. In the illustrations of the environment and trajectories, the GBSs and the jammer are marked by green triangles and a red triangle, respectively. The yellow areas indicate the communication coverage zones where the agents are able to connect with the cellular network (i.e., $\mathcal{S}_r \geq \mathcal{T}_s$). UAV trajectories are displayed as lines with dots in different colors, and the destinations are marked with crosses. It can be observed from the figure that jammers can generate disconnection/no-coverage zones (the white areas), and different jammer locations lead to different impact. Due to the jammer presence, the UAVs have to make turns and avoid flying through the no-coverage zones, leading to different trajectories.

To evaluate the performance, we choose the following metrics: 1) success rate, where success

Table 9.3: Performance comparison in terms of success rate, disconnection rate, and collision rate.

	Jammer at (0,0), $P_J = 1W$			Jammer at (25,-10), $P_J = 1W$		
	SR(%)	DR(%)	CR(%)	SR(%)	DR(%)	CR(%)
Proposed Algorithm	92.3	5.6	1.8	94.5	4	1.5
Outdated Map	65.3	33.7	1	77.1	27.5	1.4
Perfectly-Updated Map	94.6	3.2	1.9	94.5	3.3	2.2
	Jammer at (-30,10), $P_J = 1W$			Jammer at (0,0), $P_J = 0.5W$		
	SR(%)	DR(%)	CR(%)	SR(%)	DR(%)	CR(%)
Proposed Algorithm	95.75	3.75	0.5	92.3	6.2	1.2
Outdated Map	78.4	21.2	0.4	73.3	25.5	1.2
Perfectly-Updated Map	96.6	2.7	0.6	95.8	1.9	1.6

indicates one UAV arriving at its destination successfully; 2) disconnection rate, where a disconnection means one UAV being disconnected continuously more than \mathcal{T}_t ; 3) collision rate, which quantifies the collisions among UAVs. Table 9.3 provides performance comparisons with benchmarks, considering the above the three metrics. Two benchmarks are chosen: *outdated map* method in which the UAVs navigate with the trained value network plus the outdated radio map of the environment without jammers; *perfectly-updated map* method in which the UAVs navigate with the value network plus the perfect radio map of the current environment with jammers. The outdated map method does not react to the existence of the jammer, and leads to the performance lower bounds. The perfectly-updated map method is ideal, and achieves the performance upper bound. From the results in the table, we notice that low success rates and high disconnection rates are experienced when the outdated SINR map (which disregards the presence of the jammer) is used. Hence, jammer can have significant impact on the performance. On the other hand, we observe that if the perfect SINR map (which takes into account the interference introduced by the jammer) is utilized, success rates reach above 94% and disconnection rates fall below 3.3%. Hence, perfect knowledge of the SINR map is an effective defensive measure against jamming attacks. We note that even with the perfect map, path planning is performed using the deep RL agent. In our proposed approach, we have the deep RL agent operating with an online SINR learning algorithm. In this case, SINR map can be learned albeit imperfectly. We see in Table I that the proposed

approach achieves almost the same performance levels as in the case of the perfectly updated map, and hence leads to effective jamming resiliency in an online fashion. Finally, we remark that in all cases, collision rates are very small, indicating the efficacy of the RL agent operating under collision constraints.

CHAPTER 10

COLLISION-AWARE UAV TRAJECTORIES FOR DATA COLLECTION VIA REINFORCEMENT LEARNING

10.1 System Model and Problem Formulation

In this section, we first introduce the system model in detail, and then we formulate the path planning optimization problem for data collection.

10.1.1 System Model

We assume that the area of interest is a cubic volume, which can be specified by $\mathbb{C} : \mathbb{X} \times \mathbb{Y} \times \mathbb{Z}$ and $\mathbb{X} \triangleq [x_{\min}, x_{\max}]$, $\mathbb{Y} \triangleq [y_{\min}, y_{\max}]$, and $\mathbb{Z} \triangleq [z_{\min}, z_{\max}]$. There are multiple no-fly zones (obstacles) in the area through which UAVs cannot fly. And the no-fly zones are denoted as $\mathbb{N} : \mathbb{X}^N \times \mathbb{Y}^N \times \mathbb{Z}$.

UAV

In the considered multi-UAV scenario, we choose one UAV as the typical one, whose mission is to collect data from multiple ground IoT nodes. The UAV is modeled as disc-shaped with radius r . Let $\mathbf{p} = [p_x, p_y, H_V]$ denote the 3D position of the UAV, where H_V is the altitude of the UAV which is assumed to be fixed. It is assumed that the typical UAV has specific areas for departure and landing, which can be denoted by \mathbb{S} and \mathbb{D} , respectively. More specifically, $\mathbb{S} : \mathbb{X}^S \times \mathbb{Y}^S \times \mathbb{Z}$, where $\mathbb{X}^S \triangleq [x_{\min}^S, x_{\max}^S]$, $\mathbb{Y}^S \triangleq [y_{\min}^S, y_{\max}^S]$, and $\mathbb{D} : \mathbb{X}^D \times \mathbb{Y}^D \times \mathbb{Z}$, where $\mathbb{X}^D \triangleq [x_{\min}^D, x_{\max}^D]$, $\mathbb{Y}^D \triangleq [y_{\min}^D, y_{\max}^D]$. $\mathbf{p}^S = [p_{sx}, p_{sy}, H_V]$ and $\mathbf{p}^D = [p_{gx}, p_{gy}, H_V]$ are used to denote the coordinates of the starting point and the destination for the typical UAV, respectively. The typical UAV's information forms a vector that consists of the UAV's position, current velocity $\mathbf{v} = [v_x, v_y]$, radius r , destination \mathbf{p}^D , maximum speed v_{\max} , and orientation ϕ , i.e., $\mathbf{s} = [\mathbf{p}, \mathbf{v}, r, \mathbf{p}^D, v_{\max}, \phi] \in \mathbb{R}^{11}$.

In this multi-UAV scenario, there are also J other UAVs traveling within region C . None of the UAVs communicate with each other. Therefore, the missions, destinations, movements, and decision-making policies of other UAVs are unknown. It is assumed that the typical UAV is equipped with a sensor, with which it is able to sense the existence of other UAVs when they are closed than a certain distance. The circular sensing region is denoted by \mathbb{O} . Specifically, if the j^{th} UAV is in \mathbb{O} , some information of this UAV can be known by the typical UAV. The observable information includes the j^{th} UAV's position $\mathbf{p}_j = [p_{x_j}, p_{y_j}, H_V]$, current velocity $\mathbf{v}_j = [v_{x_j}, v_{y_j}]$, and radius r_j , i.e., $\mathbf{s}_j^o = [\mathbf{p}_j, \mathbf{v}_j, r_j] \in \mathbb{R}^6$. The total number of other UAVs in \mathbb{O} is denoted by J^o . It is worth noting that J^o varies over time.

IoT Nodes

In this UAV-assisted network, there are N IoT nodes that need to upload data to the typical UAV via uplink transmission. The n^{th} node has transmit power P_n , and is located at ground position $\mathbf{p}_n = [p_{x_n}, p_{y_n}]$. Each node has a finite amount of data D_{n0}^L that needs to be collected over the entire mission duration of the typical UAV. The IoT nodes have two modes: active mode, if the node still has data to be transmitted; and silent mode, if data upload is completed.

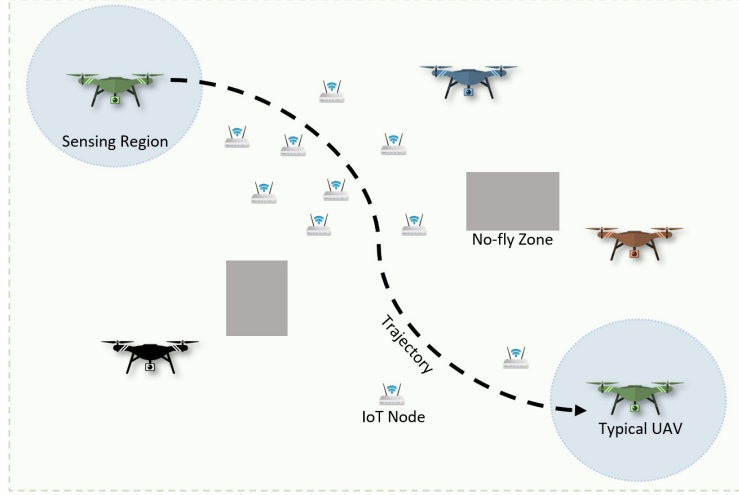


Fig. 10.1: An illustration of data collection in a multi-UAV scenario.

An illustration of the system model is provided in Fig. 10.1.

10.1.2 Channel Model

We assume that all links between the UAV and IoT nodes are LOS. Then, the path loss can be expressed as

$$L(d) = (d^2 + H_V^2)^{\alpha/2} \quad (10.1)$$

where d is the horizontal distance between the ground projection of the UAV and a node, and α is the path loss exponent.

The IoT nodes are assumed to have the omni-directional antenna gain of $G_n = 0$ dB. The UAVs are assumed to have sine antenna pattern in 2.27.

10.1.3 Signal-to-Noise Ratio (SNR) and Rate

The received signal from the n^{th} node to the typical UAV can be expressed as $P_n^r = P_n G_V(d_n) L^{-1}(d_n)$.

With this, the experienced SNR at the UAV if it is communicating with the n^{th} IoT node can be

formulated as

$$S_n \triangleq \frac{P_n}{\mathcal{N}_s} G_V(d_n) L^{-1}(d_n) = \frac{P_n}{\mathcal{N}_s} H_V (d^2 + H_V^2)^{-\frac{1+\alpha}{2}} \quad (10.2)$$

where \mathcal{N}_s is the noise power. The maximum achievable information rate if the SNR is connected with the n^{th} node is

$$R_n^{\max} = \log_2(1 + S_n). \quad (10.3)$$

To support data flows, UAV has to maintain a reliable communication link to the IoT nodes. To achieve this, it is assumed that the experienced SNR at the UAV when connecting with a node should be larger than a certain threshold \mathcal{T}_s . Then, the UAV can communicate with the node successfully. Otherwise, the UAV is not able to collect data from the node. Therefore, considering the amount of data available at each node, D_n^L , the effective information rate according to the SNR threshold \mathcal{T}_s can be given as

$$R_n = \begin{cases} R_n^{\max}, & \text{if } D_n^L \geq \Delta t R_n^{\max} \text{ and } S_n \geq \mathcal{T}_s \\ D_n^L / \Delta t, & \text{if } D_n^L < \Delta t R_n^{\max} \text{ and } S_n \geq \mathcal{T}_s \\ 0, & \text{otherwise,} \end{cases} \quad (10.4)$$

where Δt is time duration for one time step.

10.1.4 Scheduling

Since the typical UAV needs to communicate with multiple nodes, we adopt the standard time-division multiple access (TDMA) model. Then, the UAVs can communicate with at most one node

at each time. Using $q_n \in \{0, 1\}$ to indicate the connection with the n^{th} node, we have

$$\sum_n^N q_n \leq 1. \quad (10.5)$$

The scheduling is according to the largest received signal power strategy, meaning that the UAV is connected with the active node providing the largest P_n^r . We can mathematically express the scheduling strategy as

$$q_n = \begin{cases} 1, & \text{if } n = \underset{n' \in \{\text{active nodes}\}}{\operatorname{argmax}} P_{n'}^r, \\ 0, & \text{otherwise.} \end{cases} \quad (10.6)$$

10.1.5 Problem Formulation

We can partition each mission duration in the discrete time domain to a number of time steps $t \in [0, T]$, with each time step describing a period of Δt . Now, the integer-valued t is used to denote each time step. We next consider the following realistic and practical constraints in the design of UAV trajectories:

Collision Avoidance Constraints

For collision avoidance purposes, the minimum distance between the typical UAV and any other UAVs should not be smaller than the sum of their radii all the time. In addition, it is important for UAVs to navigate while staying free of collisions with obstacles and non-fly zones. In this setting, we can write the collision avoidance constraints as

$$\|\mathbf{p}_t - \mathbf{p}_{jt}\|_2 > r + r_j, \forall j, \forall t, \quad (10.7)$$

$$\mathbf{p}_t \notin \mathbb{N}, \forall t, \quad (10.8)$$

where \mathbf{p}_t is the position of the typical UAV at time step t , and \mathbf{p}_{jt} is the position of the j^{th} UAV at time t . (10.8) is to avoid collision with the obstacles and no-fly zones.

Mission Completion Deadline Constraint

A UAV with a mission has to complete the required tasks in a certain time period. Moreover, power limitation also restricts the UAV's flight time. Overall, the UAV has a mission completion deadline constraint that can be described as

$$T \cdot \Delta t \leq \mathcal{T}_t \quad (10.9)$$

where T is the total steps in discrete time domain, and \mathcal{T}_t is the maximum mission completion time.

Kinematic Constraints

In practice, the kinematic constraints should be considered in operating UAVs. We impose the speed and rotation constraints as

$$v_{s_t} \leq v_{\max}, \forall t \quad (10.10)$$

$$|\phi_t - \phi_{t-1}| \leq \Delta t \cdot \mathcal{T}_r, \forall t \quad (10.11)$$

where v_{\max} is the maximum speed of the UAV, and \mathcal{T}_r is the maximum rotation angle in unit time period.

Start and Destination Constraints

A UAV with a mission should fly from a given start point and arrive at a required destination, and hence we have

$$\mathbf{p}_0 = \mathbf{p}^S, \mathbf{p}_T = \mathbf{p}^D. \quad (10.12)$$

TDMA Constraint

Due to the utilization of TDMA, the UAV can communicate with at most one node at each time, and the constraint is given in (10.5).

Our goal is to maximize the collected data from all nodes subject to these constraints. Therefore, the objective function can be formulated as

$$\begin{aligned}
 (\text{P1}) : \operatorname{argmax}_{\{\mathbf{p}_t, \forall t\}} \quad & \sum_{t=0}^T \sum_{n=1}^N q_{nt} \Delta t R_{nt} \\
 \text{s.t.} \quad & (10.5), (10.7), (10.8), (10.9), (10.10), (10.11), (10.12).
 \end{aligned}$$

10.2 Algorithm

In this section, we first describe the RL formulation of path planning for data collection in a multi-UAV scenario, and then explain the proposed D3QN path planning algorithm in detail.

10.2.1 Reinforcement Learning Formulation

Considering the objective function in (P1) and the constraints in (10.5)-(10.12), we can translate the considered problem into an MDP, and the tuple $\langle \mathcal{S}, \mathcal{A}, \mathcal{R} \rangle$ is explained in detail below:

State

In multi-UAV scenarios, the typical UAV is able to obtain the following information:

- Its own full information vector \mathbf{s}_t in time step t .
- The observable information vector of other UAVs in \mathbb{O} , which is the sensing region of the typical UAV. The total number of observed other UAVs at time step t is $J_t^o \geq 0$, and the joint information vector can be expressed as $\mathbf{s}_t^o = [\mathbf{s}_{jt}^o : j \in \{1, 2, \dots, J_t^o\}]$.
- The location information \mathbf{p}_{nt} of each IoT node, the amount of remaining data D_{nt}^L at each

node, and the received signal power P_{nt}^r from each node. The joint vector is denoted by $\mathbf{s}_t^n = [\mathbf{s}_{nt}^n : n \in \{1, \dots, N\}]$, where $\mathbf{s}_{nt}^n = [\mathbf{p}_n, D_{nt}^L, P_{nt}^r]$.

- The available time left for the given mission, s_{tt} .

Since the typical UAV can only observe other UAVs inside its sensing region \mathbb{O} , the total number of observed other UAVs J_t^o may vary over time. However, the size of the state needs to be fixed to be the input of the DNN. Thus, we only consider the observable information vectors of the nearest J^c (which is a fixed positive integer) other UAVs. In addition, the number of nodes in the environment may be different for different missions. Thus, we only consider the information vectors of the nearest N^c active nodes. On the other hand, the policy should not be influenced by the choice of coordinates. Therefore, we parameterize the position information into agent-centric coordinates, in which the current location of the typical UAV is regarded as the origin. We can also process the observations to provide more information. Hence, the observed information vectors can be transformed into

$$\begin{aligned}\tilde{\mathbf{s}}_t &= [v_{x_t}, v_{y_t}, \tilde{p}_{gx_t}, \tilde{p}_{gy_t}, d_{g_t}, a_{g_t}, r, v_{\max}, \theta_t] \\ \tilde{\mathbf{s}}_{jt}^o &= [\tilde{p}_{x_{jt}}, \tilde{p}_{y_{jt}}, v_{x_{jt}}, v_{y_{jt}}, d_{jt}^o, a_{jt}^o, r_j], \text{ for } j \in \{1, 2, \dots, \min(J_t^o, J^c)\} \\ \tilde{\mathbf{s}}_{nt}^n &= [\tilde{p}_{x_{nt}}, \tilde{p}_{y_{nt}}, d_{nt}^n, a_{nt}^n, D_{nt}^L, P_{nt}^r], \text{ for } n \in \{1, \dots, N^c\}\end{aligned}$$

where \tilde{p} is the transformed p in the new coordinate. d_{g_t} and a_{g_t} are the distance and azimuth angle of the destination, respectively. d_{jt}^o and a_{jt}^o are the distance and azimuth angle of the j^{th} other UAV, respectively. d_{nt}^n and a_{nt}^n are the distance and azimuth angle of the n^{th} node, respectively. Note that we do zero padding if $J_t^o \leq J^c$ or the number of active nodes is smaller than N^c . Then, the joint parameterized state vector at t can be expressed as

$$\tilde{\mathbf{s}}_t^{jn} = [\tilde{\mathbf{s}}_t, [\tilde{\mathbf{s}}_{jt}^o, j \in \{1, \dots, J^c\}], [\tilde{\mathbf{s}}_{nt}^n, n \in \{1, \dots, N^c\}], s_{tt}]. \quad (10.13)$$

Action

In an ideal setting, the agent can travel in any direction at any time. However, in practice, kinematic constraints in (10.10)-(10.11) restrict the agent's movement and should be taken into account. Given these constraints, permissible velocities $[v_s, \phi_r]$ are sampled to built a velocity-set, where v_s is the permissible speed, and the ϕ_r is the permissible rotation angle. The action a is the index of each velocity in the velocity-set.

Reward

The reward can be designed according to the objective function and the constraints, and the design plays an important role on the learning speed and quality. The reward function of this path planning problem for data collection in the multi-UAV scenario can be expressed as

$$\mathcal{R}_t = \mathcal{R}_{dt} + \mathcal{R}_{ct} + \mathcal{R}_{ot} + \mathcal{R}_{tt} + \mathcal{R}_{gt} + \mathcal{R}_{st}. \quad (10.14)$$

The first term \mathcal{R}_{dt} is related to the data collected from the nodes during next time duration Δt . This reward term is used to encourage the UAV to collect data from the IoT nodes, and can be expressed as

$$\mathcal{R}_{dt} = \alpha_1 \times \left(\sum_{n=1}^N D_{nt}^L - \sum_{n=1}^N D_{nt+1}^L \right). \quad (10.15)$$

\mathcal{R}_{ct} is the term introduced to penalize collision with other UAVs and encourage the typical UAV stay further away from the other UAVs. This term can be formulated as

$$\mathcal{R}_{ct} = \begin{cases} -\alpha_2, & \text{if } d_{t_{\min}} \leq r + r_j, \\ -\alpha_2 \times \left(1 - \frac{d_{t_{\min}} - r - r_j}{d_b}\right), & \text{if } r + r_j < d_{t_{\min}} \leq d_b + r + r_j, \\ 0, & \text{otherwise,} \end{cases} \quad (10.16)$$

where $d_{t_{\min}}$ is the minimum distance from the typical UAV to other UAVs during next time duration Δt , and d_b is a constant that denotes the distance buffer. \mathcal{R}_{ot} is to penalize the collision with the obstacles or entering non-fly zones, and can be expressed as

$$\mathcal{R}_{ot} = \begin{cases} -\alpha_3, & \text{if } \mathbf{p}_{t+1} \in \mathbb{N}, \\ 0, & \text{otherwise.} \end{cases} \quad (10.17)$$

\mathcal{R}_{tt} is the reward related to mission completion deadline constraint, and it encourages the UAVs to arrive their destinations within the allowed duration of time, and can be formulated as

$$\mathcal{R}_{tt} = \begin{cases} \alpha_4 \times (s_{tt+1} - T_{gt+1}^{\min}), & \text{if } s_{tt+1} < T_{gt+1}^{\min}, \\ 0, & \text{otherwise,} \end{cases} \quad (10.18)$$

where s_{tt+1} is the available time left for the given mission, and $T_{gt+1}^{\min} = d_{gt+1}/v_{\max}$ is the minimum time duration needed to reach destination at time step $t + 1$ and d_{gt+1} is the distance to destination at time step $t + 1$. R_{gt} is the reward given for arriving the destination, and

$$\mathcal{R}_{gt} = \begin{cases} \alpha_5, & \text{if } \mathbf{p}_{t+1} = \mathbf{p}^D, \\ 0, & \text{otherwise.} \end{cases} \quad (10.19)$$

The last term $\mathcal{R}_{st} = -\alpha_6$ is a step penalty for each movement, and it is used to encourage fast arrival. Note that $\alpha_{1\sim 6}$ are positive constants, and can be varied to adjust the weight or emphasis of each reward term to adapt to different mission priorities.

10.2.2 D3QN Path Planning Algorithm for Data Collection

The main algorithm is summarized in Algorithm 4, where the input consists of the parameters of the constraints and the output is the policy, i.e., a well-trained DNN ξ . In the training phase, we first initialize the replay memory, the evaluation network parameters and the target network

parameters (line 1 - line 3). We also build an action space \mathcal{A} based on the kinematic constraints (line 4). In each training episode, the typical UAV navigates around other UAVs and obstacles to arrive its destination, while collecting data from ground IoT nodes. Particularly, at the beginning of each episode, the environment and the UAV's mission are reset (line 6), and the reset parameters are

- the starts and destinations of the typical UAV;
- the locations of IoT nodes;
- the number of IoT nodes;
- the amount of data to be collected from each node;
- the number of other UAVs;
- the starts and destinations of other UAVs.

Then, at each time step t , the typical UAV observes the environment, obtains the observation vector \mathbf{s}_t^{jn} , and parameterizes the vector following the new agent-centric coordinate as $\tilde{\mathbf{s}}_t^{jn}$ (line 8 - line 9). Using an ϵ -greedy policy, the typical UAV selects a random action with probability ϵ from \mathcal{A} (line 12), or follows the policy greedily otherwise (line 14). The Q-value can be obtained using the evaluation network ξ according to equation (2.40). After executing the chosen action, the typical UAV receives reward \mathcal{R}_t from the environment according to equation (10.14), and it observes the new state \mathbf{s}_{t+1}^{jn} from the updated environment (line 15). Then the replay memory can be updated with transition tuple $(\tilde{\mathbf{s}}_t^{jn}, \mathbf{a}_t, \mathcal{R}_t, \tilde{\mathbf{s}}_{t+1}^{jn})$ (line 17). To train the evaluation network ξ , a minibatch of N_b tuples can be randomly sampled from replay memory (line 18). Then, ξ can be updated by stochastic gradient descent (back-propagation) on the sampled minibatch (line 19 - line 22), and the target network parameters ξ^- can be updated from ξ for every N_r steps (line 23). The episode ends when the UAV arrives its destination or exceeds its mission deadline. Line 6 - line 23 can be repeated for N_e episodes.

After training, we obtain a policy, i.e., a well-trained DNN ξ , with which the UAV can perform real-time navigation.

Algorithm 4: D3QN Path Planning Algorithm for Data Collection

Input: $\mathcal{T}_s, \mathcal{T}_t, v_{\max}, \mathcal{T}_r$

- 1 Initialize replay memory \mathcal{D}
- 2 Initialize evaluation network ξ (including ξ^V and ξ^A)
- 3 Initialize target network ξ^- (including ξ^{V-} and ξ^{A-}) by copying from ξ
- 4 $\mathcal{A} \leftarrow \text{sampleActionSpact}(v_{\max}, \mathcal{T}_r)$
- 5 **for** *episode* = 0: *total episode* N_e **do**
- 6 $\mathcal{E} \leftarrow \text{resetEnvironment}()$
- 7 **while not done do**
- 8 $\mathbf{s}_t^{jn} \leftarrow \text{observeEnvironment}(\mathcal{E})$
- 9 $\tilde{\mathbf{s}}_t^{jn} \leftarrow \text{parameterizeState}(\mathbf{s}_t^{jn})$
- 10 $c \leftarrow \text{randomSample}(\text{Uniform}(0,1))$
- 11 **if** $c \leq \epsilon$ **then**
- 12 $\mathbf{a}_t \leftarrow \text{randomSample}(\mathcal{A})$
- 13 **else**
- 14 $\mathbf{a}_t \leftarrow \underset{\mathbf{a}' \in \mathcal{A}}{\text{argmax}} Q(\tilde{\mathbf{s}}_t^{jn}, \mathbf{a}'; \xi)$
- 15 $\mathcal{R}_t, \mathbf{s}_{t+1} \leftarrow \text{executeAction}(\mathbf{a}_t)$
- 16 $\tilde{\mathbf{s}}_{t+1}^{jn} \leftarrow \text{parameterizeState}(\mathbf{s}_{t+1}^{jn})$
- 17 Update \mathcal{D} with tuple $(\tilde{\mathbf{s}}_t^{jn}, \mathbf{a}_t, \mathcal{R}_t, \tilde{\mathbf{s}}_{t+1}^{jn})$
- 18 Sample a minibatch of N_b tuples $(\mathbf{s}, \mathbf{a}, \mathcal{R}, \mathbf{s}') \sim \text{Uniform}(\mathcal{D})$
- 19 **for each tuple** j **do**
- 20 Calculate target

$$y_j = \begin{cases} \mathcal{R}, & \text{if } \mathbf{s}' \text{ is terminal,} \\ \mathcal{R} + \gamma Q(\mathbf{s}', \underset{\mathbf{a}'}{\text{argmax}} Q(\mathbf{s}', \mathbf{a}'; \xi); \xi^-), & \text{o.w.} \end{cases}$$
- 21 Do a gradient descent step with loss $E[(y_j - Q(\mathbf{s}, \mathbf{a}; \xi))^2]$
- 22 Update $\xi^- \leftarrow \xi$ every N_r steps
- 23 **return** ξ

10.3 Numerical Results

In this section, we present the numerical and simulation results to evaluate the performance of the proposed algorithm. The considered performance metrics are the following: 1) success rate (SR), and a success means the UAV arrives its destination within mission completion deadline; 2) data collection rate (DR), which is the percentage of collected data within successful missions; 3) data collection and success rate (DSR), which is the product of data collection percentage and success rate; and 4) collision rate (CR), and a collision event occurs when the typical UAV collides with any of the other UAVs in the environment. In the illustration of real-time navigation scenarios, the departure and landing areas of the typical UAV are displayed by blue and green areas, respectively. The no-fly zones (obstacles) are presented in gray areas. The IoT nodes are marked by green triangles. The trajectories of the typical UAV are presented by navy lines with dots, and the trajectories of other UAVs in the environment are depicted in red lines with dots. The destination of each mission is marked by a navy cross in the landing area. Note that since the UAVs may arrive at the same location at different times, they do not necessarily collide even if their trajectories intersect. In the simulations, other UAVs use optimal reciprocal collision avoidance (ORCA) [200] in choosing actions and determining their trajectories.

10.3.1 Environment Setting and Hyperparameters

Since the agents fly at the same altitude, the area of interest becomes two-dimensional. In the simulations, the UAV flies at height $H_V = 50\text{m}$. The size of the area of interest is scaled to a (100×100) region. The IoT nodes have same transmit power of $P = 1\text{ dBm}$. Noise power is $\mathcal{N}_s = 10^{-6}$. SNR threshold is set at $\mathcal{T}_s = -5\text{ dB}$ (unless stated otherwise). Mission completion deadline is $\mathcal{T}_t = 100\text{s}$ (unless stated otherwise). Kinematic constraints are $v_{\max} = 5$ in the scaled form and $\mathcal{T}_r = \pi/3$. The radius of the UAV's sensing region is 10, N^c is 5, and J^c is set to be 2.

Fig. 10.2 shows the accumulated reward per episode in training with different DNN structures. We can observe from the figure that one-layer and two-layer structures can achieve similar con-

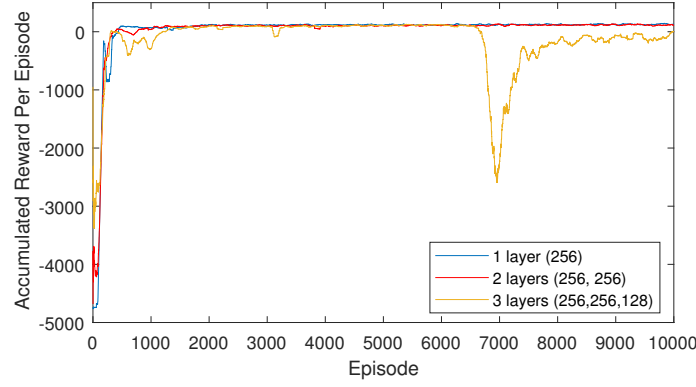


Fig. 10.2: Accumulated reward per episode in training with different DNN structures.

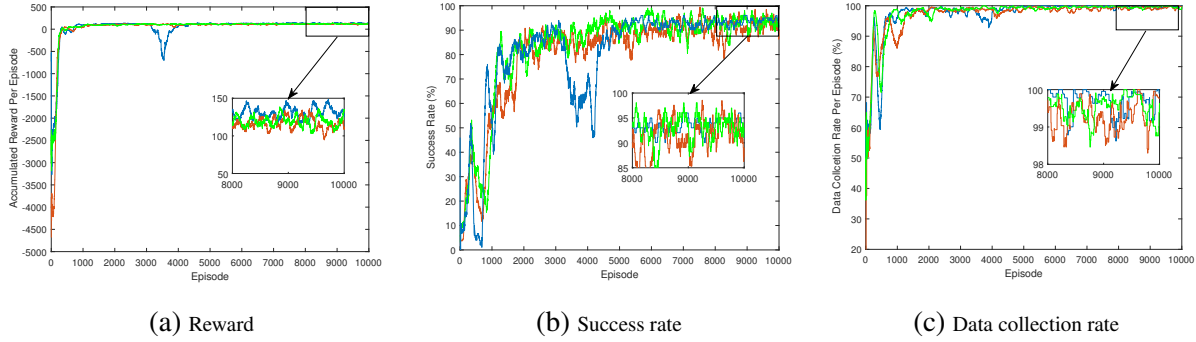


Fig. 10.3: Accumulated reward per episode, average success rate per 100 episodes and data collection rate per episode for different training cases.

vergence speeds and reward performance, while the reward from DNN with a three-layer structure drops after 6500 episodes and then grows back. Therefore, we choose to use two-layer DNN of size (256, 256). ReLU function is used as the activation function, Batch-normalization is used for each layer, and Adam optimizer is used to update parameters with learning rate 0.0003. Batch size is 256, and the regularization parameter is 0.0001. The exploration parameter ϵ decays linearly from 0.5 to 0.1. The replay memory capacity is 1000000.

10.3.2 Training

The total number of training episodes is 10000. In each episode, the following system parameters are randomly chosen from the corresponding regions and sets of values:

- the starts and destinations of the typical UAV $\mathbf{p}^S \in \mathbb{S}$ and $\mathbf{p}^D \in \mathbb{D}$;

- the locations of ground IoT nodes $\mathbf{p}_n \in \mathbb{C}$;
- the number of IoT nodes $N \in [5, 10]$;
- the amount of data to be collected from each node $D_0^L \in [1, 3]$ data units;
- the number of other UAVs $J \in [2, 10]$;
- the starts and destinations of other UAVs $\mathbf{p}_j \in \mathbb{C}$.

Figs. 10.3 (a), (b) and (c) show the accumulated reward per episode, success rate per 100 episodes and data collection rate per episode, respectively, during different training sessions with two-layer DNN. These figures show that in different training sessions, similar performances (in terms of the convergence speed and attained levels of performance metrics) are achieved, indicating the stability of the proposed algorithm. In addition, the SR eventually converges to around 92.5%, and the DR reaches 99.5%, even with the exploration strategy (i.e., $\epsilon_{\min} = 0.1$). The simulation is implemented on a Windows 10 with Intel Core i7-8753h CPU. In total, the training algorithm converges after approximately 6000 episodes for this multi-UAV scenario with highly varying parameters.

10.3.3 Testing of Navigation in Different Scenarios

With the learned policy, the UAV can perform real-time navigation in different scenarios, regarding the various parameters described in the previous subsection. We note that all the testing in this subsection uses the same policy, i.e., the policy can adapt to various missions and scenarios without further training.

Different number of IoT nodes

Fig. 10.4 displays illustrations of navigation in different scenarios in which $N \in [8, 10]$ IoT nodes are randomly located, $D_0^L = 1$ data unit, and $J \in [2, 10]$. Fig. 10.4 shows that for different numbers and locations of IoT nodes, different numbers and locations of other UAVs, and different

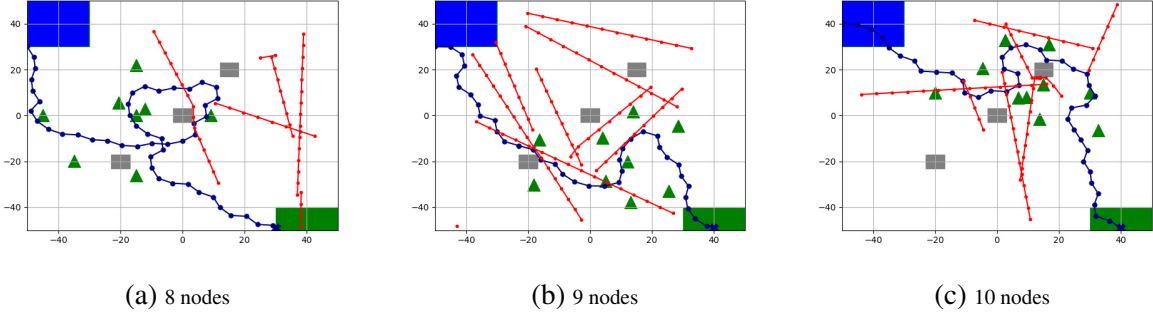


Fig. 10.4: Illustrations of navigation in different scenarios that $N \in \{8, 9, 10\}$ nodes are randomly located, and $D_0^L = 1$ data unit, $J \in [2, 10]$.

start points and destinations, the UAV can adjust its trajectory to collect data from distributed IoT nodes with the trained policy. Table 10.1 provides the SR, DR, DSR and CR performances in testing for different number of nodes from which data needs to be collected. The performances are averaged over 5000 random realizations (in each of which, we have $D_0^L \in [1, 3]$, $J \in [2, 10]$, and all UAVs have random starting points and destinations). Overall, Table 10.1 shows that the proposed algorithm can achieve above 91% success rate (for tight mission completion deadline constraint of \mathcal{T}_t) and over 99.8% DR when $N \in [5, 10]$. With increasing number of nodes, generally the UAV needs to plan a longer trajectory to get close to each node to achieve reliable communication ($S_n \geq \mathcal{T}_n$), leading to relatively longer flight durations and higher risk for collision. Therefore, when N increases, SR decreases due to the increase in CR and the increase in flight duration. In addition, when we compare row 1 (smaller \mathcal{T}_t) and row 5 (larger \mathcal{T}_t), we notice that higher SR is obtained if the mission completion deadline is relaxed.

Table 10.1: SR, DR, DSR and CR performance when different number of nodes (N) need to upload data, and $D_0^L \in [1, 3]$, $J \in [2, 10]$.

	$N=5$	$N=6$	$N=7$	$N=8$	$N=9$	$N=10$
SR(%) ($\mathcal{T}_t = 100s$)	95.5	94.4	93.8	92.9	92.5	91.5
DR(%)	99.9	99.8	99.8	99.8	99.8	99.8
DSR(%)	95.4	94.21	93.61	95.45	92.71	91.31
CR(%)	3.3	3.4	3.9	3.9	3.9	3.7
SR(%) ($\mathcal{T}_t = 200s$)	96.7	96.2	95.8	95.8	95.8	95.9

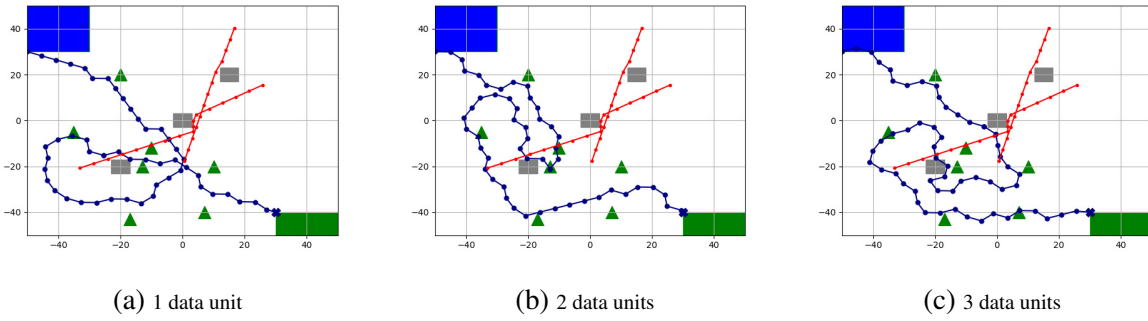


Fig. 10.5: Illustrations of navigation in different scenarios that $D_0^L \in \{1, 2, 3\}$ data units need to be collect at each node, and $N = 7$, $J = 2$.

Different amount of data at each node

Fig. 10.5 depicts illustrations of navigation in different scenarios in which $D_0^L \in [1, 3]$ data units need to be collect from each node. To display the influence of the amount of data to be collected, we fix the number of nodes as $N = 7$ and the number of other UAVs as $J = 2$ in the illustrations. Due to the different amount of data to be collected at each node, the UAV needs to fly around each node over different duration of time to complete the data collection, leading to different trajectories. Table 10.2 provides the SR, DR, DSR, and CR performance in testing, when the values of D_0^L are different. The rates are averaged over 5000 random realizations (in each of which $N \in [5, 10]$, $J \in [2, 10]$, and all UAVs have random starting points and destinations). We observe similar performance levels as in Table 10.1, i.e., when there is more data to collect, the UAV needs a longer trajectory and a longer time period to complete the mission, leading to higher CR and lower SR.

Table 10.2: SR, DR, and DSR performance when different amount of data D_0^L needs to be collected from each node, and $N \in [5, 10]$, $J \in [2, 10]$.

	$D_0^L=1$	$D_0^L=2$	$D_0^L=3$
SR(%)	94.9	93.7	92.8
DR(%)	99.8	99.8	99.7
DSR(%)	94.71	93.51	92.52
CR(%)	2.8	3.7	3.9

Different number of other UAVs

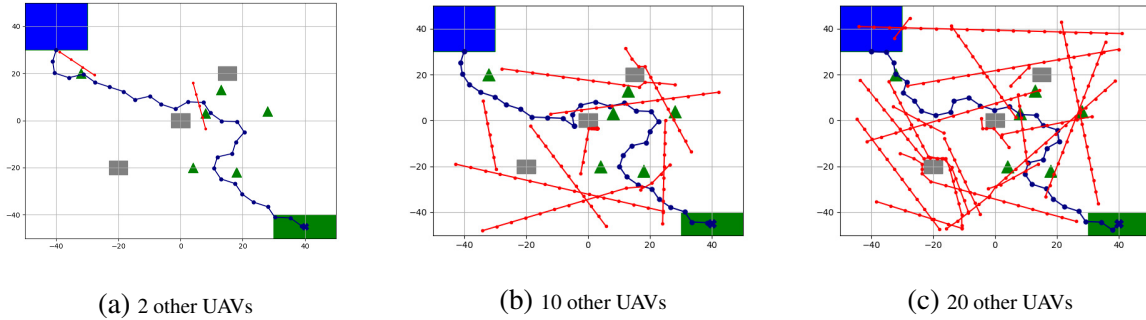


Fig. 10.6: Illustrations of navigation in different scenarios involving $J \in \{2, 10, 20\}$ other UAVs, and $N = 6$, $D_0^L = 1$ data unit.

Fig. 10.6 presents illustrations of navigation in scenarios with different number of other UAVs $J \in \{2, 10, 20\}$. Again, to display the impact of different values of J , we fix $N = 6$ and $D_0^L = 1$ in the illustrations. From Fig. 10.6, we can observe that due to the different locations and numbers of other UAVs, the typical UAV makes decisions to avoid collisions, leading to different trajectories. Table 10.2 presents the CR, SR, and DR performances as J varies, considering three different hyperparameter settings: setting 1 (S1) $\alpha_2 = 10$, $d_b = 0.2$, $T_t = 100$ s; setting 2 (S2) $\alpha_2 = 30$, $d_b = 1$, $T_t = 200$ s, and setting 3 (S3) $\alpha_2 = 50$, $d_b = 10$, $T_t = 200$ s. The rates are averaged over 5000 random realizations (with $N \in [5, 10]$, $D_0^L \in [1, 3]$, and all UAVs having random starting points and destinations). From the table, we note that with increasing number of other UAVs, the collision rate grows due to higher risk of collision. When CR performances in the three settings are compared, we can observe that if the mission completion deadline is loosened, we can increase the distance buffer, d_b , between two UAVs, and increase the penalty for collision, α_2 , to reduce CR. With setting 3, 0.9% CR can be achieved for crowded scenario with $J = 12$. This observation indicates that the hyperparameters can be tuned to adapt to different mission priorities.

To show the importance of considering collision avoidance in the presence of an arbitrary number of other UAVs in the environment, Fig. 10.7 compares the CR levels achieved with the proposed algorithm with considers collision avoidance in training and the learning algorithm that does not address collision avoidance with other UAVs in training. The figure shows us that if colli-

sion avoidance is not considered, we have significantly higher CR than the proposed algorithm, and also the gap between two methods becomes larger with increasing number of other UAVs. These observations indicate that the algorithms, which do not consider the existence of other UAVs or only consider fixed number of known UAVs, may lead to high collision risk in crowded scenarios, and the proposed algorithm greatly reduces that risk.

Table 10.3: CR, SR, and DR performance when different number of other UAVs J exist, and $N \in [5, 10]$, $D_0^L \in [1, 3]$.

		$J=2$	$J=4$	$J=6$	$J=8$	$J=10$	$J=12$
S1	CR(%)	1	2.4	3.5	5	6.3	7.9
	SR(%)	96	94.6	93.9	92.2	91.5	90.7
	DR(%)	99.8	99.8	99.8	99.8	99.8	99.9
S2	CR(%)	0.4	0.8	1.7	1.9	2.5	3.2
	SR(%)	94.4	94	92.7	93.2	92.6	91.8
	DR(%)	99.8	99.8	99.8	99.8	99.8	99.8
S3	CR(%)	0.2	0.3	0.4	0.5	0.6	0.9
	SR(%)	99	98.8	98.8	98.8	98.4	98.2
	DR(%)	99.7	99.7	99.7	99.7	99.8	99.7

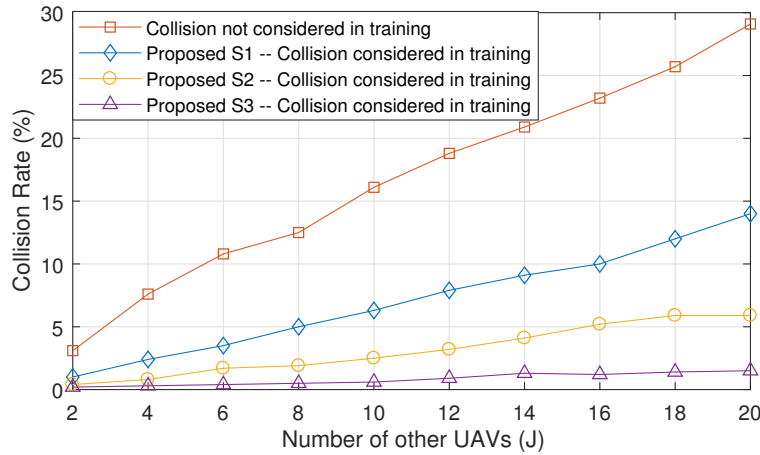


Fig. 10.7: Collision rate comparison in testing between two methods: 1) the proposed approach with setting 1 and setting 2, in which the collision avoidance in the presence of arbitrary number of other UAVs is taken into account in training; and 2) the approach in which collision with other UAVs is not considered in training.

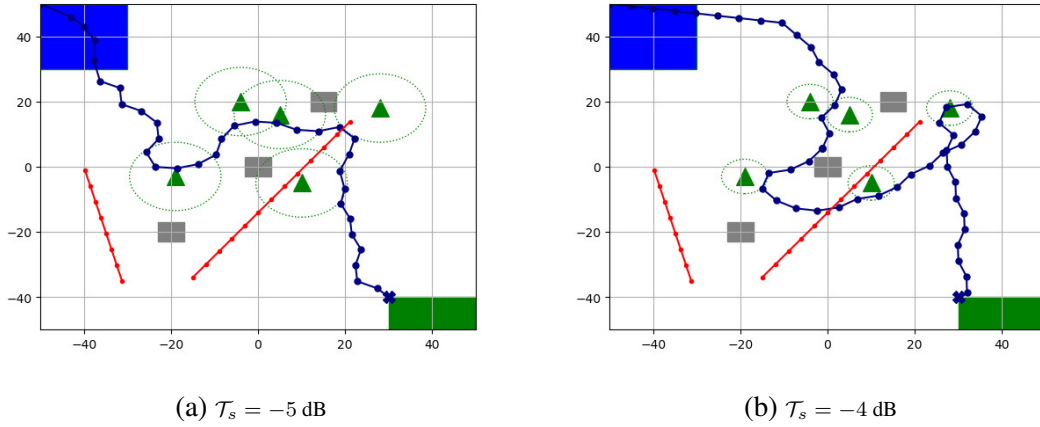


Fig. 10.8: Illustrations of navigation when SNR threshold \mathcal{T}_s is different, and $N = 5$, $D_0^L = 1$ data unit, $J = 2$.

10.3.4 Impact of the SNR Threshold

Fig. 10.8 displays the influence of the values of the SNR threshold \mathcal{T}_s on the UAV trajectories. Note that the UAV is able to achieve reliable communication with an IoT node only if the UAV experiences an SNR that exceed the threshold, i.e., $S \geq \mathcal{T}_s$ for that connection. Since SNR is a function of the distance between the UAV and a node, \mathcal{T}_s can be converted to a distance threshold. Therefore, different values of \mathcal{T}_s lead to different distance requirements for reliable connection. The green dashed circles in Fig. 10.8 approximately indicate the area inside which we have $S \geq \mathcal{T}_s$. As shown in Fig. 10.8, the UAV has to reach each circle in order to collect data from the corresponding node. We observe that with higher \mathcal{T}_s (Fig. 10.8 (b) compared with Fig. 10.8 (a)), the UAV needs to reach closer to each node for data collection, leading to different trajectories for the same mission.

10.3.5 Comparison with Other Algorithms

Table 10.4 presents the performances of different deep reinforcement learning algorithms, i.e., D3QN, Dueling DQN, DDQN and DQN, for data collection in multi-UAV scenarios. It can be clearly observed that D3QN has better performance than the other three, in terms of SR, DR, SDR and CR, although the performances are not substantially different. It is worth noting that we have

observed in training sessions that the reward of Dueling DQN, DDQN, and DQN may drop after a certain number of episode, while D3QN does not have this issue, indicating that D3QN is more stable than the other three algorithms when solving the considered problem.

Table 10.4: SR, and DR, DSR and CR performance of different algorithms, when $N \in [5, 10]$, $D_0^L \in [1, 3]$ data unit and $J \in [2, 10]$.

	SR(%)	DR(%)	SDR(%)	CR(%)
D3QN	94.1	99.8	93.91	3.5
Dueling DQN	93.5	99.7	93.22	4
DDQN	92.5	99.8	92.31	4.3
DQN	90.8	99	89.89	4.2

CHAPTER 11

CONCLUSION AND FUTURE DIRECTIONS

11.1 Summary

In this thesis, we have studied the performance analysis and learning algorithms in advanced wireless networks.

In Chapter 3, we have provided a framework to compute the SINR coverage probability in a K -tier heterogeneous downlink mmWave cellular network with user-centric small cell deployments. A heterogeneous network model is considered, with BSs in each tier being distributed according to PPPs, while UEs being deployed according to a PCP. Distinguishing features of mmWave have been incorporated into the analysis, including directional beamforming and a sophisticated path loss model addressing both LOS and NLOS transmissions. In addition, a D -ball approximation is applied, to characterize the blockage model, with different path loss exponents being assigned to LOS and NLOS links. We have determined general expressions for the association probability of each tier. Simplified association probability expressions for several special cases are provided to give more insight on the impact of different system parameters. We have also characterized the Laplace transforms of the interferences and derived the SINR coverage probability of the entire network using the stochastic geometry framework. The obtained analytical results are general, and they can be applied to any PCP distribution. We have specialized the results to two popular

PCPs, namely (i) Thomas cluster process, and (ii) Matérn cluster process. In addition, through numerical results, we have provided some interfering insights. We also demonstrated that when the cluster size tends to infinity, our PCP-based model specializes to a PPP-based model. Moreover, we extend our work to more general cases, i.e. when more practical antenna gain patterns are considered and when the shadowing is taken into account. Finally, the analytical and numerical results demonstrate that considering the correlation between the UE and BS locations is important when modeling the UE distribution, but the type of PCP does not have significant impact. The type of small-scale fading (e.g., Nakagami vs. Rayleigh fading) also has limited influence on the coverage performance of our model, while interference plays an important role. Moreover, we show that several system parameters have significant impact on coverage probability, e.g., coverage performance can be improved, by decreasing the size of UE clusters around BSs (or equivalently having UEs more compactly clustered), decreasing the beamwidth of the main lobe, or increasing the main lobe directivity gain. In addition, the effects of the biasing factor of the small-cell BSs is investigated. An extension to the dense networks is also addressed. In particular, we have shown that our analysis is applicable to dense networks, in which the small-cell BSs play an important role in terms of the coverage performance. Analysis of the uplink performance of this heterogeneous mmWave cellular network model is interesting and remains as future work. Investigating a hybrid network including both PCP and PPP distributed UEs is also considered as future work.

In Chapter 4, we have studied a K -tier heterogeneous mmWave uplink cellular network with clustered UEs. In particular, the correlation between the locations of the user UEs and BSs is characterized according to a Gaussian distribution, leading to the Thomas cluster processes. Specific and practical LOS and NLOS models are adopted with different parameters for different tiers. We have first characterized the PDFs and CCDFs of different distances from BSs to UEs. Then, we have considered the coupled association strategy, meaning that the UEs are associated with the same BS for both downlink and uplink. Largest long-term averaged biased received power criterion is considered in this chapter, and general expressions for association probabilities of different BSs to different UEs are also provided. Following the identification of the association probabilities, we

have characterized the Laplace transforms of the inter-cell interference and the interference from the cluster. Using tools from stochastic geometry, we have provided general expressions of the SINR coverage probability in each tier. Additionally, we have extended our work to the Nakagami fading model and the case in which fractional power control is adopted by the UEs. Moreover, we have addressed several special cases, e.g., the noise-limited case, interference-limited case, and one-tier model. Finally, we have addressed the average ergodic spectral efficiency. Via numerical and simulation results, we have confirmed the analytical characterizations and the derived expressions, and investigated the impact of important system parameters. For instance, we have observed that the interference has a noticeable influence on the coverage performance and the type of fading has a certain impact on the SINR coverage performance but Nakagami and Rayleigh fading lead to similar performance trends. Coverage probability can be improved by decreasing the cluster size, increasing the biasing factor and the transmit power of the small-cell BSs. The densities of BSs also affect the system performance.

In Chapter 5, we have proposed a multi-agent DDQN algorithm for beamforming in mmWave MIMO networks. Largest received power association criterion has been considered for BS association of the UEs. BSs act as reinforcement learning agents, and according to the limited information obtained from the associated UEs, they automatically and dynamically adjust their beams to improve the received power of the associated UEs. Via simulations, we have demonstrated that the proposed algorithm can achieve comparable network performance with respect to exhaustive search, and better performance than the random selection, which leads to especially poor performance when there are multiple BSs. We have noted that location information is not critical in our algorithm. In addition, the pre-trained model is not restricted to the same number of UEs as in the testing phase and can be applied to multiple testing scenarios with different number of UEs.

In Chapter 6, a three-tier HetNet has been studied, where APs, SBSs and MBSs transmit in THz, mmWave, microwave frequency bands, respectively. Distinguishing features of transmission in each frequency band are taken into account, including the blockage model, path loss model, beamforming and small-scale fading. To make the UEs receive larger signal power from the serv-

ing BS, path loss based association criterion has been considered. By using tools from stochastic geometry, the CCDF of the received signal power, the Laplace transform of the aggregate interference, and the SINR coverage probability are investigated, and general expressions have been derived. The analysis has been validated via Monte-Carlo simulation. Finally, numerical results demonstrate the following: making the APs more densely distributed can enhance the received signal power but decrease the SINR coverage probability; and narrower beamwidth of the main lobe at the APs leads to larger received signal power and the SINR coverage probability.

In Chapter 7, we have jointly considered the downlink SWIPT and uplink information transmission in UAV-assisted mmWave cellular networks, in which the UE locations are modeled using Thomas cluster processes and Matérn cluster processes. Distinguishing features of mmWave communications, such as different path loss models for LOS and NLOS links, and directional transmissions, are taken into account. We have characterized the CCDF and PDF of the distance from the typical UE to its own cluster center UAV, the nearest PPP-distributed UAV and the nearest GBS. In the downlink phase, we have determined the association probabilities of each tier BS. In addition, we have considered the power splitting technique in the SWIPT scenario, which allows the UEs to harvest energy and decode information simultaneously using the same received signal. We have characterized the energy and SINR coverage probabilities of the considered UAV-assisted mmWave cellular network. Moreover, we have defined the successful transmission probability to jointly analyze the energy and SINR coverages and we have provided general expressions. In the uplink phase, we have considered the scenario that each UAV receives information from its own cluster member UEs. SINR coverage has been derived and general expressions are provided. In addition, we have formulated the average uplink throughput, aiming to find the optimal time division multiplexing for downlink and uplink phases. Extensions to UAV-assisted cellular networks with realistic 3D antenna patterns have been provided. Finally, via numerical results we have investigated the impact of key system parameters on the network performance. We have shown that the system performance is improved when the cluster size becomes smaller. In addition, we have analyzed the optimal height of UAVs and optimal power splitting value that maximize the sys-

tem performance. Optimal time division has also been addressed to maximize the average uplink throughput. We have verified that Thomas cluster processes and Matérn cluster processes can lead to similar system performance trends.

In Chapter 8, we have investigated cellular-connected UAV networks with 3D antenna patterns, in which the UAVs are aerial UEs served by the GBSs. A realistic ground-to-air channel model has been incorporated into the analysis, where LOS and NLOS transmissions are distinguished. 3D antenna patterns have been considered for both GBSs and UAVs. More specifically, antenna patterns combining the vertical and horizontal gains are taken into account for the GBSs. Also, four types of 3D antenna patterns are considered for the UAVs. In particular, we compare the performances of a omni-directional pattern, a doughnut-shaped sine pattern, a doughnut-shaped cosine pattern, and a directional pattern with tilting angle toward the serving GBS. Via numerical results, we demonstrate that the directional pattern with tilting angle provides the best SINR coverage probability. We have also seen that the optimal UAV altitude varies depending on the environment and antenna patterns.

In Chapter 9, we have studied multi-UAV trajectory optimization with collision avoidance and wireless connectivity constraints. In establishing the wireless connectivity, we have taken into account the antenna radiation patterns, path loss, and SINR levels. In Section 9.1, we have formulated trajectory optimization as a sequential decision making problem and proposed a decentralized deep reinforcement learning algorithm. Particularly, a value neural network has been developed to obtain the values from the agent's joint states. An SINR-prediction neural network has been designed, using accumulated SINR measurements obtained when interacting with the cellular network, to map the GBS locations into the SINR levels in order to predict the UAV's SINR levels. We have investigated the performance in terms of success rate, collision rate, disconnection rate, and average more time. In the numerical results, we have considered various scenarios (e.g., with GBS deployments different from the setting in the training environment, different UAV heights, different antenna patterns, and obstacles/no-fly zones) and we have shown that with the value network and SINR-prediction network, real-time navigation for multi-UAVs can be efficiently performed in dif-

ferent environments with high success rates. In Section 9.2, we have addressed jamming-resilient trajectory design for multiple cellular-connected UAVs. We proposed an offline TD learning algorithm for the RL agent with online SINR mapping to solve the problem. More specifically, a value network has been trained offline by TD method to encode the interactions among the UAVs and between the UAVs and the environment; and an online SINR mapping DNN has been constructed and trained by supervised learning, to encode the influence of the jammer. Numerical results have shown that, without any information on the jammer, the proposed algorithm can achieve performance levels close to that of the ideal scenario with the perfect SINR-map. Hence, real-time navigation for multi-UAVs can be efficiently performed with high success rates, and collisions are avoided.

In Chapter 10, we have studied the UAV trajectory optimization to maximize the collected data from distributed IoT nodes in a multi-UAV scenario under realistic constraints, e.g., collision avoidance, mission completion deadline, and kinematic constraints. In establishing the wireless connection, we have taken into account the antenna radiation pattern, path loss, SNR, and largest received signal power based scheduling strategy. We have translated the considered problem into an MDP with parameterized states, permissible actions and detailed reward functions. D3QN is utilized for learning the policy, without any prior knowledge of the environment (e.g., channel propagation model, locations of the obstacles) and other UAVs (e.g., their missions, movements, and policies). We have shown that the proposed algorithm has high adaptive capability. More specifically, without further training, the offline learned policy can be used for real-time navigation for various missions with different numbers and locations of IoT nodes, different amount of data to collect, in various scenarios with different number and locations of other UAVs. Through numerical results, we have demonstrated that real-time navigation can be efficiently performed with high success rate, high data collection rate and low collision rate. We also showed that the proposed algorithm can achieve much lower collision rate in testing compared with the learning algorithm that does not consider collision avoidance. Furthermore, we have demonstrated that D3QN has better performance than Dueling DQN, DDQN, and DQN when solving the considered problem.

11.2 Future Research Directions

11.2.1 UAV-to-UAV Communications

In Chapter 7, we have analyzed the coverage probabilities in UAV-assisted cellular networks, where the UAVs are aerial BSs serving ground UEs. In Chapter 8, we have studied the coverage in cellular-connected UAV networks, where the UAVs are aerial UEs served by GBSs. Coverage analysis in UAV-enabled networks where the UAVs communicate with other UAVs is interesting, and is considered as future work.

11.2.2 Power Constrained UAV Trajectory Design

The power constraint of UAVs poses critical limits on their endurance and communication capabilities. In Chapter 9, we have aimed to reduce UAV power consumption by minimizing the mission completion time. In Chapter 10, we have considered the mission completion deadline to restrict the power consumption. Directly considering the power constraint in UAV path planning problems is one of our future directions.

11.2.3 Three-Dimensional (3D) UAV Path Planning

In Chapters 9 and 10, we have assumed that the UAVs fly at the same height. However, UAVs are able to travel in 3D area in practice. Therefore, finding 3D UAV trajectory is considered as future work.

11.2.4 Jamming Attacks in UAV-Enabled Networks

The LOS-dominant air-to-ground links make UAV communications more susceptible to the jamming/eavesdropping attacks by malicious ground nodes compared to the terrestrial communications. In Section 9.2, we have investigated the cellular-connected UAV path design in the presence of a dynamic jammer. Finding jamming-resilient path for UAVs, as either UEs or BSs, in the

presence of intelligent jamming attacks is motivated to be one of our future research directions.

APPENDIX A

PROOF OF THEOREMS AND LEMMAS

1 Proof of Lemma 3.1

The CCDF of path loss $L_{0,s}$ (for $s \in \{\text{LOS}, \text{NLOS}\}$) from the typical UE to a LOS/NLOS BS in the 0^{th} tier can be expressed as

$$\begin{aligned} \overline{F}_{L_{0,s}}(x) &= \mathbb{P}(l_{0,s} \geq x) \stackrel{(a)}{=} \mathbb{P}\left(\kappa_1^s y_0^{\alpha_1^{0s}} \geq x\right) = \mathbb{P}\left(y_0 \geq \left(\frac{x}{\kappa_1^s}\right)^{\frac{1}{\alpha_1^{0s}}}\right) \stackrel{(b)}{=} \overline{F}_{Y_0}\left(\left(\frac{x}{\kappa_1^s}\right)^{\frac{1}{\alpha_1^{0s}}}\right) \\ &\stackrel{(c)}{=} \begin{cases} \exp\left(-\frac{1}{2\sigma_j^2}\left(\frac{x}{\kappa_1^s}\right)^{\frac{2}{\alpha_1^{0s}}}\right) & (x \geq 0), & \text{for Thomas cluster process,} \\ 1 - \frac{x^{\frac{2}{\alpha_1^{ks}}}}{\kappa_1^s \alpha_1^{ks} R_j^2} & (0 \leq x \leq \kappa_1^s R_j^{\alpha_1^{ks}}), & \text{for Matérn cluster process,} \end{cases} \end{aligned} \quad (\text{A.1})$$

where (a) follows from the expression of path loss L_0 in (3.2) on the link in the 0^{th} tier, (b) follows from the definition of CCDF, and (c) is due to the expressions of $\overline{F}_{Y_0}(y_0)$ given in (2.7) and (2.9) for Thomas cluster process and Matérn cluster process, respectively.

Thus, the PDF of path loss $L_{0,s}$ can be obtained as follows:

$$f_{L_{0,s}}(x) = -\frac{d\bar{F}_{L_{0,s}}(x)}{dx} = \begin{cases} \frac{x^{\frac{2}{\alpha_1^{0s}}-1}}{\alpha_1^{0s}\kappa_1^{\frac{2}{\alpha_1^{0s}}}\sigma_j^2} \exp\left(-\frac{1}{2\sigma_j^2}\left(\frac{x}{\kappa_1^s}\right)^{\frac{2}{\alpha_1^{0s}}}\right) & (x \geq 0), \\ \text{for Thomas cluster process,} \\ \frac{2x^{\frac{2}{\alpha_1^{ks}}-1}}{\alpha_1^{ks}\kappa_1^{\frac{2}{\alpha_1^{ks}}}R_j^2} & (0 \leq x \leq \kappa_1^s R_j^{\alpha_1^{ks}}), \\ \text{for Matérn cluster process.} \end{cases} \quad (\text{A.2})$$

2 Proof of Lemma 3.2

We first define two events, $S_1 = \{\text{The typical UE is associated with a } j^{\text{th}} \text{ tier BS}\}$ and $S_2 = \{\text{The associated link is in } s \in \{\text{LOS, NLOS}\} \text{ transmission}\}$. Then the association probability of a LOS/NLOS BS in the j^{th} tier is

$$\begin{aligned} A_{j,s} &= \mathbb{P}(S_1 \text{ and } S_2) = \mathbb{P}(S_2|S_1)\mathbb{P}(S_1) \\ &\stackrel{(a)}{=} \mathbb{P}(P_j B_j L_{j,s}^{-1} > P_j B_j L_{j,s'}^{-1}) \mathbb{P}(P_j B_j L_{j,s}^{-1} \geq P_k B_k L_k^{-1}, k \in \mathcal{K}_1, k \neq j) \\ &= \mathbb{P}(L_{j,s'} > L_{j,s}) \mathbb{P}\left(L_k \geq \frac{P_k B_k}{P_j B_j} L_{j,s}, k \in \mathcal{K}_1, k \neq j\right) \\ &\stackrel{(b)}{=} \mathbb{P}(L_{j,s'} > L_{j,s}) \prod_{\substack{k=0 \\ k \neq j}}^K \mathbb{P}\left(L_k \geq \frac{P_k B_k}{P_j B_j} L_{j,s}\right), \end{aligned} \quad (\text{A.3})$$

where $s' \in \{\text{LOS, NLOS}\}$, $s \neq s'$, (a) follows from the definition of association probability, and (b) is due to the fact that the distributions of $\{L_k\}$ are independent.

For the 0^{th} Tier ($j=0$)

$$A_{0,s} = \mathbb{P}(L_{0,s'} > L_{0,s}) \prod_{k=1}^K \mathbb{P}\left(L_k \geq \frac{P_k B_k}{P_0 B_0} L_{0,s}\right) \stackrel{(a)}{=} p_{L_{0,s}} \mathbb{E}_{L_{0,s}} \left[\left(\prod_{k=1}^K \bar{F}_{L_k} \left(\frac{P_k B_k}{P_0 B_0} l_{0,s} \right) \right) \right], \quad (\text{A.4})$$

where (a) follows the definition of CCDF of the path loss L_k by noting the fact that there is only one BS in the 0^{th} tier, and therefore $\mathbb{P}(L_{0,s'} > L_{0,s})$ can be expressed as $p_{L_{0,LOS}}$ and $p_{L_{0,NLOS}}$ for LOS and NLOS links, respectively.

For the j^{th} Tier ($j \in \mathcal{K}$)

$$\begin{aligned} A_{j,s} &\stackrel{(a)}{=} \mathbb{E}_{L_{j,s}} \left[\bar{F}_{L_{j,s'}}(l_{j,s}) \left(\prod_{\substack{k=0 \\ k \neq j}}^K \bar{F}_{L_k} \left(\frac{P_k B_k}{P_j B_j} l_{j,s} \right) \right) \right] \\ &\stackrel{(b)}{=} \mathbb{E}_{L_{j,s}} \left[\left(\bar{F}_{L_{j,s'}}(l_{j,s}) \bar{F}_{L_0} \left(\frac{P_0 B_0}{P_j B_j} l_{j,s} \right) \prod_{\substack{k=1 \\ k \neq j}}^K \bar{F}_{L_k} \left(\frac{P_k B_k}{P_j B_j} l_{j,s} \right) \right) \right], \end{aligned} \quad (A.5)$$

where (a) follows from the definition of the CCDF of the path loss L_k and CCDF of the path loss $L_{j,s'}$ and (b) is due to the fact that the CCDF of the path loss L_0 is different from the CCDF of the path loss L_k , hence they are separately considered.

3 Proof of Lemma 3.3

Define the event $S = \{\text{The typical UE is associated with a LOS/NLOS BS in the } j^{th} \text{ tier}\}$. Given the event S , we can mathematically express the CDF of the path loss $L_{j,s}$ as

$$\begin{aligned} \hat{F}_{L_{j,s}}(x) &= \mathbb{P}(l_{j,s} < x | S) \stackrel{(a)}{=} \frac{\mathbb{P}(l_{j,s} < x, S)}{\mathbb{P}(S)} \stackrel{(b)}{=} \frac{\mathbb{P}(l_{j,s} < x) \mathbb{P}(L_{j,s'} > l_{j,s}) \prod_{\substack{k=0 \\ k \neq j}}^K \mathbb{P}\left(L_k \geq \frac{P_k B_k}{P_j B_j} l_{j,s}\right)}{A_{j,s}} \\ &= \begin{cases} \frac{1}{A_{0,s}} \int_0^x f_{L_{0,s}}(l_{0,s}) p_{L_{0,s}} \left(\prod_{k=1}^K \bar{F}_{L_k} \left(\frac{P_k B_k}{P_0 B_0} l_{0,s} \right) \right) dl_{0,s}, & \text{for } j = 0, \\ \frac{1}{A_{j,s}} \int_0^x f_{L_{j,s}}(l_{j,s}) \bar{F}_{L_{j,s'}}(l_{j,s}) \left(\bar{F}_{L_0} \left(\frac{P_0 B_0}{P_j B_j} l_{j,s} \right) \prod_{\substack{k=1 \\ k \neq j}}^K \bar{F}_{L_k} \left(\frac{P_k B_k}{P_j B_j} l_{j,s} \right) \right) dl_{j,s}, & \text{for } j \in \mathcal{K}, \end{cases} \end{aligned} \quad (A.6)$$

where, (a) is due to Bayes's rule, and (b) follows from the definition of association probability and the independence of $L_{j,s}$, $L_{j,s'}$ and L_k . Therefore,

$$\begin{aligned} \hat{f}_{L_{j,s}}(x) &= \frac{d\hat{F}_{L_{j,s}}(x)}{dx} \\ &= \begin{cases} \frac{1}{A_{0,s}} f_{L_{0,s}}(x) p_{L_{0,s}} \left(\prod_{k=1}^K \bar{F}_{L_k} \left(\frac{P_k B_k}{P_0 B_0} x \right) \right), & \text{for } j = 0, \\ \frac{1}{A_{j,s}} f_{L_{j,s}}(x) \bar{F}_{L_{j,s'}}(x) \left(\bar{F}_{L_0} \left(\frac{P_0 B_0}{P_j B_j} x \right) \prod_{\substack{k=1 \\ k \neq j}}^K \bar{F}_{L_k} \left(\frac{P_k B_k}{P_j B_j} x \right) \right), & \text{for } j \in \mathcal{K}. \end{cases} \end{aligned} \quad (\text{A.7})$$

4 Proof of Theorem 3.1

Given that the typical UE is associated with a LOS/NLOS BS in the j^{th} tier, the coverage probability can be expressed as

$$\begin{aligned} P_{C_{j,s}}^c &= \mathbb{P}(\text{SINR}_{j,s} > T_j | t = j) \\ &\stackrel{(a)}{=} \mathbb{P} \left(\frac{P_j G_0 h_j l_{j,s}^{-1}}{\sigma_{n,j}^2 + \sum_{k=0}^K I_{j,k}} > T_j \right) = \mathbb{P} \left(h_j > \frac{T_j l_{j,s}}{P_j G_0} \left(\sigma_{n,j}^2 + \sum_{k=0}^K I_{j,k} \right) \right) \\ &\stackrel{(b)}{=} \mathbb{E} \left[\sum_{n=1}^{N_s} (-1)^{n+1} \binom{N_s}{n} \exp \left(-\frac{n \eta_s T_j l_{j,s}}{P_j G_0} \left(\sigma_{n,j}^2 + \sum_{k=0}^K I_{j,k} \right) \right) \right] \\ &\stackrel{(c)}{=} \begin{cases} \mathbb{E}_{L_{0,s}} \left[\sum_{n=1}^{N_s} (-1)^{n+1} \binom{N_s}{n} e^{-\mu_{0,s} \sigma_{n,0}^2} \prod_{k=1}^K \mathcal{L}_{I_{0,k}}(\mu_{0,s}) \right] & \text{for } j = 0, \\ \mathbb{E}_{L_{j,s}} \left[\sum_{n=1}^{N_s} (-1)^{n+1} \binom{N_s}{n} e^{-\mu_{j,s} \sigma_{n,j}^2} \mathcal{L}_{I_{j,0}}(\mu_{j,s}) \prod_{k=1}^K \mathcal{L}_{I_{j,k}}(\mu_{j,s}) \right] & \text{for } j = \mathcal{K}, \end{cases} \\ &\stackrel{(d)}{=} \begin{cases} \mathbb{E}_{L_{0,s}} \left[\sum_{n=1}^{N_s} (-1)^{n+1} \binom{N_s}{n} e^{-\mu_{0,s} \sigma_{n,0}^2} \prod_{k=1}^K \left(\mathcal{L}_{I_{0,k}^{\text{LOS}}}(\mu_{0,s}) \mathcal{L}_{I_{0,k}^{\text{NLOS}}}(\mu_{0,s}) \right) \right], & \text{for } j = 0, \\ \mathbb{E}_{L_{j,s}} \left[\sum_{n=1}^{N_s} (-1)^{n+1} \binom{N_s}{n} e^{-\mu_{j,s} \sigma_{n,j}^2} \left(\sum_a p_{L_{0,a}} \mathcal{L}_{I_{j,0}^a}(\mu_{j,s}) \right) \prod_{k=1}^K \left(\mathcal{L}_{I_{j,k}^{\text{LOS}}}(\mu_{j,s}) \mathcal{L}_{I_{j,k}^{\text{NLOS}}}(\mu_{j,s}) \right) \right] & \text{for } j = \mathcal{K}, \end{cases} \end{aligned} \quad (\text{A.8})$$

where $\mu_{j,s} = \frac{n\eta_s T_j l_{j,s}}{P_j G_0}$, $\eta_s = N_s(N_s!)^{-\frac{1}{N_s}}$, (a) follows from the fact that if the typical UE is associated with a j^{th} tier BS, then $\text{SINR}_{j,s} = \frac{P_j G_0 h_j l_{j,s}^{-1}}{\sigma_j^2 + \sum_{k=0}^K I_{j,k}}$, (b) follows from the moment generating function (MGF) of the gamma random variable h_j , (c) is due to the independence of noise and interference terms, and follows from the fact that for the 0^{th} tier main link, interference links come from all K tier BSs, while for the j^{th} tier ($j \in \mathcal{K}$) main link, interference links come from the 0^{th} tier BS in addition to all K tier BSs, and (d) is obtained by taking into account that there is only one BS in the 0^{th} tier, and hence we rewrite the Laplace transform expression, $\mathcal{L}_{I_{j,0}}(\mu_{j,s})$, as

$$\begin{aligned} \mathcal{L}_{I_{j,0}}(\mu_{j,s}) &= p_{L_{0,\text{LOS}}} \mathcal{L}_{I_{j,0}^{\text{LOS}}}(\mu_{j,s}) + p_{L_{0,\text{NLOS}}} \mathcal{L}_{I_{j,0}^{\text{NLOS}}}(\mu_{j,s}) \\ &= \sum_{a \in \{\text{LOS}, \text{NLOS}\}} p_{L_{0,a}} \mathcal{L}_{I_{j,0}^a}(\mu_{j,s}), \end{aligned} \quad (\text{A.9})$$

and for the j^{th} tier, since LOS and NLOS links are independent, Laplace transform $\mathcal{L}_{I_{j,k}}(\mu_{j,s})$ can be rewritten as

$$\mathcal{L}_{I_{j,k}}(\mu_{j,s}) = \mathcal{L}_{I_{j,k}^{\text{LOS}}}(\mu_{j,s}) \mathcal{L}_{I_{j,k}^{\text{NLOS}}}(\mu_{j,s}). \quad (\text{A.10})$$

5 Proof of Lemma 3.4

Interference from the k^{th} Tier ($k \in \mathcal{K}$)

Tools from stochastic geometry can be applied to compute the Laplace transform of the interference from the LOS/NLOS BSs in the k^{th} tier, by splitting the interference into three independent PPPs for each effective antenna gain $G \in \{MM, Mm, mm\}$ as follows:

$$I_{j,k}^a = I_{j,k}^{a,MM} + I_{j,k}^{a,Mm} + I_{j,k}^{a,mm} = \sum_{G \in \{MM, Mm, mm\}} I_{j,k}^{a,G}, \quad (\text{A.11})$$

where $a \in \{\text{LOS}, \text{NLOS}\}$, $I_{j,k}^{a,G}$ denotes the interference with random effective antenna gain G given in (2.22) and it has a density of $\lambda_j p_G$ according to the thinning theorem of Poisson process

[57].

Hence, Laplace transform of the interference from the k^{th} tier can be expressed as

$$\begin{aligned}\mathcal{L}_{I_{j,k}^a}(u_{j,s}) &= \mathbb{E} \exp(-\mu_{j,s} I_{j,k}^a) = \mathbb{E} \exp\left(-\mu_{j,s} \sum_G I_{j,k}^{a,G}\right) \\ &= \prod_G \mathbb{E} \exp(-\mu_{j,s} I_{j,k}^{a,G}) = \prod_G \mathcal{L}_{I_{j,k}^{a,G}}(\mu_{j,s}),\end{aligned}\quad (\text{A.12})$$

where $G \in \{MM, Mm, mm\}$, and $\mathcal{L}_{I_{j,k}^{a,G}}(\mu_{j,s})$ can be calculated using stochastic geometry as follows:

$$\begin{aligned}\mathcal{L}_{I_{j,k}^{a,G}}(\mu_{j,s}) &= e^{-\int_{\frac{P_j B_j}{P_j B_j} l_{j,s}}^{\infty} (1 - \mathbb{E}_{h_j} [\exp(-\mu_{j,s} P_j h_j G l_{j,a}^{-1})]) p_G \Lambda'_{k,a}([0, dl_{k,a}])} \\ &\stackrel{(a)}{=} e^{-\int_{\frac{P_j B_j}{P_j B_j} l_{j,s}}^{\infty} \left(1 - \frac{1}{(1 + \mu_{j,s} P_j G l_{k,a}^{-1} N_a^{-1})^{N_a}}\right) p_G \Lambda'_{k,a}([0, dl_{k,a}])},\end{aligned}\quad (\text{A.13})$$

where N_a is Nakagami fading parameter and (a) follows by computing the MGF of the gamma random variable h_j .

Interference from the 0th Tier (k=0)

Since there is only one BS in the 0th tier, Laplace transform of the interference from the 0th tier BS in $a \in \{\text{LOS}, \text{NLOS}\}$ link, $\mathcal{L}_{I_{j,0}^a}(\mu_{j,s})$, can be obtained as

$$\begin{aligned}\mathcal{L}_{I_{j,0}^a}(\mu_{j,s}) &= \mathbb{E} \exp(-\mu_{j,s} I_{j,0}^a) = \mathbb{E}_G [\mathbb{E} \exp(-\mu_{j,s} I_{j,0}^{a,G})] \\ &= \sum_{G \in \{MM, Mm, mm\}} p_G \mathbb{E} \exp(-\mu_{j,s} I_{j,0}^{a,G}) = \sum_G p_G \mathcal{L}_{I_{j,0}^{a,G}}(\mu_{j,s}),\end{aligned}\quad (\text{A.14})$$

where $\mathcal{L}_{I_{j,0}^{a,G}}(\mu_{j,s})$ is computed as follows:

$$\begin{aligned}\mathcal{L}_{I_{j,0}^{a,G}}(\mu_{j,s}) &\stackrel{(a)}{=} \mathbb{E}_{L_{0,a}} \left[\mathbb{E}_{h_0} [\exp(-\mu_{j,s} P_0 h_0 G l_{0,a}^{-1})] \middle| l_{0,a} > \frac{P_0 B_0}{P_j B_j} l_{j,s} \right] \\ &\stackrel{(b)}{=} \mathbb{E}_{L_{0,a}} \left[\frac{1}{(1 + \mu_{j,s} P_0 G l_{0,a}^{-1} N_a^{-1})^{N_a}} \middle| l_{0,a} > \frac{P_0 B_0}{P_j B_j} l_{j,s} \right]\end{aligned}$$

$$\begin{aligned}
& \stackrel{(c)}{=} \int_{\frac{P_0 B_0}{P_j B_j} l_{j,s}}^{\infty} \frac{1}{(1 + \mu_{j,s} P_0 G l_{0,a}^{-1} N_a^{-1})^{N_a}} f_{L_{0,a}} \left(l_{0,a} \middle| l_{0,a} > \frac{P_0 B_0}{P_j B_j} l_{j,s} \right) dl_{0,a} \\
& = \int_{\frac{P_0 B_0}{P_j B_j} l_{j,s}}^{\infty} \frac{1}{(1 + \mu_{j,s} P_0 G l_{0,a}^{-1} N_a^{-1})^{N_a}} \frac{f_{L_{0,a}}(l_{0,a})}{F_{L_{0,a}} \left(\frac{P_0 B_0}{P_j B_j} l_{j,s} \right)} dl_{0,a}
\end{aligned} \tag{A.15}$$

where, (a) follows from the expression of $I_{j,0}^{a,G}$, (b) follows from the MGF of the gamma random variable, (c) follows from the definition of expected value with respect to $L_{0,a}$.

6 Proof of Lemma 3.5

Defining the function $f(l_{0,a}) = \frac{1}{(1 + \mu_{j,s} P_0 G l_{0,a}^{-1} N_a^{-1})^{N_a}}$, we have

$$\mathcal{L}_{I_{j,0}^{a,G}}(\mu_{j,s}) = \mathbb{E}_{L_{0,a}} \left[f(l_{0,a}) \middle| l_{0,a} > \frac{P_0 B_0}{P_j B_j} l_{j,s} \right]. \tag{A.16}$$

Since $\frac{P_0 B_0}{P_j B_j} l_{j,s} \leq l_{0,a} \leq \infty$ and $f(l_{0,a})$ is a monotone increasing function with respect to $l_{0,a}$ in the region, we obtain

$$f \left(\frac{P_0 B_0}{P_j B_j} l_{j,s} \right) \leq \mathcal{L}_{I_{j,0}^{a,G}} \leq f(\infty), \tag{A.17}$$

leading to the bounds in Lemma 5.

7 Proof of Lemma 3.6

Using a scale parameter ς , we can express the path loss as $l_{0,a} = \varsigma l'_{0,a}$. Again defining the function

$f(l_{0,a}) = \frac{1}{(1 + \mu_{j,s} P_0 G l_{0,a}^{-1} N_a^{-1})^{N_a}}$, when the cluster size tends to infinity, we have

$$\begin{aligned}
\lim_{l_{0,a} \rightarrow \infty} \mathcal{L}_{I_{j,0}^a} &= \lim_{l_{0,a} \rightarrow \infty} \sum_G p_G \mathbb{E}_{L_{0,a}} \left[f(l_{0,a}) \middle| l_{0,a} > \frac{P_0 B_0}{P_j B_j} l_{j,s} \right] \\
&\stackrel{(a)}{=} \sum_G p_G \lim_{\varsigma \rightarrow \infty} \mathbb{E}_{L'_{0,a}} \left[f(\varsigma l'_{0,a}) \middle| \varsigma l'_{0,a} > \frac{P_0 B_0}{P_j B_j} l_{j,s} \right]
\end{aligned}$$

$$\begin{aligned}
&\stackrel{(b)}{=} \sum_G p_G \lim_{\varsigma \rightarrow \infty} \int_{\frac{P_0 B_0}{\varsigma P_j B_j} l_{j,s}}^{\infty} f(\varsigma l'_{0,a}) \frac{f_{L'_{0,a}}(l'_{0,a})}{F_{L'_{0,a}}\left(\frac{P_0 B_0}{\varsigma P_j B_j} l_{j,s}\right)} dl'_{0,a} \\
&\stackrel{(c)}{=} \sum_G p_G \int_0^{\infty} f_{L'_{0,a}}(l'_{0,a}) dl'_{0,a} \\
&= \sum_G p_G = 1
\end{aligned} \tag{A.18}$$

where (a) is because we can change the order of summation and limit, (b) is obtained by plugging in $l_{0,a} = \varsigma l'_{0,a}$, (c) is obtained because as $\varsigma \rightarrow \infty$, $F_{L'_{0,a}}\left(\frac{P_0 B_0}{\varsigma P_j B_j} l_{j,s}\right) \rightarrow F_{L'_{0,a}}(0) = 1$, and $f(\varsigma l'_{0,a}) \rightarrow 1$.

8 Proof for Lemma 4.1

We have

$$\begin{aligned}
\bar{F}_{r_{i0}}^s(x) &= \mathbb{P}(r > x | \text{the link is } s) = \frac{\mathbb{P}(r > x, \text{ the link is } s)}{\mathbb{P}(\text{the link is } s)} \\
&= \frac{E_r[\mathbb{P}(r > x | s) \mathbb{P}(s)]}{D_{i0}^s} = D_{i0}^{s-1} \int_x^{\infty} f_{r_{i0}}(r) p_{\alpha i}^s(r) dr,
\end{aligned} \tag{A.19}$$

where $D_{i0}^s = \mathbb{P}(s) = E_{r_{i0}}[p_{\alpha i}^s(r)]$ is the probability that the link between the BS and its cluster member is s . Then, we can obtain the PDF as

$$f_{r_{i0}}^s(x) = -\frac{\bar{F}_{r_{i0}}^s(x)}{dx} = D_{i0}^{s-1} f_{r_{i0}}(x) p_{\alpha i}^s(x). \tag{A.20}$$

9 Proof for Lemma 4.2

For $j = 0$, the probability that the typical UE is served by its own cluster center BS can be determined as follows

$$\begin{aligned}
A_{i0,s} &= \mathbb{P}(S_{i0,s}) \\
&\stackrel{(a)}{=} \mathbb{P}(\text{the typical UE is served by the cluster center BS} | s)
\end{aligned}$$

$$\begin{aligned}
& \times \mathbb{P}(\text{ the link is in } s \text{ transmission}) \\
& \stackrel{(b)}{=} \mathbb{E}_{r_{i0}^s} \left[\mathbb{P}(P_0 B_0 \kappa_s^{-1} r_{i0}^{s-\alpha_s} \geq P_k B_k \kappa^{-1} r_k^{-\alpha} \text{ for } k \in \mathcal{K}) p_{\alpha i}^s(r_{i0}^s) \right] \\
& \stackrel{(c)}{=} D_{i0}^s \mathbb{E}_{r_{i0}^s} \left[\mathbb{P}(r_k \geq \left(\frac{P_k B_k \kappa_s}{P_0 B_0 \kappa} r_{i0}^{s-\alpha_s} \right)^{\frac{1}{\alpha}} \text{ for } k \in \mathcal{K}) \right] \\
& \stackrel{(d)}{=} D_{i0}^s \mathbb{E}_{r_{i0}^s} \left[\prod_{k=1}^K \prod_b D_k^b \mathbb{P} \left(r_k^b \geq \left(\frac{P_k B_k \kappa_s}{P_0 B_0 \kappa_b} r_{i0}^{s-\alpha_s} \right)^{\frac{1}{\alpha_b}} \right) \right] \\
& \stackrel{(e)}{=} D_{i0}^s \mathbb{E}_{r_{i0}^s} \left[\prod_{k=1}^K \prod_b D_k^b \bar{F}_{r_k^b} [(C_{k0}^{bs} r_{i0}^{s-\alpha_s})^{\frac{1}{\alpha_b}}] \right] \tag{A.21}
\end{aligned}$$

where $C_{kj}^{bs} = \frac{P_k B_k \kappa_s}{P_j B_j \kappa_b}$, and $D_k^b = 1 - e^{-2\pi\lambda_k \int_0^\infty x p_{\alpha k}^b(x) dx}$ is the probability that a UE has at least one $b \in \{\text{LOS}, \text{NLOS}\}$ BS in the k^{th} tier. (a) arises from the definition of association probability and the conditional probability. (b) is from the association criterion that in this case the 0^{th} tier BS (the cluster center BS) provides the largest long-term averaged biased received power. (c) comes from that $D_{i0}^s = \mathbb{E}_{r_{i0}^s} [p_{\alpha i}^s(r_{i0}^s)]$ is the probability that the link is in s transmission. (d) is due to the fact that the distributions of $\{r_k^b\}$ are independent, i.e., BSs in each tier are independent, and in the k^{th} tier, the LOS/NLOS BSs can be regarded as independent ([61] has proved the dependence is weak and can be ignored in analysis). (e) is by the application of the definition of CCDF.

For $j \in \mathcal{K}$, similarly as in the derivation of $A_{i0,s}$, the probability that the typical UE (from the i^{th} tier) is associated with a LOS/NLOS BS in the j^{th} tier can be obtained as follows

$$\begin{aligned}
A_{ij,s} &= \mathbb{P}(S_{ij,s}) \\
& \stackrel{(a)}{=} \mathbb{P}(\text{the typical UE is served by a LOS/NLOS BS in the } j^{\text{th}} \text{ tier BS} | s) \\
& \quad \times \mathbb{P}(\text{ the link is in } s \text{ transmission}) \\
& \stackrel{(b)}{=} \mathbb{E}_{r_j^s} \left[D_j^s \mathbb{P}((r_j^s)^{-\alpha_s} \geq (r_j^{s'})^{-\alpha_{s'}}) \mathbb{P}(P_j B_j \kappa_s^{-1} r_j^{s-\alpha_s} \geq P_0 B_0 \kappa^{-1} r_{i0}^{-\alpha}) \right. \\
& \quad \left. \times \mathbb{P}(P_j B_j \kappa_s^{-1} r_j^{s-\alpha_s} \geq P_k B_k \kappa^{-1} r_k^{-\alpha}) \right] \\
& \stackrel{(c)}{=} \mathbb{E}_{r_j^s} \left[D_j^s D_j^{s'} \mathbb{P} \left(r_j^{s'} \geq \frac{\kappa_{s'}}{\kappa_s} (r_j^s)^{\frac{\alpha_s}{\alpha_{s'}}} \right) \left[\sum_a D_{i0}^a \mathbb{P} \left(r_{i0}^a \geq (C_{0j}^{as} r_j^{s-\alpha_s})^{\frac{1}{\alpha_a}} \right) \right] \right]
\end{aligned}$$

$$\begin{aligned}
& \times \left[\prod_{\substack{k=1 \\ k \neq j}}^K \prod_b D_k^b \mathbb{P} \left(r_k^b \geq (C_{kj}^{bs} r_j^{s\alpha_s})^{\frac{1}{\alpha_b}} \right) \right] \\
& \stackrel{(d)}{=} \mathbb{E}_{r_j^s} \left[D_j^s D_j^{s'} \bar{F}_{r_j^{s'}} \left(\frac{\kappa_{s'}}{\kappa_s} r_i^{s \frac{\alpha_s}{\alpha_{s'}}} \right) \left[\sum_a D_{i0}^a \bar{F}_{r_{i0}^s} ((C_{0j}^{as} r_j^{s\alpha_s})^{\frac{1}{\alpha_a}}) \right] \right. \\
& \quad \left. \times \left[\prod_{\substack{k=1 \\ k \neq i}}^K \prod_b D_k^b \bar{F}_{r_k^b} ((C_{kj}^{bs} r_j^{s\alpha_s})^{\frac{1}{\alpha_b}}) \right] \right] \quad (\text{A.22})
\end{aligned}$$

where (a) is due to the definition of association probability. In the expectation in (b), the first two terms come from $\mathbb{P}(s)$, the third term is due to that the associated BS should provide larger power than the cluster center BS of the typical UE, and the fourth term is due to that the associated BS should provide larger power than the k^{th} ($k \neq j$) tier BSs. In (c), the second term is due to the fact that there is only one cluster center and $\mathbb{P}(r_{j0} > (Cr^{\alpha_s})^{\frac{1}{\alpha}}) = \mathbb{P}(r_{j0} > (Cr^{\alpha_s})^{\frac{1}{\alpha_{\text{LOS}}}} | \text{LOS}) \mathbb{P}(\text{LOS}) + \mathbb{P}(r_{j0} > (Cr^{\alpha_s})^{\frac{1}{\alpha_{\text{NLOS}}}} | \text{NLOS}) \mathbb{P}(\text{NLOS})$, and the third term follows the same reason as in part 1) step (d). (d) is by the application of the definition of CCDF.

10 Proof of Theorem 4.1

Given $S_{ij,s}$, the SINR coverage probability can be obtained as follows:

$$\begin{aligned}
P_{C_{ij,s}}^c &= \mathbb{P}(\text{SINR}_{ij,s} > T_j | S_{ij,s}) \stackrel{(a)}{=} \mathbb{P} \left(\frac{P_u G_0 h_j \kappa_s^{-1} r_{ij,s}^{-\alpha_s}}{\sigma_n^2 + I_{j0} + \sum_{k=1}^{K_u} I_{jk}} > T_j \right) \\
&= \mathbb{P} \left(h_j > \frac{T_j \kappa_s r_{ij,s}^{\alpha_s}}{P_u G_0} \left(\sigma_n^2 + I_{j0} + \sum_{k=1}^{K_u} I_{jk} \right) \right) \\
&\stackrel{(b)}{=} \mathbb{E}_{r_{ij,s}} \left[\exp \left(-\frac{T_j \kappa_s r_{ij,s}^{\alpha_s}}{P_u G_0} \left(\sigma_n^2 + I_{j0} + \sum_{k=1}^{K_u} I_{jk} \right) \right) \right] \\
&\stackrel{(c)}{=} \mathbb{E}_{r_{ij,s}} \left[e^{-\mu_{ij}^s \sigma_n^2} \mathcal{L}_{I_{i0}}(\mu_{ij}^s) \prod_{k=1}^{K_u} \mathcal{L}_{I_{ik}}(\mu_{ij}^s) \right], \quad (\text{A.23})
\end{aligned}$$

where $\mu_{ij}^s = \frac{T_i \kappa_s r_{ij,s}^{\alpha_s}}{P_u G_0}$, and $\mathcal{L}_I(\mu) = \mathbb{E} \exp(-\mu I)$ is the Laplace transform of I evaluated at μ . (a) follows from the expression of SINR given $S_{ij,s}$ is true. (b) follows from the MGF of $h \sim \exp(1)$. (c) is due to the fact that the noise component and the interference from each tier are independent of each other. Note that when $I_{j0} = 0$, $\mathcal{L}_{I_{i0}}(\mu_{ij}^s) = 1$.

11 Proof of Theorem 4.2

1) For $k \in \mathcal{K}$, we have $\mathcal{L}_{I_{ik}}(\mu_{ij}^s) = \prod_G \prod_{a \in \{L, N\}} \mathcal{L}_{I_{ik}^{Ga}}(\mu_{ij}^s)$. Using $\mathbf{x}_{jk,n}$ to denote the vector from the reference BS to the n^{th} BS in the k^{th} tier, and \mathbf{y}_{k0} to denote the vector from the k^{th} tier BS to its active cluster member UE, we get $r_{jk,n} = \|\mathbf{x}_{jk,n} + \mathbf{y}_{k0}\|$.

$$\begin{aligned}
\mathcal{L}_{I_{jk}^{Ga}}(\mu_{ij}^s) &= \mathbb{E}[\exp(-\mu_{ij}^s I_{jk}^{Ga})] \stackrel{(a)}{=} \mathbb{E} \left[\exp \left(-\mu_{ij}^s \sum_{n \in \Phi_k} P_u G h_k \kappa_a^{-1} r_{jk,n}^{-\alpha_a} \right) \right] \\
&= \mathbb{E} \left[\prod_{n \in \Phi_k} \mathbb{E}_{h_k} [\exp(-\mu_{ij}^s P_u G h_k \kappa_a^{-1} r_{jk,n}^{-\alpha_a})] \right] \stackrel{(b)}{=} \mathbb{E} \left[\prod_{n \in \Phi_k} \frac{1}{1 + \mu_{ij}^s P_u G \kappa_a^{-1} r_{jk,n}^{-\alpha_a}} \right] \\
&= \mathbb{E} \left[\prod_{n \in \Phi_k} \frac{1}{1 + \mu_{ij}^s P_u G \kappa_a^{-1} \|\mathbf{x}_{jk,n} + \mathbf{y}_{k0}\|^{-\alpha_a}} \right] \\
&= \mathbb{E}_{\mathbf{x}_{jk,n}} \left[\prod_{n \in \Phi_k} \mathbb{E}_{\mathbf{y}_{k0}} \left[\frac{1}{1 + \mu_{ij}^s P_u G \kappa_a^{-1} \|\mathbf{x}_{jk,n} + \mathbf{y}_{k0}\|^{-\alpha_a}} \right] \right] \\
&\stackrel{(c)}{=} e^{-\int_{\mathbb{R}^2} \lambda'_u \left(1 - \mathbb{E}_{\mathbf{y}_{k0}} \left[\frac{1}{1 + \mu_{ij}^s P_u G \kappa_a^{-1} \|\mathbf{x}_{jk,n} + \mathbf{y}_{k0}\|^{-\alpha_a}} \right] \right) d\mathbf{x}_{jk,n}} \\
&\stackrel{(d)}{=} e^{-\int_{\mathbb{R}^2} \lambda'_u \mathbb{E}_{\mathbf{y}_{k0}} \left[\frac{1}{1 + (\mu_{ij}^s P_u G \kappa_a^{-1} \|\mathbf{x}_{jk,n} + \mathbf{y}_{k0}\|^{-\alpha_a}) - 1} \right] d\mathbf{x}_{jk,n}} \\
&\stackrel{(e)}{=} e^{-\int_{\mathbb{R}^2} \int_{\mathbb{R}^2} \lambda'_u \left(\frac{1}{1 + (\mu_{ij}^s P_u G \kappa_a^{-1} \|\mathbf{x}_{jk,n} + \mathbf{y}_{k0}\|^{-\alpha_a}) - 1} \right) f_Y(\mathbf{y}_{k0}) d\mathbf{y}_{k0} d\mathbf{x}_{jk,n}} \\
&\stackrel{(f)}{=} e^{-2\pi \int_0^\infty \int_0^\infty \lambda'_u \left(\frac{1}{1 + (\mu_{ij}^s P_u G \kappa_a^{-1} r_{jk,n}^{-\alpha_a}) - 1} \right) f_R(r_{jk,n} | v_{jk,n}) dr_{jk,n} v_{jk,n} dv_{jk,n}} \\
&\stackrel{(g)}{=} e^{-2\pi \int_0^\infty \lambda_k p_{GP_{\alpha k}^a}(r_{jk,n}) \left(\frac{1}{1 + (\mu_{ij}^s P_u G \kappa_a^{-1} r_{jk,n}^{-\alpha_a}) - 1} \right) r_{jk,n} dr_{jk,n}} \tag{A.24}
\end{aligned}$$

where $\lambda'_u = p_G \lambda_{us}^{jk}(r) = p_G p_{\alpha k}^s(r) \lambda_k$. By the definition of interference, we obtain (a). (b) follows from the fact that $h \sim \exp(1)$. (c) is due to the computation of the probability generating function (PGFL) of PPP, which describes the distribution of BSs, since we compute the expectation with respect to $x_{jk,n}$ in this step. (d) is determined from the fact that $1 - \mathbb{E}[\frac{1}{1+x}] = \mathbb{E}[\frac{x}{1+x}] = \mathbb{E}[\frac{1}{1+x^{-1}}]$. (e) follows by plugging in the expression of the expected value with respect to y_{k0} . (f) is obtained by converting the coordinates from Cartesian to polar, and $v_{jk,n} = \|\mathbf{x}_{jk,n}\|$. (g) follows from an approximation based on the property of the Rician distribution that $\int_0^\infty f_R(r|v) v dv = r$.

2) For $k = 0$, we have

$$\mathcal{L}_{I_{j0}}(\mu_{ij}^s) = \sum_G \sum_{a \in \{L, N\}} p_G D_{j0}^a \mathcal{L}_{I_{j0}^{Ga}}(\mu_{ij}^s) \quad (\text{A.25})$$

and since only one UE in the cluster inflicts interference, which can be via either a LOS or NLOS link, and the antenna gain is selected from $\{MM, Mm, mm\}$, we can express

$$\begin{aligned} \mathcal{L}_{I_{j0}^{Ga}}(\mu_{ij}^s) &= \mathbb{E} \exp(-\mu_{ij}^s I_{j0}^{Ga}) = \mathbb{E} \exp[-\mu_{ij}^s P_u G h \kappa_a^{-1} r_{j0}^{-\alpha_a}] \\ &\stackrel{(a)}{=} \int_0^\infty \frac{1}{1 + \mu_{ij}^s P_u G \kappa_a^{-1} r_{j0}^{-\alpha_a}} f_{R_{j0}^s}(r_{j0}) dr_{j0} \end{aligned} \quad (\text{A.26})$$

where (a) is obtained by using the MGF of $h \sim \exp(1)$.

12 Proof of Lemma 4.3

1) For the interfering cluster member UEs $k = 0$, we have

$$\begin{aligned} \mathcal{L}_{I_{j0mb}^{Ga}}(\mu_{ij}^s) &= \mathbb{E} \exp(-\mu_{ij}^s I_{j0}^{Ga}) = \mathbb{E} \exp[-\mu_{ij}^s (\kappa_b t^{\alpha_b})^\tau G h \kappa_a^{-1} r_{j0}^{-\alpha_a}] \\ &\stackrel{(a)}{=} \int_0^\infty \int_0^\infty \frac{1}{1 + \mu_{ij}^s (\kappa_b t^{\alpha_b})^\tau G \kappa_a^{-1} r_{j0}^{-\alpha_a}} \hat{f}_{r_{km,b}}(t) f_{R_{j0}^s}(r_{j0}) dt dr_{j0} \end{aligned} \quad (\text{A.27})$$

where (a) is obtained by computing the expectation with respect to t and applying the MGF of h .

2) For $k \in K_u$, we have

$$\begin{aligned}
\mathcal{L}_{I_{jkm}^{Ga}}(\mu_{ij}^s) &= \mathbb{E}[\exp(-\mu_{ij}^s I_{jkm}^{Ga})] = \mathbb{E}\left[\exp\left(-\mu_{ij}^s \sum_{n \in \Phi_k} (\kappa_b t^{\alpha_b})^\tau G h_k \kappa_a^{-1} r_{jk,n}^{-\alpha_a}\right)\right] \\
&= \mathbb{E}\left[\prod_{n \in \Phi_k} \mathbb{E}[\exp(-\mu_{ij}^s (\kappa_b t^{\alpha_b})^\tau G h_k \kappa_a^{-1} r_{jk,n}^{-\alpha_a})]\right] \stackrel{(a)}{=} \mathbb{E}\left[\prod_{n \in \Phi_k} \mathbb{E}_t\left[\frac{1}{1 + \mu_{ij}^s (\kappa_b t^{\alpha_b})^\tau G \kappa_a^{-1} r_{jk,n}^{-\alpha_a}}\right]\right] \\
&\stackrel{(b)}{=} e^{-2\pi A_{km,b} \int_0^\infty \lambda_k p_{GP_{\alpha k}^a}(r_{jk,n}) \left(1 - \mathbb{E}_t\left[\frac{1}{1 + \mu_{ij}^s (\kappa_b t^{\alpha_b})^\tau G \kappa_a^{-1} r_{jk,n}^{-\alpha_a}}\right]\right) r_{jk,n} dr_{jk,n}} \\
&\stackrel{(c)}{=} e^{-2\pi A_{km,b} \int_0^\infty \lambda_k p_{GP_{\alpha k}^a}(r_{jk,n}) \left(1 - \left(\int_0^\infty \frac{\hat{f}_{r_{km,b}(t)}}{1 + \mu_{ij}^s (\kappa_b t^{\alpha_b})^\tau G \kappa_a^{-1} r_{jk,n}^{-\alpha_a}} dt\right)\right) r_{jk,n} dr_{jk,n}} \tag{A.28}
\end{aligned}$$

where (a) is obtained by applying the MGF of h , (b) is due to the computation of the PGFL of PPP, and (c) is the expectation with respect to t , which is the distance from the interfering UE to its serving BS.

13 Proof of Lemma 4.4

Given the special case, we have

$$\begin{aligned}
A_{10} &= \mathbb{E}_{r_{i0}} \left[\bar{F}_{r_1}(r) \bar{F}_{r_2} \left(\left(\frac{P_2 B_2}{P_1 B_1} \right)^{\frac{1}{2}} r \right) \right] = \int_0^\infty e^{\pi \lambda_1 r^2} e^{\pi \lambda_1 r^2 \frac{P_2 B_2}{P_1 B_1}} \frac{r}{\sigma^2} e^{-\frac{r^2}{2\sigma^2}} dr \\
&= \frac{1}{\sigma^2} \int_0^\infty r e^{-(\pi \lambda_1 + \pi \lambda_1 \frac{P_2 B_2}{P_1 B_1} + \frac{1}{2\sigma^2}) r^2} dr = \frac{1}{\sigma^2} \int_0^\infty r e^{-C_0 r^2} dr \\
&= \frac{1}{\sigma^2} \left(-\frac{1}{2C_0} e^{-C_0 r^2} \right) \Big|_0^\infty = \frac{1}{2C_0 \sigma^2} \tag{A.29}
\end{aligned}$$

Following a similar approach, we can obtain A_{11} and A_{12} . Then, we can have the PDFs of the conditional distances as $\hat{f}_{r10}(x) = \frac{x}{\sigma^2} e^{-C_0 x^2} / A_{10}$, $\hat{f}_{r11}(x) = 2\pi \lambda_1 x e^{-C_0 x^2} / A_{11}$, and $\hat{f}_{r12}(x) = 2\pi \lambda_2 x e^{-C_2 x^2} / A_{12}$, where C_0 and C_2 are given in Lemma 4. Using the PDFs, we can calculate the SNR coverage probability as

$$P_{C10}^c = \mathbb{E}_{r_{10}} \left[e^{-\mu \sigma_n^2} \right] = \int_0^\infty e^{-\frac{T \sigma_n^2}{P_u G_0} r^2} \frac{r}{\sigma^2} e^{-C_0 r^2} / A_{10} dr = \frac{1}{2\sigma^2 (C_0 + \frac{T \sigma_n^2}{P_u G_0}) A_{10}}. \tag{A.30}$$

$P_{C_{11}}^c$ and $P_{C_{12}}^c$ can be obtained similarly.

14 Proof of Theorem 6.1

Given that the typical UE is associated with a $s \in \{L, N\}$ BS in the 1^{st} tier, the association probability can be derived as follows:

$$\begin{aligned}
A_1^s &= \mathbb{P}(S_1^s) \stackrel{(a)}{=} \mathbb{P}(P_1 l_1^s > P_1 l_1^{s'} \cap P_1 l_1^s > P_2 l_2^L \cap P_1 l_1^s > P_2 l_2^N \cap P_1 l_1^s > P_3 l_3) \\
&\stackrel{(b)}{=} \mathbb{P}(P_1 l_1^s > P_1 l_1^{s'}) \mathbb{P}(P_1 l_1^s > P_2 l_2^L) \mathbb{P}(P_1 l_1^s > P_2 l_2^N) \mathbb{P}(P_1 l_1^s > P_3 l_3) \\
&= \mathbb{P}(\kappa_1^s e^{-\kappa x} x^{-\alpha_1^s} > \kappa_1^{s'} e^{-\kappa x} r_1^{-\alpha_1^{s'}}) \mathbb{P}(P_1 \kappa_1^s e^{-\kappa x} x^{-\alpha_1^s} > P_2 \kappa_2^L (r_2^2 + H_2^2)^{-\alpha_2^L/2}) \\
&\quad \mathbb{P}(P_1 \kappa_1^s e^{-\kappa x} x^{-\alpha_1^s} > P_2 \kappa_2^N (r_2^2 + H_2^2)^{-\alpha_2^N/2}) \mathbb{P}(P_1 \kappa_1^s e^{-\kappa x} x^{-\alpha_1^s} > P_3 \kappa_3^3 (r_3^2 + H_3^2)^{-\alpha_3/2}) \\
&\stackrel{(c)}{\approx} \mathbb{P}(\kappa_1^s x^{-\alpha_1^s} > \kappa_1^{s'} r_1^{-\alpha_1^{s'}}) \mathbb{P}(P_1 \kappa_1^s x^{-\alpha_1^s} > P_2 \kappa_2^L (r_2^2 + H_2^2)^{-\alpha_2^L/2}) \\
&\quad \mathbb{P}(P_1 \kappa_1^s x^{-\alpha_1^s} > P_2 \kappa_2^N (r_2^2 + H_2^2)^{-\alpha_2^N/2}) \mathbb{P}(P_1 \kappa_1^s x^{-\alpha_1^s} > P_3 \kappa_3^3 (r_3^2 + H_3^2)^{-\alpha_3/2}) \\
&= \mathbb{P}\left(r_1 > \left(\frac{\kappa_1^{s'}}{\kappa_1^s} x^{\alpha_1^s}\right)^{\frac{1}{\alpha_1^{s'}}}\right) \mathbb{P}\left(r_2 > \left(\left(\frac{P_2 \kappa_2^L}{P_1 \kappa_1^s} x^{\alpha_1^s}\right)^{\frac{2}{\alpha_2^L}} - H_2^2\right)^{\frac{1}{2}}\right) \\
&\quad \mathbb{P}\left(r_2 > \left(\left(\frac{P_2 \kappa_2^N}{P_1 \kappa_1^s} x^{\alpha_1^s}\right)^{\frac{2}{\alpha_2^N}} - H_2^2\right)^{\frac{1}{2}}\right) \mathbb{P}\left(r_3 > \left(\left(\frac{P_3 \kappa_3}{P_1 \kappa_1^s} x^{\alpha_1^s}\right)^{\frac{2}{\alpha_3}} - H_3^2\right)^{\frac{1}{2}}\right) \\
&\stackrel{(d)}{=} \mathbb{E}_{R_1^s} \left[\bar{F}_{R_1^{s'}} \left[\left(\frac{\kappa_1^{s'}}{\kappa_1^s} x^{\alpha_1^s}\right)^{\frac{1}{\alpha_1^{s'}}} \right] \bar{F}_{R_2^L} \left[\left(\left(\frac{P_2 \kappa_2^L}{P_1 \kappa_1^s} x^{\alpha_1^s}\right)^{\frac{2}{\alpha_2^L}} - H_2^2\right)^{\frac{1}{2}} \right] \right. \\
&\quad \left. \bar{F}_{R_2^N} \left[\left(\left(\frac{P_2 \kappa_2^N}{P_1 \kappa_1^s} x^{\alpha_1^s}\right)^{\frac{2}{\alpha_2^N}} - H_2^2\right)^{\frac{1}{2}} \right] \bar{F}_{R_3} \left[\left(\left(\frac{P_3 \kappa_3}{P_1 \kappa_1^s} x^{\alpha_1^s}\right)^{\frac{2}{\alpha_3}} - H_3^2\right)^{\frac{1}{2}} \right] \right]
\end{aligned} \tag{A.31}$$

where (a) is due to the definition of association probability. (b) is due to the fact that the thinned PPPs can be assumed independent. We replace the exponential decay with 1 for analysis tractability in (c), and this approximation is proved suitable through numerical simulation in Section V. And (d) is due to the fact the if the nearest distance from a j^{th} tier BS to the typical UE r_j is larger

than a certain value, then all the distances in that tier is larger than that value, and then we can use CCDFs of the nearest distances provided in (4.3) and (2.4). Using the same method, we can derive A_2^s and A_3 .

15 Proof of Theorem 6.2

According to [160, 197, 205], for a normalized Gamma random variable $u \sim \Gamma(N, \frac{1}{N})$, the probability $\mathbb{P}(u < x)$ can be tightly upper-bounded by $\mathbb{P}(u < x) < (1 - e^{-ax})^N$, where the constant $x > 0$ and $a = N(N!)^{\frac{1}{N}}$. Therefore, we have

$$\begin{aligned}
 M_j^s &= \mathbb{P}(P_j^{ms} > T) = \mathbb{E}_r[\mathbb{P}(P_j^{ms} > T|r)] \\
 &= \int_0^\infty \mathbb{P}(P_j G_j^m h^s l_j^s(r) > T) \hat{f}_{R_j^s}(r) dr \\
 &= \int_0^\infty \mathbb{P}\left(h^s > \frac{T}{P_j G_j^m l_j^s(r)}\right) \hat{f}_{R_j^s}(r) dr \\
 &\stackrel{(a)}{\approx} \int_0^\infty \left(1 - (1 - e^{-\frac{\xi N_s T}{P_j G_j^m l_j^s(r)}})^{N_s}\right) \hat{f}_{R_j^s}(r) dr \\
 &\stackrel{(b)}{=} \int_0^\infty \left(\sum_{n=1}^{N_s} (-1)^{n+1} \binom{N_s}{n} e^{-\frac{n \xi_s N_s T}{P_j G_j^m l_j^s(r)}}\right) \hat{f}_{R_j^s}(r) dr \\
 &= \sum_{n=1}^{N_s} (-1)^{n+1} \binom{N_s}{n} \int_0^\infty e^{-\frac{n \xi_s N_s T}{P_j G_j^m l_j^s(r)}} \hat{f}_{R_j^s}(r) dr
 \end{aligned} \tag{A.32}$$

where (a) is obtained by using the Gamma random variable approximation, and (b) is due to the Binomial theorem and the assumption that N_s is an integer.

16 Proof of Theorem 6.3

The Laplace transform of the interference from the k^{th} tier can be derived as follows:

$$\begin{aligned}
 \mathcal{L}_{I_k}(\mu) &= \mathbb{E}[e^{-\mu I_k}] \\
 &= \mathbb{E}[e^{\sum_{i \in \Phi_k \setminus \mathbb{Q}(r)} I_k^i}]
 \end{aligned}$$

$$\begin{aligned}
&\stackrel{(a)}{=} \exp \left(- \int_S (1 - \mathbb{E}[e^{-\mu I_k^i}]) \lambda_k dS \right) \\
&\stackrel{(b)}{=} \exp \left(- \sum_{s=L,N} \sum_G \int_S (1 - \mathbb{E}[e^{-\mu I_k^i}]) p_k^s p_k^G \lambda_k dS \right) \\
&\stackrel{(c)}{=} e^{-\sum_{s=L,N} \sum_G \int_{R_c(r)}^\infty (1 - \mathbb{E}[e^{-\mu I_k^i}]) p_k^s(x) p_k^G(x) \lambda_k 2\pi x dx} \\
&\stackrel{(d)}{=} e^{-\sum_s \sum_G \int_{R_c(r)}^\infty (1 - \frac{1}{(1 + \mu P_j G_j^G l_k^s(x) N^s)^{N^s}}) p_k^s(x) p_k^G(x) \lambda_k 2\pi x dx}
\end{aligned} \tag{A.33}$$

where r is the distance of the main link and x is the 2D length of one interfering link. (a) is due to the moment generating functional (MGFL) of PPP. (b) follows the fact that each interfering link can be in LOS/NLOS transmission and the antenna gain can be G_j^G . We expressed the area increment dS by distance increment $2\pi x dx$ in (c). And (d) comes from the application of the moment generating function (MGF) of gamma distribution $\mathbb{E}[e^{-\mu I_j^i}] = \mathbb{E}[e^{-\mu P_j G_j^G h^i l_j^s(x)}] = (1 + \mu P_j G_j^G l_j^s(x) N^s)^{-N^s}$.

17 Proof of Theorem 6.4

Given the typical UE is served by a s BS in the j^{th} tier, the SINR can be expressed in (6.17).

Therefore, the conditional SINR coverage probability can be derived as follows:

$$\begin{aligned}
C_j^s &= \mathbb{P}(\text{SINR}_j^s > T) = \mathbb{P} \left(\frac{P_j G_j^m h^s l_j^s(r)}{N + I} > T \right) \\
&= \mathbb{E} \left[\mathbb{P} \left(P_j G_j^m h^s l_j^s(r) > T(N + I) \right) \right] \\
&= \mathbb{E} \left[\mathbb{P} \left(h^s > \frac{T(N + I)}{P_j G_j^m l_j^s(r)} \right) \right] \\
&\stackrel{(a)}{=} \mathbb{E}_r \left[\sum_{n=1}^{N^s} (-1)^{n+1} \binom{N^s}{n} e^{-\frac{n \xi_s N^s T (N+I)}{P_j G_j^m l_j^s(r)}} \right] \\
&\stackrel{(b)}{=} \sum_{n=1}^{N^s} (-1)^{n+1} \binom{N^s}{n} \int_0^\infty e^{-\frac{n \xi_s N^s T N}{P_j G_j^m l_j^s(r)}} \mathbb{E} \left[e^{-\frac{n \xi_s N^s T I}{P_j G_j^m l_j^s(r)}} \right] \hat{f}_{R_j^s}(r) dr
\end{aligned} \tag{A.34}$$

where r is the distance from a UE to its serving BS, the PDF of which is $\hat{f}_{R_j^s}(r)$ given in (6.9). (a) is due to the MGF of h^s , and (b) is obtained by using the expectation with respect to r .

18 Proof of Lemma 7.1

We can express the CCDF as

$$\begin{aligned}
 \bar{F}_{R_0^s}(x) &= \mathbb{P}(r > x | \text{the link can be } s) = \frac{\mathbb{P}(r > x, \text{the link is } s)}{\mathbb{P}(\text{the link can be } s)} \\
 &= \frac{\mathbb{E}_D[\mathbb{P}(r > x | s, D) \mathbb{P}(s | D)]}{D_0^s} = (D_0^s)^{-1} \mathbb{E}_D[\mathbb{P}(\sqrt{D^2 + H^2} > x | s, D) p_j^s(\sqrt{D^2 + H^2})] \\
 &= (D_0^s)^{-1} \mathbb{E}_D[\mathbb{P}(D > \sqrt{x^2 - H^2}) p_j^s(\sqrt{D^2 + H^2})] \\
 &= (D_0^s)^{-1} \int_{\sqrt{x^2 - H^2}}^{\infty} p_j^s(\sqrt{d^2 + H^2}) f_D(d) dd
 \end{aligned} \tag{A.35}$$

where $x \geq H$, $s \in \{\text{LOS}, \text{NLOS}\}$, and $D_0^s = \int_0^\infty p_U^s(r) f_{R_0}(r) dr$ is the probability that the link between the typical UE and its cluster center UAV is in s transmission.

Therefore, we can get the PDF as follows:

$$f_{R_0^s}(x) = -\frac{d\bar{F}_{R_0^s}(x)}{dx} = \frac{x}{\sqrt{x^2 - H^2}} p_U^s(x) f_D(\sqrt{x^2 - H^2}) / D_0^s.$$

19 Proof of Lemma 7.2

Let us define two events $S_1 = \{\text{The typical UE is associated with a } j^{\text{th}} \text{ tier BS}\}$ and $S_2 = \{\text{The associated link is in } s \in \{\text{LOS}, \text{NLOS}\} \text{ transmission}\}$. Now we have

$$A_{j,s} \stackrel{(a)}{=} \mathbb{P}(S_1 S_2) \stackrel{(b)}{=} \mathbb{P}(S_2) \mathbb{P}(S_1 | S_2) \tag{A.36}$$

where (a) is due to the definition of the association probability, and (b) follows from the Bayes' theorem.

The association probability of the 0th tier UAV

$$\begin{aligned}
A_{0,s} &\stackrel{(a)}{=} D_0^s \mathbb{P}(P_0 B_0 L_{0,s}^{-1} > P_k B_k L_k^{-1}, k \in \{1, 2\}) = D_0^s \mathbb{P}\left(L_k > \frac{P_k B_k}{P_0 B_0} L_{0,s}, k \in \{1, 2\}\right) \\
&= \mathbb{E}_{R_0^s} \left[D_0^s \prod_k \prod_b D_k^b \mathbb{P}(\kappa_k^b r_k^{\alpha_k^b} > C_{k0} \kappa_0^s r_0^{\alpha_0^s}) \right] = \mathbb{E}_{R_0^s} \left[D_0^s \prod_k \prod_b D_k^b \bar{F}_{R_k^b}(Q_{k0}^{sb}(r_0)) \right] \quad (\text{A.37})
\end{aligned}$$

where $C_{kj} = \frac{P_k B_k}{P_j B_j}$, $Q_{kj}^{sb}(r) = \left(\frac{P_k B_k \kappa_j^s}{P_j B_j \kappa_k^b} r^{\alpha_j^s}\right)^{\frac{1}{\alpha_k^b}}$, $D_0^s = \int_0^\infty p_U^s(r) f_{R_0}(r) dr$ is the probability that the link from the typical UE to its own cluster center UAV can be in s transmission, and (a) is due to the fact that there is only one UAV in the 0th tier and the LOS BSs and NLOS BSs in the 1st and 2nd tier are independent.

The association probability of the j^{th} tier BSs

$$\begin{aligned}
A_{j,s} &= \mathbb{P}(L_{j,s}^{-1} > L_{j,s'}^{-1}) \mathbb{P}(P_j B_j L_{j,s}^{-1} > P_k B_k L_k^{-1}, k \in \{0, 1, 2\}, k \neq j) \\
&= \mathbb{P}(L_{j,s'} > L_{j,s}) \mathbb{P}(L_k > \frac{P_k B_k}{P_j B_j} L_{j,s}, k \in \{0, 1, 2\}, k \neq j) \\
&= \mathbb{P}(L_{j,s'} > L_{j,s}) \mathbb{P}(L_{0,L} > C_{0j} L_{j,s} \text{ or } L_{0,N} > C_{0j} L_{j,s}) \\
&\quad \times \mathbb{P}(L_{k,L} > C_{kj} L_{j,s} \text{ and } L_{k,N} > C_{kj} L_{j,s}, k \neq j) \\
&= D_j^s \mathbb{E}_{R_j^s} \left[D_j^{s'} \mathbb{P}(\kappa_j^{s'} r_j^{\alpha_j^{s'}} > \kappa_j^s r_j^{\alpha_j^s}) \left(\sum_b D_0^b \mathbb{P}(\kappa_0^b r_0^{\alpha_0^b} > C_{0j} \kappa_j^s r_j^{\alpha_j^s}) \right) \prod_b D_k^b \mathbb{P}(\kappa_k^b r_k^{\alpha_k^b} > C_{kj} \kappa_j^s r_j^{\alpha_j^s}) \right] \\
&= D_j^s \mathbb{E}_{R_j^s} \left[D_j^{s'} \bar{F}_{R_j^{s'}}(Q_{jj}^{ss'}(r_j)) \left(\sum_b D_0^b \bar{F}_{R_0^b}(Q_{0j}^{sb}(r_j)) \right) \prod_b D_k^b \bar{F}_{R_k^b}(Q_{kj}^{sb}(r_j)) \right] \quad (\text{A.38})
\end{aligned}$$

where $s, s' \in \{\text{LOS}, \text{NLOS}\}$, $s' \neq s$, $D_j^s = 1 - e^{-2\pi\lambda_j \int_0^\infty tp_j^s(t)dt}$ is the probability that the typical UE has at least one LOS/NLOS j^{th} tier BS around.

20 Proof of Theorem 7.1

Given $S_{j,s} = \{\text{The typical UE is associated with a LOS/NLOS BS in the } j^{th} \text{ tier}\}$, we can express the conditional energy coverage probability as

$$\begin{aligned}
 P_{E_{j,s}}^c(\rho, \tau, \gamma_E) &\stackrel{(a)}{=} \mathbb{P}(\tau(1-\rho)(P_m + I) > \gamma_E | S_{j,s}) \stackrel{(b)}{=} \sum_{n=0}^N (-1)^n \binom{N}{n} \mathbb{E} [e^{-\hat{a}(P_m + I)}] \\
 &\stackrel{(c)}{=} \sum_{n=0}^N (-1)^n \binom{N}{n} \mathbb{E} \left[\mathbb{E}_{h_0} [e^{-\hat{a}P_m}] \prod_k \mathbb{E} [e^{-\hat{a}I_k}] \right] \\
 &\stackrel{(d)}{=} \sum_{n=0}^N (-1)^n \binom{N}{n} \mathbb{E} \left[(1 + \hat{a}P_j G(\kappa_j^s r^{\alpha_j^s} N_s)^{-1})^{-N_s} \prod_k \mathcal{L}_{I_k}(\hat{a}) \right] \quad (\text{A.39})
 \end{aligned}$$

where P_m is the received power of the main link, $I = I_0 + I_1 + I_2$ is the total interference, $\hat{a} = \frac{a n \tau (1-\rho)}{T}$, $a = N(N!)^{-\frac{1}{N}}$. (a) follows from the definition of energy coverage. (b) is modified from [197, Appendix A]. (c) is due to the independence of P_m , I_0 , I_1 and I_2 given $S_{j,s}$. (d) is calculated by using the MGF of a normalized Gamma random variable.

For I_0

Since I_0 only exists when the typical UE is associated with the 1^{th} tier UAVs or the 2^{nd} tier GBSs, we have

$$\mathcal{L}_{I_0}(\hat{a}) \stackrel{(a)}{=} \sum_G \sum_b p_G D_0^b \mathcal{L}_{I_0^{bG}}(\hat{a}) \quad (\text{A.40})$$

$$\begin{aligned}
 \mathcal{L}_{I_0^{bG}}(\hat{a}) &= \mathbb{E}_{r_0 | S_{j,s}} \left[\mathbb{E}_{h_0} \left[\exp \left(-\hat{a} P_0 G h_0 \left(\kappa_0^b r_0^{\alpha_0^b} \right)^{-1} \right) \right] \right] \\
 &\stackrel{(b)}{=} \mathbb{E}_{r_0 | S_{j,s}} \left[\left(1 + \hat{a} P_0 G (\kappa_0^b r_0^{\alpha_0^b} N_b)^{-1} \right)^{-N_b} \right] \\
 &= \int_{\max(H, Q_{0j}^{sb}(r))}^{\infty} \frac{f_{R_0^b}(r_0 | r_0 > Q_{0j}^{sb}(r))}{\left(1 + \hat{a} P_0 G (\kappa_0^b r_0^{\alpha_0^b} N_b)^{-1} \right)^{N_b}} dr_0 \\
 &= \int_{\max(H, Q_{0j}^{sb}(r))}^{\infty} \frac{f_{R_0^b}(r_0) dr_0}{\left(1 + \hat{a} P_0 G (\kappa_0^b r_0^{\alpha_0^b} N_b)^{-1} \right)^{N_b} D_0^b \bar{F}_{R_0^b}(Q_{0j}^{sb}(r))} \quad (\text{A.41})
 \end{aligned}$$

where $s, b \in \{\text{LOS}, \text{NLOS}\}$, $G \in \{M_b M_u, M_b m_u, m_b M_u, m_b m_u\}$, p_G is the probability for G , (a) is due to the fact that there is only one BS in the 0^{th} tier which can be in LOS or NLOS transmission with antenna gain G , and (b) is because of the MGF of a normalized Gamma random variable.

For I_k ($k = 1, 2$)

$$\mathcal{L}_{I_k}(\hat{a}) = \prod_G \prod_b \mathcal{L}_{I_k^{bG}}(\hat{a}) \quad (\text{A.42})$$

$$\begin{aligned} \mathcal{L}_{I_0^{bG}}(\hat{a}) &= E_{r_k|S_{j,s}} \left[\left(1 + \hat{a} P_k G (\kappa_k^b r_k^{\alpha_k^b} N_b)^{-1} \right)^{-N_b} \right] \\ &\stackrel{(a)}{=} e^{-2\pi\lambda_k p_G \int_{B_{d2}}^\infty \left(1 - \left(1 + \hat{a} P_k G (\kappa_k^b r_k^{\alpha_k^b} N_b)^{-1} \right)^{-N_b} \right) p_k^b(r_k) r_k dr_k} \end{aligned} \quad (\text{A.43})$$

where $B_{d2} = \max(H, Q_{kj}^{sb}(r))$ for $k = 1$, and $B_{d2} = Q_{kj}^{sb}$ for $k = 2$. (a) follows by computing the MGFL of PPP.

Therefore, by substituting (A.40) - (A.43) into (A.39), we can obtain (7.22).

21 Proof of Theorem 7.2

Given $S_{j,s}$, we can express the conditional successful transmission probability as

$$\begin{aligned} &P_{\text{suc}_{j,s}}^c(\rho, \tau, \gamma_E, \gamma_{\text{sinr}}) \\ &\stackrel{(a)}{=} \mathbb{P} \left(\tau(1 - \rho)(P_m + I) > \gamma_E, \frac{P_m}{\frac{\sigma_c^2}{\rho} + \sigma_n^2 + I} > \gamma_{\text{sinr}} \middle| S_{j,s} \right) \\ &= \mathbb{P} \left(P_m > T_1, P_m > T_2 \middle| S_{j,s} \right) \\ &= \mathbb{P} \left(P_m > T_1, \middle| S_{j,s} \right) \mathbb{1} \left(T_1 > T_2 \middle| S_{j,s} \right) + \mathbb{P} \left(P_m > T_2 \middle| S_{j,s} \right) \mathbb{1} \left(T_1 \leq T_2 \middle| S_{j,s} \right) \\ &\stackrel{(b)}{=} \mathbb{E}_I \left[\mathbb{P} \left(P_m > T_1, \middle| S_{j,s} \right) \right] \mathbb{E}_I \left[\mathbb{1} \left(T_1 > T_2 \middle| S_{j,s} \right) \right] \\ &\quad + \mathbb{E}_I \left[\mathbb{P} \left(P_m > T_2, \middle| S_{j,s} \right) \right] \mathbb{E}_I \left[\mathbb{1} \left(T_1 \leq T_2 \middle| S_{j,s} \right) \right] \\ &\stackrel{(c)}{=} P_{E_{j,s}}^c(\rho, \gamma_E) \mathbb{E}_I \left[\mathbb{1} \left(I < \omega \middle| S_{j,s} \right) \right] + P_{\text{SINR}_{j,s}}^c(\rho, \gamma_{\text{sinr}}) \mathbb{E}_I \left[\mathbb{1} \left(I \geq \omega \middle| S_{j,s} \right) \right] \end{aligned}$$

$$= P_{E_{j,s}}^c(\rho, \gamma_E)(1 - \hat{F}_I(\omega)) + P_{SINR_{j,s}}^c(\rho, \gamma_{sinr})\hat{F}_I(\omega) \quad (\text{A.44})$$

where $T_1 = \frac{\gamma_E}{\tau(1-\rho)} - I$, $T_2 = \gamma_{sinr} \left(\frac{\sigma_c^2}{\rho} + \sigma_n^2 + I \right)$, $\omega = \frac{1}{1+\gamma_{sinr}} \left(\frac{\gamma_E}{\tau(1-\rho)} - \gamma_{sinr} \left(\frac{\sigma_c^2}{\rho} + \sigma_n^2 \right) \right)$, $\hat{F}_I(x)$ is the CCDF of I , (a) follows from the definition of the successful transmission probability, (b) is due to the fact that given I , the indicator function is a constant and is independent to P_m , (c) follows from the definition of energy and SINR coverage probability and ω is obtained by $\frac{\gamma_E}{\tau(1-\rho)} - I > \gamma_{sinr} \left(\frac{\sigma_c^2}{\rho} + \sigma_n^2 + I \right)$.

Since $\hat{F}_I(x) = \mathbb{P}(I > x)$ and this is similar as the energy coverage probability when $P_m = 0$, we can obtain the expression of $\hat{F}_I(x)$ following the derivation in Appendix 7.1 by replacing γ_E and ρ with x and 0.

22 Proof of Theorem 7.3

We can express the SINR coverage probability in the uplink phase as

$$\begin{aligned} P_{SINR}^{UL}(\gamma_{UL}) &= \mathbb{P} \left(\frac{P_t^{UL} G_0 h_0 (k_U^s r_0^{\alpha_U^s})^{-1}}{\sigma_n^2 + I_{user}} \geq \gamma^{UL} \right) \\ &= \mathbb{P} \left(h_0 \geq \frac{\gamma^{UL} r_0^{\alpha_U^s}}{P_t^{UL} G_0 k_U^s} (\sigma_n^2 + I_{user}) \right) \\ &\stackrel{(a)}{=} \mathbb{E}_{R_0^s} \left[\sum_{n=0}^{N_s} (-1)^{n+1} \binom{N_s}{n} \exp \left(-\frac{n \eta_s \gamma^{UL} r_0^{\alpha_U^s}}{P_t^{UL} G_0 k_U^s} (\sigma_n^2 + I_{user}^L + I_{user}^N) \right) \right] \\ &= \mathbb{E}_{R_0^s} \left[\sum_{n=0}^{N_s} (-1)^{n+1} \binom{N_s}{n} e^{-\mu_s^{UL} \sigma_n^2} \mathcal{L}_{I_{user}^L}(\mu_s^{UL}) \mathcal{L}_{I_{user}^N}(\mu_s^{UL}) \right] \end{aligned} \quad (\text{A.45})$$

where $\mu_s^{UL} = \frac{n \eta_s \gamma^{UL} r_0^{\alpha_U^s}}{P_t^{UL} G_0 k_U^s}$ and (a) follows by computing the MGF of the gamma random variable h_0 . $\mathcal{L}_{I_{user}^b}(\mu_s^{UL})$ is the Laplace transform expression and can be further analyzed as follows:

$$\mathcal{L}_{I_{user}^b}(\mu_s^{UL}) = \prod_G \mathcal{L}_{I_{user}^{bG}}(\mu_s^{UL}) \quad (\text{A.46})$$

where

$$\begin{aligned}
\mathcal{L}_{I_{user}^{bG}}(\mu_s^{UL}) &= \mathbb{E} [\exp(-\mu_s^{UL} I_{user}^{bG})] \\
&= \mathbb{E} \left[\exp \left(-\mu_s^{UL} \sum_{i \in \Phi_{user}^b} P_t^{UL} G_i h_i (\kappa_U^b r_i^{\alpha_U^b})^{-1} \right) \right] \\
&= \mathbb{E}_{\mathbf{x}} \left[\prod_{\mathbf{x} \in \Phi_{\mathbf{U}}} \mathbb{E}_{\mathbf{y}} \left[\mathbb{E}_{h_i} \left[\exp \left(-\mu_s^{UL} P_t^{UL} G_i h_i (\kappa_U^b (\|\mathbf{x} + \mathbf{y}\|^2 + H^2)^{\frac{\alpha_U^b}{2}})^{-1} \right) \right] \right] \right] \\
&\stackrel{(a)}{=} \mathbb{E}_{\mathbf{x}} \left[\prod_{\mathbf{x} \in \Phi_{\mathbf{U}}} \mathbb{E}_{\mathbf{y}} \left[\frac{1}{\left(1 + \mu_s^{UL} P_t^{UL} G_i (\kappa_U^b (\|\mathbf{x} + \mathbf{y}\|^2 + H^2)^{\frac{\alpha_U^b}{2}} N_b)^{-1} \right)^{N_b}} \right] \right] \\
&\stackrel{(b)}{=} \mathbb{E}_{\mathbf{x}} \left[\prod_{\mathbf{x} \in \Phi_{\mathbf{U}}} \iint_{R^2} \frac{1}{\left(1 + \mu_s^{UL} P_t^{UL} G_i (\kappa_U^b (\|\mathbf{x} + \mathbf{y}\|^2 + H^2)^{\frac{\alpha_U^b}{2}} N_b)^{-1} \right)^{N_b}} f_{\mathbf{Y}}(y) dy \right] \\
&\stackrel{(c)}{=} \exp \left(-p_G \lambda_{user}^b \iint_{R^2} \left(1 - \iint_{R^2} \left(1 + \frac{\mu_s^{UL} P_t^{UL} G_i}{\kappa_U^b (\|\mathbf{x} + \mathbf{y}\|^2 + H^2)^{\frac{\alpha_U^b}{2}} N_b} \right)^{-N_b} f_{\mathbf{Y}}(y) dy \right) dx \right) \\
&\stackrel{(d)}{=} \exp \left(-2\pi p_G \lambda_{user}^b \int_0^\infty \left(1 - \int_0^\infty \left(1 + \frac{\mu_s^{UL} P_t^{UL} G_i}{\kappa_U^b (\| \mathbf{x} + \mathbf{y} \|^2 + H^2)^{\frac{\alpha_U^b}{2}} N_b} \right)^{-N_b} f(v|w) dv \right) w dw \right)
\end{aligned} \tag{A.47}$$

where \mathbf{y} is the coordinate of the interfering UE with respect to the projection of its cluster center, \mathbf{x} is the coordinate of the ground projection of that cluster center with respect to the ground projection of the typical UAV, and $w = \|\mathbf{x}\|$ and $v = \|\mathbf{x} + \mathbf{y}\|$. (a) is due to the MGF of h_i . (b) follows from the definition of expectation. (c) is due to the computation of the PGFL of PPP. (d) is obtained by converting the coordinates from Cartesian to polar.

REFERENCES

- [1] M. R. Akdeniz, Y. Liu, M. K. Samimi, S. Sun, S. Rangan, T. S. Rappaport, and E. Erkip, “Millimeter wave channel modeling and cellular capacity evaluation,” *IEEE Journal on Selected Areas in Communications*, vol. 32, no. 6, pp. 1164–1179, June 2014. 1, 30, 60
- [2] G. Yao, N. Liu, Z. Pan, and X. You, “Coverage and rate analysis for non-uniform millimeter-wave heterogeneous cellular network,” in *2016 8th International Conference on Wireless Communications Signal Processing (WCSP)*, October 2016, pp. 1–6. 1
- [3] Z. Pi and F. Khan, “An introduction to millimeter-wave mobile broadband systems,” *IEEE Communications Magazine*, vol. 49, no. 6, pp. 101–107, June 2011. 1, 34
- [4] J. Kokkonen, J. Lehtomäki, and M. Juntti, “Stochastic geometry analysis for mean interference power and outage probability in THz networks,” *IEEE Transactions on Wireless Communications*, vol. 16, no. 5, pp. 3017–3028, 2017. 2, 8, 26, 32, 111
- [5] J. M. Jornet and I. F. Akyildiz, “Channel modeling and capacity analysis for electromagnetic wireless nanonetworks in the terahertz band,” *IEEE Transactions on Wireless Communications*, vol. 10, no. 10, pp. 3211–3221, 2011. 2, 32, 33
- [6] Y. Wu and C. Han, “Interference and coverage analysis for indoor terahertz wireless local area networks,” in *2019 IEEE Globecom Workshops (GC Wkshps)*, 2019, pp. 1–6. 2, 8, 32, 33, 111
- [7] V. Petrov, M. Komarov, D. Moltchanov, J. M. Jornet, and Y. Koucheryavy, “Interference and SINR in millimeter wave and terahertz communication systems with blocking and di-

- rectional antennas,” *IEEE Transactions on Wireless Communications*, vol. 16, no. 3, pp. 1791–1808, 2017. 2, 8, 32, 111, 118
- [8] D. Moltchanov, P. Kustarev, and Y. Koucheryavy, “Analytical approximations for interference and SIR densities in terahertz systems with atmospheric absorption, directional antennas and blocking,” *Physical Communication*, vol. 26, pp. 21–30, 2018. 2, 8, 32, 111
- [9] A. H. Sakr and E. Hossain, “Analysis of K -tier uplink cellular networks with ambient RF energy harvesting,” *IEEE Journal on Selected Areas in Communications*, vol. 33, no. 10, pp. 2226–2238, October 2015. 2
- [10] Y. J. Chun, M. O. Hasna, and A. Ghrayeb, “Modeling and analysis of HetNet interference using Poisson cluster processes,” in *2014 IEEE 25th Annual International Symposium on Personal, Indoor, and Mobile Radio Communication (PIMRC)*, September 2014, pp. 681–686. 2
- [11] H. S. Dhillon, R. K. Ganti, F. Baccelli, and J. G. Andrews, “Modeling and analysis of K -tier downlink heterogeneous cellular networks,” *IEEE Journal on Selected Areas in Communications*, vol. 30, no. 3, pp. 550–560, April 2012. 2
- [12] H. S. Jo, Y. J. Sang, P. Xia, and J. G. Andrews, “Heterogeneous cellular networks with flexible cell association: A comprehensive downlink SINR analysis,” *IEEE Transactions on Wireless Communications*, vol. 11, no. 10, pp. 3484–3495, October 2012. 2, 52
- [13] C. Saha, M. Afshang, and H. S. Dhillon, “3GPP-inspired HetNet model using Poisson cluster process: Sum-product functionals and downlink coverage,” *IEEE Transactions on Communications*, vol. 66, no. 5, pp. 2219–2234, May 2018. 2, 3, 8, 56
- [14] A. Jaziri, R. Nasri, and T. Chahed, “System-level analysis of heterogeneous networks under imperfect traffic hotspot localization,” *IEEE Transactions on Vehicular Technology*, vol. 65, no. 12, pp. 9862–9872, December 2016. 2

- [15] M. Afshang and H. S. Dhillon, "Poisson cluster process based analysis of HetNets with correlated user and base station locations," *IEEE Transactions on Wireless Communications*, vol. 17, no. 4, pp. 2417–2431, April 2018. 3, 9
- [16] C. Saha, M. Afshang, and H. S. Dhillon, "Poisson cluster process: Bridging the gap between PPP and 3GPP hetnet models," in *2017 Information Theory and Applications Workshop (ITA)*, February 2017, pp. 1–9. 3
- [17] Y. Zhou, Z. Zhao, Y. Louët, Q. Ying, R. Li, X. Zhou, X. Chen, and H. Zhang, "Large-scale spatial distribution identification of base stations in cellular networks," *IEEE Access*, vol. 3, pp. 2987–2999, 2015. 3
- [18] F. Boccardi, R. W. Heath, A. Lozano, T. L. Marzetta, and P. Popovski, "Five disruptive technology directions for 5G," *IEEE Communications Magazine*, vol. 52, no. 2, pp. 74–80, February 2014. 3
- [19] Y. Zeng, Q. Wu, and R. Zhang, "Accessing from the sky: A tutorial on UAV communications for 5G and beyond," *Proceedings of the IEEE*, vol. 107, no. 12, pp. 2327–2375, 2019. 3, 4, 5, 161, 162
- [20] Y. Zeng, J. Lyu, and R. Zhang, "Cellular-connected UAV: Potential, challenges, and promising technologies," *IEEE Wireless Communications*, vol. 26, no. 1, pp. 120–127, February 2019. 3
- [21] M. Mozaffari, W. Saad, M. Bennis, Y. Nam, and M. Debbah, "A tutorial on UAVs for wireless networks: Applications, challenges, and open problems," *IEEE Communications Surveys Tutorials*, pp. 1–1, 2019. 3, 12
- [22] P. K. Sharma and D. I. Kim, "Coverage probability of 3D mobile UAV networks," *IEEE Wireless Communications Letters*, pp. 1–1, 2018. 3, 11

- [23] C. Liu, M. Ding, C. Ma, Q. Li, Z. Lin, and Y. Liang, "Performance analysis for practical unmanned aerial vehicle networks with LoS/NLoS transmissions," in *2018 IEEE International Conference on Communications Workshops (ICC Workshops)*, May 2018, pp. 1–6. 3, 4, 11, 142
- [24] M. M. Azari, F. Rosas, and S. Pollin, "Cellular connectivity for UAVs: Network modeling, performance analysis and design guidelines," *IEEE Transactions on Wireless Communications*, pp. 1–1, 2019. 4, 12
- [25] W. Guo, C. Devine, and S. Wang, "Performance analysis of micro unmanned airborne communication relays for cellular networks," in *2014 9th international symposium on communication systems, networks & digital sign (CSNDSP)*. IEEE, 2014, pp. 658–663. 4
- [26] K. Gomez, T. Rasheed, L. Reynaud, and S. Kandeepan, "On the performance of aerial LTE base-stations for public safety and emergency recovery," in *2013 IEEE Globecom Workshops (GC Wkshps)*. IEEE, 2013, pp. 1391–1396. 4
- [27] K. Gomez, A. Hourani, L. Goratti, R. Riggio, S. Kandeepan, and I. Bucaille, "Capacity evaluation of aerial LTE base-stations for public safety communications," in *2015 European conference on networks and communications (EuCNC)*. IEEE, 2015, pp. 133–138. 4
- [28] V. V. Chetlur and H. S. Dhillon, "Downlink coverage analysis for a finite 3-D wireless network of unmanned aerial vehicles," *IEEE Transactions on Communications*, vol. 65, no. 10, pp. 4543–4558, 2017. 4
- [29] B. Galkin, J. Kibilda, and L. A. DaSilva, "Coverage analysis for low-altitude UAV networks in urban environments," in *GLOBECOM 2017-2017 IEEE Global Communications Conference*. IEEE, 2017, pp. 1–6. 4
- [30] C. Liu, M. Ding, C. Ma, Q. Li, Z. Lin, and Y.-C. Liang, "Performance analysis for practical unmanned aerial vehicle networks with LoS/NLoS transmissions," in *2018 IEEE Interna-*

tional Conference on Communications Workshops (ICC Workshops). IEEE, 2018, pp. 1–6.

4

- [31] H. Bayerlein, M. Theile, M. Caccamo, and D. Gesbert, “Multi-UAV path planning for wireless data harvesting with deep reinforcement learning,” *arXiv preprint arXiv:2010.12461*, 2020. 4, 15, 16
- [32] U. Challita, W. Saad, and C. Bettstetter, “Interference management for cellular-connected UAVs: A deep reinforcement learning approach,” *IEEE Transactions on Wireless Communications*, vol. 18, no. 4, pp. 2125–2140, 2019. 4, 14, 15
- [33] D. Wang, B. Bai, W. Zhao, and Z. Han, “A survey of optimization approaches for wireless physical layer security,” *IEEE Communications Surveys & Tutorials*, vol. 21, no. 2, pp. 1878–1911, 2018. 5
- [34] S. Bhattacharya and T. Başar, “Game-theoretic analysis of an aerial jamming attack on a UAV communication network,” in *Proceedings of the 2010 American Control Conference*. IEEE, 2010, pp. 818–823. 5
- [35] P. Henderson, R. Islam, P. Bachman, J. Pineau, D. Precup, and D. Meger, “Deep reinforcement learning that matters,” in *Proceedings of the AAAI Conference on Artificial Intelligence*, vol. 32, no. 1, 2018. 5
- [36] T. P. Lillicrap, J. J. Hunt, A. Pritzel, N. Heess, T. Erez, Y. Tassa, D. Silver, and D. Wierstra, “Continuous control with deep reinforcement learning,” *arXiv preprint arXiv:1509.02971*, 2015. 5
- [37] D. Silver, A. Huang, C. J. Maddison, A. Guez, L. Sifre, G. Van Den Driessche, J. Schrittwieser, I. Antonoglou, V. Panneershelvam, M. Lanctot *et al.*, “Mastering the game of go with deep neural networks and tree search,” *nature*, vol. 529, no. 7587, pp. 484–489, 2016.

5

- [38] V. Mnih, K. Kavukcuoglu, D. Silver, A. Graves, I. Antonoglou, D. Wierstra, and M. Riedmiller, "Playing atari with deep reinforcement learning," *arXiv preprint arXiv:1312.5602*, 2013. 5
- [39] O. Vinyals, T. Ewalds, S. Bartunov, P. Georgiev, A. Vezhnevets, M. Yeo, A. Makhzani, H. Küttler, J. Agapiou, J. Schrittwieser *et al.*, "A new challenge for reinforcement learning," *arXiv preprint ArXiv:1708.04782*, 2017. 5
- [40] V. d. N. Silva and L. Chaimowicz, "MOBA: a new arena for game AI," *arXiv preprint arXiv:1705.10443*, 2017. 5
- [41] N. C. Luong, D. T. Hoang, S. Gong, D. Niyato, P. Wang, Y. Liang, and D. I. Kim, "Applications of deep reinforcement learning in communications and networking: A survey," *IEEE Communications Surveys Tutorials*, vol. 21, no. 4, pp. 3133–3174, 2019. 5
- [42] K. Arulkumaran, M. P. Deisenroth, M. Brundage, and A. A. Bharath, "A brief survey of deep reinforcement learning," *CoRR*, vol. abs/1708.05866, 2017. [Online]. Available: <http://arxiv.org/abs/1708.05866> 6
- [43] M. Mohammadi, A. Al-Fuqaha, M. Guizani, and J.-S. Oh, "Semisupervised deep reinforcement learning in support of IoT and smart city services," *IEEE Internet of Things Journal*, vol. 5, no. 2, pp. 624–635, 2017. 6
- [44] X. He, K. Wang, H. Huang, T. Miyazaki, Y. Wang, and S. Guo, "Green resource allocation based on deep reinforcement learning in content-centric IoT," *IEEE Transactions on Emerging Topics in Computing*, 2018. 6
- [45] M. Chu, H. Li, X. Liao, and S. Cui, "Reinforcement learning-based multiaccess control and battery prediction with energy harvesting in IoT systems," *IEEE Internet of Things Journal*, vol. 6, no. 2, pp. 2009–2020, 2018. 6

- [46] Y. Yu, T. Wang, and S. C. Liew, “Deep-reinforcement learning multiple access for heterogeneous wireless networks,” *IEEE Journal on Selected Areas in Communications*, vol. 37, no. 6, pp. 1277–1290, 2019.
- [47] R. Amiri, M. A. Almasi, J. G. Andrews, and H. Mehrpouyan, “Reinforcement learning for self organization and power control of two-tier heterogeneous networks,” *IEEE Transactions on Wireless Communications*, vol. 18, no. 8, pp. 3933–3947, 2019. 6
- [48] N. Zhao, Y.-C. Liang, D. Niyato, Y. Pei, and Y. Jiang, “Deep reinforcement learning for user association and resource allocation in heterogeneous networks,” in *2018 IEEE Global Communications Conference (GLOBECOM)*. IEEE, 2018, pp. 1–6. 6
- [49] C. H. Liu, Z. Chen, J. Tang, J. Xu, and C. Piao, “Energy-efficient UAV control for effective and fair communication coverage: A deep reinforcement learning approach,” *IEEE Journal on Selected Areas in Communications*, vol. 36, no. 9, pp. 2059–2070, 2018. 6
- [50] X. Liu, Y. Liu, and Y. Chen, “Reinforcement learning in multiple-UAV networks: Deployment and movement design,” *IEEE Transactions on Vehicular Technology*, vol. 68, no. 8, pp. 8036–8049, 2019. 6
- [51] J. Cui, Y. Liu, and A. Nallanathan, “Multi-agent reinforcement learning-based resource allocation for UAV networks,” *IEEE Transactions on Wireless Communications*, vol. 19, no. 2, pp. 729–743, 2019. 6
- [52] H. X. Pham, H. M. La, D. Feil-Seifer, and L. V. Nguyen, “Autonomous UAV navigation using reinforcement learning,” *arXiv preprint arXiv:1801.05086*, 2018. 6
- [53] N. Imanberdiyev, C. Fu, E. Kayacan, and I.-M. Chen, “Autonomous navigation of UAV by using real-time model-based reinforcement learning,” in *2016 14th International Conference on Control, Automation, Robotics and Vision (ICARCV)*. IEEE, 2016, pp. 1–6.

- [54] C. Wang, J. Wang, X. Zhang, and X. Zhang, "Autonomous navigation of UAV in large-scale unknown complex environment with deep reinforcement learning," in *2017 IEEE Global Conference on Signal and Information Processing (GlobalSIP)*. IEEE, 2017, pp. 858–862. 6
- [55] Y. Niu, Y. Li, D. Jin, L. Su, and A. V. Vasilakos, "A survey of millimeter wave communications (mmWave) for 5G: opportunities and challenges," *Wireless networks*, vol. 21, no. 8, pp. 2657–2676, 2015. 6, 34
- [56] M. D. Renzo, "Stochastic geometry modeling and analysis of multi-tier millimeter wave cellular networks," *IEEE Transactions on Wireless Communications*, vol. 14, no. 9, pp. 5038–5057, September 2015. 6, 30, 60, 65
- [57] E. Turgut and M. C. Gursoy, "Coverage in heterogeneous downlink millimeter wave cellular networks," *IEEE Transactions on Communications*, vol. 65, no. 10, pp. 4463–4477, October 2017. 6, 30, 44, 46, 47, 52, 57, 65, 227
- [58] B. Yang, G. Mao, X. Ge, M. Ding, and X. Yang, "On the energy-efficient deployment for ultra-dense heterogeneous networks with NLoS and LoS transmissions," *IEEE Transactions on Green Communications and Networking*, vol. 2, no. 2, pp. 369–384, June 2018. 7
- [59] M. Rebato, J. Park, P. Popovski, E. D. Carvalho, and M. Zorzi, "Stochastic geometric coverage analysis in mmWave cellular networks with a realistic channel model," in *2017 IEEE Global Communications Conference*, December 2017, pp. 1–6. 7
- [60] C. H. Liu, D. C. Liang, J. R. Yang, and J. Chen, "A generalized analytical framework for coverage evaluation in mmWave heterogeneous cellular networks in urban areas," in *2017 IEEE International Conference on Communications (ICC)*, May 2017, pp. 1–7. 7
- [61] O. Onireti, A. Imran, and M. A. Imran, "Coverage, capacity, and energy efficiency analysis in the uplink of mmWave cellular networks," *IEEE Transactions on Vehicular Technology*, vol. 67, no. 5, pp. 3982–3997, May 2018. 7, 82, 84, 230

- [62] M. Shi, K. Yang, C. Xing, and R. Fan, “Decoupled heterogeneous networks with millimeter wave small cells,” *IEEE Transactions on Wireless Communications*, vol. 17, no. 9, pp. 5871–5884, September 2018. 7, 76, 88
- [63] H. Elshaer, M. N. Kulkarni, F. Boccardi, J. G. Andrews, and M. Dohler, “Downlink and uplink cell association with traditional macrocells and millimeter wave small cells,” *IEEE Transactions on Wireless Communications*, vol. 15, no. 9, pp. 6244–6258, September 2016. 7
- [64] T. Ding, M. Ding, G. Mao, Z. Lin, and D. López-Pérez, “Uplink performance analysis of dense cellular networks with LoS and NLoS transmissions,” in *2016 IEEE International Conference on Communications (ICC)*, May 2016, pp. 1–6. 7
- [65] M. Zeng, W. Hao, O. A. Dobre, and H. V. Poor, “Energy-efficient power allocation in uplink mmwave massive MIMO with NOMA,” *IEEE Transactions on Vehicular Technology*, vol. 68, no. 3, pp. 3000–3004, 2019. 7
- [66] X. Yu, F. Xu, K. Yu, and N. Li, “Joint energy-efficient power allocation and beamforming for uplink mmWave-NOMA system,” *IEEE Transactions on Vehicular Technology*, vol. 69, no. 10, pp. 12 291–12 295, 2020. 7
- [67] A. Shafie, N. Yang, Z. Sun, and S. Durrani, “Coverage analysis for 3D terahertz communication systems with blockage and directional antennas,” *arXiv preprint arXiv:2004.07466*, 2020. 7, 32
- [68] C. Wang, X. Yao, C. Han, and W. Wang, “Interference and coverage analysis for terahertz band communication in nanonetworks,” in *GLOBECOM 2017 - 2017 IEEE Global Communications Conference*, 2017, pp. 1–6. 8
- [69] Y. Zhong and W. Zhang, “Multi-channel hybrid access femtocells: A stochastic geometric analysis,” *IEEE Transactions on Communications*, vol. 61, no. 7, pp. 3016–3026, July 2013.

- [70] C. Chen, R. C. Elliott, and W. A. Krzymień, “Downlink coverage analysis of n -tier heterogeneous cellular networks based on clustered stochastic geometry,” in *2013 Asilomar Conference on Signals, Systems and Computers*, November 2013, pp. 1577–1581. 9
- [71] H. Tabassum, E. Hossain, and J. Hossain, “Modeling and analysis of uplink non-orthogonal multiple access in large-scale cellular networks using Poisson cluster processes,” *IEEE Transactions on Communications*, vol. 65, no. 8, pp. 3555–3570, August 2017. 9
- [72] C. Saha, M. Afshang, and H. S. Dhillon, “Enriched K -tier HetNet model to enable the analysis of user-centric small cell deployments,” *IEEE Transactions on Wireless Communications*, vol. 16, no. 3, pp. 1593–1608, March 2017. 9, 44
- [73] W. Yi, Y. Liu, A. Nallanathan, and M. ElKashlan, “Clustered millimeter-wave networks with non-orthogonal multiple access,” *IEEE Transactions on Communications*, vol. 67, no. 6, pp. 4350–4364, June 2019. 9
- [74] M. Afshang, H. S. Dhillon, and P. H. J. Chong, “Modeling and performance analysis of clustered device-to-device networks,” *IEEE Transactions on Wireless Communications*, vol. 15, no. 7, pp. 4957–4972, July 2016. 9, 76, 129
- [75] X. Wu and Z. Ma, “Modeling and performance analysis of cellular and device-to-device heterogeneous networks,” in *2017 IEEE Globecom Workshops (GC Wkshps)*, December 2017, pp. 1–6. 9
- [76] M. Afshang, H. S. Dhillon, and P. H. J. Chong, “Fundamentals of cluster-centric content placement in cache-enabled device-to-device networks,” *IEEE Transactions on Communications*, vol. 64, no. 6, pp. 2511–2526, June 2016. 9
- [77] W. Yi, Y. Liu, and A. Nallanathan, “Modeling and analysis of D2D millimeter-wave networks with Poisson cluster processes,” *IEEE Transactions on Communications*, vol. 65, no. 12, pp. 5574–5588, December 2017. 9

- [78] E. Turgut and M. C. Gursoy, "Uplink performance analysis in D2D-enabled millimeter-wave cellular networks with clustered users," *IEEE Transactions on Wireless Communications*, vol. 18, no. 2, pp. 1085–1100, February 2019. 9
- [79] H. Tabassum, E. Hossain, and J. Hossain, "Modeling and analysis of uplink non-orthogonal multiple access in large-scale cellular networks using Poisson cluster processes," *IEEE Transactions on Communications*, vol. 65, no. 8, pp. 3555–3570, 2017. 9
- [80] M. Arif, S. Wyne, K. Navaie, and S. J. Nawaz, "Decoupled downlink and uplink access for aerial terrestrial heterogeneous cellular networks," *IEEE Access*, 2020. 10
- [81] A. Alkhateeb, S. Alex, P. Varkey, Y. Li, Q. Qu, and D. Tujkovic, "Deep learning coordinated beamforming for highly-mobile millimeter wave systems," *IEEE Access*, vol. 6, pp. 37 328–37 348, 2018. 10
- [82] T. Maksymyuk, J. Gazda, O. Yaremko, and D. Nevinskiy, "Deep learning based massive MIMO beamforming for 5G mobile network," in *2018 IEEE 4th International Symposium on Wireless Systems within the International Conferences on Intelligent Data Acquisition and Advanced Computing Systems (IDAACS-SWS)*, September. 2018, pp. 241–244. 10
- [83] W. Xia, G. Zheng, Y. Zhu, J. Zhang, J. Wang, and A. P. Petropulu, "A deep learning framework for optimization of MISO downlink beamforming," *CoRR*, vol. abs/1901.00354, 2019. [Online]. Available: <http://arxiv.org/abs/1901.00354> 10
- [84] X. Li and A. Alkhateeb, "Deep learning for direct hybrid precoding in millimeter wave massive MIMO systems," *CoRR*, vol. abs/1905.13212, 2019. [Online]. Available: <http://arxiv.org/abs/1905.13212> 10
- [85] F. B. Mismar, B. L. Evans, and A. Alkhateeb, "Deep reinforcement learning for 5G networks: Joint beamforming, power control, and interference coordination," *arXiv preprint arXiv:1907.00123*, 2019. 11, 101

- [86] R. Shafin, H. Chen, Y. H. Nam, S. Hur, J. Park, J. Reed, L. Liu *et al.*, “Self-tuning sectorization: Deep reinforcement learning meets broadcast beam optimization,” *arXiv preprint arXiv:1906.06021*, 2019. 11
- [87] L. Zhou, Z. Yang, S. Zhou, and W. Zhang, “Coverage probability analysis of UAV cellular networks in urban environments,” in *2018 IEEE International Conference on Communications Workshops (ICC Workshops)*, May 2018, pp. 1–6. 11, 34
- [88] B. Galkin, J. Kibilda, and L. A. DaSilva, “Coverage analysis for low-altitude UAV networks in urban environments,” in *GLOBECOM 2017 - 2017 IEEE Global Communications Conference*, December 2017, pp. 1–6. 11
- [89] V. V. Chetlur and H. S. Dhillon, “Downlink coverage analysis for a finite 3-D wireless network of unmanned aerial vehicles,” *IEEE Transactions on Communications*, vol. 65, no. 10, pp. 4543–4558, October 2017. 11
- [90] A. M. Hayajneh, S. A. R. Zaidi, D. C. McLernon, M. Di Renzo, and M. Ghogho, “Performance analysis of UAV enabled disaster recovery networks: A stochastic geometric framework based on cluster processes,” *IEEE Access*, vol. 6, pp. 26 215–26 230, 2018. 11
- [91] E. Turgut and M. C. Gursoy, “Downlink analysis in unmanned aerial vehicle (UAV) assisted cellular networks with clustered users,” *IEEE Access*, vol. 6, pp. 36 313–36 324, 2018. 11
- [92] W. Yi, Y. Liu, M. ElKashlan, and A. Nallanathan, “Modeling and coverage analysis of downlink UAV networks with mmWave communications,” in *2019 IEEE International Conference on Communications Workshops (ICC Workshops)*, May 2019, pp. 1–6. 11
- [93] W. Yi, Y. Liu, E. L. Bodanese, A. Nallanathan, and G. K. Karagiannidis, “A unified spatial framework for UAV-aided mmWave networks,” *CoRR*, vol. abs/1901.01432, 2019. [Online]. Available: <http://arxiv.org/abs/1901.01432> 12

- [94] A. Kumbhar, H. Binol, I. Guvenç, and K. Akkaya, “Interference coordination for aerial and terrestrial nodes in three-tier LTE-advanced HetNet,” in *2019 IEEE Radio and Wireless Symposium (RWS)*, Jan 2019, pp. 1–4. 12
- [95] N. Cherif, M. Alzenad, H. Yanikomeroglu, and A. Yongacoglu, “Downlink coverage and rate analysis of an aerial user in integrated aerial and terrestrial networks,” *arXiv preprint arXiv:1905.11934*, 2019. 12, 157
- [96] B. Galkin, J. Kibilda, and L. A. DaSilva, “Impact of UAV antenna configuration on wireless connectivity in urban environments,” *CoRR*, vol. abs/1807.00696, 2018. [Online]. Available: <http://arxiv.org/abs/1807.00696> 12, 13, 38
- [97] H. Chang, J. Bian, C. Wang, Z. Bail, J. Sun, and X. Gao, “A 3D wideband geometry-based stochastic model for UAV air-to-ground channels,” in *2018 IEEE Global Communications Conference (GLOBECOM)*, December 2018, pp. 206–212. 12
- [98] H. Wang, J. Wang, J. Chen, Y. Gong, and G. Ding, “Network-connected UAV communications: Potentials and challenges,” *China Communications*, vol. 15, no. 12, pp. 111–121, Dec 2018. 12
- [99] J. Lyu and R. Zhang, “Network-connected UAV: 3D system modeling and coverage performance analysis,” *arXiv preprint arXiv:1901.07887*, 2019. 12, 13
- [100] S. M. Razavizadeh, M. Ahn, and I. Lee, “Three-dimensional beamforming: A new enabling technology for 5G wireless networks,” *IEEE Signal Processing Magazine*, vol. 31, no. 6, pp. 94–101, November 2014. 12
- [101] J. Lyu and R. Zhang, “Network-connected UAV: 3-D system modeling and coverage performance analysis,” *IEEE Internet of Things Journal*, vol. 6, no. 4, pp. 7048–7060, 2019. 12

- [102] Wookbong Lee, S. Lee, Han-Bae Kong, and I. Lee, “3D beamforming designs for single user MISO systems,” in *2013 IEEE Global Communications Conference (GLOBECOM)*, December 2013, pp. 3914–3919. 13, 140
- [103] M. Baianifar, S. Khavari, S. M. Razavizadeh, and T. Svensson, “Impact of user height on the coverage of 3D beamforming-enabled massive MIMO systems,” in *2017 IEEE 28th Annual International Symposium on Personal, Indoor, and Mobile Radio Communications (PIMRC)*, October 2017, pp. 1–5. 13
- [104] S. Zhang and R. Zhang, “Trajectory optimization for cellular-connected UAV under outage duration constraint,” *Journal of Communications and Information Networks*, vol. 4, no. 4, pp. 55–71, 2019. 13
- [105] Y. Zeng, X. Xu, and R. Zhang, “Trajectory design for completion time minimization in UAV-enabled multicasting,” *IEEE Transactions on Wireless Communications*, vol. 17, no. 4, pp. 2233–2246, 2018. 13
- [106] Y. Zeng and R. Zhang, “Energy-efficient UAV communication with trajectory optimization,” *IEEE Transactions on Wireless Communications*, vol. 16, no. 6, pp. 3747–3760, 2017. 13
- [107] S. De Bast, E. Vinogradov, and S. Pollin, “Cellular coverage-aware path planning for UAVs,” in *2019 IEEE 20th International Workshop on Signal Processing Advances in Wireless Communications (SPAWC)*, 2019, pp. 1–5. 13
- [108] B. Khamidehi and E. S. Sousa, “Power efficient trajectory optimization for the cellular-connected aerial vehicles,” in *2019 IEEE 30th Annual International Symposium on Personal, Indoor and Mobile Radio Communications (PIMRC)*, 2019, pp. 1–6. 13
- [109] H. Yang, J. Zhang, S. Song, and K. B. Lataief, “Connectivity-aware UAV path planning with aerial coverage maps,” in *2019 IEEE Wireless Communications and Networking Conference (WCNC)*. IEEE, 2019, pp. 1–6. 13

- [110] S. Zhang and R. Zhang, "Radio map based 3D path planning for cellular-connected UAV," *IEEE Transactions on Wireless Communications*, 2020. 13
- [111] X. Mu, Y. Liu, L. Guo, and J. Lin, "Non-orthogonal multiple access for air-to-ground communication," *IEEE Transactions on Communications*, vol. 68, no. 5, pp. 2934–2949, 2020. 13
- [112] S. Zhang, Y. Zeng, and R. Zhang, "Cellular-enabled UAV communication: A connectivity-constrained trajectory optimization perspective," *IEEE Transactions on Communications*, vol. 67, no. 3, pp. 2580–2604, 2019. 14, 15
- [113] E. Bulut and I. Guevenc, "Trajectory optimization for cellular-connected UAVs with dis-connectivity constraint," in *2018 IEEE International Conference on Communications Workshops (ICC Workshops)*, 2018, pp. 1–6. 14, 15
- [114] B. Khamidehi and E. S. Sousa, "A double Q-learning approach for navigation of aerial vehicles with connectivity constraint," *arXiv preprint arXiv:2002.10563*, 2020. 14
- [115] Y. Zeng, X. Xu, S. Jin, and R. Zhang, "Simultaneous navigation and radio mapping for cellular-connected UAV with deep reinforcement learning," *IEEE Transactions on Wireless Communications*, 2021. 14, 163, 170
- [116] R. W. Beard and T. W. McLain, "Multiple UAV cooperative search under collision avoidance and limited range communication constraints," in *42nd IEEE International Conference on Decision and Control (IEEE Cat. No.03CH37475)*, vol. 1, 2003, pp. 25–30 Vol.1. 14
- [117] D. Bauso, L. Giarre, and R. Pesenti, "Multiple UAV cooperative path planning via neuro-dynamic programming," in *2004 43rd IEEE Conference on Decision and Control (CDC) (IEEE Cat. No.04CH37601)*, vol. 1, 2004, pp. 1087–1092 Vol.1. 14

- [118] B. D. Song, J. Kim, and J. R. Morrison, “Rolling horizon path planning of an autonomous system of UAVs for persistent cooperative service: MILP formulation and efficient heuristics,” *Journal of Intelligent & Robotic Systems*, vol. 84, no. 1-4, pp. 241–258, 2016. 14
- [119] T. B. Wolf and M. J. Kochenderfer, “Aircraft collision avoidance using Monte Carlo real-time belief space search,” *Journal of Intelligent & Robotic Systems*, vol. 64, no. 2, pp. 277–298, 2011. 14
- [120] S. Temizer, M. Kochenderfer, L. Kaelbling, T. Lozano-Pérez, and J. Kuchar, “Collision avoidance for unmanned aircraft using Markov decision processes,” in *AIAA guidance, navigation, and control conference*, 2010, p. 8040. 14
- [121] H. Bai, D. Hsu, M. J. Kochenderfer, and W. S. Lee, “Unmanned aircraft collision avoidance using continuous-state POMDPs,” *Robotics: Science and Systems VII*, vol. 1, pp. 1–8, 2012. 14
- [122] Y. Lin and S. Saripalli, “Collision avoidance for UAVs using reachable sets,” in *2015 International Conference on Unmanned Aircraft Systems (ICUAS)*, 2015, pp. 226–235. 14
- [123] T. Yu, J. Tang, L. Bai, and S. Lao, “Collision avoidance for cooperative UAVs with rolling optimization algorithm based on predictive state space,” *Applied Sciences*, vol. 7, no. 4, p. 329, 2017. 14
- [124] Y. Chen, J. Yu, X. Su, and G. Luo, “Path planning for multi-UAV formation,” *Journal of Intelligent & Robotic Systems*, vol. 77, no. 1, pp. 229–246, 2015. 14
- [125] M. Kothari, I. Postlethwaite, and D.-W. Gu, “Multi-UAV path planning in obstacle rich environments using rapidly-exploring random trees,” in *Proceedings of the 48th IEEE Conference on Decision and Control (CDC) held jointly with 2009 28th Chinese Control Conference*. IEEE, 2009, pp. 3069–3074. 14

- [126] C. Zhan and Y. Zeng, "Aerial-ground cost tradeoff for multi-UAV-enabled data collection in wireless sensor networks," *IEEE Transactions on Communications*, vol. 68, no. 3, pp. 1937–1950, 2019. 15
- [127] Z. Wang, R. Liu, Q. Liu, J. S. Thompson, and M. Kadoch, "Energy-efficient data collection and device positioning in UAV-assisted IoT," *IEEE Internet of Things Journal*, vol. 7, no. 2, pp. 1122–1139, 2019. 15
- [128] J. Li, H. Zhao, H. Wang, F. Gu, J. Wei, H. Yin, and B. Ren, "Joint optimization on trajectory, altitude, velocity, and link scheduling for minimum mission time in UAV-aided data collection," *IEEE Internet of Things Journal*, vol. 7, no. 2, pp. 1464–1475, 2019. 15
- [129] M. Samir, S. Sharafeddine, C. M. Assi, T. M. Nguyen, and A. Ghrayeb, "UAV trajectory planning for data collection from time-constrained IoT devices," *IEEE Transactions on Wireless Communications*, vol. 19, no. 1, pp. 34–46, 2019. 15
- [130] Q. Wu, Y. Zeng, and R. Zhang, "Joint trajectory and communication design for multi-UAV enabled wireless networks," *IEEE Transactions on Wireless Communications*, vol. 17, no. 3, pp. 2109–2121, 2018. 15
- [131] C. Zhan, Y. Zeng, and R. Zhang, "Energy-efficient data collection in UAV enabled wireless sensor network," *IEEE Wireless Communications Letters*, vol. 7, no. 3, pp. 328–331, 2017. 15
- [132] M. Hua, L. Yang, Q. Wu, and A. L. Swindlehurst, "3D UAV trajectory and communication design for simultaneous uplink and downlink transmission," *IEEE Transactions on Communications*, vol. 68, no. 9, pp. 5908–5923, 2020. 15
- [133] H. Wang, G. Ren, J. Chen, G. Ding, and Y. Yang, "Unmanned aerial vehicle-aided communications: Joint transmit power and trajectory optimization," *IEEE Wireless Communications Letters*, vol. 7, no. 4, pp. 522–525, 2018. 15

- [134] J. Baek, S. I. Han, and Y. Han, "Energy-efficient UAV routing for wireless sensor networks," *IEEE Transactions on Vehicular Technology*, vol. 69, no. 2, pp. 1741–1750, 2019. 15
- [135] M. Yi, X. Wang, J. Liu, Y. Zhang, and B. Bai, "Deep reinforcement learning for fresh data collection in UAV-assisted IoT networks," in *IEEE INFOCOM 2020-IEEE Conference on Computer Communications Workshops (INFOCOM WKSHPS)*. IEEE, 2020, pp. 716–721. 16
- [136] B. Zhang, C. H. Liu, J. Tang, Z. Xu, J. Ma, and W. Wang, "Learning-based energy-efficient data collection by unmanned vehicles in smart cities," *IEEE Transactions on Industrial Informatics*, vol. 14, no. 4, pp. 1666–1676, 2017. 16
- [137] K. Li, W. Ni, E. Tovar, and A. Jamalipour, "On-board deep Q-network for UAV-assisted online power transfer and data collection," *IEEE Transactions on Vehicular Technology*, vol. 68, no. 12, pp. 12 215–12 226, 2019. 16
- [138] O. Bouhamed, H. Ghazzai, H. Besbes, and Y. Massoud, "A UAV-assisted data collection for wireless sensor networks: Autonomous navigation and scheduling," *IEEE Access*, vol. 8, pp. 110 446–110 460, 2020. 16
- [139] S. Fu, Y. Tang, Y. Wu, N. Zhang, H. Gu, C. Chen, and M. Liu, "Energy-efficient UAV enabled data collection via wireless charging: A reinforcement learning approach," *IEEE Internet of Things Journal*, 2021. 16
- [140] H. Bayerlein, P. De Kerret, and D. Gesbert, "Trajectory optimization for autonomous flying base station via reinforcement learning," in *2018 IEEE 19th International Workshop on Signal Processing Advances in Wireless Communications (SPAWC)*. IEEE, 2018, pp. 1–5. 16
- [141] S. Khairy, P. Balaprakash, L. X. Cai, and Y. Cheng, "Constrained deep reinforcement learning for energy sustainable multi-UAV based random access IoT networks with NOMA," *IEEE Journal on Selected Areas in Communications*, 2020. 16

- [142] R. Zhang, M. Wang, L. X. Cai, and X. Shen, "Learning to be proactive: Self-regulation of UAV based networks with UAV and user dynamics," *IEEE Transactions on Wireless Communications*, 2021. 16
- [143] X. Liu, Y. Liu, Y. Chen, and L. Hanzo, "Trajectory design and power control for multi-UAV assisted wireless networks: A machine learning approach," *IEEE Transactions on Vehicular Technology*, vol. 68, no. 8, pp. 7957–7969, 2019. 16, 17
- [144] Y.-H. Hsu and R.-H. Gau, "Reinforcement learning-based collision avoidance and optimal trajectory planning in UAV communication networks," *IEEE Transactions on Mobile Computing*, 2020. 16, 17
- [145] B. Duan, D. Yin, Y. Cong, H. Zhou, X. Xiang, and L. Shen, "Anti-jamming path planning for unmanned aerial vehicles with imperfect jammer information," in *2018 IEEE International Conference on Robotics and Biomimetics (ROBIO)*. IEEE, 2018, pp. 729–735. 17, 18
- [146] L. Xiao, C. Xie, M. Min, and W. Zhuang, "User-centric view of unmanned aerial vehicle transmission against smart attacks," *IEEE Transactions on Vehicular Technology*, vol. 67, no. 4, pp. 3420–3430, 2017. 17
- [147] W. Wang, X. Lu, S. Liu, L. Xiao, and B. Yang, "Energy efficient relay in UAV networks against jamming: A reinforcement learning based approach," in *2020 IEEE 91st Vehicular Technology Conference (VTC2020-Spring)*. IEEE, 2020, pp. 1–5. 17
- [148] X. Zhou, Q. Wu, S. Yan, F. Shu, and J. Li, "UAV-enabled secure communications: Joint trajectory and transmit power optimization," *IEEE Transactions on Vehicular Technology*, vol. 68, no. 4, pp. 4069–4073, 2019. 17
- [149] Y. Gao, Y. Wu, Z. Cui, H. Chen, and W. Yang, "Robust design for turning and climbing angle-constrained UAV communication under malicious jamming," *IEEE Communications Letters*, 2020. 18

- [150] Y. Wu, W. Fan, W. Yang, X. Sun, and X. Guan, "Robust trajectory and communication design for multi-UAV enabled wireless networks in the presence of jammers," *IEEE Access*, vol. 8, pp. 2893–2905, 2019. 18
- [151] B. Duo, Q. Wu, X. Yuan, and R. Zhang, "Anti-jamming 3D trajectory design for UAV-enabled wireless sensor networks under probabilistic LoS channel," *IEEE Transactions on Vehicular Technology*, 2020. 18
- [152] H. Wang, J. Chen, G. Ding, and J. Sun, "Trajectory planning in UAV communication with jamming," in *2018 10th International Conference on Wireless Communications and Signal Processing (WCSP)*. IEEE, 2018, pp. 1–6. 18
- [153] Z. Lin, X. Lu, C. Dai, G. Sheng, and L. Xiao, "Reinforcement learning based UAV trajectory and power control against jamming," in *International Conference on Machine Learning for Cyber Security*. Springer, 2019, pp. 336–347. 18
- [154] M. Haenggi, J. G. Andrews, F. Baccelli, O. Dousse, and M. Franceschetti, "Stochastic geometry and random graphs for the analysis and design of wireless networks," *IEEE Journal on Selected Areas in Communications*, vol. 27, no. 7, pp. 1029–1046, 2009. 26
- [155] R. K. Ganti and M. Haenggi, "Interference and outage in clustered wireless Ad Hoc networks," *IEEE Transactions on Information Theory*, vol. 55, no. 9, pp. 4067–4086, 2009. 28
- [156] S. N. Chiu, D. Stoyan, W. S. Kendall, and J. Mecke, *Stochastic geometry and its applications*. John Wiley & Sons, 2013. 28
- [157] T. Bai, R. Vaze, and R. W. Heath, "Analysis of blockage effects on urban cellular networks," *IEEE Transactions on Wireless Communications*, vol. 13, no. 9, pp. 5070–5083, 2014. 29, 84

- [158] T. S. Rappaport, S. Sun, R. Mayzus, H. Zhao, Y. Azar, K. Wang, G. N. Wong, J. K. Schulz, M. Samimi, and F. Gutierrez, “Millimeter wave mobile communications for 5G cellular: It will work!” *IEEE Access*, vol. 1, pp. 335–349, 2013. 30, 64
- [159] T. S. Rappaport, F. Gutierrez, E. Ben-Dor, J. N. Murdock, Y. Qiao, and J. I. Tamir, “Broadband millimeter-wave propagation measurements and models using adaptive-beam antennas for outdoor urban cellular communications,” *IEEE Transactions on Antennas and Propagation*, vol. 61, no. 4, pp. 1850–1859, 2013. 30
- [160] T. Bai and R. W. Heath, “Coverage and rate analysis for millimeter-wave cellular networks,” *IEEE Trans. Wireless Commun.*, vol. 14, no. 2, pp. 1100–1114, February 2015. 30, 34, 36, 44, 46, 60, 66, 75, 118, 142, 236
- [161] R. W. Heath, M. Kountouris, and T. Bai, “Modeling heterogeneous network interference using Poisson point processes,” *IEEE Transactions on Signal Processing*, vol. 61, no. 16, pp. 4114–4126, 2013. 30
- [162] M. Ding, P. Wang, D. López-Pérez, G. Mao, and Z. Lin, “Performance impact of LoS and NLoS transmissions in dense cellular networks,” *IEEE Transactions on Wireless Communications*, vol. 15, no. 3, pp. 2365–2380, March 2016. 30, 60, 69
- [163] A. Al-Hourani, S. Kandeepan, and S. Lardner, “Optimal LAP altitude for maximum coverage,” *IEEE Wireless Communications Letters*, vol. 3, no. 6, pp. 569–572, December 2014. 33
- [164] S. Kutty and D. Sen, “Beamforming for millimeter wave communications: An inclusive survey,” *IEEE Communications Surveys Tutorials*, vol. 18, no. 2, pp. 949–973, Secondquarter 2016. 34
- [165] J. Mietzner, R. Schober, L. Lampe, W. H. Gerstacker, and P. A. Hoeher, “Multiple-antenna techniques for wireless communications - a comprehensive literature survey,” *IEEE Communications Surveys Tutorials*, vol. 11, no. 2, pp. 87–105, Second 2009. 34

- [166] X. Yu, J. Zhang, M. Haenggi, and K. B. Letaief, "Coverage analysis for millimeter wave networks: The impact of directional antenna arrays," *IEEE Journal on Selected Areas in Communications*, vol. 35, no. 7, pp. 1498–1512, July 2017. 34, 35, 66
- [167] N. Deng and M. Haenggi, "A novel approximate antenna pattern for directional antenna arrays," *IEEE Wireless Communications Letters*, pp. 1–1, 2018. 35
- [168] J. Ikuno, M. Wrulich, and M. Rupp, "3GPP TR 36.814 (v9. 0.0): Evolved universal terrestrial radio access (E-UTRA); further advancements for E-UTRA physical layer aspects," *Tech. Rep.*, 2010. 36, 111, 118, 157, 162
- [169] J. Chen, D. Raye, W. Khawaja, P. Sinha, and I. Guvenc, "Impact of 3D UWB antenna radiation pattern on air-to-ground drone connectivity," in *2018 IEEE 88th Vehicular Technology Conference (VTC-Fall)*, Aug 2018, pp. 1–5. 38
- [170] Y. F. Chen, M. Liu, M. Everett, and J. P. How, "Decentralized non-communicating multi-agent collision avoidance with deep reinforcement learning," in *2017 IEEE international conference on robotics and automation (ICRA)*. IEEE, 2017, pp. 285–292. 39, 166, 167, 168, 169, 171, 178
- [171] M. Everett, Y. F. Chen, and J. P. How, "Collision avoidance in pedestrian-rich environments with deep reinforcement learning," *IEEE Access*, vol. 9, pp. 10 357–10 377, 2021. 39, 168, 171
- [172] R. S. Sutton and A. G. Barto, *Reinforcement learning: An introduction*. MIT press, 2018. 39, 40
- [173] C. J. Watkins and P. Dayan, "Q-learning," *Machine learning*, vol. 8, no. 3-4, pp. 279–292, 1992. 41
- [174] P. Lv, X. Wang, Y. Cheng, and Z. Duan, "Stochastic double deep Q-network," *IEEE Access*, vol. 7, pp. 79 446–79 454, 2019. 41

- [175] H. Van Hasselt, A. Guez, and D. Silver, “Deep reinforcement learning with double q-learning,” in *Thirtieth AAAI conference on artificial intelligence*, 2016. 41
- [176] Z. Wang, T. Schaul, M. Hessel, H. Hasselt, M. Lanctot, and N. Freitas, “Dueling network architectures for deep reinforcement learning,” in *International conference on machine learning*. PMLR, 2016, pp. 1995–2003. 42
- [177] N. Zhao, Y.-C. Liang, D. Niyato, Y. Pei, M. Wu, and Y. Jiang, “Deep reinforcement learning for user association and resource allocation in heterogeneous cellular networks,” *IEEE Transactions on Wireless Communications*, vol. 18, no. 11, pp. 5141–5152, 2019. 42
- [178] J. G. Andrews, T. Bai, M. N. Kulkarni, A. Alkhateeb, A. K. Gupta, and R. W. Heath, “Modeling and analyzing millimeter wave cellular systems,” *IEEE Transactions on Communications*, vol. 65, no. 1, pp. 403–430, January 2017. 44, 46
- [179] S. Singh, H. S. Dhillon, and J. G. Andrews, “Offloading in heterogeneous networks: Modeling, analysis, and design insights,” *IEEE Transactions on Wireless Communications*, vol. 12, no. 5, pp. 2484–2497, May 2013. 49, 129
- [180] L. Zhang, H. C. Yang, and M. O. Hasna, “Generalized area spectral efficiency: An effective performance metric for green wireless communications,” *IEEE Transactions on Communications*, vol. 62, no. 2, pp. 747–757, February 2014. 58
- [181] A. K. Gupta, J. G. Andrews, and R. W. Heath, “On the feasibility of sharing spectrum licenses in mmWave cellular systems,” *IEEE Transactions on Communications*, vol. 64, no. 9, pp. 3981–3995, September 2016. 64
- [182] M. R. Akdeniz, Y. Liu, M. K. Samimi, S. Sun, S. Rangan, T. S. Rappaport, and E. Erkip, “Millimeter wave channel modeling and cellular capacity evaluation,” *IEEE Journal on Selected Areas in Communications*, vol. 32, no. 6, pp. 1164–1179, June 2014. 65

- [183] G. Ghatak, A. D. Domenico, and M. Coupechoux, "Coverage analysis and load balancing in HetNets with millimeter wave multi-RAT small cells," *IEEE Transactions on Wireless Communications*, vol. 17, no. 5, pp. 3154–3169, May 2018. 68
- [184] B. Yang, G. Mao, M. Ding, X. Ge, and X. Tao, "Dense small cell networks: From noise-limited to dense interference-limited," *IEEE Transactions on Vehicular Technology*, vol. 67, no. 5, pp. 4262–4277, May 2018. 69
- [185] I. Atzeni, J. Arnau, and M. Kountouris, "Downlink cellular network analysis with LOS/NLOS propagation and elevated base stations," *IEEE Transactions on Wireless Communications*, vol. 17, no. 1, pp. 142–156, January 2018. 69
- [186] A. Simonsson and A. Furuskar, "Uplink power control in LTE - overview and performance, subtitle: Principles and benefits of utilizing rather than compensating for SINR variations," in *2008 IEEE 68th Vehicular Technology Conference*, 2008, pp. 1–5. 83
- [187] J. G. Andrews, A. K. Gupta, and H. S. Dhillon, "A primer on cellular network analysis using stochastic geometry," *CoRR*, vol. abs/1604.03183, 2016. [Online]. Available: <http://arxiv.org/abs/1604.03183> 83
- [188] H. ElSawy and E. Hossain, "On stochastic geometry modeling of cellular uplink transmission with truncated channel inversion power control," *IEEE Transactions on Wireless Communications*, vol. 13, no. 8, pp. 4454–4469, 2014. 83
- [189] O. E. Ayach, S. Rajagopal, S. Abu-Surra, Z. Pi, and R. W. Heath, "Spatially sparse precoding in millimeter wave MIMO systems," *IEEE Transactions on Wireless Communications*, vol. 13, no. 3, pp. 1499–1513, March 2014. 99
- [190] 3GPP, "3GPP TR 36.828 (v11. 0.0): Further enhancements to LTE time division duplex (TDD) for downlink-uplink (DL-UL) interference management and traffic adaptation," 2012. 100, 157

- [191] J. Jiang and D. Kong, "Joint user scheduling and MU-MIMO hybrid beamforming algorithm for mmwave FDMA massive MIMO system," *International Journal of Antennas and Propagation*, vol. 2016, 2016. 101
- [192] A. Alkhateeb, G. Leus, and R. W. Heath, "Limited feedback hybrid precoding for multi-user millimeter wave systems," *IEEE Transactions on Wireless Communications*, vol. 14, no. 11, pp. 6481–6494, November 2015. 101, 104
- [193] H. Elshaer, M. N. Kulkarni, F. Boccardi, J. G. Andrews, and M. Dohler, "Downlink and uplink cell association with traditional macrocells and millimeter wave small cells," *IEEE Transactions on Wireless Communications*, vol. 15, no. 9, pp. 6244–6258, 2016. 111
- [194] J. Tang, G. Chen, J. P. Coon, and D. E. Simmons, "Distance distributions for Matérn cluster processes with application to network performance analysis," in *2017 IEEE International Conference on Communications (ICC)*, May 2017, pp. 1–6. 129
- [195] X. Wang, E. Turgut, and M. C. Gursoy, "Coverage in downlink heterogeneous mmWave cellular networks with user-centric small cell deployment," *IEEE Transactions on Vehicular Technology*, vol. 68, no. 4, pp. 3513–3533, April 2019. 129, 134
- [196] M. Mozaffari, W. Saad, M. Bennis, and M. Debbah, "Unmanned aerial vehicle with underlaid device-to-device communications: Performance and tradeoffs," *IEEE Transactions on Wireless Communications*, vol. 15, no. 6, pp. 3949–3963, June 2016. 142
- [197] T. A. Khan, A. Alkhateeb, and R. W. Heath, "Millimeter wave energy harvesting," *IEEE Transactions on Wireless Communications*, vol. 15, no. 9, pp. 6048–6062, September 2016. 142, 236, 240
- [198] Y. Zeng, J. Lyu, and R. Zhang, "Cellular-connected UAV: Potential, challenges, and promising technologies," *IEEE Wireless Communications*, vol. 26, no. 1, pp. 120–127, 2018. 161

- [199] “Study on enhanced LTE support for aerial vehicles,” *3GPP TR 36.777 V15.0.0*, Dec 2017. 162
- [200] J. Van Den Berg, S. J. Guy, M. Lin, and D. Manocha, “Reciprocal n-body collision avoidance,” in *Robotics research*. Springer, 2011, pp. 3–19. 167, 169, 173, 174, 205
- [201] H. Kretzschmar, M. Spies, C. Sprunk, and W. Burgard, “Socially compliant mobile robot navigation via inverse reinforcement learning,” *The International Journal of Robotics Research*, vol. 35, no. 11, pp. 1289–1307, 2016. [Online]. Available: <https://doi.org/10.1177/0278364915619772> 167
- [202] C. Chen, Y. Liu, S. Kreiss, and A. Alahi, “Crowd-robot interaction: Crowd-aware robot navigation with attention-based deep reinforcement learning,” *CoRR*, vol. abs/1809.08835, 2018. [Online]. Available: <http://arxiv.org/abs/1809.08835> 168, 171
- [203] J. van den Berg, Ming Lin, and D. Manocha, “Reciprocal velocity obstacles for real-time multi-agent navigation,” in *2008 IEEE International Conference on Robotics and Automation*, 2008, pp. 1928–1935. 169
- [204] J. Snape, J. v. d. Berg, S. J. Guy, and D. Manocha, “The hybrid reciprocal velocity obstacle,” *IEEE Transactions on Robotics*, vol. 27, no. 4, pp. 696–706, 2011. 169
- [205] H. Alzer, “On some inequalities for the incomplete gamma function,” *Mathematics of Computation*, vol. 66, no. 218, pp. 771–778, 1997. 236

VITA

NAME OF AUTHOR: Xueyuan Wang

MAJOR: Electrical and Computer Engineering

EDUCATION:

M.S. 2016 Syracuse University, Syracuse, N.Y.

B.E. 2013 Beijing University of Posts and Telecommunications, Beijing, China

AWARDS AND HONORS:

The LePage Fellowship Award

Certified in University Teaching, Future Professoriate Program